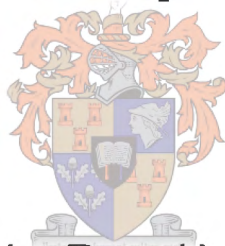


# **Borehole Radar System Analysis in Stratified Geological Systems Applied to Imaging of Platiniferous Reefs in the Bushveld Igneous Complex**



Paul Le Roux Herselman

Dissertation presented for the Degree of Doctor of Philosophy in Engineering  
at the University of Stellenbosch.

Promoters:

Prof. J. H. Cloete

Prof. I. M. Mason

December 2003

UNIV.STELLENBOSCH



300 783 4320

# DECLARATION

I, the undersigned, hereby declare that the work contained in this dissertation is my own original work, unless stated otherwise, and has not been previously, in its entirety or in part, submitted at any university for a degree.



P. Le R. Herselman

Date: 11 November 2003

# ABSTRACT

The imaging of platinumiferous reefs in the Bushveld Igneous Complex (BIC) is of great economical and sociological importance. Borehole radar technology has been identified as a viable mapping tool to be used in day-to-day mining operations, but a critical assessment has to be made on the feasibility of this postulation.

The system analysis made of the borehole radar deployed in the BIC is presented in this dissertation. The analysis is done using a specific example - the GeoMole borehole radar system.

A novel procedure, based on the basic theory of electromagnetic radiation and propagation, is proposed by which the entire physical radar system can be characterized. The power transmitted by an unconventional borehole-deployed transmitter is estimated by a sequence of free space measurements, numerical simulations and theoretic derivations and approximations. Antenna transfer functions (magnitude and phase) are numerically simulated for a variety of deployment configurations. The total system transfer function of the receiver analogue and digital chain is determined. This enables the calculation of the radar's performance figures necessary to determine the applicability of the radar in a specific geological setting.

A radar system is only complete when considered in its environment. The BIC is a stratified system of numerous rock layers. An in-depth study is done on the propagation of radiowaves in stratified lossy media. Only the case for non-magnetic media is discussed in this dissertation. The developed theory is used to predict the system response to a typical transmitted radar pulse in the UG1 – UG2 stratigraphy of the BIC, determine the maximum detection range of reef horizons and estimate the reflectivity of the reefs.

Resolution is one of the key parameters that determine the performance and accuracy of imaging. An algorithm is proposed, developed and tested by which the resolution of the system is increased and overlapping echoes become resolvable.

Even though some of the techniques are developed with a specific system in mind, the applicability of the concepts and algorithms is universal.

# OPSOMMING

Beeldvorming van die platinumryke rotsriwwe in die Bosveldsisteem is van kardinale ekonomiese en sosiologiese belang. Boorgatradar tegnologie is geïdentifiseer as 'n moontlike beeldvormingsinstrument wat gebruik kan word in die beplanning van mynwerke op 'n dag-tot-dag basis. 'n Kritiese analise moet egter eers gedoen word om hierdie moontlikheid te ondersoek.

Die kwantitatiewe stelselanalise van 'n ontplooië boorgatradar in die Bosveldsisteem word in hierdie proefskrif aangebied. Dit word gedoen aan die hand van 'n bestaande stelsel – die GeoMole boorgatradar.

'n Nuwe prosedure word voorgestel waarmee die hele stelsel gekarakteriseer word. Dit is gebaseer op die basiese beginsels van elektromagnetiese straling en voortplanting. Die stralingsdrywing van 'n sender antenna in 'n boorgat word benader deur 'n reeks vrye ruimte metings, numeriese simulاسies en teoretiese afleidings en benaderings. Die oordragsfunksie van die antennes in verskeie ontplooiing konfigurasies word bepaal deur numeriese simulاسies. Die totale oordragsfunksie van die analoog en digitale ontvangerketting word ook bepaal. Gevolglik kan die nodige werkverrigting parameters van die stelsel bereken word wat bepaal of die radarstelsel suksesvol in die gegewe omgewing gebruik kan word.

'n Radarstelsel is slegs volledig wanneer dit in sy omgewing beskou word. Die Bosveldsisteem is 'n gestratifiseerde stelsel van veelvuldige rotslae. 'n Studie word gedoen oor die voortplanting van radiogolwe in gestratifiseerde lae met diëlektriese verliese. Slegs die geval van nie-magnetiese materie word in hierdie proefskrif ondersoek. Die ontwikkelde teorie word gebruik om die reaksie van 'n tipiese uitgestraalde radarpuls in die UG1 – UG2 stratigrafie van die Bosveldsisteem te voorspel. Die maksimum waarneembare afstand van die rifhorisonne word bepaal en skattings word gemaak oor die sterkte van rifweerkaatsings.

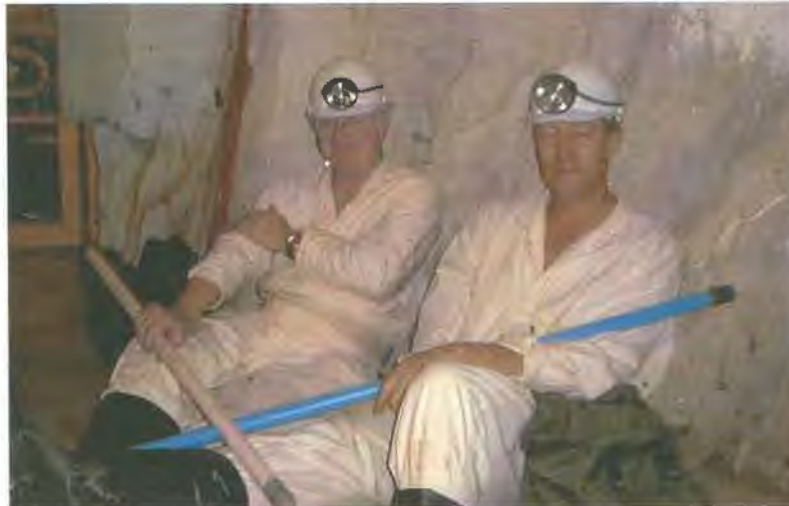
Resolusie bepaal die werksverrigting en akkuraatheid van beeldvormingstegnieke. 'n Algoritme word voorgestel, ontwikkel en getoets waarmee die resolusie van die stelsel verbeter en oorvleuelende weerkaatsings herwin kan word.

Die tegnieke, konsepte en algoritmes in hierdie proefskrif is ontwikkel vir 'n spesifieke stelsel, maar het universele toepassings.

# ACKNOWLEDGEMENTS

I would like to use this opportunity to thank the following people. Without you this dissertation would not have been possible.

Professors Johannes Cloete and Iain Mason,



I deeply thank you for all your support, enthusiasm and guidance from the first time that we set foot 3000 meters below the surface. The knowledge gained by just listening to you has enriched me for life. Professor Cloete, you taught me the importance of physical reasoning and to enjoy the goodness of the Winelands. Professor Mason, your teachings and remarks were invaluable.

Professor Keith Palmer for your help whenever I needed a quick answer to an annoying problem.

Wessel Croukamp, Wessel van Brakel, Marc Rütshlin, Jonathan Hargreaves and Carina Simmat for the times we spent together underground and your assistance in numerous ways.

The guys from Molshoop – Paul, Max, Marius, Brian, Beukes and Wernich (*bona fide*) – I will never forget the times we spent talking, laughing, drinking coffee, playing office cricket and working (I almost forgot).

André du Toit (*alias* Koos Kombuis) for helping me through the rough times.

My mother and father, family and friends for believing in me, praying for me and supporting me.

Luzanne, there are no words to thank you enough or express my deepest appreciation for being there for me all the way, supporting me, encouraging me and most of all loving me.

Finally and most importantly I want to thank God, my heavenly father, for being in control and giving us a peek at His awesome nature, of which electromagnetic wave propagation is an integral part.

# CONTENTS

<b>LIST OF FIGURES</b> .....	<b>x</b>
<b>LIST OF TABLES</b> .....	<b>xix</b>
<b>LIST OF ABBREVIATIONS</b> .....	<b>xx</b>
<b>GLOSSARY OF GEOLOGICAL TERMS</b> .....	<b>xxii</b>
<b>CHAPTER 1: INTRODUCTION</b> .....	<b>1</b>
1.1 BACKGROUND.....	1
1.2 PROBLEM DEFINITION.....	3
1.3 DESCRIPTION OF GEOMOLE BHR SYSTEM.....	4
1.4 OUTLINE OF DISSERTATION.....	7
1.5 LITERATURE REVIEW.....	8
1.6 ORIGINAL CONTRIBUTIONS.....	9
<b>CHAPTER 2: BOREHOLE RADAR SYSTEM ANALYSIS</b> .....	<b>10</b>
2.1 LITERATURE REVIEW.....	10
2.2 MOTIVATION FOR GEOMOLE BHR SYSTEM ANALYSIS.....	11
2.3 BHR SYSTEM ANALYSIS AND CALIBRATION.....	12
2.4 SUMMARY OF GEOMOLE BHR SYSTEM ANALYSIS.....	13
<b>CHAPTER 3: CHARACTERIZATION OF TX AND RX PROBES</b> .....	<b>15</b>
3.1 LITERATURE REVIEW.....	15
3.2 OVERVIEW OF TRANSMITTER ELECTRONICS AND THE ANTENNAS.....	16
3.3 DESIGN OF A FREE SPACE CALIBRATION FACILITY.....	18
3.3.1 <i>Calibration Facility Topology</i> .....	18
3.3.2 <i>Electromagnetic Propagation Constraints</i> .....	19
3.3.3 <i>Dynamic Range Constraints</i> .....	21
3.3.4 <i>EMI Considerations</i> .....	22
3.4 REALIZATION OF CALIBRATION FACILITY.....	22
3.4.1 <i>Qualitative Description</i> .....	23
3.4.2 <i>Quantitative Description</i> .....	24
3.4.3 <i>Low-Power Calibration Transmitter</i> .....	27
3.4.4 <i>Reference Receiver</i> .....	33
3.4.5 <i>Desensitised Calibration Receiver</i> .....	35
3.4.6 <i>Instrumentation Optic Link</i> .....	37
3.5 FREE SPACE TRANSMITTER CHARACTERISTICS.....	38
3.5.1 <i>GeoMole TX Antenna Response</i> .....	38
3.5.2 <i>Rooftop Calibration Measurement Results</i> .....	40
3.5.3 <i>Transmitter Power Estimation</i> .....	43
3.6 FREE SPACE RECEIVER CHARACTERISTICS.....	44
3.6.1 <i>Power Delivered by Calibration TX Estimation</i> .....	45
3.6.2 <i>GeoMole RX Antenna Response</i> .....	45
3.6.3 <i>GeoMole RX RF &amp; Optic Electronics</i> .....	47
3.6.4 <i>Rooftop Calibration Measurements</i> .....	48
3.6.5 <i>Relative Receiver Performance</i> .....	50

3.7	TRANSFER FUNCTION WHEN RADAR IS DEPLOYED IN ROCK BOREHOLES .....	51
3.7.1	<i>Quantitative Coupling Description</i> .....	51
3.7.2	<i>Deployed Antenna Characteristics</i> .....	53
3.7.3	<i>Power Delivered to TX Antenna</i> .....	57
3.8	CONCLUDING REMARKS .....	58
<b>CHAPTER 4: CHARACTERIZATION OF RECEIVER CHAIN.....</b>		<b>59</b>
4.1	QUANTITATIVE DESCRIPTION OF RF CHAIN .....	59
4.2	DEFINITION OF A CALIBRATION STANDARD AND RELATIVE GAINS .....	62
4.3	CALIBRATION STANDARD AND RELATIVE GAIN MEASUREMENTS.....	64
4.3.1	<i>Measurement of Fibre Optic Loss Factor</i> .....	64
4.3.2	<i>Total Reference Gain of the Two Topologies</i> .....	65
4.3.3	<i>Relative Gain of Optic &amp; Electronic Components</i> .....	68
4.3.4	<i>Comments on Repeatable Fibre Optic Measurements</i> .....	72
4.4	NOISE FIGURE MEASUREMENTS.....	72
4.4.1	<i>The HP 8970B Noise Figure Meter System</i> .....	73
4.4.2	<i>Dynamic Range Analysis</i> .....	74
4.4.3	<i>Dynamic Range Improvement</i> .....	75
4.4.4	<i>Noise Figure Measurement Results</i> .....	76
4.5	CHARACTERIZATION OF DATA ACQUISITION UNIT .....	77
4.5.1	<i>Long-Pulse Response Measurement</i> .....	78
4.5.2	<i>Short-Pulse Response Measurement</i> .....	82
4.5.3	<i>SFCW Response Measurement</i> .....	85
4.5.4	<i>Theory of Digitisation and Stacking Process</i> .....	86
4.5.5	<i>Comparing Practical and Theoretical Results</i> .....	90
4.6	SYSTEM PARAMETER EXTRACTION.....	91
4.6.1	<i>Maximum Available Power</i> .....	91
4.6.2	<i>Noise Figure Estimation</i> .....	93
4.6.3	<i>Permissible Signal Attenuation</i> .....	96
4.6.4	<i>Time-offset Estimation</i> .....	97
4.7	CONCLUDING REMARKS .....	100
<b>CHAPTER 5: PULSE RECOMPRESSION .....</b>		<b>102</b>
5.1	LITERATURE REVIEW .....	102
5.2	INFERRING THE INPUT VOLTAGE OF THE RX CHAIN.....	103
5.3	ESTIMATING THE ELECTRIC FIELD AT THE RECEIVER ANTENNA.....	103
5.4	WINDOWING THE INFERRED AND ESTIMATED RESPONSES .....	106
5.5	PRELIMINARY RESULTS .....	108
5.5.1	<i>Laboratory Experiment</i> .....	108
5.5.2	<i>Field Experiment</i> .....	110
5.6	FIELD EXPERIMENT PULSE RECOMPRESSION .....	111
5.6.1	<i>Batch Pulse Recompression Algorithm</i> .....	112
5.6.2	<i>Field Experiment Results</i> .....	113
5.7	CONCLUDING REMARKS .....	118

<b>CHAPTER 6: PROPAGATION IN THE ROCK STRATA OF THE UG1 – UG2 SYSTEM OF THE BUSHVELD IGNEOUS COMPLEX .....</b>	<b>120</b>
6.1 LITERATURE REVIEW .....	120
6.2 GEOLOGY OF THE BIC UG1 – UG2 STRATIGRAPHY .....	121
6.2.1 <i>Layered Cr-Pt Complexes</i> .....	121
6.2.2 <i>Bushveld Igneous Complex</i> .....	122
6.2.3 <i>Generalization of UG1 – UG2 Stratigraphy</i> .....	123
6.2.4 <i>Geometry of Perturbations</i> .....	127
6.3 SIMPLIFIED PLANAR MODEL APPROXIMATION .....	128
6.4 DIELECTRIC PROPERTIES OF ROCKS .....	130
6.5 RADIATION IN A LOSSY HOMOGENEOUS MEDIUM .....	134
6.6 POSSIBLE DETECTION RANGE IN BIC .....	136
6.7 PROPAGATION VELOCITY ESTIMATES .....	137
6.7.1 <i>Bleskop I Propagation Velocity Estimate</i> .....	138
6.7.2 <i>Bleskop II Propagation Velocity Estimate</i> .....	139
6.8 QUALITY FACTOR ESTIMATES .....	142
6.9 CONCLUDING REMARKS .....	151
<b>CHAPTER 7: THEORY OF PLANE WAVE PROPAGATION IN STRATIFIED LOSSY MATTER .....</b>	<b>152</b>
7.1 LITERATURE REVIEW .....	152
7.2 ELECTROMAGNETIC PRELIMINARIES .....	153
7.2.1 <i>Vector Wave Equation for Isotropic Media</i> .....	154
7.2.2 <i>Scalar Wave Equations for One-Dimensional Planar Inhomogeneity</i> .....	155
7.3 REFLECTION FROM A HALF-SPACE .....	156
7.3.1 <i>Incident Field</i> .....	158
7.3.2 <i>Reflected and Transmitted Fields</i> .....	158
7.3.3 <i>Branch Choice for TE Waves</i> .....	160
7.3.4 <i>TE Beam Wave Incident on Planar Inhomogeneity</i> .....	168
7.3.5 <i>Energy Conservation for TE Waves</i> .....	171
7.3.6 <i>Branch Choice for TM Waves</i> .....	174
7.4 REFLECTION AND TRANSMISSION IN A MULTILAYERED PLANAR SYSTEM ..	177
7.4.1 <i>Branch Choice for TE Waves</i> .....	179
7.4.2 <i>Branch Choice for TM Waves</i> .....	180
7.5 CONCLUDING REMARKS .....	181
<b>CHAPTER 8: PROPAGATION AND DETECTION IN THE STRATIFIED UG1 – UG2 SYSTEM .....</b>	<b>182</b>
8.1 LITERATURE REVIEW .....	182
8.2 PULSE SHAPE APPROXIMATION FOR THEORETICAL PREDICTIONS .....	183
8.3 PLANAR INTERFACE PULSE REFLECTION .....	188
8.3.1 <i>Interface Reflections for TE Polarized Pulses</i> .....	189
8.3.2 <i>Interface Reflections for TM Polarized Pulses</i> .....	193
8.4 SANDWICHED LAYER PULSE REFLECTION .....	195
8.5 MULTIPLE LAYER PULSE REFLECTION AND TRANSMISSION .....	201
8.5.1 <i>Illuminating the UG2 Reef From Below</i> .....	201
8.5.2 <i>Illuminating the UG1 Layers From Above</i> .....	205
8.6 UG2 DETECTION RANGE PREDICTION .....	208

8.7	UG2 REFLECTIVITY ESTIMATION .....	213
8.7.1	<i>Experimental Subset that Satisfies Criteria Set</i> .....	213
8.7.2	<i>Borehole and UG2 Reef Horizon Delineation</i> .....	215
8.7.3	<i>Radar Configuration and Calibration</i> .....	220
8.7.4	<i>Calculating <math>R^{TM}</math> Using Power Relations</i> .....	221
8.8	CONCLUDING REMARKS .....	222
<b>CHAPTER 9: CONCLUSIONS &amp; RECOMMENDATIONS .....</b>		<b>223</b>
9.1	CONCLUSIONS .....	223
9.1.1	<i>Characterization of System Transfer Function</i> .....	223
9.1.2	<i>Novel Pulse Recompression Algorithm</i> .....	224
9.1.3	<i>Plane Wave EM Propagation in Stratified Absorbing Layers</i> .....	225
9.1.4	<i>Estimation of the Reflected Waveforms</i> .....	225
9.1.5	<i>Limitations Imposed on Geometry Delineation Using BHR Technology</i> .....	226
9.2	RECOMMENDATIONS FOR FUTURE WORK .....	226
9.2.1	<i>System Characterization and Pulse Recompression</i> .....	226
9.2.2	<i>Radiowave Propagation in Stratified Lossy Media</i> .....	227
9.2.3	<i>Software Implementation of Pulse Recompression Algorithm</i> .....	227
<b>APPENDIX A: KLEINZEE FIELD EXPERIMENT .....</b>		<b>228</b>
<b>APPENDIX B: FEKO SIMULATIONS .....</b>		<b>234</b>
<b>APPENDIX C: ADDITIONAL DAQ MEASUREMENT RESULTS .....</b>		<b>250</b>
<b>APPENDIX D: BLESKOP I FIELD EXPERIMENT .....</b>		<b>253</b>
<b>APPENDIX E: BRAKSPRUIT I FIELD EXPERIMENT .....</b>		<b>259</b>
<b>APPENDIX F: BLESKOP II FIELD EXPERIMENT .....</b>		<b>268</b>
<b>APPENDIX G: PULSE RECOMPRESSION PROGRAM .....</b>		<b>279</b>
<b>APPENDIX H: CALIBRATION FACILITY CIRCUIT DIAGRAMS .....</b>		<b>282</b>
<b>BIBLIOGRAPHY .....</b>		<b>284</b>

# LIST OF FIGURES

<i>Figure 1-1: Basic GeoMole BHR deployment configuration.</i>	2
<i>Figure 1-2: GeoMole borehole radar system with deployment equipment and operators.</i>	5
<i>Figure 1-3: Block diagram of GeoMole borehole radar.</i>	5
<i>Figure 3-1: Block diagram of line type modulator [75].</i>	16
<i>Figure 3-2: Asymmetric resistively loaded dipole antenna.</i>	17
<i>Figure 3-3: Geometry of rooftop calibration facility.</i>	19
<i>Figure 3-4: Masts, probes and optic fibres of the free space, open air calibration facility.</i>	23
<i>Figure 3-5: SCU and data capturing units of calibration facility with captured trace insert.</i>	23
<i>Figure 3-6: Simplified block diagram of rooftop calibration system.</i>	23
<i>Figure 3-7: Power flow schematic for rooftop calibration facility.</i>	24
<i>Figure 3-8: Complete schematic diagram of calibration facility receiver chain.</i>	26
<i>Figure 3-9: Block diagram of calibration transmitter.</i>	27
<i>Figure 3-10: Bottom layer of calibration transmitter electronics.</i>	28
<i>Figure 3-11: Top layer of calibration transmitter electronics.</i>	28
<i>Figure 3-12: Implementation of pulse generator using logic gates and MOSFET driver.</i>	29
<i>Figure 3-13: Timing diagram of pulse generator circuit.</i>	29
<i>Figure 3-14: Calibration transmitter antenna characteristics.</i>	31
<i>Figure 3-15: Inferred transmitted waveforms for different time and voltage settings.</i>	32
<i>Figure 3-16: Power spectral densities for different time and voltage settings.</i>	32
<i>Figure 3-17: Reference receiver antenna characteristics.</i>	34
<i>Figure 3-18: Reference receiver transfer function and 1 dB compression point.</i>	35
<i>Figure 3-19: Transfer function of the calibration receiver front-end.</i>	36
<i>Figure 3-20: Calibration receiver electronics, antenna, power supply and connectors.</i>	37
<i>Figure 3-21: Instrumentation SCU developed for rooftop calibration facility.</i>	37
<i>Figure 3-22: Transfer functions of the reference and calibration optic links.</i>	37
<i>Figure 3-23: GeoMole transmitter free space antenna characteristics.</i>	40
<i>Figure 3-24: Time and frequency domain response of the USTX 01 transmitter.</i>	41
<i>Figure 3-25: Time and frequency domain responses of the USTX transmitters.</i>	42

Figure 3-26: Trigger signal of different transmitter topologies.	42
Figure 3-27: Power delivered to the RF front-end and TX antenna for the USTX 01 transmitter.	43
Figure 3-28: Comparing the power delivered to the TX antennas for the different transmitters.	44
Figure 3-29: Power delivered to the RF front-end and TX antenna for the calibration transmitter.	45
Figure 3-30: GeoMole receiver free space antenna characteristics.	46
Figure 3-31: GeoMole receiver transfer function and 1 dB compression point.	47
Figure 3-32: Transfer functions of the GeoMole receiver and instrumentation optic link.	48
Figure 3-33: Time and frequency domain response of USRX 02 receiver for a 2 MHz PRF.	48
Figure 3-34: EMI reduction for USRX 02 receiver by time-gating.	49
Figure 3-35: Resampled response of the different GeoMole receivers.	49
Figure 3-36: Relative receiver patchcord gain of different receivers.	50
Figure 3-37: Power flow schematic for probes deployed in boreholes surrounded by host medium.	52
Figure 3-38: GeoMole TX antenna response when deployed in a norite host medium borehole.	54
Figure 3-39: GeoMole TX antenna response when deployed in a water-filled (low salt content), norite host medium borehole.	55
Figure 3-40: GeoMole RX antenna response when deployed in a norite host medium borehole.	56
Figure 3-41: Power delivered to TX antenna in free space and borehole deployed (norite rock).	57
Figure 3-42: Increase in power delivered to TX antenna when borehole deployed.	57
Figure 4-1: Signal flow through the first receiver chain.	60
Figure 4-2: Differences in the receiver chain signal flow diagram for the second receiver.	61
Figure 4-3: Physical configuration for loss factor measurements.	64
Figure 4-4: Estimated loss factor for a wound up 100/140 $\mu\text{m}$ optic fibre.	65
Figure 4-5: Reference fibre optic configuration for 1 <sup>st</sup> RF chain.	66
Figure 4-6: Total reference gain of the first receiver chain.	66
Figure 4-7: Reference fibre optic configuration for 2 <sup>nd</sup> RF chain.	67
Figure 4-8: Total reference gain of the second receiver chain.	67
Figure 4-9: Relative gain and phase response of the different reinforced optic cables.	68
Figure 4-10: Relative gain of the different DAQ patchcords.	69
Figure 4-11: Relative gain and phase response of the different SCU's (1).	69
Figure 4-12: Relative gain and phase response of the different SCU's (2).	70

Figure 4-13: Relative gain of coupling patchcord.	71
Figure 4-14: Relative gain of the SMA barrels.	71
Figure 4-15: Relative gain of the different FORJ's.	71
Figure 4-16: HP 8970B noise figure meter.	73
Figure 4-17: HP 346B noise source.	73
Figure 4-18: Block diagram of noise measurement of DUT.	74
Figure 4-19: Circuit diagram of low noise front-end amplifier.	75
Figure 4-20: Noise figure of various cascaded systems.	76
Figure 4-21: Gain of various cascaded systems.	76
Figure 4-22: Gain and noise figure of GeoMole receiver amplifier cascaded with optic link.	77
Figure 4-23: Gain and noise figure of optic link.	77
Figure 4-24: Chase CS2250 analogue-to-digital converter unit.	78
Figure 4-25: Measurement configuration for pulse response measurement.	79
Figure 4-26: Reference pulse for ADC characterization measurements.	79
Figure 4-27: Frequency spectrum of input reference pulse.	79
Figure 4-28: Comparison of ADC channel responses to a 125 ns pulse.	80
Figure 4-29: Actual and Resampled Response of Channel 1 of ADC serial number #208.	81
Figure 4-30: Magnitude response for channel 1 of ADC #208 with 0.5 V clipping and 128 stacking.	81
Figure 4-31: Phase response for channel 1 of ADC #208 with 0.5 V clipping and 128 stacking.	81
Figure 4-32: Magnitude response for channel 1 of ADC #208 with 0.5 V clipping for different stackings.	82
Figure 4-33: Magnitude response for different ADC channels and clippings with 512 stacking.	82
Figure 4-34: Reference pulse used to measure the short-pulse response of the ADC units.	82
Figure 4-35: Frequency spectrum of the short reference pulse.	82
Figure 4-36: Short pulse responses for the two main ADC units (serial numbers #208 and #207).	83
Figure 4-37: Actual and Resampled Response of Channel 1 of ADC serial number #208.	84
Figure 4-38: Magnitude response of channel 1 of ADC serial number #208 at 0.5 V clipping and 512 stacking for a short pulse.	84
Figure 4-39: Phase response of channel 1 of ADC serial number #208 at 0.5 V clipping and 512 stacking for a short pulse.	84
Figure 4-40: Stepped frequency continuous wave response measurement setup.	85

<i>Figure 4-41: SFCW magnitude response of ADC unit channels.</i>	86
<i>Figure 4-42: EM coupling between different channels on the ADC units.</i>	86
<i>Figure 4-43: Stacking process of the Chase CS2250 ADC units.</i>	87
<i>Figure 4-44: Stacking process of phasors in the presence of asynchronous triggering.</i>	89
<i>Figure 4-45: Magnitude response of asynchronous trigger filter function.</i>	89
<i>Figure 4-46: Phase response of asynchronous trigger filter function.</i>	89
<i>Figure 4-47: Comparison of theoretical and measured magnitude response of the ADC.</i>	90
<i>Figure 4-48: Comparison of theoretical and measured phase response of the ADC.</i>	90
<i>Figure 4-49: Maximum available power for different transmitter configurations.</i>	92
<i>Figure 4-50: Subsystems in the GeoMole receiver RF chain.</i>	93
<i>Figure 4-51: Thévenin equivalent of intercepted noise.</i>	93
<i>Figure 4-52: Noise figures for 2 cascaded GeoMole receiver chains.</i>	95
<i>Figure 4-53: Equivalent input noise powers for two GeoMole receiver chain configurations.</i>	95
<i>Figure 4-54: Maximum permissible signal attenuation for SNR = 1.</i>	96
<i>Figure 4-55: Timing diagram for the trigger and signal channels.</i>	97
<i>Figure 4-56: Illustrative definition of timing nomenclature.</i>	97
<i>Figure 4-57: Configuration of experiment to measure the pre-triggering time.</i>	99
<i>Figure 4-58: Captured trace for the measurement of the pre-triggering time.</i>	99
<i>Figure 5-1: Norton equivalent circuit of receiver antenna connected to a resistive load.</i>	105
<i>Figure 5-2: Window function in pulse recompression algorithm.</i>	107
<i>Figure 5-3: Deconvolution results for calibration transmitter and reference receiver.</i>	108
<i>Figure 5-4: Deconvolution results for USTX 03 transmitter and reference receiver.</i>	109
<i>Figure 5-5: Deconvolution results for USTX 03 transmitter and USRX 02 receiver in a cross-hole configuration in a norite host medium.</i>	111
<i>Figure 5-6: Comparison of estimated E-field with bandpass filtered data – GHB46 profile.</i>	114
<i>Figure 5-7: Comparison of estimated E-field with bandpass filtered data – GHB47 profile.</i>	115
<i>Figure 5-8: Comparison of estimated E-field with bandpass filtered data – GHB2 profile.</i>	116
<i>Figure 5-9: Comparison of estimated E-field with bandpass filtered data – LIB19B profile.</i>	118
<i>Figure 6-1: Geological map of the Bushveld Igneous Complex [34].</i>	123
<i>Figure 6-2: Stratigraphic column of UG1 - UG2 layering at RPM's Bleskop Mine.</i>	124

Figure 6-3: UG1 chromitite layers (Courtesy of K. Chotoki, Anglo Platinum).	125
Figure 6-4: Single chromitite stringer (Courtesy of K. Chotoki, Anglo Platinum).	125
Figure 6-5: Bleskop marker sequence.	125
Figure 6-6: UG2 chromitite reef.	126
Figure 6-7: Chromitite leader.	127
Figure 6-8: Chromitite triplets.	127
Figure 6-9: Schematic dip section demonstrating local changes in dip, strike and thickness [30].	127
Figure 6-10: Real part of normalized dielectric permittivity for BIC rocks.	132
Figure 6-11: Propagation velocity for rock layers in BIC.	132
Figure 6-12: Quality factor for rock layers in BIC.	133
Figure 6-13: Borehole trajectories with TX and RX feedpoints used for velocity estimation.	140
Figure 6-14: Automatic picking of first trough signal event.	141
Figure 6-15: First trough auto picking for the entire radar scan.	141
Figure 6-16: Local and average estimated pulse peak velocity.	142
Figure 6-17: Section of raw radar data where direct wave is spatially separated.	143
Figure 6-18: Reconstructed incident E-field for trace 30.	144
Figure 6-19: Power budget for trace 30.	144
Figure 6-20: Borehole trajectories with transmitter and receiver locations for Q estimation.	145
Figure 6-21: Translated and rotated coordinates of TX/RX feed- and endpoints for Q estimation.	146
Figure 6-22: Directivity and polarization angles for the different traces used in Q estimation.	147
Figure 6-23: Individual and average $Q_{\text{horite}}$ estimates as a function of frequency.	147
Figure 6-24: $Q_{\text{horite}}$ approximated by a quadratic polynomial.	148
Figure 6-25: Section of raw radar data where direct wave is spatially separated for 2 <sup>nd</sup> Q estimate.	149
Figure 6-26: Interference of secondary pulse	150
Figure 6-27: Spatially separated direct wave and secondary pulses for trace 25.	150
Figure 6-28: Second $Q_{\text{horite}}$ estimate approximated by a cubic polynomial and compared to the first estimate approximation.	151
Figure 7-1: Q as a function of frequency.	154
Figure 7-2: Reflection and transmission of a TE inhomogeneous plane wave at an interface.	157
Figure 7-3: Mapping of $k_{2z}^2$ for $\text{Im}\{k_{2z}^2\} \geq 0$ to the $k_{2z}$ space.	162

Figure 7-4: Mapping of $k_{2z}^2$ for $\text{Im}\{k_{2z}^2\} \leq 0$ and $\text{Re}\{k_{2z}^2\} \geq 0$ to the $k_{2z}$ space.	163
Figure 7-5: The behaviour of the squares of $k_1$ , $k_1 \sin \theta_1$ , $k_2$ and $k_{2z}$ in the complex plane for $\delta_2 < \delta_1$ .	164
Figure 7-6: Mapping of $k_{2z}^2$ for $\text{Im}\{k_{2z}^2\} \leq 0$ , $\text{Re}\{k_{2z}^2\} \geq 0$ and $\delta_2 < \delta_1$ to the $k_{2z}$ space.	165
Figure 7-7: The behaviour of the squares of $k_1$ , $k_1 \sin \theta_1$ , $k_2$ and $k_{2z}$ in the complex plane for $\delta_2 > \delta_1$ .	166
Figure 7-8: Mapping of $k_{2z}^2$ for $\text{Im}\{k_{2z}^2\} \leq 0$ , $\text{Re}\{k_{2z}^2\} \geq 0$ and $\delta_2 > \delta_1$ to the $k_{2z}$ space.	166
Figure 7-9: Beam wave incident on planar inhomogeneity	168
Figure 7-10: Closed volume $V$ for energy conservation calculations.	172
Figure 7-11: Mapping of $k_{2z}^2$ to the $k_{2z}$ space for region C.	176
Figure 7-12: Mapping of $k_{2z}^2$ to the $k_{2z}$ space for region D.	177
Figure 7-13: Reflection and transmission in a multilayered system.	178
Figure 8-1: Digitally stored direct wave pulse for GeoMole BHR.	184
Figure 8-2: Time domain comparison of Ricker wavelet to actual pulse.	185
Figure 8-3: Frequency domain comparison of Ricker wavelet to actual pulse.	185
Figure 8-4: Deconvolved E-field for trace 30.	186
Figure 8-5: Time domain comparison of monocycle wavelet to deconvolved E-field.	187
Figure 8-6: Frequency domain comparison of monocycle wavelet to deconvolved E-field.	187
Figure 8-7: Geometry for planar interface pulse reflection.	188
Figure 8-8: Reflection coefficient for TE polarized pulses with norite and chromitite half-spaces as a function of incidence angle.	189
Figure 8-9: Reflection coefficient for TE polarized pulses with norite and chromitite half-spaces as a function of frequency.	190
Figure 8-10: Effective path length increase for TE pulses as a function of frequency.	191
Figure 8-11: Observed interface depth increase for TE pulses as a function of frequency.	191
Figure 8-12: Modified time domain reflected E-fields for TE waves incident on planar interface.	192
Figure 8-13: Time domain reflected TE wave for normal incidence indicating time retardation.	192
Figure 8-14: Reflection coefficient for TM polarized pulses with norite and chromitite half-spaces as a function of incidence angle.	193
Figure 8-15: Reflection coefficient for TM polarized pulses with norite and chromitite half-spaces as a function of frequency for different incidence angles.	194
Figure 8-16: Modified time domain reflected H-fields for TM waves incident on planar interface.	195
Figure 8-17: Geometry for sandwiched layer pulse reflection.	196

Figure 8-18: Reflection coefficient for interface between regions 1 and 2 as a function of frequency and incidence angle. _____	198
Figure 8-19: Reflection coefficient for interface between regions 2 and 3 as a function of frequency and incidence angle. _____	198
Figure 8-20: The time domain reflections from the two interfaces yielding the total reflection of the sandwiched layer. _____	199
Figure 8-21: Total time domain reflected field as a function of incidence angle. _____	200
Figure 8-22: Total time domain reflected field as a function of the sandwich thickness $h_2$ . _____	200
Figure 8-23: Time domain reflections for a TM polarized pulse incident on the UG2 from below. _	203
Figure 8-24: Individual contributions to the total reflection of the UG2 reef horizon. _____	205
Figure 8-25: One-way transmissivity of the Bleskop Marker sequence. _____	205
Figure 8-26: Time domain reflections for a TM polarized pulse incident on the UG1 from above. _	207
Figure 8-27: Maximum available power spectral density for a typical configuration. _____	209
Figure 8-28: Front-end noise power spectral density for a typical configuration. _____	209
Figure 8-29: Maximum signal attenuation with SNR = 0 dB for the GeoMole borehole radar. ____	210
Figure 8-30: Signal power attenuation as a function of frequency for discrete ranges. _____	211
Figure 8-31: Signal power attenuation as a function of frequency and range. _____	211
Figure 8-32: Section of raw data used to estimate UG2 reflectivity. _____	214
Figure 8-33: Transmitter and receiver locations for reflectivity estimation. _____	215
Figure 8-34: Transmitter and receiver feedpoints and nadir points for reflectivity estimation. ____	216
Figure 8-35: Rotated TX and RX coordinates for reflectivity estimation – side view. _____	217
Figure 8-36: Rotated TX and RX coordinates for reflectivity estimation – top view. _____	217
Figure 8-37: TM and TE polarization components defined. _____	218
Figure 8-38: TM polarization components for transmitter and receiver. _____	219
Figure 8-39: Delineated geometry for reflectivity estimation. _____	219
Figure 8-40: Time-gated E-field for reflectivity estimation. _____	220
Figure 8-41: Reflectivity estimate of the UG2 reef interface. _____	221
Figure A-1: Geometry of the lined holes indicating depth and spacing. _____	229
Figure A-2: Geometry and photos of the cross-hole survey. _____	230
Figure A-3: Reflection coefficient at interface between layers L17m and L20m. _____	232
Figure A-4: Attenuation in L17m at 50 MHz. _____	232

<i>Figure A-5: Attenuation in L20m at 50 MHz.</i>	232
<i>Figure A-6: Radar B-scan of Up 2 shoot with 512 stacking.</i>	233
<i>Figure A-7: Cross-hole B-scan of Up 2 shoot with 512 stacking.</i>	233
<i>Figure B-1: Feed point of antenna with conducting half cylinder.</i>	236
<i>Figure B-2: Real part of antenna input impedance.</i>	236
<i>Figure B-3: Imaginary part of antenna input impedance.</i>	236
<i>Figure B-4: Geometry of third simulation, including the test environment.</i>	237
<i>Figure B-5: Magnitude of reflection coefficient.</i>	238
<i>Figure B-6: Phase of reflection coefficient.</i>	238
<i>Figure B-7: Segmented structure for TX and RX calibration antennas.</i>	239
<i>Figure B-8: Feed segment of the calibration antennas.</i>	240
<i>Figure B-9: Free space GeoMole antenna constructed in FEKO.</i>	241
<i>Figure B-10: Section of borehole deployed GM antenna as constructed in FEKO.</i>	242
<i>Figure B-11: Deployed GeoMole RX antenna directivity as calculated by FEKO.</i>	243
<i>Figure B-12: Antenna directivity and efficiency as calculated with algorithm.</i>	245
<i>Figure B-13: GeoMole TX antenna deployed in a borehole in pyroxenite (PX1) host medium.</i>	246
<i>Figure B-14: GeoMole TX antenna deployed in a borehole in pyroxenite (PX2) host medium.</i>	247
<i>Figure B-15: GeoMole TX antenna deployed in a borehole in UG2 bottom host medium.</i>	247
<i>Figure B-16: GeoMole TX antenna deployed in a borehole in UG2 top host medium.</i>	248
<i>Figure B-17: GeoMole RX antenna deployed in a borehole in VCR hanging wall host medium.</i>	249
<i>Figure C-1: 125 ns pulse response of ADC serial number #208.</i>	250
<i>Figure C-2: 125 ns pulse response of ADC serial number #207.</i>	251
<i>Figure C-3: 125 ns pulse response of ADC serial number #0000.</i>	251
<i>Figure C-4: Zoomed response of ADC serial number #208 indicating repetitive bit error.</i>	252
<i>Figure D-1: Part of BL1W_12 winze and the radar boreholes.</i>	253
<i>Figure D-2: Three boreholes (collars circled) at one of the stations.</i>	254
<i>Figure D-3: Cross-section of station B showing intersections with different strata. (Courtesy of Mr Kabelo Tlhapi, Senior Geologist, Bleskop ARD)</i>	254
<i>Figure D-4: Cross-hole survey between holes A3 and B3.</i>	255
<i>Figure D-5: Cross-hole survey between holes B3 and C3.</i>	256

<i>Figure D-6: Cross-hole survey between holes A3 and C3.</i>	256
<i>Figure D-7: Cross-hole survey between holes GBH6 and GBH7.</i>	258
<i>Figure E-1: Location of Brakspruit and Bleskop mines.</i>	260
<i>Figure E-2: Proposed location of boreholes in experimental site at Brakspruit Level 11.</i>	260
<i>Figure E-3: GBH1 - GBH3 boreholes at Brakspruit Level 11.</i>	261
<i>Figure E-4: Comparison of navigator inferred trajectory vs. the straight-line trajectory.</i>	262
<i>Figure E-5: Profile (ingoing) of GBH1 with basic interpretations.</i>	263
<i>Figure E-6: Profile (ingoing) of GBH2 with basic interpretations.</i>	265
<i>Figure E-7: Cross-hole survey between GBH2 (TX ingoing) and GBH1 (RX stationary @ 40 m).</i>	266
<i>Figure F-1: Proposed location of boreholes at 13 Level West Haulage, Bleskop.</i>	269
<i>Figure F-2: GBH46 - GBH50 borehole collars at 13 Level West Haulage, Bleskop.</i>	270
<i>Figure F-3: Plan view of boreholes in relation to site geometry at 13 Level West Haulage, Bleskop.</i>	270
<i>Figure F-4: Projection of boreholes on the west-to-east – elevation plane.</i>	271
<i>Figure F-5: Stratigraphic sections of the GBH46 and GBH47 boreholes.</i>	272
<i>Figure F-6: Stratigraphic sections of the GBH48, GBH49 and GBH50 boreholes.</i>	273
<i>Figure F-7: Physical configuration of profile scans at Bleskop, 13 Level West Haulage.</i>	274
<i>Figure F-8: Profile scans of GBH46 - GBH48 with elementary interpretations.</i>	275
<i>Figure F-9: Profile scans of GBH49 – GBH50 with elementary interpretations.</i>	276
<i>Figure F-10: Cross-hole surveys between GBH46 and GBH48, and GBH49 and GBH50.</i>	277
<i>Figure G-1: Main GUI console of batch-processing pulse recompression algorithm.</i>	279
<i>Figure G-2: GeoMole BHR system configuration console.</i>	280
<i>Figure G-3: Field experiment data control interface.</i>	280
<i>Figure G-4: Time-gating interface.</i>	280
<i>Figure G-5: Plot and export control interface.</i>	281
<i>Figure H-1: Calibration receiver circuit diagram.</i>	282
<i>Figure H-2: Calibration transmitter circuit diagram.</i>	283

# LIST OF TABLES

<i>Table 3-1: Resistive profile of resistively loaded calibration antenna.</i>	30
<i>Table 3-2: Time and voltage codes for calibration transmitter.</i>	32
<i>Table 3-3: Discrete resistor values for the resistively loaded GeoMole antenna arms.</i>	39
<i>Table 3-4: Calibration TX settings for GeoMole RX calibration.</i>	45
<i>Table 3-5: Average relative receiver patchcord gain.</i>	50
<i>Table 4-1: Configuration of 1<sup>st</sup> reference receiver chain.</i>	65
<i>Table 4-2: Configuration of 2<sup>nd</sup> reference receiver chain.</i>	67
<i>Table 4-3: Noise measurement system performance.</i>	73
<i>Table 4-4: Configuration of two optic links for noise figure calculations.</i>	95
<i>Table 4-5: First break and event time offsets with a 3.1 m optic spacer.</i>	100
<i>Table 5-1: Optic link configuration for cross-hole survey between holes 46 and 48.</i>	110
<i>Table 5-2: Receiver chain configuration for the GBH46 profile.</i>	113
<i>Table 5-3: Receiver chain configuration for the GBH2 profile.</i>	117
<i>Table 6-1: Simplified planar UG1 - UG2 stratigraphy at Bleskop.</i>	129
<i>Table 6-2: Jonscher parameters for BIC rocks [39].</i>	131
<i>Table 8-1: Stratigraphy for numeric simulation of TM pulse incident on UG2 reef from below.</i>	202
<i>Table 8-2: Stratigraphy for numeric simulation of TM pulse incident on UG1 layers from above.</i>	206
<i>Table 8-3: Assumptions and approximation used in the UG2 detection range prediction.</i>	208
<i>Table A-1: Dielectric properties of L17m layer sample.</i>	231
<i>Table A-2: Dielectric properties of L20m layer sample.</i>	231
<i>Table E-1: Comparison between actual and intended borehole collar coordinates and directions.</i>	261
<i>Table F-1: Designed vs. true borehole lengths and directions.</i>	271

# LIST OF ABBREVIATIONS

ADC	Analogue-to-digital converter
AGC	Automatic gain control
BHR	Borehole radar
BIC	Bushveld Igneous Complex
BITE	Built-in test equipment
CW	Continuous wave
DAQ	Data acquisition unit
dB	Decibel
DC	Direct current
DFT	Discrete Fourier transform
DPSD	Double-sided power spectral density
DUT	Device under test
EM	Electromagnetic
EMI	Electromagnetic interference
ENR	Excess noise ratio
EOH	End of hole
FDTD	Finite difference time domain
FORJ	Fibre optic rotary joint
GBH	Geological borehole
GCA	Gain calculation algorithm
GHz	Gigahertz
GM	GeoMole
GMRX	GeoMole receiver
GMTX	GeoMole transmitter
GPR	Ground penetrating radar
GUI	Graphical user interface
HF	High frequency
IC	Integrated circuit
IDFT	Inverse discrete Fourier transform
IEEE	Institute for Electrical and Electronics Engineering
IF	Intermediate frequency
kV	Kilovolt
LIB	Long inclined borehole
LNA	Low-noise amplifier
mA	Milliampere

MDS	Minimum detectable signal
MHz	Megahertz
MOM	Method of moments
MOSFET	Metaloxide silicon field effect transistor
MPIE	Mixed-potential integral equation
Msp/s	Megasamples per second
ns	Nanosecond
PC	Personal computer
PCB	Printed-circuit board
PFN	Pulse-forming network
PGM	Platinum group metal
PR I	Pulse repetition interval
PRF	Pulse repetition frequency
RAM	Random access memory
RCF	Rooftop calibration facility
RCS	Radar cross section
RF	Radio frequency
RPM	Rustenburg Platinum Mines
RX	Receiver
SCU	Signal conditioning unit
SFCW	Stepped frequency continuous wave
SNR	Signal-to-noise ratio
TE	Transverse electric
TM	Transverse magnetic
TX	Transmitter
UG	Upper group
UWB	Ultra wideband
VCR	Ventersdorp contact reef
VED	Vertical electric dipole
VHF	Very high frequency
VNA	Vector network analyzer
XOR	Exclusive or

# GLOSSARY OF GEOLOGICAL TERMS<sup>1</sup>

<b>Anorthosite</b>	<i>Plutonic monomineralic (usually labradorite) rock equivalent of gabbro without monoclinic pyroxene.</i>
<b>Archean</b>	<i>Said of rocks of the earlier part of the Precambrian time (+2.5 gigayears).</i>
<b>Chromite</b>	<i>An isometric mineral, <math>8[\text{FeCr}_2\text{O}_4]</math>. Occurs in black crystals, weakly to moderately ferromagnetic and the major source of chromium.</i>
<b>Chromitite</b>	<i>A rock composed mostly of the mineral chromite.</i>
<b>Diorite</b>	<i>A group of plutonic rock characteristically composed of dark-coloured amphibole (especially hornblende), acid plagioclase, pyroxene and sometimes a small amount of quartz.</i>
<b>Dunite</b>	<i>Peridotite in which the mafic mineral is almost entirely olivine, with accessory chromite almost always present.</i>
<b>Feldspathic</b>	<i>Said of a rock or mineral aggregate containing feldspar, a monoclinic or triclinic mineral with the general formula <math>\text{XZ}_4\text{O}_8</math>, where <math>\text{X} = \text{Ba}, \text{Ca}, \text{K}, \text{Na}, \text{NH}_4</math> and <math>\text{Z} = \text{Al}, \text{B}, \text{Si}</math>.</i>
<b>Pyroxenite</b>	<i>A coarse-grained, holocrystalline igneous rock consisting of 90% pyroxenes.</i>
<b>Pyroxene</b>	<i>A group of chiefly magnesium-iron minerals. Colours are mostly green, but range from white to black.</i>
<b>Felsic</b>	<i>A mnemonic adjective derived from (fe) for feldspar, (l) for lenad or feldspathoid, and (s) for silica. Applied to light-coloured rocks containing an abundance of one or all of these.</i>
<b>Gabbro</b>	<i>Dark-coloured, basic intrusive igneous rocks composed of basic plagioclase and clinopyroxene, with or without olivine and orthopyroxene.</i>
<b>Gneiss</b>	<i>A foliated rock formed by regional metamorphism.</i>
<b>Haulages</b>	<i>The gangway, entry or tunnels through which mine cars are hauled.</i>
<b>Karoo Supergroup</b>	<i>Consists of a continuous glaciomarine (sedimentary) to terrestrial (volcanic) sequence (max. of 12 km thick) that covers 2/3 of South Africa's land surface. Deposition began 280 megayears ago and terminated 100 megayears ago.</i>
<b>Leuconorite</b>	<i>A light-coloured norite.</i>
<b>Mafic</b>	<i>Composed dominantly of the ferromagnesian rock-forming silicates.</i>
<b>Melanorite</b>	<i>A dark-coloured norite.</i>
<b>Mesonorite</b>	<i>A medium-coloured norite.</i>
<b>Norite</b>	<i>A coarse-grained plutonic rock containing basic plagioclase (labradorite) as chief constituent and orthopyroxene as the dominant mafic material.</i>
<b>Paleozoic</b>	<i>Referring to the era 230 – 544 megayears ago.</i>
<b>Pegmatoidal</b>	<i>Texture of an exceptionally coarsely crystalline igneous rock.</i>

---

<sup>1</sup> Brief description of some important geological and mining terms extracted from [92],[93].

<b><i>Peridotite</i></b>	<i>Coarse-grained plutonic rock composed mainly of olivine, with or without other mafic materials.</i>
<b><i>Platinum group metals</i></b>	<i>Any of the minerals native platinum, osmium, iridium, palladium, rhodium, ruthenium and their alloys.</i>
<b><i>Plutonic</i></b>	<i>Relevant to igneous rock formed at great depths.</i>
<b><i>Postkinematic</i></b>	<i>Geological process or event occurring after any kind of tectonic activity.</i>
<b><i>Raises</i></b>	<i>Inclined opening driven upward from a level to connect with the level above.</i>
<b><i>Stopes</i></b>	<i>An excavation made solely for the purpose of extracting ore.</i>
<b><i>Synkinematic</i></b>	<i>Geological process or event occurring during any kind of tectonic activity.</i>
<b><i>Transvaal Supergroup</i></b>	<i>Also the Chuniespoort Group, which is 2.6 – 2.4 gigayears old.</i>
<b><i>Ultramafic</i></b>	<i>Said of an igneous rock chiefly composed of mafic minerals.</i>
<b><i>Winzes</i></b>	<i>Declined opening driven downward from a level to connect with the level below.</i>

# CHAPTER 1

## INTRODUCTION

### 1.1 Background

Borehole radar (BHR) is a specialised subset of ground penetrating radar (GPR), where GPR is defined as ... *the general term applied to techniques which employ radio waves, typically in the 1 to 1000 MHz frequency range, to map structures and features buried in the ground* [1].

The basic principle of GPR is the transmission of radiowave signals from the surface into the ground and the reception of the radiowaves reflected back by the surface itself and from any structure in the ground with an electromagnetic contrast. The first subsurface electromagnetic (EM) exploration techniques were patented in 1910 in Germany [2]. Developments only took off in the late 1960's. GPR has found many applications, including looking for ore bodies in a mine, locating fractures in mine rock, searching for subsurface tunnels, locating pipes below concrete, to name but a few [3]. In general GPR applications, the system (electronics and antennas) are located above the surface and usually suspended in the air. In BHR however, at least the antennas are embedded in the propagating medium (ground or hard rock). Boreholes are drilled in the volume to be illuminated and the antennas are positioned in these boreholes. BHR is particularly useful when the volume to be investigated is inaccessible from the surface. Detection ranges in excess of 100 m have not been reported in GPR literature, but boreholes in excess of 300 m can easily be drilled.

BHR has found a potential niche market in the hard-rock (crystalline) deep mining environment. Very promising results have been obtained in the South African platinum and gold mines over the past decade. Nature created a window for BHR to accurately map economically important reefs and geological structures in a number of geological settings. Host rocks are translucent to radiowaves in the HF and VHF frequency bands and provide adequate dielectric contrast between the propagating medium and the important structures. The South African mining industry is continually striving to extract ore at deeper levels. There are two main reasons why

## CHAPTER 1: Introduction

the accurate mapping of geological structures is important. Firstly, if the geologist and mining engineer know where the ore body is located and where it is disrupted they can plan their mining activities ahead and increase productivity and efficiency. Secondly, a high premium is placed on safety. Working depths in South African platinum and gold mines vary from less than 100 m to more than 3500 m. The immense stresses at play are evident. Knowing what to expect, the miners can plan ahead to avoid the hazards associated with potholes, dykes, fractures, faults and rolls.

The GeoMole BHR system [4],[3] was developed specifically for mining environments. It is a 32 mm diameter bistatic baseband pulse radar with a 10 – 100 MHz operating bandwidth that can be deployed in boreholes of up to 300 m. The radar can be configured as either a truly bistatic system (transmitter and receiver in different boreholes or at different positions in the same borehole) or a pseudo monostatic system where the transmitter and receiver are collocated with a minimum spacing distance of 1.5 m. The system has sub-metre resolution capabilities and a maximum detection range in excess of 70 m [5]. A typical deployment configuration is depicted in Figure 1-1.

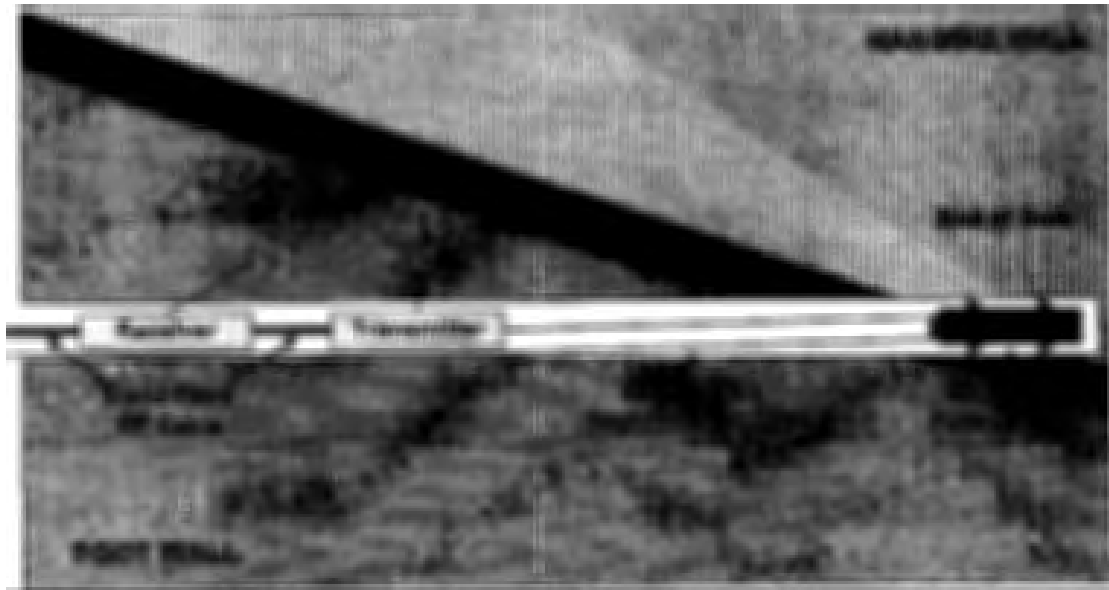


*Figure 1-1: Basic GeoMole BHR deployment configuration.*

The GeoMole BHR research program started in the early 1990's in Oxford, England. Mason, Hargreaves and Claassen [4],[3] were the pioneers of the system – initially called the ARCOLab borehole radar. Mason and Hargreaves moved to the University of Sydney, Australia in the 1990's where the radar underwent a series of improvements, facelifts and name changes. Current research is continued

internationally, with a joint effort between Mason's group in Sydney and Cloete's group in Stellenbosch.

## 1.2 Problem Definition

The fascinating results obtained with the GeoMole BHR system in the famous LIB19B borehole at Mponeng [5],[6] triggered a significant interest in the application of BHR technology for mapping geological defects in the Bushveld Igneous Complex (BIC).

The BIC of South Africa is host to the richest platinum group metal (PGM) deposits in the world [7]. In 1999 the second upper group (UG2) reef in the BIC provided 42% of the platinum-bearing ore processed in South Africa [8]. This reef has been described as being tabular and uniform. This description is only superficial, since potholes, rolls, dykes, etc. frequently disrupt the reef. Of these, potholing poses the greatest threat to mining operations. A UG2 pothole is defined as a localised depression in the reef where the hanging wall erodes into and often through the plane of the footwall [30]. Potholes are generally not mined.

No regular distribution has been determined for potholes, but they are often concentrated in clusters. The non-destructive mapping of potholes has been tried with the obvious techniques, with limited success. These include seismic sounding, the projection of known potholes in the Merensky Reef above and predictions based on geological analysis.

A feasibility study is necessary to assess the applicability of BHR technology in the specific setting. In the past this has been done qualitatively, with the radar deployed in the setting being considered and the returned echoes inspected to determine the applicability of the system in that setting. Relatively little was known on the quantitative performance of the BHR system and even less was known about the propagation of radiowaves in a complex geological setting like the BIC. A need developed for the quantitative assessment of the radar in this specific setting.

A rigorous subsystem level analysis of the BHR system is therefore necessary. Every subsystem has to be characterized quantitatively by means of practical measurements, theoretical analysis or numerical simulations. A clear understanding has to be developed on the interactions between the transmitter electronics, the transmitter

antenna and the surrounding medium (lossy dielectric). The interaction between the receiver antenna and its surrounding medium is of equal importance.

The propagation of radiowaves in the stratified geological setting of the BIC also has to be investigated. The stratigraphy of the BIC can be approximated as a vertical sequence of lossy dielectric layers. The theory of propagation in a stratified system has been studied for decades, but little has been published on the case where the transmitter (source) is embedded in one of the lossy layers. The reflection and transmission of radiowaves from the interface between different dielectric media (both with dielectric losses) still have to be studied. It is also important to determine the maximum distance at which we can expect to receive echoes above the noise floor of the receiver. In order to do this the system has to be characterized, while the propagation in the host rock and the reflection mechanism of the dielectric discontinuity have to be quantified.

One of the requirements for accurate mapping of geological structures is spatial resolution. It is therefore important to determine the current resolution of the radar and to investigate means by which the resolution can be increased. Since a large number of surveys have been done with the current system it would be of great benefit to raise resolution by means of a post-processing algorithm.

### **1.3 Description of GeoMole BHR System**

In the South African mining environment the economical reefs to be surveyed are usually encountered hundreds of metres below the surface. GPR has detection ranges of less than 100 m. The only feasible method of bringing the target (interface with dielectric contrast) within the detection range of the BHR is by deploying it in boreholes drilled for exploration or mining purposes or for the sole purpose of a BHR survey.

Due to the confined space available in a borehole (typically  $\leq 48$  mm diameter), unique limitations are placed on the topology and technology deployed, as well as on the antennas. A block diagram description of the GeoMole BHR system, depicted in Figure 1-2, is given in Figure 1-3.

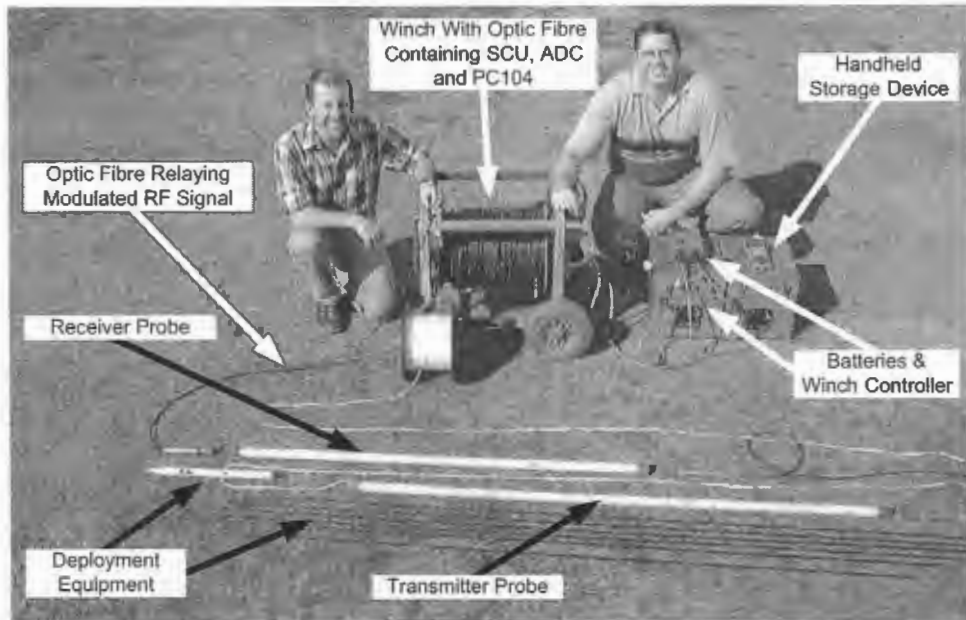


Figure 1-2: GeoMole borehole radar system with deployment equipment and operators.

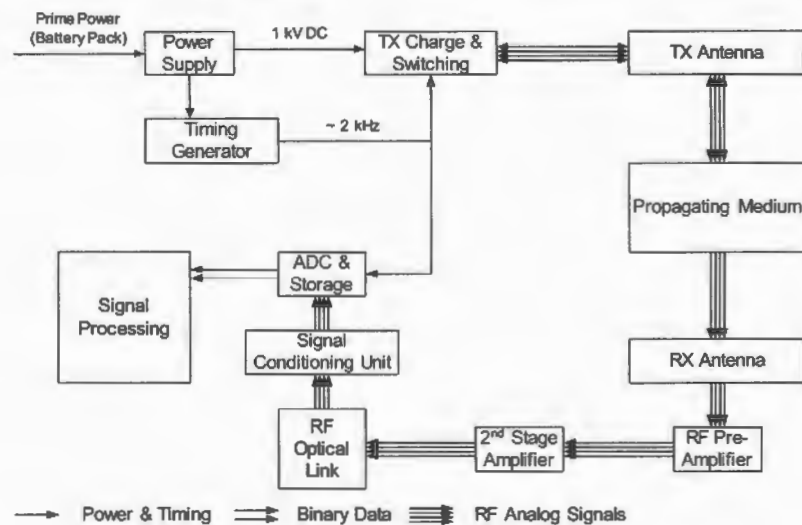


Figure 1-3: Block diagram of GeoMole borehole radar.

The GeoMole BHR system is in some regards significantly less complicated than a conventional radar [67] - [70], especially with regard to the IF and RF subsystems. It is however, notably more intricate with regard to the interaction between the transmitter circuitry, the transmitter (TX) antenna and the propagating medium.

The essence of this system encompasses the radiation of an electromagnetic pulse by an antenna stimulated with a transient current, into a propagating medium – usually a single homogeneous rock layer or a sequence of rock layers. The EM wave propagates through the medium and scattering occurs at any discontinuity of the dielectric profile of the surrounding medium. The effective area of the receiver

antenna at an arbitrary location intercepts the scattered waves and the radar can be characterized as being bistatic. In some cases the receiver can be located very close to the transmitter in a semi-monostatic configuration. The miniscule RF intercepted signal is delivered to the RF low-noise amplifier (LNA) and is amplified by a secondary amplifier stage in the receiver probe. Since the radar has to be deployed in a borehole, the captured data either has to be stored in the receive probe in the borehole (up to 300 m from the collar) or transmitted to a capturing device at the collar of the borehole. The RF bandwidth of the received signal can exceed 100 MHz depending on the exact transmitter topology and the attenuation coefficient of the propagating medium. The state-of-the-art of analogue-to-digital conversion at the design phase of this radar forced the conversion process to be carried out outside the borehole due to physical size and power limitations. The RF signal therefore has to be either retransmitted or relayed from the receiver to the ADC unit at the deployment site of the radar. A fibre optic link was chosen as the optimal RF link for the frequency range of the system (10 – 100 MHz). An optic modulator and demodulator are used to convert the RF electrical signals to optical signals and vice versa. A signal conditioning unit (SCU) ensures that the power levels at the output of the optical demodulator are compatible with that of the input of the ADC unit with respect to dynamic range. The ADC unit digitises the analogue RF signal to an 8-bit word at a sampling frequency of 250 Msps (megasamples per second). 512 bytes are stored yielding a radar trace of length 2.048  $\mu$ s. The ADC is triggered by a signal sent from the transmitter via another optic link. The ADC unit passes the 8-bit word to a PC104 module, which acts as the interface between the ADC and a handheld storage device. It also performs a stacking (averaging) process, adding a preset number of traces coherently, in order to increase the signal-to-noise ratio (SNR). After the stacking process, the data is stored as a series of 16-bit words to accommodate the increased dynamic range of post addition. The 16-bit, 512 word traces are stored on a minicomputer and downloaded at the end of the survey for post processing. No signal processing (excluding stacking) is done in real time and only the raw data are captured.

The abovementioned description of the GeoMole BHR system is only a brief summary. The system has been described extensively in literature mainly comprising

of internal reports [26], project reports [27], theses [16],[71],[72] and dissertations [4],[3]. The reader is referred to these sources for detailed information.

## 1.4 Outline of Dissertation

The research and work done with regard to the abovementioned problem are presented in this dissertation (divided into 9 chapters and 8 appendices).

Chapters 2 to 4 describe the system characterization procedure designed to quantify the performance of a BHR system in the specific geological setting – the UG1 – UG2 stratigraphy in the BIC. Chapter 2 motivates the need for a comprehensive system analysis, while the experiment used as motivation is presented in Appendix A. The important considerations to be kept in mind in the analysis of a GPR system are also stated in this chapter. Furthermore, it provides a brief overview of the procedure as described in detail in Chapters 3 and 4.

Chapter 3 is concerned with the characterization of the TX and receiver (RX) probes. A calibration facility is designed in which the transfer functions and performance figures of the probes are measured in free space. Based on numeric simulations, the characteristics and transfer functions of the probes when deployed in boreholes are inferred. Appendix B presents additional information on the numeric simulation of the antennas. Additional transfer functions of the antennas in a variety of deployment configurations are also presented. The circuit diagrams of the instrumentation electronics built for the characterization of the probes are described in Appendix H.

The receiver radio frequency (RF) and digital chain is characterized in Chapter 4. The concept of reference and relative gains is defined and a procedure is developed by which the transfer function of any given optic fibre configuration can be estimated. It furthermore presents the measurement and prediction of the analogue-to-digital converter (ADC) unit's transfer function. Based on the characterization of the system transfer function, this chapter concludes with the extraction of the basic performance figures of the BHR system.

Chapter 5 sets out the development of a pulse recompression algorithm. This is tested on laboratory measurements and also on field experiment data. The algorithm is adapted for the batch processing of field experiment data. It was provided with a graphical user interface (GUI) that allows the user to set up the radar configuration

and filter parameters (Appendix G). Summaries of the field experiments conducted during the research of this dissertation are presented in Appendices D to F.

Chapter 6 discusses propagation in the host rock of the BIC UG1 – UG2 stratigraphy. A brief overview of layered chromium-platinum complexes is given, with specific attention to the BIC. A generalization is made of the UG1 – UG2 stratigraphy and this generalized stratigraphy is further simplified to the form of a planar model made up of layers whose dielectric properties have been measured. A theoretical description of radiation in a lossy medium is presented. Estimates are made of the pulse peak velocity of radiowaves in the BIC host rocks and the quality factor thereof.

The theory of plane wave propagation in stratified lossy media is formalized in Chapter 7. Attention is given to the choice of the correct branch for both transverse electric (TE) and transverse magnetic (TM) polarizations. A paradox is identified where the reflection coefficient of a proper mode is larger than unity - a possibility not investigated in electromagnetic literature. This paradox is investigated and the solution is proved to be valid. Finally, propagation in a multilayered system is considered.

The theory developed in Chapter 7 is applied to investigate propagation and detection in the UG1 – UG2 system in Chapter 8. Reflections of a time domain Ricker wavelet are simulated for a planar interface, a sandwiched layer and for multilayered systems in the UG1 – UG2 stratigraphy. Predictions are made on the detection range of UG2 reef reflections when illuminated from the footwall. This chapter concludes with an estimation of the reflectivity of the UG2 reef, also from field experiment data. These predictions and estimations confirm the accuracy of the work presented in this dissertation.

Chapter 9 concludes the dissertation with a summary of the basic outcomes. Recommendations are also made on possible future fields of study and work.

## **1.5 Literature Review**

A wide range of literature in different engineering and geological disciplines have been studied and used during the research presented in this dissertation. Since the research covers such a wide range of topics, it was decided to include the literature review at relevant places closer to the points of discussion.

At this point it should be noted however, that the IEEE standard definitions of terms for radio wave propagation [65] are used throughout this dissertation.

## 1.6 Original Contributions

Five main contributions were made during the research presented in this dissertation:

- The characterization of the system transfer function of a borehole (or surface penetrating) radar where the transmit and receive antennas are deployed in air- or water-filled boreholes drilled into an absorbing, geologically stratified rock mass. A combination of experimental, numerical and theoretical techniques was used.
- A novel pulse recompression algorithm to restore the range resolution of the system, which exploits the newly characterized system transfer function.
- A careful study of plane wave EM propagation in stratified absorbing layers. Literature and textbooks do not adequately deal with the problem of transmission and reflection at the boundary between two absorbing dielectric half-spaces. An apparent paradox where the physical solution yields a reflection coefficient larger than unity is resolved.
- The estimation of the received waveforms reflected from the different reef horizons in the UG1 – UG2 system in the BIC for various deployment configurations. These can be used in signal processing techniques to extract information from the actual captured data.
- The partial delineation of the limitations imposed on ore body delineation using BHR technology. The reflectivity, detection range and resolution of the UG2 reef in the BIC have been estimated empirically.

# CHAPTER 2

## BOREHOLE RADAR SYSTEM ANALYSIS

Currently there are no standard set of parameters and performance figures by which a BHR system can be characterized and different systems compared. One of the key aspects of this dissertation is the description of a system analysis (characterization) procedure that was developed to fulfil this void in BHR technology.

In this chapter a brief discussion follows on the history of GPR system analysis, the necessity for a quantitative system analysis and the basic process thereof. The system analysis for the GeoMole BHR is extensively covered in Chapters 3 and 4. Even though this analysis was developed for the GeoMole system in particular, the principles apply to any BHR system and can be adapted accordingly.

### 2.1 Literature Review

Very little has been published on the characterization of borehole radar systems. Only two relevant publications were found on the characterization of GPR systems. Scheers *et al.* [25] developed a time domain technique to characterize their laboratory ultra wideband (UWB) GPR system for landmine detection. These authors viewed the entire radar system, including the antennas, as a cascaded series of convolution operators. Mikhnev *et al.* [20] developed a frequency domain calibration technique for GPR antennas. These authors based their calibration technique on the two-port error model frequently used in the calibration of vector network analysers. Three measurements are required to solve the unknown error coefficients. One of these is a free space measurement (matched load), while the other two are done with a big metallic reflector at different distances from the antenna.

Hargreaves and Claassen designed the GeoMole BHR system. Hargreaves [4] gives a basic system overview in which he characterizes the receiver and optic link. Attention is given to the impulse response, saturation, noise figure, crosstalk, settling time, reverberations and the power budget. The analysis was used as a proof of concept rather than a comprehensive reference. Claassen [3] designed the antennas currently used in the GeoMole system. He analysed the antennas with respect to their

characteristic parameters. Results were also presented on the field trials of the antennas. Basic system analysis of the current GeoMole BHR system was done by Van der Merwe and Woods [26] and by Du Sautoy [27].

Most of the developmental research described here is based on basic principles as found in undergraduate electronic engineering handbooks [9] - [14]. Some of the concepts and techniques previously developed by the author were used throughout [15].

## **2.2 Motivation for GeoMole BHR System Analysis**

The GeoMole borehole radar has been operating very effectively ever since its inception in the early 90's. A number of improvements have been proposed primarily based on qualitative observations. A percentage of the proposals actually lead to improved system performance. Even though a number of subsystems have been analysed and characterized, the entire system has never been analysed and characterized as an integrated system operating in its actual deployment environment. The complexity of system analysis for a system such as the GeoMole BHR (as will be seen in Chapters 3 and 4) and the extremely promising results obtained with the uncalibrated radar up to March 2001 led to this radar not being analysed as a complete system. This is quite unlike conventional radar where calibration of the radar is of utmost importance. A field experiment conducted in March 2001 saw a turning point in the reasoning behind the uncalibrated radar system and led to the extensive system analysis and calibration of the GeoMole BHR.

In March 2001 a viability study was undertaken on the exploitation of BHR in the delineation of stratigraphy in the vicinity of Kleinzee, South Africa [73]. The area around Kleinzee on the northwest coast of South Africa is a region of alluvial diamond mining. Geologically, stratified layers of different sand and clay compositions are found. The purpose of the radar was to detect these interfaces. Based on the measurement of the dielectric properties of these layers and theoretic calculation (see Appendix A) the GeoMole radar should have been able to detect the interfaces with a moderate SNR. The results, also included in Appendix A, indicated clearly that the returned signals from the reflections and the direct wave between transmitter and receiver were both lower than the minimum detectable signal (MDS),

irrespective of how close the antennas were located to each other and the interface. Concerns grew with regard to the anticipated dynamic range, sensitivity and overall performance of the radar.

It was decided that the only certain way to determine the cause of the disastrous results of the March 2001 survey was to accurately and systematically analyze and characterize the GeoMole radar system. It was established that the actual culprit in the Kleinzee trials was the wet kaolinitic clay with a very high attenuation constant [74], which surrounded the air-filled boreholes in which the antennas were deployed. The radiated power never propagated much further than the wet clay surrounding the boreholes. This further encouraged the viewpoint established in Section 1.3 that the radar has to be viewed as a system composed of interdependent subsystems. The importance to quantitatively know the performance of the radar and the parameters influencing the performance figures is emphasized here.

### **2.3 BHR System Analysis and Calibration**

The current system analysis and radar calibration procedures used in conventional radars have to be modified for application to GPR in general and specifically for BHR applications. The main motivation for this is the critical fact that the propagating medium is not free space, but a complicated inhomogeneous dielectric media with significant dielectric loss mechanisms. In the specific case of the GeoMole BHR, the interdependence of the transmitter, antenna and propagating medium further complicates analysis and calibration.

In recently published literature advances in the procedures of system analysis on a subsystems level have been reported with special attention to the antenna transfer functions. There is a current drive towards the effective numerical simulation of complicated antenna structures. The accuracy of numerical simulations is determined by the correlation between the actual and simulated geometry, providing no violations of parametric restriction of the simulation method occur. Even though these results are never exact (a percentage error is always present), simulations can yield more accurate results than physical response measurements.

Since the propagation medium is ground, it is very difficult to set up a controlled *in situ* environment in which the radiation patterns can be measured. In some limiting

cases however, it is possible to measure the response of the antennas in free space. Miknhev *et al.* [20] developed an antenna analysis procedure by which they calibrated the antenna transient responses using a 2-port error model often incorporated in vector network analysers. A pulse compression ratio of more than 2:1 was obtained with this technique. Scheers *et al.* [25] comments, ... *the deconvolution of the signal source and antenna impulse responses is an ill posed operation.* These authors succeeded however, in calculating the impulse response of their UWB GPR system to such a high degree of accuracy that they were able to use it in deconvolution techniques on captured data. The measurements were done in the time domain. Each subsystem was characterized by its time domain convolution function (operator).

The procedures incorporated by Scheers *et al.* [25] were found to be the most comprehensive and accurate published in current literature on GPR. The system analysis and characterization procedures developed for the GeoMole radar, introduced in Section 2.4 and described in Chapters 3 and 4, are based on that of Scheers *et al.* Due to a number of factors, described in the subsequent chapters, the analysis, characterization and calibration were done in the frequency domain. The inherent differences of the two radar systems required the development of unique analysis and calibration tools (hardware and software) and procedures.

## 2.4 Summary of GeoMole BHR System Analysis

It was stated in Section 2.3 that the system analysis was carried out in the frequency domain. Due to the intricate nature of the GeoMole BHR system, the different blocks depicted in Figure 1-3 had to be grouped different from the conventional grouping (i.e. transmitter, antenna, receiver and signal processing, and control and interface).

The transmitter (electronics and antenna), propagating medium and the receiver antenna were grouped as the first subsystem. The interdependency of the transmitter and the two antennas on the dielectric properties of the propagating medium dictated this grouping.

The second subsystem grouping was that of the entire RF receiver chain including the front-end LNA, the power amplifier, RF optic link and the SCU. Each component had to be characterized by its transfer function and noise figure. The phase responses

## CHAPTER 2: Borehole Radar System Analysis

were of critical importance since they determine the pulse distortion introduced by the RF electronics. The optic link is a highly configurable subsystem that will almost invariably change from survey to survey. This led to the introduction of a calibration (standard) optic fibre set with measurements of the different optic fibres made in reference to this calibration standard. A procedure was derived in which the total transfer function can be derived by using a lookup table for the transfer function of the different optic fibre cables.

The final subsystem grouping was that of analogue-to-digital conversion and data storage. The triggering mechanism in the GeoMole radar and the architecture of the sampling card led to a peculiar transfer function with respect to its magnitude and phase responses. It was subsequently measured and derived theoretically.

By the analysis and characterization of these three subsystem groupings, the entire system was characterized and calibrated in the sense that transfer functions were quantified exactly. Calibrated data by means of post-processing can only be produced offline if the exact radar deployment is logged, as will be discussed in Chapter 5. Signal processing was not analysed since it is an offline procedure carried out at the end of a survey on the raw captured RF data. It should be noted that BHR is a small subset of radar where the RF data streams are actually quantified and captured!

The three main groupings of the different subsystems are examined in Chapters 3 and 4. Based on the results of these chapters, the derived basic system performance figures are set out in the latter part of Chapter 4.

# CHAPTER 3

## CHARACTERIZATION OF TX AND RX PROBES

The grouping of the transmitter electronics and the two antennas as a subsystem for analysis was briefly motivated in Section 2.4. The rationale behind this grouping as well as its detailed analysis is described in this chapter. Attention is given to the various techniques, hardware and software developed to assist in the analysis procedure.

### 3.1 Literature Review

The modelling of complex antenna structures has received considerable attention due to increased capabilities of today's modern personal computers. Van Wyk [16] modelled antennas similar (not exactly the same) to the current GeoMole antennas using two numerical simulation techniques. He used the method of moment (MoM) frequency domain technique as well as the finite difference time domain (FDTD) technique. Lestari *et al.* [17] characterized a transient bow-tie antenna structure for GPR applications. The formulation of the problem was based on the frequency-domain mixed-potential integral equation (MPIE) and solved with the MoM technique. Yaravoy *et al.* [18] consider the time domain modelling of GPR antennas above ground by means of the FDTD technique. Ellefsen and Wright [19] numerically simulated a borehole radar antenna in a water-filled borehole using the FDTD technique. They studied the effect of resistive loading and the surrounding water on the radiation pattern of the antennas.

Bantin [21] characterised the communications link between two dipoles for pulsed excitation. This characterisation was done in the frequency domain and transformed to the equivalent time domain convolution operators. Smith [22] - [24] analysed antenna radiation, reception and scattering for simple wire antennas with a generalised excitation, e.g. a pulse in time. In order to have done this he introduced the travelling-wave element – an ... *idealized model for a practical travelling-wave antenna*. He

modelled more complicated wire antennas by superimposing these elements. Van Wyk [16] used this technique in his analysis.

## 3.2 Overview of Transmitter Electronics and the Antennas

The transmitter topology used in the GeoMole radar has been described using a number of different approaches [4],[26],[72],[27]. In this section, the aim is not to redo this or to elaborate on the theory involved. The aim is rather to give a basic description of the source of radiation and the reason why the transmitter, antenna and propagating medium are so interdependent.

The GeoMole radar incorporates, in essence, a line type modulator with a number of subtle differences. Consider the block diagram of such a line type modulator as depicted in Figure 3-1 [75].

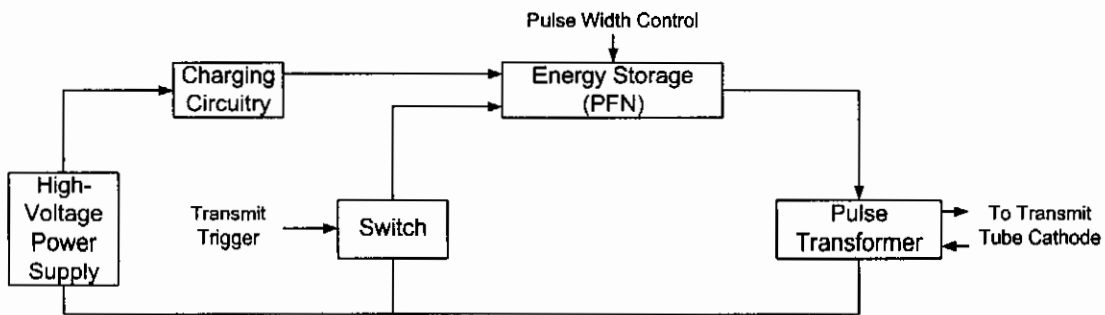
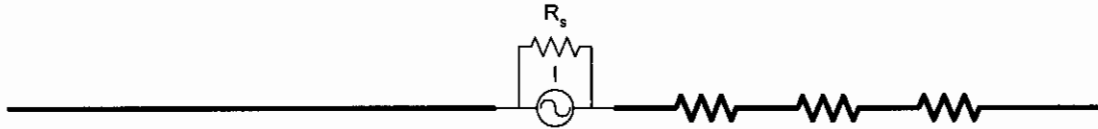


Figure 3-1: Block diagram of line type modulator [75].

The pulse-forming network (PFN) acts as an energy storage device when the transmitter is off and charged through the charging circuitry from the high-voltage power supply. The equivalent impedance of the PFN in series with the pulse transformer determines the envelope of the RF signal excited by the transmitter tube not shown in the diagram. For the GeoMole radar, the transmitter block diagram is a variation on Figure 3-1 with the pulse transformer short-circuited and the antenna as an integral part of the PFN. A very basic equivalent circuit of the TX antenna is a resistance (ohmic and radiation) in series with a capacitance. In essence the antenna is a distributed, non-uniform RC transmission line. The energy in the PFN is stored in the distributed capacitance of the antenna, which is charged through the charging circuitry to a total DC voltage of 1000 V. At the instant when the switch is closed, the charged transmission line is short-circuited and a dispersive discharge process occurs.

The energy stored in the capacitance is dissipated in the resistance, which in turn is made up of an ohmic and radiation component. The ohmic component produces heat, while the radiation component provides a radiated field with its frequency content determined by the rate of change of the current. Clearly the transient response of the transmitter is dependant on the impedance characteristics of the antenna.



*Figure 3-2: Asymmetric resistively loaded dipole antenna.*

Both antennas (TX and RX) are electrically short, asymmetric, resistively loaded dipoles as depicted in Figure 3-2. The antennas are asymmetric in geometry as well as in their resistive profiles. The one arm of the dipole consists of a metallic pipe containing the TX/RX electronics. Due to a number of physical constraints this arm is unloaded, i.e. a  $0 \Omega$  resistive profile. The transmitter has a higher power consumption than the receiver and therefore requires a larger battery pack, which is also contained within the metallic pipe section. This requires the unloaded dipole arm of the transmitter to be somewhat longer than that of the receiver. The resistively loaded arms of the transmitter and receiver are realized by 48 discrete resistors and 49 metallic segments interconnecting the resistors. These arms are identical for the receiver and the transmitter. The purpose of resistive loading in an electrically short antenna is to minimize pulse reflection from the ends of the antenna structure over a wide band. Without this resistive loading the charges will bounce from the one end of the antenna to the other with little attenuation and cause a ringing effect. In the deployed radar the antenna (including the electronics) is potted in a 32 mm diameter PVC pipe. The metallic surfaces of the resistively loaded arm are in contact with the actual potting material, which has a further, loading effect on the antenna. Finally the antenna is positioned inside a borehole (usually of 48 mm or greater diameter) in the host medium with given dielectric parameters.

As will become evident in the subsequent sections, the input impedance of the antenna is influenced by the physical geometry of the metallic arm (no loading), the resistive profile, the potting material, the diameter of the borehole and also the dielectric properties of the host medium. It was stated previously that the transmitted pulse shape depends on the impedance of the PFN, which in the case of the GeoMole

radar, is the antenna itself. The significant interdependence of the transmitter electronics and the antennas on the dielectric properties of the host medium is clearly visible. It should be noted however, that the resistive profile used (adopted from the Wu-King profile [76]) minimized the impedance dependency on the dielectric properties of the host medium.

The abovementioned discussion on the antennas used in the GeoMole system only serves as a brief introduction to the antennas used and motivates the use of such an antenna topology. It also highlights the interdependency of the antenna on the surrounding medium. For a comprehensive discussion on the antennas refer to [3], [4], [16],[72].

### **3.3 Design of a Free Space Calibration Facility**

The value of calibrating a radar cannot be reiterated enough. The frequency band of operation of the GeoMole BHR is from 10 MHz (HF) to 100 MHz (VHF) with the associated free space wavelength range of 30 m to 3 m. A facility is needed with minimum reflection interference between the TX and RX antennas and where the electromagnetic interference (EMI) can be minimised.

An anechoic chamber to accommodate the antenna in the frequency range under consideration would have been ideal. The physical size of the anechoic chamber at the University of Stellenbosch and the effective frequency band of the radiowave absorbing ( $f > 2$  GHz) excluded this facility. The open-air test facility at Houwteq was considered, but the geometries involved (considered in Section 3.3.2) also eliminated that facility. The decision was eventually taken to design and build a test facility exclusively for the GeoMole BHR system.

#### **3.3.1 Calibration Facility Topology**

In any calibration facility a transmit and receive antenna is deployed in a confined space in order to make various radiation and propagation measurements. Even though it might sometimes be required to make near field antenna measurements, it is usually necessary to make measurements when the receiver antenna is in the far field region of the transmit antenna and vice versa. In addition it is also necessary to minimize interference effects due to reflections from the physical structures composing the

facility. Finally the existence of parasitic elements to the antennas has also to be eliminated, since they can adversely affect its radiation pattern.

The characteristics of a calibration facility can therefore be summarized as a physical structure in which antennas can be deployed with a placement such that they are in each other's far field region, where minimum interference occurs and no parasitic elements are located 'near' the antennas. The proposed calibration facility for the GeoMole radar is an open-air facility on the rooftop of the Stellenbosch engineering building with masts onto which the antennas can be deployed as depicted in Figure 3-3.

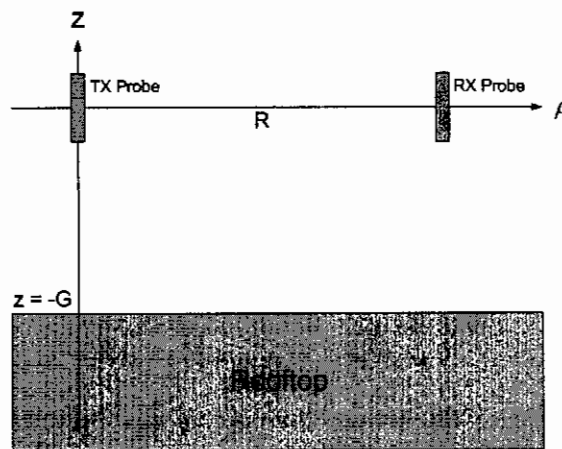


Figure 3-3: Geometry of rooftop calibration facility.

The realization of this facility is discussed in Section 3.4, taking into account the abovementioned criteria and restrictions.

### 3.3.2 Electromagnetic Propagation Constraints

In the near field region of a radiator, the field includes quasi-static and induction fields that vary with an  $r^{-3}$  and  $r^{-2}$  relationship respectively. This is in addition to the radiation field that varies as  $r^{-1}$ . The region where the  $r^{-3}$  term is dominant is often referred to as the reactive near field zone, while the region where the  $r^{-2}$  term is dominant is referred to as the radiation near field or Fresnel zone. Outside the latter, the dominant part of the field decays as  $r^{-1}$  and is referred to as the radiation far field or Fraunhofer zone of the antenna [65]. The range associated with the border between these two zones is often given as  $2L^2/\lambda$  [77] ( $L$  is the maximum antenna dimension) without mentioning the physical implication of this distance. It is the distance, such that the maximum phase deviation from any point on the antenna, to a

observation point at broadside and that distance away from the phase centre of the antenna, is less than or equal to a 16<sup>th</sup> of a wavelength. This condition was adopted to be slightly more stringent for this calibration facility, since the receiver antenna cannot be viewed as a discrete observation point. The imposed restriction was that, if the antennas are positioned with their feedpoints on broadside to each other, the maximum phase deviation from any point on the TX antenna to any point on the RX antenna should be less than  $\lambda/16$ . If the total length of the antenna is taken as L, the approximated boundary of the Fraunhofer region is given as

$$R_{fh} = \frac{8L^2}{\lambda}. \quad (3.1)$$

With a maximum frequency content of 100 MHz and an antenna length L of 1.6 m nominally, the maximum value  $R_{fh}$  over the frequency band of interest is

$$R_{fh}(\text{max}) = 6.827m. \quad (3.2)$$

Ideally we would therefore like to have the antennas separated by at least this distance.

The second constraint is that we want to measure only the direct wave without any secondary reflections. In practice this is virtually impossible. For the geometry shown in Figure 3-3, it is clear that we will receive the direct wave and then a wave reflected off the rooftop. We know however, that the energy transmitted by the transmit antenna is of finite duration with a pulse length  $\tau_{\text{pulse}}$ . It is known that for a pulse with a rectangular, passband frequency spectrum of finite bandwidth, the pulse length is the inverse of the bandwidth. For a bandwidth of 90 MHz, the pulse length would therefore be around 11.1 ns. The spectrum is, however, far from rectangular and the pulse length will be substantially broader than 11.1 ns. Assume that it is less than 30 ns.

$$\tau_{\text{pulse}} \leq 30 \text{ ns} \quad (3.3)$$

For the reflected wave to be separated in time from the direct wave, the relationship between R and G should be:

$$\sqrt{4G^2 + R^2} - R \geq c\tau_{\text{pulse}} \quad (3.4)$$

A maximum ground clearance,  $G$ , of 6.5 m could practically be obtained. The theoretical maximum value of  $R$  is therefore 4.89 m. A practical value of  $R$  was 6 m, corresponding to a maximum pulse length of:

$$\begin{aligned} R &= 6 \text{ m} \\ \tau_{\text{pulse}} &= 27.7 \text{ ns} \end{aligned} \tag{3.5}$$

This was sub-optimal, but still a good compromise between the Fraunhofer distance and the distance required for resolution of the direct and reflected pulses. The transmit and receive antennas are both short with respect to wavelength and their radiation pattern will be close to that of a Hertzian dipole. For the transmit and receive antennas with the given geometry, the gain of the antennas in the direction of the reflected wave is approximately  $-7.55$  dB. Also, since the calibration facility is erected at the edge of the rooftop, there will be a further reduction of  $-3$  dB relative to the direct pulse (disregarding diffraction at the edge of the roof). The reflected pulse signal level will thus be at least  $-18.1$  dB below the direct pulse signal level.

### **3.3.3 Dynamic Range Constraints**

The GeoMole BHR has been designed to operate in a dielectric propagating medium (rock) with a large attenuation constant relative to free space. Its dynamic range and sensitivity were optimized to detect reflections from targets at 40 – 50 m, as well as close in targets at  $\pm 5$  m. Even though the sensitivity can be increased by means of averaging (a 1024 averaging increases the sensitivity by nominally 30 dB against an uncorrelated thermal noise background), the constraints on the dynamic range to allow the abovementioned detection ranges are quite severe. A trade-off had to be made on either the saturation level or sensitivity and it was decided to optimize for the best possible sensitivity. Since the radar was to operate in a known environment, i.e. a lossy dielectric, the power level and amplification could be optimised to allow merely enough attenuation in the lossy dielectric for close-in targets not to saturate the front-end amplifiers. If the radar was to operate in free space with the antennas separated only 6 m at broadside, saturation of the LNA was inevitable.

The need arose for a calibration transmitter and receiver that could cope with the sensitivity and dynamic range of the actual receiver and the high transmitted power of the actual transmitter. A transmitter with approximately 40 dB less power radiated had to be designed, as well as a receiver with the same decrease in amplification.

### **3.3.4 EMI Considerations**

Since the calibration facility was to be on the rooftop of a 5-storey building and in open air, the EMI of radiowaves in our frequency band of interest posed a serious threat to the fidelity of calibration measurements. FM transmissions in the 80 – 100 MHz region were found to be the strongest signals with HF communication signals also quite strong.

Fortunately the superposition of all these radiowave fields did not saturate the GeoMole receivers and means of suppressing the interference of these signals with the calibration waveform had to be found. Since the calibration transmitter provides a trigger signal, it is possible to integrate the captured waveforms coherently. Analogue-to-digital conversion at the facility was done with a Tektronix oscilloscope with a sampling frequency of 2 Gsps (gigasamples per second) and an RF bandwidth of 400 MHz. The EMI signals are uncorrelated with the transmitted waveform and can therefore be suppressed with coherent averaging. EMI signals are in general far from white noise in which case the improvement in SNR theoretically is  $10\log_{10}N$  in decibels, where  $N$  is the number of samples averaged. A practical experiment indicated that, even though the noise (EMI) is not white, comparable SNR improvement occurs with coherent averaging. EMI is a continuous interference signal where the transmitted waveform is of finite duration. The energy of EMI in a captured waveform can be suppressed even further relative to the energy of the transmitted waveform by means of time-gating.

## **3.4 Realization of Calibration Facility**

In this section, the physical realization of the free space, open air calibration facility is discussed. Attention is given to the basic calibration procedure, the mathematical description of the processes involved and the building of the instrumentation equipment used in the calibration facility. Credit for the collaboration with Van Wyk [16] on the design, realization and testing of the facility is given at this point. This work would not have been possible without the diligence with which he worked on this project.

The core of the facility is depicted in Figure 3-4 and Figure 3-5.



Figure 3-4: Masts, probes and optic fibres of the free space, open air calibration facility.

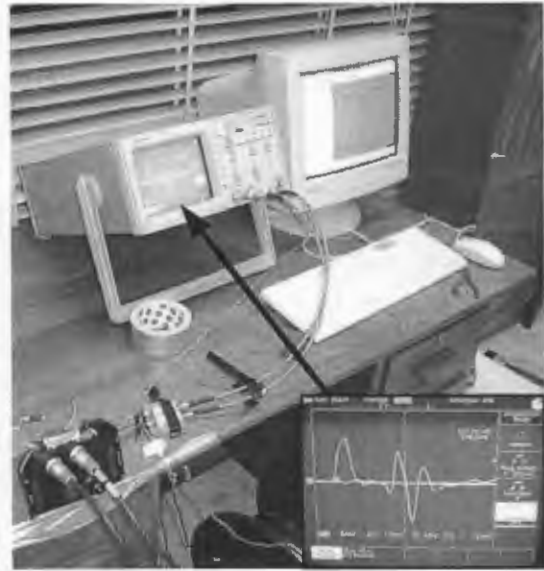


Figure 3-5: SCU and data capturing units of calibration facility with captured trace insert.

Two 7 m high PVC pipes were erected on the rooftop of the engineering building of the University of Stellenbosch with a spacing distance of 6 m. The masts were equipped with pulley systems for hoisting the transmitter and receiver probes. The trigger and RF signals from the two probes were relayed to the SCU and data capturing units via two 200 m fibre optic cables. The Tektronix TDS380 sampling oscilloscope was used to digitise and store the captured traces whilst triggering on the trigger pulse from the transmitter.

### 3.4.1 Qualitative Description

A simplified block diagram of the calibration system is shown in Figure 3-6.

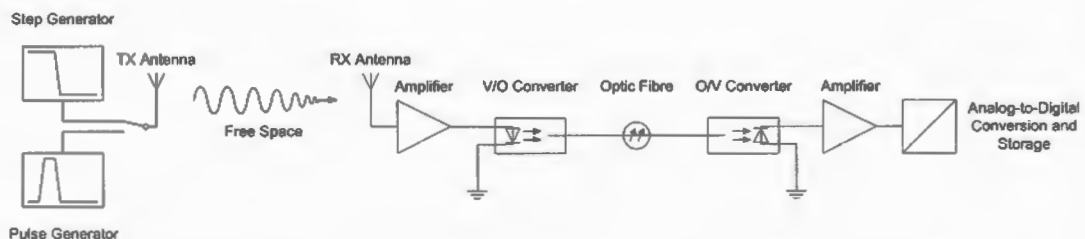


Figure 3-6: Simplified block diagram of rooftop calibration system.

The transmit antenna radiates a pulse into free space, excited by either a step- or a pulse generator. The standard GeoMole transmitters generate a step function of 1 kV, while the calibration transmitter generates a pulse waveform of variable amplitude (15 V max.) and pulse length. The calibration receiver with less amplification is used in

conjunction with the powerful GeoMole transmitter. The standard GeoMole receivers are used with the calibration transmitter. The signal received by the receiver antenna is amplified and converted into an optic signal by an optic modulator. The signal propagates through the multimode 100/140  $\mu\text{m}$  optic fibre cable to the SCU where a demodulator converts the optical signal back to an electrical signal. The analogue-to-digital converter samples and digitises the signal into binary 16-bit words, which are stored on a PC.

### 3.4.2 Quantitative Description

The quantitative description of the calibration facility is done in the  $\omega$ -domain. Consider the power flow schematic shown in Figure 3-7:

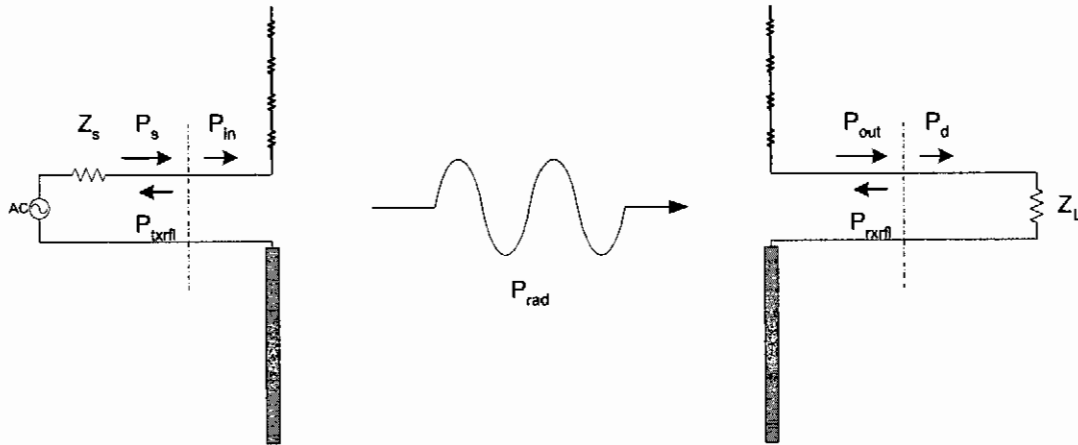


Figure 3-7: Power flow schematic for rooftop calibration facility.

The amount of power radiated into free space can be calculated if the power delivered by the source  $P_s$ , the input impedance  $Z_{in(tx)}$  and efficiency  $e_{tx}$  of the transmit antenna are known:

$$P_{rad} = P_{in} e_{tx} = (1 - |\Gamma_{tx}|^2) e_{tx} P_s \quad (3.6)$$

$$\Gamma_{tx} = \frac{Z_{in(tx)} - Z_s}{Z_{in(tx)} + Z_s}$$

The efficiency of the antenna can be rewritten in terms of the power loss and the incident power. For a general antenna, there are two basic power loss mechanisms – ohmic losses in discrete or distributed resistors and also near field losses. In free space the near field losses are negligible. Since the discrete resistors in the resistively loaded arm are in place, there will be finite ohmic losses in these resistors. If the

currents flowing in each resistor can be determined, the free space efficiency of the antenna can be calculated:

$$e_{tx} = 1 - \frac{P_{loss}}{P_{in}} = 1 - \frac{\sum_{n=1}^N |I_n|^2 R_n / 2}{P_{in}}. \quad (3.7)$$

The power flux density at the receive antenna needs to be determined before the amount of power received can be calculated. For this the directivity of the transmit antenna is needed. Directivity is defined as the ratio of the radiation intensity in a certain spherical direction  $(\theta, \phi)$  to the average radiation intensity [11]:

$$D(\theta, \phi) = \frac{\frac{1}{2} \text{Re} \{ \bar{E}(r, \theta, \phi) \times \bar{H}^*(r, \theta, \phi) \} \cdot \hat{r}}{\int_0^{2\pi} \int_0^\pi \left[ \frac{1}{2} \text{Re} \{ \bar{E}(r, \theta', \phi') \times \bar{H}^*(r, \theta', \phi') \} \cdot \hat{r} \right] r^2 \sin \theta' d\theta' d\phi' / 4\pi r^2}. \quad (3.8)$$

In addition to the actual measurement of the directivity, evaluating (3.8) can approximate the directivity of the asymmetric antenna. An omni-directional antenna (rotational invariance of H-field around the z-axis in this case) (3.8) reduces to a one-dimensional integral that can be evaluated numerically if no closed form solution exists. Assuming that the receiver antenna is in the far field region of the transmitter, the real part of the radial component of the Poynting vector can be approximated as:

$$S_{r(avg)} = \text{Re} \{ S_r(r, \theta, \phi) \} = \frac{P_{rad} D_{tx}(\theta, \phi)}{4\pi r^2}. \quad (3.9)$$

For an electrically small receive antenna at broadside relative to the transmitter, the power received can be written in terms of the effective area of the antenna (related to its directivity) and the average incident power flux density, i.e.

$$\begin{aligned} P_{rec} &= A_{erx} S_{r(avg)} \\ &= \left( \frac{\lambda^2 D_{rx}(0,0)}{4\pi} \right) S_{r(avg)} \\ &\simeq \frac{\lambda^2 P_{rad} D_{tx}(0,0) D_{rx}(0,0)}{(4\pi r)^2}. \end{aligned} \quad (3.10)$$

The power delivered to the load is

$$\begin{aligned} P_d &= (1 - |\Gamma_{rx}|^2) e_{rx} P_{rec} \\ \Gamma_{rx} &= \frac{Z_L - Z_{in(rx)}}{Z_L + Z_{in(rx)}}. \end{aligned} \quad (3.11)$$

In (3.11),  $Z_L$  is the input impedance of the LNA. To determine the source impedance is extremely difficult as it is time-dependant and non-linear. The power transfer function, written in terms of the transmit antenna input power and the power delivered to the receiver load, is

$$P_d = P_{in} \frac{\lambda^2 (1 - |\Gamma_{rx}|^2) e_{rx} e_{lx} D_{rx}(0,0) D_{lx}(0,0)}{(4\pi r)^2}. \quad (3.12)$$

The next step is to find the transfer function from the power delivered to the actual digitised signal at the output of the ADC. A complete schematic diagram of the receiver chain as used in the calibration facility is shown in Figure 3-8.

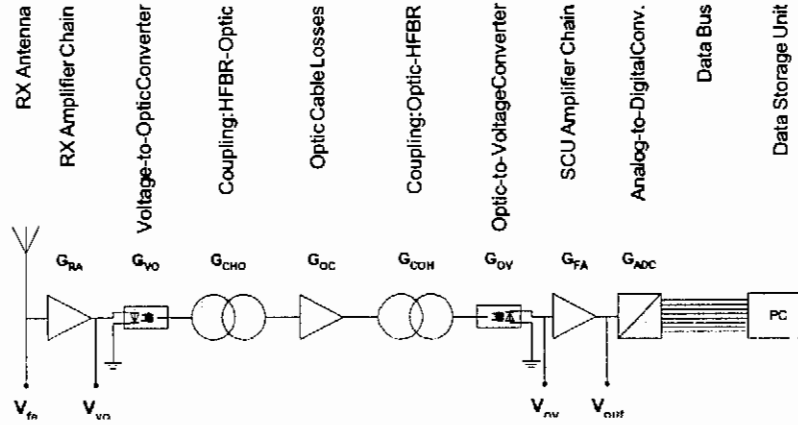


Figure 3-8: Complete schematic diagram of calibration facility receiver chain.

The voltage transfer function from the input of the receiver amplifier chain to the output of the SCU can be written in terms of the various gain blocks:

$$\begin{aligned} V_{out} &= V_{fe} \left( \frac{V_{vo}}{V_{fe}} \right) \left( \frac{V_{ov}}{V_{vo}} \right) \left( \frac{V_{out}}{V_{ov}} \right) \\ &= V_{fe} G_{RA} (G_{VO} G_{CHO} G_{OC} G_{COH} G_{OV}) G_{FA} \\ &= V_{fe} G_{RA} G_O G_{FA} \\ &= V_{fe} G_{CRC}. \end{aligned} \quad (3.13)$$

The main objective of the rooftop calibration facility (RCF) is to measure the exact waveform transmitted, the total amount of energy transmitted and delivered to the antenna, and how well the receiver probe receives and distorts the signal.

### 3.4.3 Low-Power Calibration Transmitter

In preliminary free space measurements it became evident that a transmitter with 40 dB less power than the GeoMole transmitters was needed, in other words a transmitted waveform similar in dynamics with a voltage factor of approximately 0.01. A calibration transmitter with maximum amplitude of 15 V (-36.5 dB relative to GeoMole TX) was designed, built and tested. During the prototype design phase it was decided to use a pulse generator rather than a step generator. This was due to the lowered power constraints and the availability of faster digital and driver IC's at the lower voltages. Only the final design is discussed in this section.

#### 3.4.3.1 Conceptual Design

The basic requirements imposed on the calibration transmitter were to transmit a waveform with a bandwidth exceeding that of the GeoMole transmitter and relative signal strength of -40 dB. It should also be compatible with the current system and include built-in test equipment (BITE) to evaluate the performance of the transmitter *in situ*. The basic block diagram of the transmitter is shown in Figure 3-9.

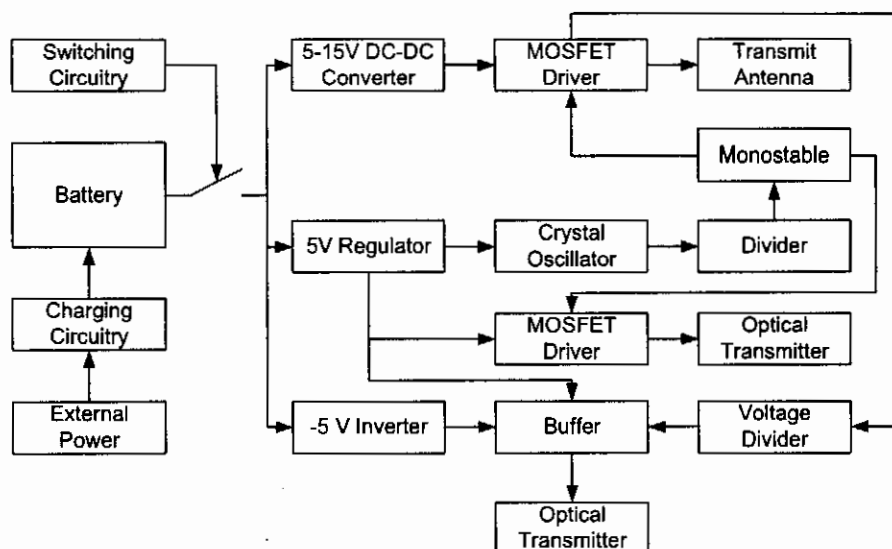


Figure 3-9: Block diagram of calibration transmitter.

The core of the transmitter is the MOSFET (metaloxide silicon field effect transistor) driver that drives the antenna with a voltage pulse of variable amplitude and pulse length. The MOSFET driver was found to be the ideal driving element for a capacitive antenna due to its high source and drain current ratings (necessary for charging and discharging the antenna). A low 'on' resistance also allows fast transient responses.

The battery-operated transmitter excites a new transmit cycle with a crystal oscillator module at 2 MHz, which is divided with a  $2^{12}$  counter to yield a  $\pm 488$  Hz pulse repetition frequency (PRF). A monostable creates a 10 – 20 ns pulse on the leading edge of the transmit cycle. The monostable in turn triggers two MOSFET drivers. The first MOSFET driver delivers the pulse to the antenna, while the second driver drives the optic modulator that provides the trigger signal for the ADC. The BITE of the system is parasitic to the MOSFET driver that measures the voltage of the generated waveform. A wide bandwidth buffer replicates the signal. It drives either a 50  $\Omega$  coaxial line for direct measurement or an optic modulator for fibre optic measurements using the SCU.

### 3.4.3.2 Hardware Implementation

The conceptual design was implemented in hardware on a double-sided printed-circuit board (PCB) with 23 mm x 141 mm dimensions as depicted in Figure 3-10 and Figure 3-11. It operates from 6 x 1.2 V AAA NiMH rechargeable batteries with a total length of 100 mm and a diameter of less than 23 mm. The circuit diagram of the hardware is given in Appendix H, with the four main components (DC power supply, pulse generator, trigger generator and BITE) highlighted.



Figure 3-10: Bottom layer of calibration transmitter electronics.

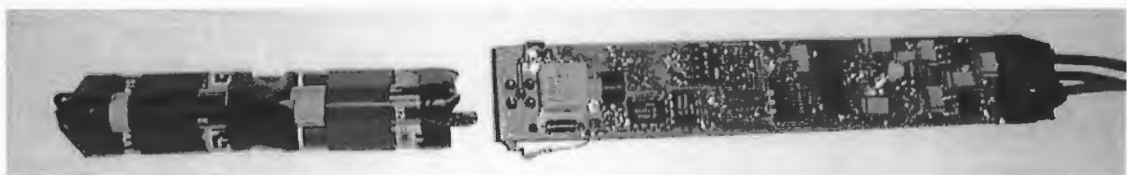


Figure 3-11: Top layer of calibration transmitter electronics.

A two-stage pulse generator was designed. In the first stage, a low-power voltage pulse is generated with a variable pulse width. This reference pulse is then used as the input to a MOSFET driver with a variable output amplitude and a current rating of 2 A. The MOSFET driver drives the resistive antenna arm against the ground plane, which is connected to the unloaded antenna arm. A basic component diagram of the pulse generator is shown in Figure 3-12. The associated timing diagram is shown in Figure 3-13.

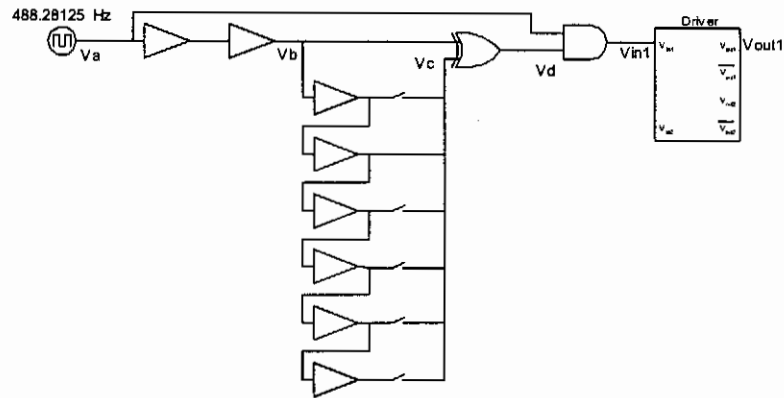


Figure 3-12: Implementation of pulse generator using logic gates and MOSFET driver.

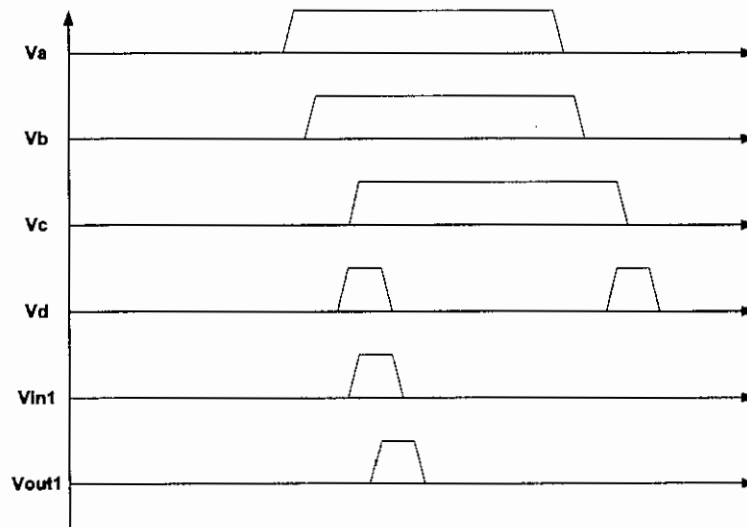


Figure 3-13: Timing diagram of pulse generator circuit.

The logic operation of the XOR (exclusive or) gate enables the generation of a short pulse on the rising and falling edges of a long pulse if the one input is slightly delayed. The length of the pulse is determined by the lag of the second input. In this design a series of buffers were used to create different delay times and therefore different pulse lengths. The second input signal is tapped from one of the buffer outputs (for example, the second buffer in Figure 3-12). Since the rise and fall times of logic gates are rarely matched, the characteristics of the two pulses associated with the rising and falling edge of the primary input are slightly different. An AND gate is used to mask the falling edge pulse. The bias voltage of the driver determines the output voltage driving the antenna.

### 3.4.3.3 Antenna Characteristics

It was decided to use an asymmetric resistively loaded dipole as the radiating structure for the calibration TX and RX probes. The resistive profile and length of the arms

were designed by Van Wyk [16]. The resistively loaded arm has a length of 1007 mm with 9 discrete resistors with equal spacing distances. The discrete resistor values are summarized in Table 3-1.

*Table 3-1: Resistive profile of resistively loaded calibration antenna.*

Discrete Resistor #	Resistor Value
1	22 $\Omega$
2	51 $\Omega$
3	68 $\Omega$
4	75 $\Omega$
5	82 $\Omega$
6	110 $\Omega$
7	150 $\Omega$
8	220 $\Omega$
9	470 $\Omega$

This resistive profile correlates with a 100% Wu-King loading in a free space environment [76]. The transmitter has a 431 mm long metallic cylinder of 27.5 mm diameter as the ground arm against which the resistively loaded arm is driven.

The input impedance, radiation pattern and gain of the antenna were numerically simulated with FEKO [78], a numerical electromagnetic analysis code based on the MOM. The modelling of the antenna is discussed in Appendix B. It was found that FEKO, with the model and the parameters as in Appendix B, had difficulty to accurately calculate the directivity of an antenna with discrete resistive loading in a lossy propagating medium. A procedure incorporating numeric integration was used to find the correct antenna gain. Refer to Appendix B for more detail. The basic antenna properties for the calibration transmitter are plotted in Figure 3-14. The direction  $\theta = 0^\circ$  is coaxial to the antenna axis in the direction of the resistively loaded arm. The efficiency has been calculated using two different techniques. In the top graph of Figure 3-14 (a) efficiency was calculated using (3.7), while it was calculated with the help of (3.16) (see Section 3.7.1) for the top graph. The latter incorporates the resistive and near field losses, while the first only accounts for the resistive losses. In free space we have no near field losses and the two should be equal. Figure 3-14 (d) graphs the antenna E-field phase response. This is the far field phase of the  $\theta$ -

CHAPTER 3: Characterization of TX and RX Probes

directed E-field referenced to the feedpoint  $E_{\theta}(r,\theta,f)e^{jkr}$  with respect to the input voltage  $V_{in}(f)$  and current  $I_{in}(f)$ . FEKO uses the positive  $e^{+j\omega t}$  time convention.

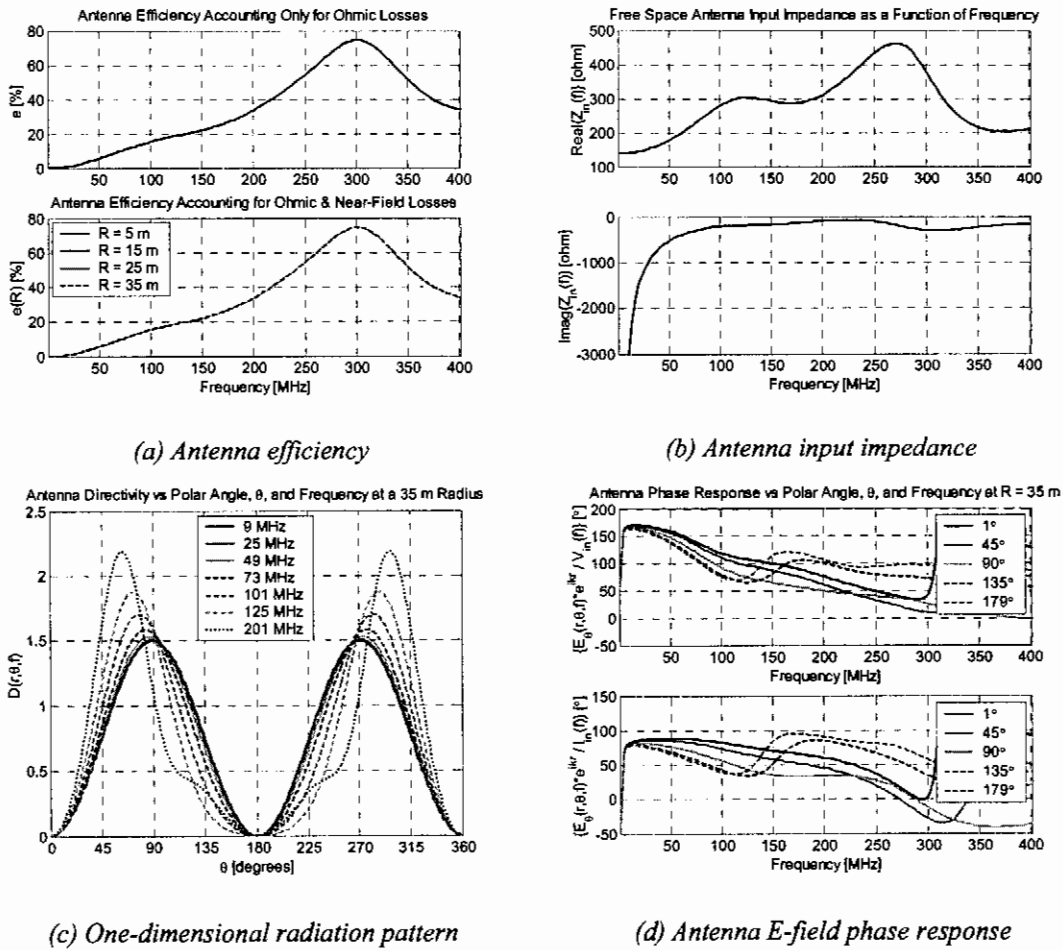


Figure 3-14: Calibration transmitter antenna characteristics.

Antenna efficiency is less than 20 % below 100 MHz and can be ascribed to the heavy resistive loading used. It rises almost linearly to about 80% at 300 MHz after which it drops down again. Analysing the input impedance reveals the capacitive nature of the antenna topology and profile. Since the antenna is electrically short below 100 MHz, the radiation pattern is closely correlated to the sine-squared pattern of a Hertzian dipole. Beyond 125 MHz, the radiation pattern becomes distorted since the electrically short assumption is no longer valid and the antenna starts to behave like a travelling wave radiator. The formation of a sidelobe is just visible at 201 MHz. The antenna has a relatively linear phase response up to 125 MHz with the typical 90° phase difference between the E-field and the excitation current at low frequencies.

### 3.4.3.4 Pulse Generator Measurements

The BITE on the calibration transmitter allows the real-time measurement of the antenna excitation waveform with the antenna as load, without the additional parasitic loading of a probe. A resistive voltage divider network allows the 900 MHz bandwidth, open-loop BUF601 (Texas Instruments) voltage buffer to probe a fraction of the transmitter waveform. It has unity gain with a ripple of 0.1 dB up to 300 MHz and is capable of driving a 100 Ω load with a minimum voltage swing of 5 V<sub>pp</sub>. In this case it either drives a 50 Ω coaxial probe cable or the optic modulator for electrically isolated measurements.

With the resistive network as given in Appendix H, the fraction of actual voltage that is probed with a 50 Ω system is calculated as

$$v_{probe} = 0.5 \left( \frac{23.5}{23.5 + 480} \right) v_{actual} = 2.334 \times 10^{-2} v_{actual}. \quad (3.14)$$

The inferred transmitted waveforms for 4 different time settings are plotted in Figure 3-15 for given voltage settings, with their respective power spectral densities plotted in Figure 3-16. The latter were calculated as the power delivered to a 1 Ω load at a PRF of 10 MHz. The time and voltage setting codes are summarized in Table 3-2.

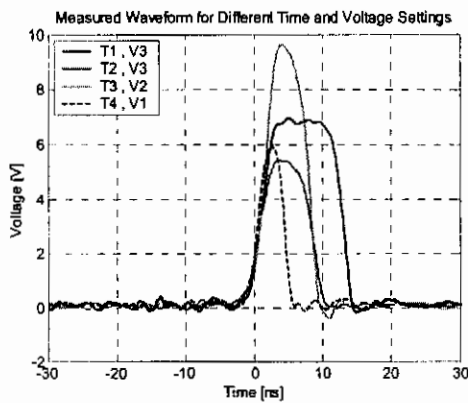


Figure 3-15: Inferred transmitted waveforms for different time and voltage settings.

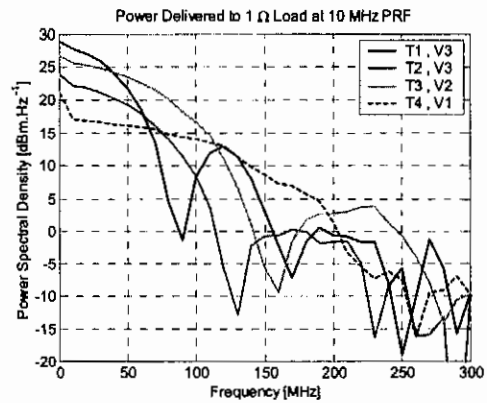


Figure 3-16: Power spectral densities for different time and voltage settings.

Table 3-2: Time and voltage codes for calibration transmitter.

Time Code	# of Buffers	Voltage Code	Voltage Level
T1	4	V1	12.5 V
T2	3	V2	10 V
T3	2	V3	7.5 V
T4	1	V4	5 V

The four time settings allow pulse widths in the range of 5 ns to 14 ns, while the four voltage settings allow a peak amplitude range of 5 V to approximately 10 V in reality. For a given voltage setting, the peak amplitude will decrease as the number of buffers decrease below a certain threshold dependant on the voltage setting. Time setting T1 only produces a pulse, for example, when the voltage is set at 12.5 V. The MOSFET driver utilizes a push-pull technology to form the drive signal. For short input pulses, the driver starts to 'pull' while it is still 'pushing', i.e. it starts to decelerate charge flow while it is still accelerating it. The power spectral densities are quite intuitive, with the first nulls associated with the pulse width. They clearly translate to higher frequencies as the pulse width decreases. The first null for T1 lies at 90 MHz that translates to 260 MHz for T4. For the purpose of this study, the interest is on the GeoMole transmitter characteristics up to a maximum frequency of 125 MHz (due to 250 MHz sampling frequency). Any of time settings T2-T4 can be used since they do not have a null in their spectrum.

### **3.4.4 Reference Receiver**

For the calibration process a reference receiver with a known transfer function is required. It is necessary that this receiver has comparable performance figures to the GeoMole receivers to be characterized. The reference receiver for the rooftop calibration facility was designed and built by Van Wyk [16].

The antenna for this receiver has exactly the same resistively loaded arm as the calibration transmitter with an unloaded cylindrical arm of 526 mm length and 27.5 mm diameter. The basic antenna parameters are plotted in Figure 3-17.

### CHAPTER 3: Characterization of TX and RX Probes

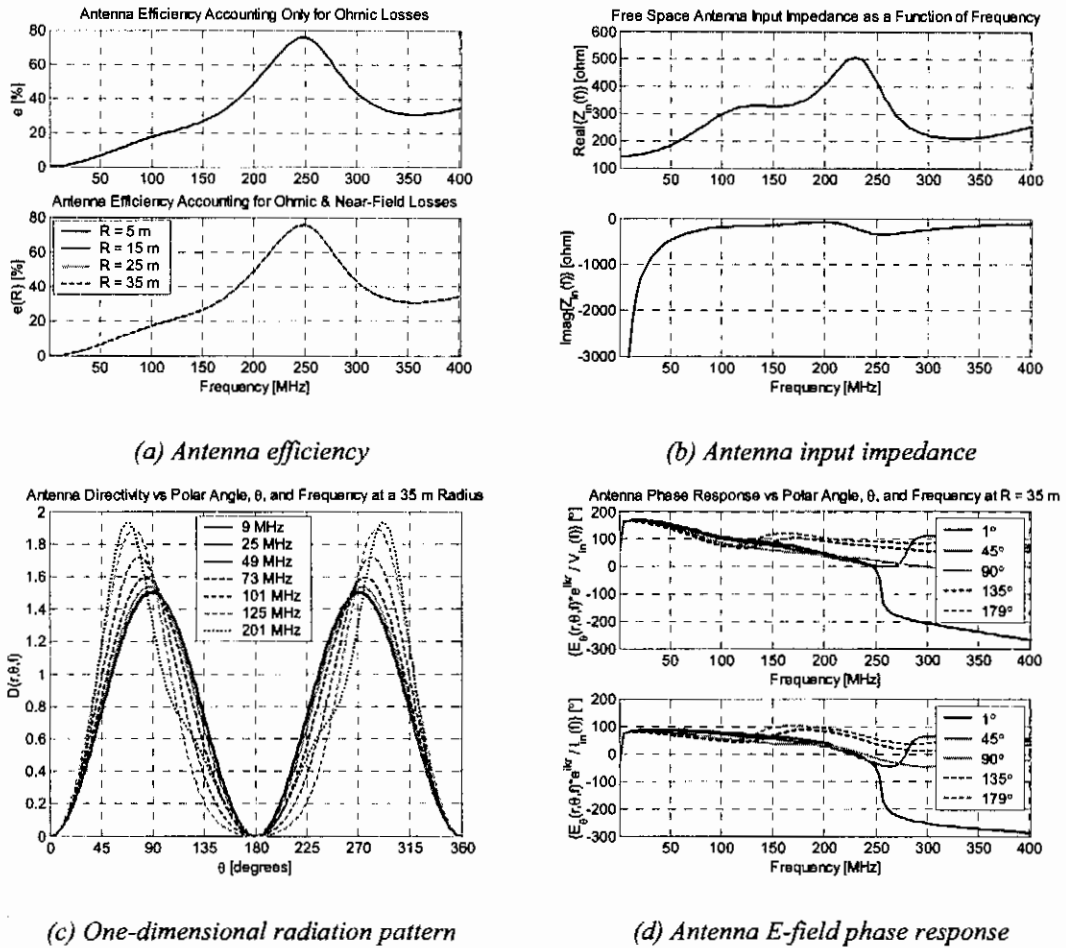


Figure 3-17: Reference receiver antenna characteristics.

The antenna characteristics are similar to that of the calibration transmitter, with the quasi-resonant frequency shifted lower due to the increased length of the unloaded segment. The phase response is also relatively linear up to at least 125 MHz, which reduces pulse shape distortion.

The RF receiver electronics comprises a voltage buffer, a three-stage amplification circuit and the optic modulator [16]. The transfer function and 1 dB compression point of the buffer and amplifier stages are plotted in Figure 3-18.

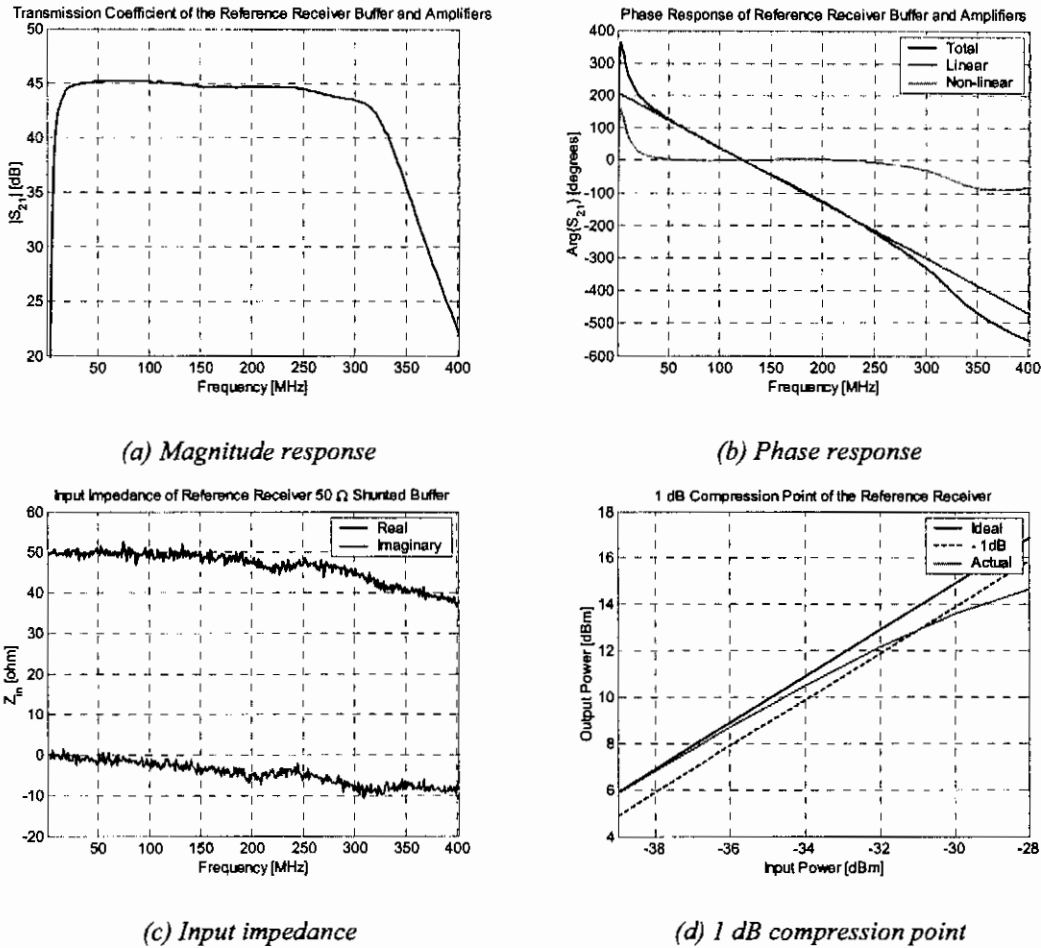


Figure 3-18: Reference receiver transfer function and 1 dB compression point.

The receiver has a 3 dB bandwidth of 12 – 320 MHz, a linear phase response from about 25 MHz and an input 1 dB compression point of  $-31$  dBm continuous wave (CW) across the bandwidth.

### 3.4.5 Desensitised Calibration Receiver

In Section 3.3.3 the necessity of an insensitive calibration receiver for the GeoMole transmitters in free space was highlighted. The topology, antenna and physical packaging of the reference receiver were used for the calibration receiver.

The dynamic range of the subsystems in the receiver, especially the RF optical link, is of critical importance in high fidelity signal measurements. A decent SNR and a linear region of operation are of the utmost importance. It was found that the linearity of the optic link was the major concern in the design of the calibration receiver. The forward current vs. forward voltage slope of the HFBR1404 optical modulator [79] can be divided into two quasi-linear regions. With the bias current in a specific region, the current swing should be limited to the specific linear region in order to

## CHAPTER 3: Characterization of TX and RX Probes

avoid harmonic distortions. The dynamic range of the HFBR2406 demodulator [79] should also be considered. The circuit diagram of the final calibration receiver is given in Appendix H.

The RF transfer function of the calibration receiver front-end buffer is plotted in Figure 3-19. The attenuation network with a  $50 \Omega$  input impedance is treated as integral to the optical link and not considered a part of the RF front-end.

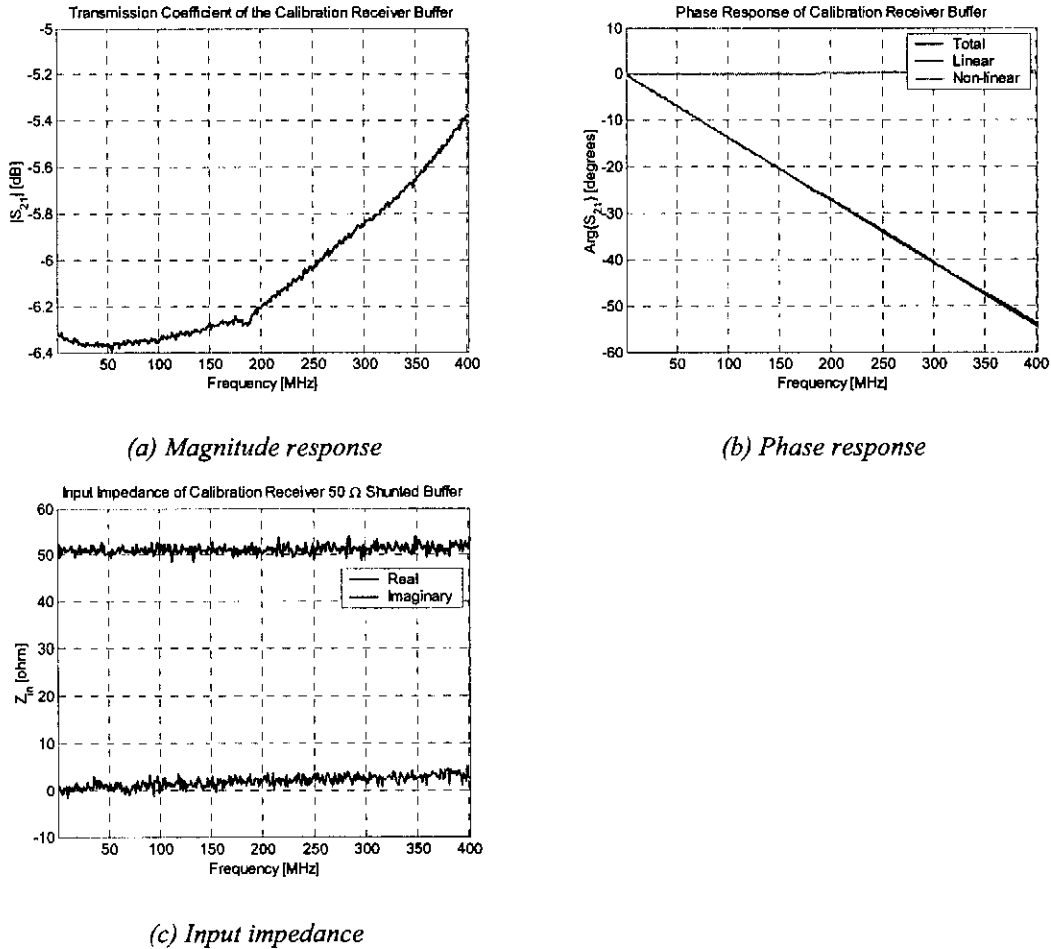


Figure 3-19: Transfer function of the calibration receiver front-end.

The buffer has a voltage gain of approximately 0.5 with a 1 dB variation over the 1 – 401 MHz frequency band. The buffer has a linear phase response over the entire band with input impedance very close to  $50 \Omega$  (within  $5 \Omega$ ).

The electronics of the calibration receiver was interchanged with the electronics of the reference receiver when deployed. The exact antenna, power supply, PVC housing and connectors, as depicted in Figure 3-20, were used.



Figure 3-20: Calibration receiver electronics, antenna, power supply and connectors.

### 3.4.6 Instrumentation Optic Link

The final stage of the rooftop calibration facility is the optic link consisting of the optic modulator, fibre optic cable, optic demodulator and the final amplification (if any) as depicted in Figure 3-8.



Figure 3-21: Instrumentation SCU developed for rooftop calibration facility.

The instrumentation SCU depicted in Figure 3-21 was built by Van Wyk [16]. The total transfer functions of the optic link,  $G_oG_{fb}$ , have been measured with a vector network analyzer (VNA) for both the reference and the calibration receivers and are plotted in Figure 3-22.

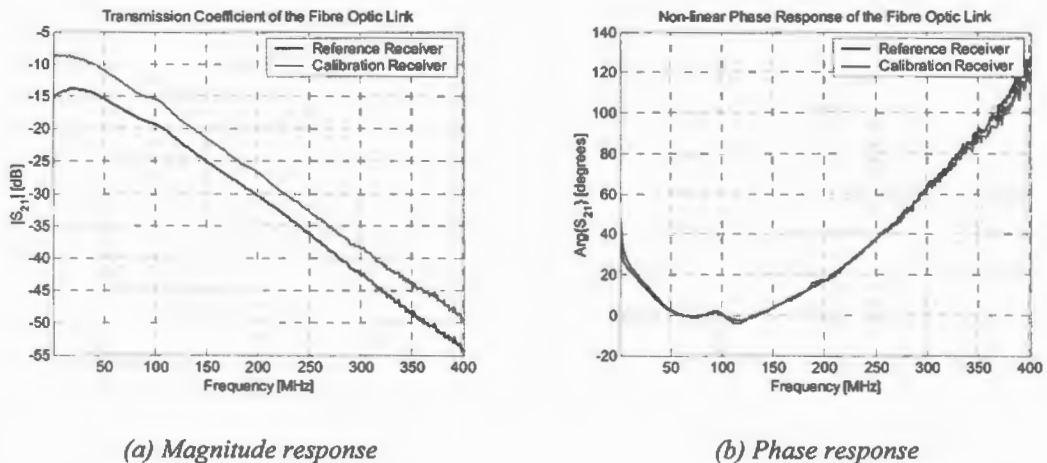


Figure 3-22: Transfer functions of the reference and calibration optic links.

A multimode optic fibre has a narrow bandwidth (compared to the single mode fibres) due to dispersion. It is clearly visible in both optic links as the frequency increases above 125 MHz. Above 250 MHz the loss is greater than 30 dB. The calibration receiver optic link has a 4.4 dB higher gain than the reference receiver at 50 MHz. The calibration receiver also has a better low frequency response due to a different choice of coupling capacitors. Both links have a non-linear phase response in the DC – 200 MHz frequency range, but deviate from linearity by less than 22.5 degrees ( $\pi/8$  radians) over this range. The non-linear response was calculated by subtracting the linear phase (determined by a least square error algorithm) in the 50 – 150 MHz frequency range.

## 3.5 Free Space Transmitter Characteristics

The transfer function and characteristics of the GeoMole transmitter in free space are summarized in this section. These are based on numerical simulations, practical measurements in the rooftop calibration facility and on the transfer functions of the calibration receiver and instrumentation optic link.

### 3.5.1 GeoMole TX Antenna Response

The GeoMole transmitter antenna has been described in literature [4],[3],[81] as an asymmetric dipole with a 1 m unloaded metallic arm (27.5 mm diameter copper cylindrical pipe) and a 0.61 m resistively loaded arm with 48 discrete resistors. The resistively loaded arm is potted in dielectric potting material. The entire antenna structure is encapsulated in a tight fitting PVC housing. The 48 resistor values (indexed from the feedpoint) are tabulated in Table 3-3 and the dielectric properties of the potting material was measured as

$$\begin{aligned}\tilde{\epsilon}' &= 3.7 \\ \tan \delta &= 0.02\end{aligned}\tag{3.15}$$

over the frequency range of interest.

Table 3-3: Discrete resistor values for the resistively loaded GeoMole antenna arms.

Res. Index	Res. Value	Res. Index	Res. Value								
1	18 $\Omega$	9	22 $\Omega$	17	27 $\Omega$	25	36 $\Omega$	33	56 $\Omega$	41	110 $\Omega$
2	20 $\Omega$	10	24 $\Omega$	18	30 $\Omega$	26	39 $\Omega$	34	62 $\Omega$	42	130 $\Omega$
3	20 $\Omega$	11	24 $\Omega$	19	30 $\Omega$	27	43 $\Omega$	35	62 $\Omega$	43	150 $\Omega$
4	20 $\Omega$	12	24 $\Omega$	20	30 $\Omega$	28	43 $\Omega$	36	68 $\Omega$	44	180 $\Omega$
5	20 $\Omega$	13	24 $\Omega$	21	33 $\Omega$	29	47 $\Omega$	37	75 $\Omega$	45	220 $\Omega$
6	20 $\Omega$	14	24 $\Omega$	22	33 $\Omega$	30	47 $\Omega$	38	82 $\Omega$	46	300 $\Omega$
7	22 $\Omega$	15	27 $\Omega$	23	36 $\Omega$	31	51 $\Omega$	39	91 $\Omega$	47	470 $\Omega$
8	22 $\Omega$	16	27 $\Omega$	24	36 $\Omega$	32	51 $\Omega$	40	100 $\Omega$	48	910 $\Omega$

This antenna was simulated with FEKO in a free space environment. The meshing and simulation are elaborated on in Appendix B. The antenna characteristic parameters (efficiency, input impedance, gain and phase response) are plotted in Figure 3-23. The gain was once again calculated with the algorithm developed in Appendix B.

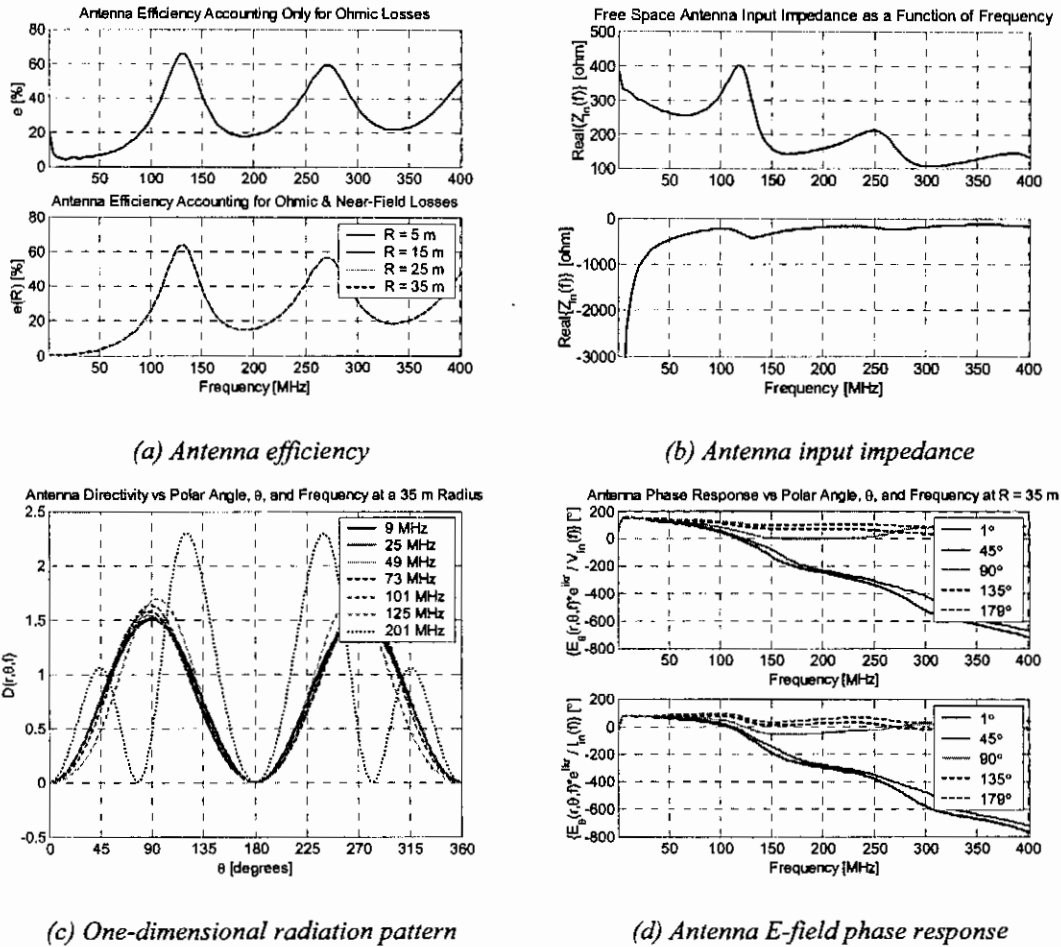


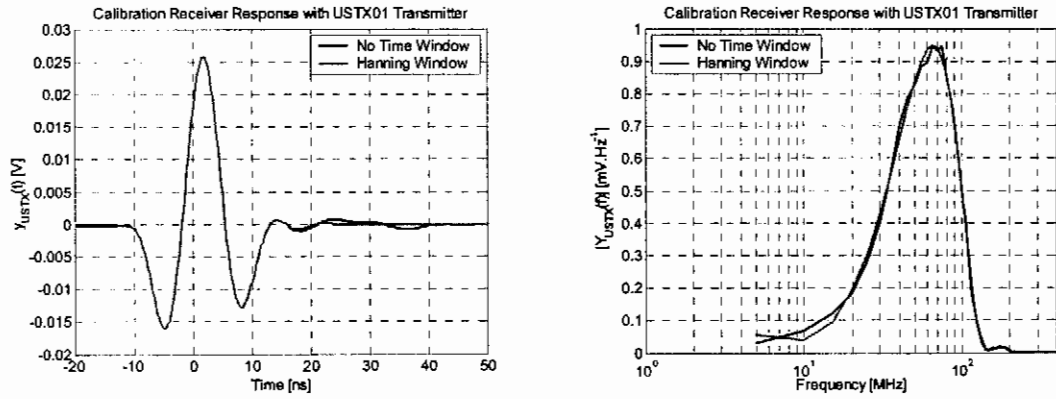
Figure 3-23: GeoMole transmitter free space antenna characteristics.

Antenna efficiency peaks at 130 MHz and the effect of the potting material is evident in the efficiency calculations. Additional near field losses due to the finite dielectric losses in the potting material decreases the efficiency slightly. Refer to Appendix B for a concise description of the efficiency calculations. In the DC – 125 MHz frequency range, the real part of the input impedance has an average value of 300  $\Omega$ , while the capacitive nature of the antenna is clearly visible in the exponential-like reactance response. Due to the relatively long (1 m) metallic pipe, beam squinting (from broadside) starts at a lower frequency. Up to 125 MHz, the pattern closely resembles  $\sin^2\theta$ , but deviates rapidly thereafter with a pseudo null approaching broadside at 201 MHz. In this frequency range (DC – 125 MHz) the antenna phase response is almost purely linear with minimum pulse shape distortion.

### 3.5.2 Rooftop Calibration Measurement Results

The GeoMole transmitter probes were deployed with the calibration receivers in the rooftop calibration facility. The oscilloscope sampled the receiver response at 5 Gbps

with an amplitude resolution of  $10 \text{ ns.div}^{-1}$ . A captured trace consisted of 2048 coherently averaged samples. Five GeoMole transmitters (USTX 01 – 03 and GMTX 01 – 02) were characterized. The measured frequency and time domain responses of USTX 01 are plotted in Figure 3-24.



(a) Time domain response of USTX 01

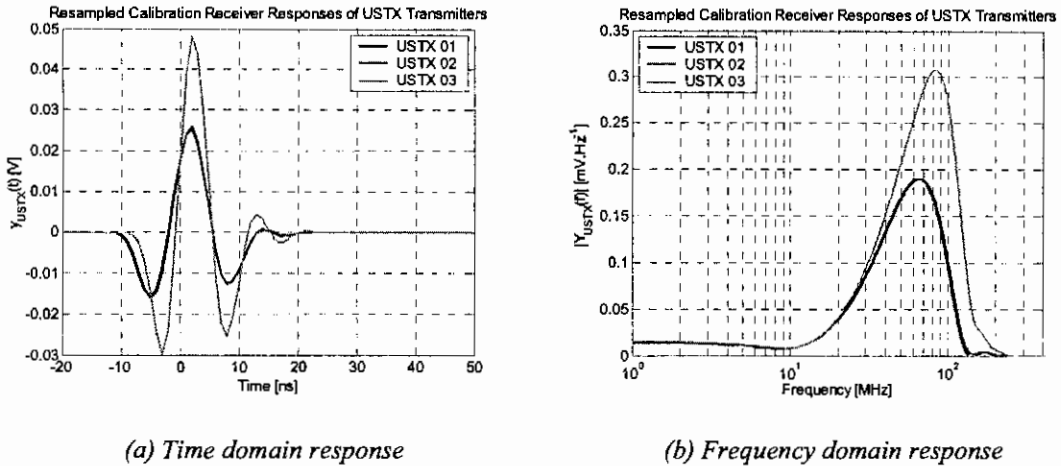
(b) Frequency domain response of USTX 01

Figure 3-24: Time and frequency domain response of the USTX 01 transmitter.

The response was time-gated with Hanning window rising and falling edges to remove resolved secondary reflections. Unresolved interference effects were not removed, but the facility was designed to minimize those effects. The measured response very closely resembles a Ricker wavelet [60]-[64] with a spectral density peak at 65 MHz after which it drops off rapidly with a pseudo null at 155 MHz. Time-gating removes the ripples in the frequency domain associated with secondary reflections.

For signal processing purposes it was necessary to resample the data at 1 ns intervals (decimate by 5) with a 1 MHz frequency resolution. The effect of this is a 5-fold decrease in the spectral density of the response (two  $5^{1/2}$  factors due to a five times longer pulse repetition interval (PRI) and a five times denser spectrum). The resampled responses of the three USTX transmitters are plotted in Figure 3-25.

## CHAPTER 3: Characterization of TX and RX Probes



(a) Time domain response

(b) Frequency domain response

Figure 3-25: Time and frequency domain responses of the USTX transmitters.

The USTX 01 and 02 transmitters have closely correlated transmitted waveforms both in frequency and time domain. The USTX 03 transmitter has a shorter and higher amplitude transmitted waveform with an associated higher (+ 4 dB) and broader (up to 250 MHz) spectral density. The USTX 03 uses a different MOSFET with faster rise and fall times than the other two transmitters – thus a broader spectrum with better high frequency response. It was established in undocumented trials that the GMTX 01 transmitter has the same characteristics as the USTX 03 transmitter, while the response of the GMTX 02 closely resembles that of the USTX 01 and 02 transmitters. The two different classes of transmitters also have different trigger signals, indicative of an undocumented upgrade. The measured trigger signals are plotted in Figure 3-26.

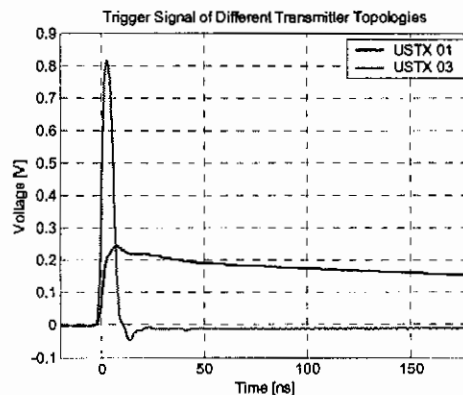


Figure 3-26: Trigger signal of different transmitter topologies.

The one set of transmitters (USTX 01 – 02 and GMTX 02) delivers a slow-recovery step trigger, while the other set delivers a high amplitude pulse trigger. This proved to be valuable information in field experiments when spur of the moment decisions had

to be made with regard to transmitter choice, especially when trigger problems occurred.

### 3.5.3 Transmitter Power Estimation

From the digitised voltage it is possible to determine the voltage at the input of the RF front-end if the transfer functions of the front-end amplifiers, optic link, SCU and ADC are quantified and the dynamic range constraints of the entire chain are adhered to. The power delivered to the front-end,  $P_d$ , can be estimated from this voltage with the front-end taken as a  $50 \Omega$  system. Equation (3.11) uses the receiver antenna characteristics plotted in Figure 3-19 to calculate the power received (intercepted) by the antenna,  $P_{rec}$ , from  $P_d$ . Equation (3.10) relates the received power to the actual transmitted power,  $P_{rad}$ , based on geometric spreading, frequency and the directivities of the antennas. Finally, (3.6) relates the power radiated to the power delivered to the antenna by the transmitter electronics,  $P_{in}$ . This is the actual parameter that was not measured previously due to the intricate intertwined transmitter and antenna topology. In addition to the inverse equations used to estimate  $P_{in}$ , a frequency domain weighting function had to be employed to weight these inverse functions. Due to the severe attenuation of the higher frequencies (above 200 MHz) by the optic link, data and noise (mostly) are highly accentuated and adversely affects the SNR of the time domain reconstructed signal. The estimations of the power delivered to the receive electronics and the transmit antenna are plotted for the USTX 01 transmitter in Figure 3-27.

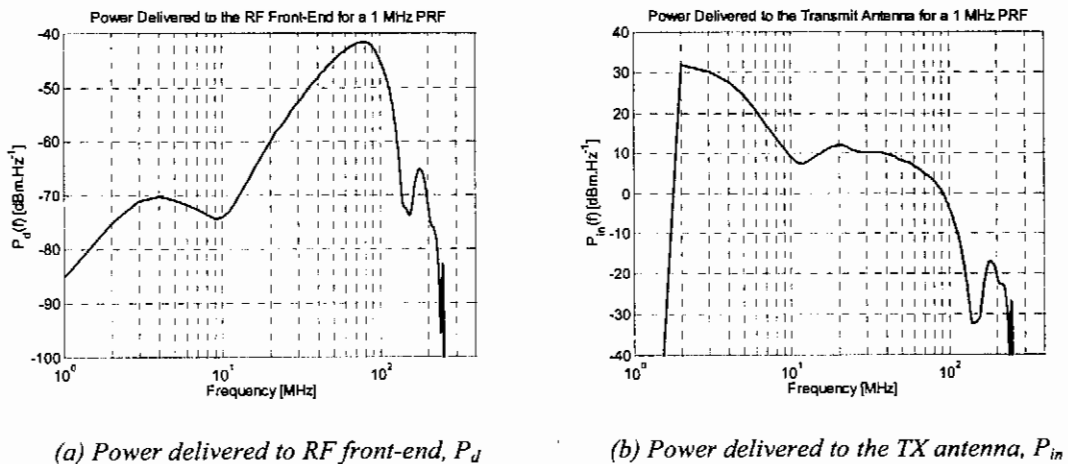


Figure 3-27: Power delivered to the RF front-end and TX antenna for the USTX 01 transmitter.

The window function used in these estimations was a 0 MHz to 250 MHz bandpass filter with 5 MHz Hanning window rising and falling edges. The power delivered to

the RF front-end rises by more than 30 dB from 10 MHz to 80 MHz after which it drops down very rapidly. The weak low frequency response can be ascribed to the low efficiency of the antennas at lower frequencies. When the power delivered to the TX antenna is estimated, it is clear that the peak power resides at the lower frequency range, but is dissipated in the resistors and near field. The high response of the transmitter below 10 MHz is disregarded, since the antennas in general radiate these frequencies very poorly. The frequency contents of the power delivered by the TX electronics are typical of an impulse current excitation (caused by the step in voltage) with finite rise and fall times. The position of the first null is indicative of the pulse width. The power delivered to the TX electronics for the different transmitters are compared in Figure 3-28.

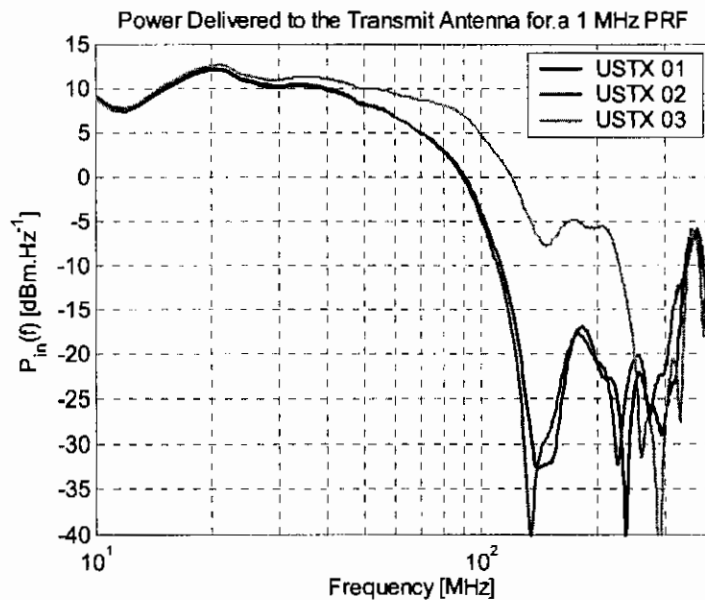


Figure 3-28: Comparing the power delivered to the TX antennas for the different transmitters.

As expected, the performance of the USTX 01 and 02 probes is comparable. The USTX 03 probe has a similar low frequency response, but exhibits a much stronger high frequency response. This is indicative of a faster fall time of the MOSFET driving the antenna. One possible explanation for this is the use of different MOSFET in the USTX 03 and GMTX 01 transmitters. This could not be verified since the probes are potted and no design alterations were documented.

### 3.6 Free Space Receiver Characteristics

As the GeoMole transmitters were characterized in free space in the previous section, the receivers are characterized in this section. It is done through using vector network

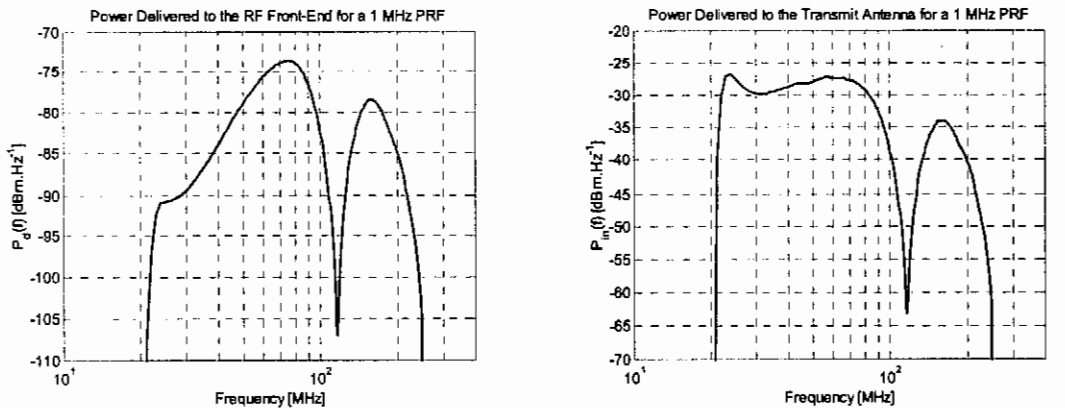
analyser measurements, time domain measurements in the RCF and numeric simulations. In the RCF measurements the calibration transmitter was used in conjunction with the reference and GeoMole receivers.

### 3.6.1 Power Delivered by Calibration TX Estimation

Only by means of a calibrated receiver can the power transmitted (radiated) by the calibration transmitter be measured (estimated). For this specific reason, the reference receiver were designed, built and characterized (Section 3.4.4). Similar to the method used in Section 3.5, the power transmitted by and delivered to the TX antenna of the calibration transmitter was estimated. The settings of the transmitter are summarized in Table 3-4 and the estimated power values are plotted in Figure 3-29.

Table 3-4: Calibration TX settings for GeoMole RX calibration.

Time Setting	Voltage Setting
T3 (2 buffers)	V1 (12.5 V)



(a) Power delivered to RF front-end,  $P_d$

(b) Power delivered to the TX antenna,  $P_{in}$

Figure 3-29: Power delivered to the RF front-end and TX antenna for the calibration transmitter.

The amplifiers in the reference receiver do not have a good low-frequency (< 25 MHz) response and only the frequency contents above 20 MHz are of any relevance. The calibration transmitter excites a pulse with a first null at 115 MHz with a higher frequency contents than the GeoMole transmitter (well above 200 MHz). This allows the accurate high frequency characterization of the GeoMole receivers.

### 3.6.2 GeoMole RX Antenna Response

The GeoMole receiver has a similar antenna structure to the corresponding transmitter, with the only difference the length of the cylindrical copper pipe. The

total length of the unloaded arm is 0.65 m (1 m for the TX). The antenna response and characteristics were once again simulated with FEKO and processed with the gain calculation algorithm (GCA). The main characteristics are plotted in Figure 3-30.

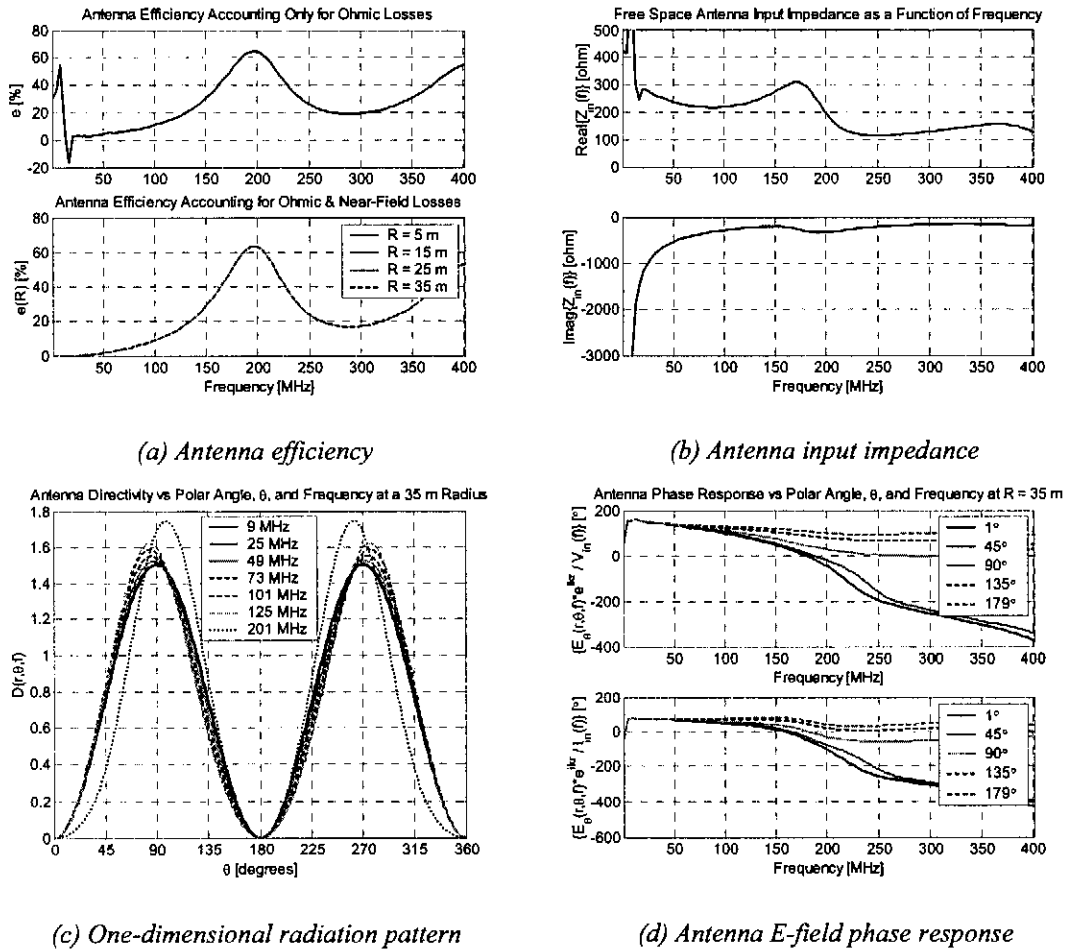


Figure 3-30: Geomole receiver free space antenna characteristics.

An obvious error occurred in the simulation of the antenna at the low frequencies (< 25 MHz) due to the RAM constraints placed on meshing and the physical spacing of the various layers and metallic structures. The characteristics of the antenna are still clearly visible. The shortened metallic arm shifted the first pseudo resonance to 200 MHz with an efficiency peak of 60 % and an average real input impedance (DC – 200 MHz) of 250  $\Omega$ , which is slightly lower than the transmitter antenna. The radiation pattern is more stable with the pattern starting to squint only at 200 MHz. Phase linearity of the antenna is also extremely good, especially up to 100 MHz.

### 3.6.3 GeoMole RX RF & Optic Electronics

A reference RX electronics subsystem was built up and characterized by means of vector network analyser measurements. The 2-port transfer function and 1 dB compression point of the RF amplifiers are plotted in Figure 3-31.

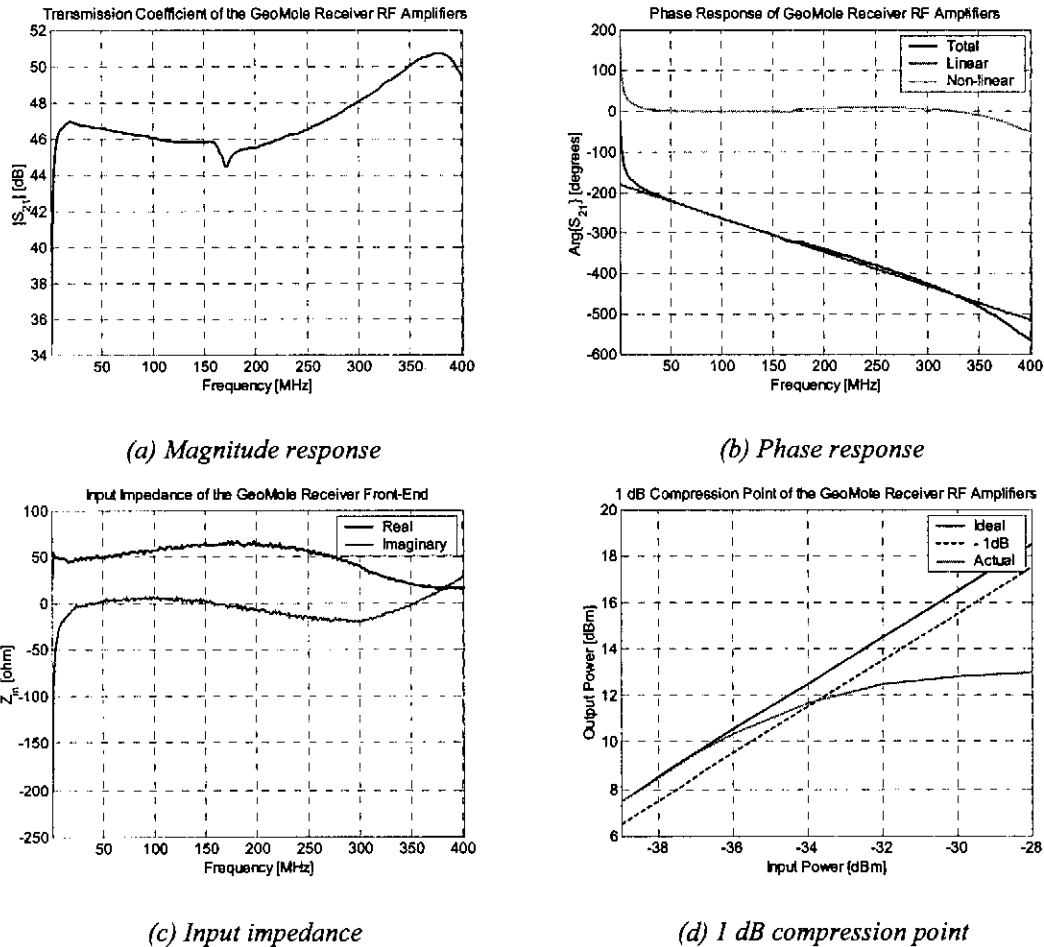


Figure 3-31: GeoMole receiver transfer function and 1 dB compression point.

The GeoMole RX has a  $46 \pm 1$  dB gain up to 250 MHz with a linear phase (only from 25 MHz) and relatively stable  $50 \Omega$  input impedance. The gain is 1 dB more than the reference receiver, but the 1 dB compression point is 3 dB lower.

The forward transfer function of the GeoMole optic modulator circuitry in conjunction with the optic link and the instrumentation SCU are plotted in Figure 3-32.

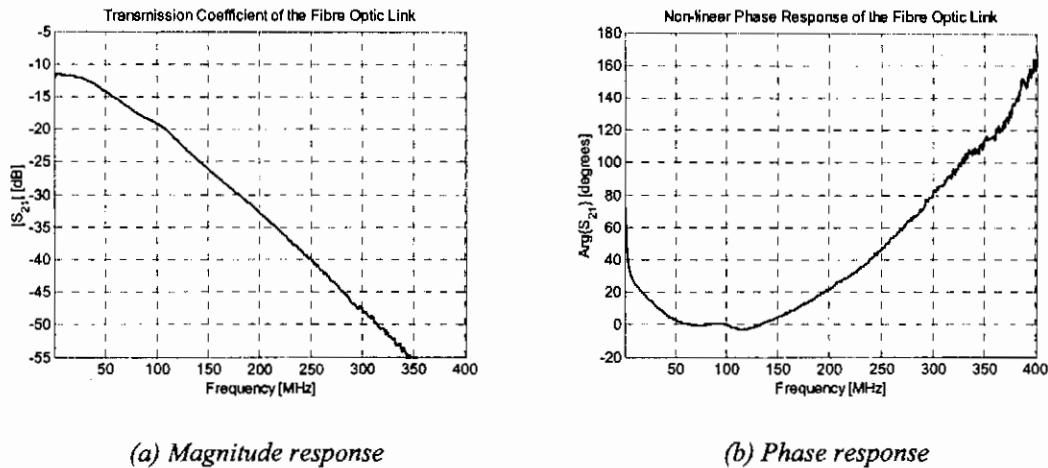


Figure 3-32: Transfer functions of the GeoMole receiver and instrumentation optic link.

The low frequency (< 100 MHz) response is between that of the reference and calibration receiver, but the high frequency response is more than 6 dB lower at 350 MHz. The phase response is quasi-linear (error less than 22.5°) in the 15 – 200 MHz frequency range.

### 3.6.4 Rooftop Calibration Measurements

The calibration TX probe (V1, T3) was deployed with the GeoMole receivers (USRX 01 – 03 and GMRX 01 – 03) in the RCF. The oscilloscope sampled the received signal at 2 Gps with an amplitude resolution of 50 mV/div and averaged the response of 2048 samples coherently. Since these receivers have a much higher sensitivity than the calibration RX, they were more vulnerable to EMI as discussed in Section 3.3.4. The coherently averaged signals for the USRX 02 probe are plotted in Figure 3-33 for 256 and 2048 averaging factors. The PRF was synthetically set at 2 MHz, yielding a frequency resolution of 2 MHz.

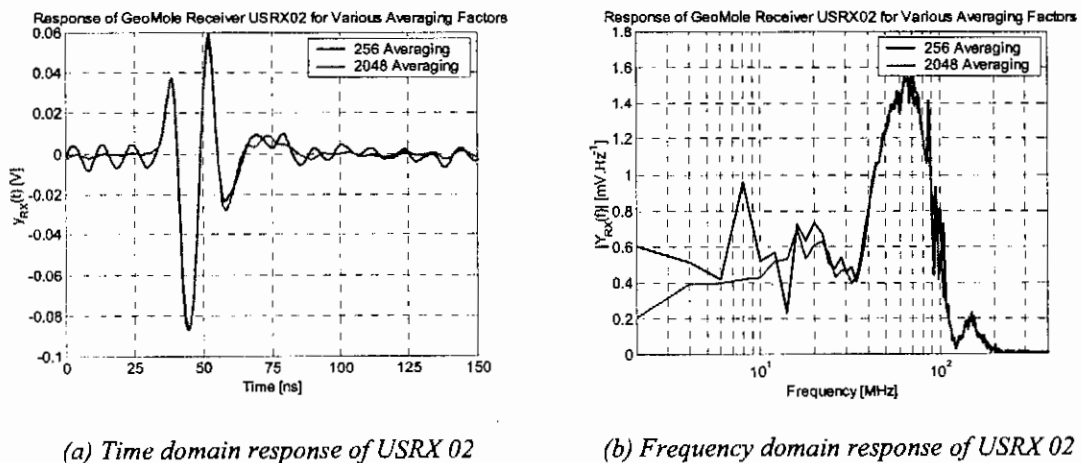
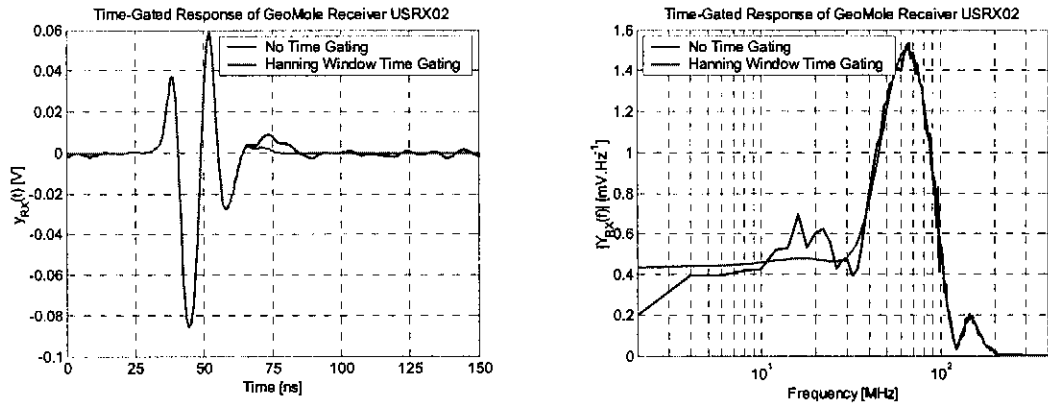


Figure 3-33: Time and frequency domain response of USRX 02 receiver for a 2 MHz PRF.

## CHAPTER 3: Characterization of TX and RX Probes

The decrease in EMI with an increased averaging factor is clearly visible. The EMI average power can be reduced even further by means of time-gating due to the finite duration of the transmitted pulse. The time-gated response is compared with the ungated response in Figure 3-34.

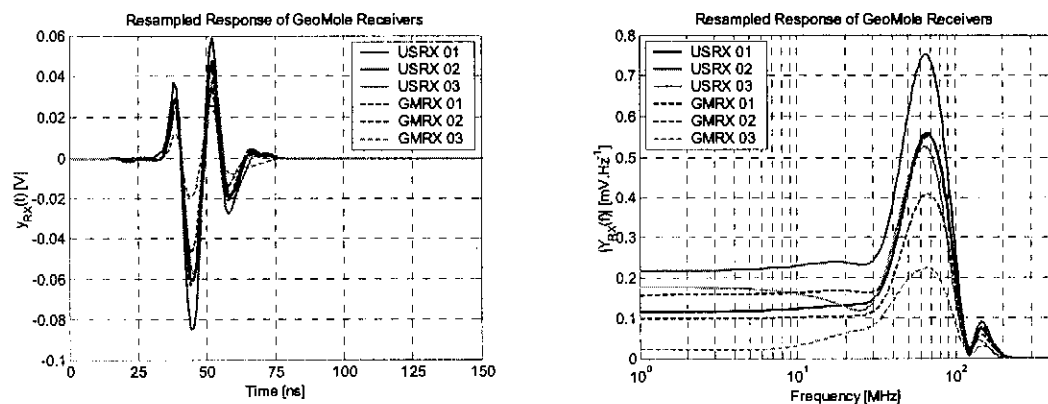


(a) Time domain response of USRX 02

(b) Frequency domain response of USRX 02

Figure 3-34: EMI reduction for USRX 02 receiver by time-gating.

The reduction in EMI is clear, with the added reduction in secondary reflections. The received signal peaks at 65 MHz with a first null at 122 MHz and a sidelobe of moderate amplitude when the weak high frequency response of the optic link is considered. The responses were decimated by a factor of two and the length of the trace adjusted for a frequency resolution of 1 MHz, resulting in a spectral magnitude reduction of 6 dB. The resampled responses of the six different probes are plotted in Figure 3-35.



(a) Time domain response

(b) Frequency domain response

Figure 3-35: Resampled response of the different GeoMole receivers.

The USRX 02 receiver is the most sensitive receiver, followed by the USRX 01 & 03 and GMRX 01 receivers with comparable moderate sensitivity. The response of the

GMRX 02 receiver is less sensitive than the average, while the GMRX 03 receiver has poor sensitivity with erratic behaviour encountered during calibration runs.

### 3.6.5 Relative Receiver Performance

The power transmitted by the calibration transmitter was calculated for each receiver through using the procedure described in Section 3.5.3. It was then compared with the power calculations done with the reference receiver to calculate a relative gain for each receiver probe. Since the antenna structure is rigged and the same for all the probes (assumed) and the RF electronics are also universal, the relative gain was assigned to the optic modulator and patchcord of the receiver. The performances of these two components are highly likely to change from part to part. The exact theory of relative gain in the optic link is explained in detail in Chapter 4. Since the optic modulator and the patchcords are intertwined in the receiver, it is impossible to separate their performance. For ease of computation, the relative gain of a RX probe was assigned to the patchcord,  $G_{PCRr}$ . The relative gains of the GeoMole receivers are plotted in Figure 3-36, with the average gain over the plotted frequency range given in Table 3-5.

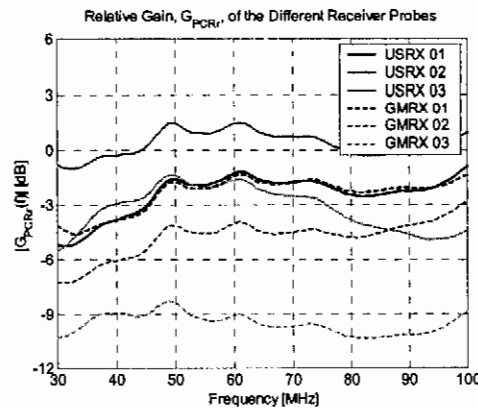


Figure 3-36: Relative receiver patchcord gain of different receivers.

Table 3-5: Average relative receiver patchcord gain.

Probe	$G_{PCRr}$	Probe	$G_{PCRr}$
USRX 01	-2.32 dB	GMRX 01	-2.34 dB
USRX 02	-0.34 dB	GMRX 02	-4.67 dB
USRX 03	-3.07 dB	GMRX 03	-9.52 dB

Observations made on the SNR of the different probes in field experiments (before the probes were characterized) indeed confirmed the relative gain (sensitivity) of the

probes. The GMRX 03 receiver is less sensitive than the USRX 02 receiver by a factor of more than 9 dB.

## **3.7 Transfer Function when Radar is Deployed in Rock Boreholes**

The geometry, environment and system configuration when the radar system is deployed in hard rock boreholes are much more complicated than the free space system described up to now. Firstly, the transmitter and receiver probes are deployed in a borehole with an arbitrary diameter (say between 40 and 80 mm diameter; with 48 mm typical) in a lossy dielectric medium – hard rock. Secondly, a long and complex system of optic cables, optic connectors and possibly even a rotating joint is incorporated to route the optic signal to the SCU. In this section the coupling of the EM energy into the rock and back to the receiver is considered. The optic link is discussed in detail in Chapter 4.

### **3.7.1 Quantitative Coupling Description**

Transmitter and receiver probes are deployed in boreholes, which may be air- or water filled, in the host rock. For a quantitative study of power flow, the coupling of the antennas to the rock is of utmost importance. One of the major difficulties presenting itself in our enormous underground laboratory is the virtual impossibility of measuring field strengths around the transmitter. The receiver probe can only be deployed in boreholes, thus covering a limited angular spectrum around the transmitter. Secondly, even though the host medium appears to be homogeneous for a finite volume, the dielectric properties of the host medium between transmitter and receiver remains unknown. The only insight to be gained is from theoretic calculations or numeric simulations. FEKO provides a very good platform to numerically simulate the performance of antennas encapsulated in a borehole, surrounded by a host medium. The restrictions of FEKO in such simulations are considered in Appendix B. The more complex power flow schematic is depicted in Figure 3-37.

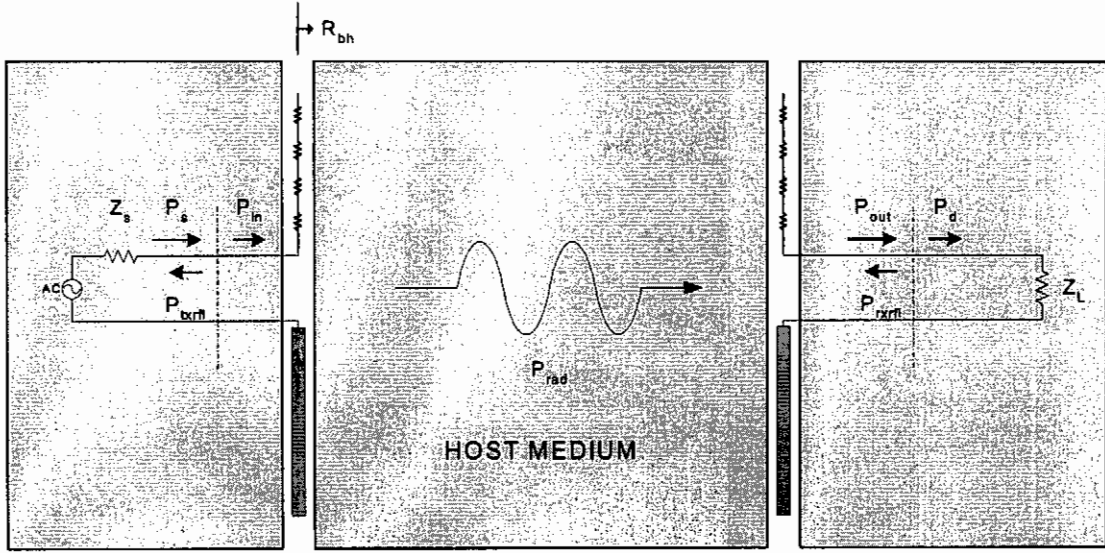


Figure 3-37: Power flow schematic for probes deployed in boreholes surrounded by host medium.

For an antenna surrounded by a lossy medium, the near field power loss contribute to the total power loss and therefore influences the efficiency of the antenna. The total power radiated into the far field region of the antenna can be written in terms of the various losses and the input power:

$$\begin{aligned}
 P_{rad}(\text{far field}) &= P_{in} - P_{loss}(\text{ohmic}) - P_{loss}(\text{reactive near field}) \\
 &= \int_0^{2\pi} \int_0^{\pi} \left[ \frac{1}{2} \text{Re} \{ \bar{\mathbf{E}}(r, \theta, \phi) \times \bar{\mathbf{H}}^*(r, \theta, \phi) \} \cdot \hat{\mathbf{r}} \right] r^2 e^{2\alpha r} \sin \theta d\theta d\phi \quad (3.16)
 \end{aligned}$$

$$\begin{aligned}
 k &= \beta + i\alpha \\
 &= \frac{2\pi f}{c} \sqrt{\mu_r \tilde{\epsilon}' (1 + i \tan \delta)}. \quad (3.17)
 \end{aligned}$$

The definition of (3.16) implies that the effective source of  $P_{rad}$  is a point source located at the origin. It is therefore necessary to choose the radial distance at which (3.16) is evaluated so that this assumption is valid. This can be done using a convergence criterion on  $P_{rad}$  as a function of radial distance.

The power delivered to the transmit antenna,  $P_{in}$ , has been measured for the various probes in the RCF. The question posed here is: Is it correct to assume that the same amount of power will be delivered to the antenna when the antenna is surrounded by a lossy medium? Numeric simulations indicated that the reactive part of the input impedance of the antenna is influenced by the surrounding host medium. In line with this

$$P_{in} = \frac{1}{2} \text{Re} \{ V_{ant} I_{ant}^* \} = \frac{1}{2} \frac{|V_{ant}|^2 R_{in}}{|Z_{in}|^2} \quad (3.18)$$

and it is clear that the delivered power is dependant on the magnitude and real component of the input impedance. Because of the transmitter electronics' topology, the voltage at the terminals of the antenna  $V_{ant}$  is almost independent of the surrounding medium. Exploiting this, the power delivered to the antenna in rock can be estimated as

$$P_{in}(\text{rock}) = P_{in}(\text{air}) \frac{|Z_{in}(\text{air})|^2 R_{in}(\text{rock})}{|Z_{in}(\text{rock})|^2 R_{in}(\text{air})} \quad (3.19)$$

In the far field region of the antenna, the real part of the radial component of the complex Poynting vector, is now

$$S_{r(\text{avg})} = \text{Re} \{ S_r(r, \theta, \phi) \} = \frac{P_{rad} D_{tx}(\theta, \phi)}{4\pi r^2 e^{2\alpha r}} \quad (3.20)$$

The power transfer function, equivalent to (3.12) for free space, is

$$P_d = P_{in} \frac{\lambda^2 (1 - |\Gamma_{rx}|^2) e_{rx} e_{tx} D_{rx}(0,0) D_{tx}(0,0)}{(4\pi r)^2 e^{2\alpha r}} \quad (3.21)$$

where  $\lambda$  in a lossy medium [42] is

$$\begin{aligned} \lambda &= \frac{\lambda_0}{\text{Re} \sqrt{\epsilon' (1 + i \tan \delta)}} \\ &\approx \frac{\lambda_0}{\sqrt{\epsilon'}} \quad \text{for } \tan \delta \ll 1. \end{aligned} \quad (3.22)$$

The coupling of the transmit antenna into the ground, as well as the power received by the receive antenna, have now been quantified. With the proper measured and simulated parameters the actual performance of the GeoMole BHR system deployed in hard rock boreholes can be estimated.

### 3.7.2 Deployed Antenna Characteristics

The characteristics and transfer function of the TX and RX antennas are modified from their free space values when deployed in hard rock boreholes. The input impedance, efficiency and gain, have an influence on the radar range equation, while the phase response influences the pulse shape of the captured waveform. In this dissertation the environment (lossy dielectric) is an integral part of the radiating

## CHAPTER 3: Characterization of TX and RX Probes

structure. The antenna structure was approximated as a three layer cylindrical structure. The first layer consists of the potting material. The metallic and resistive sections of the antenna are submerged in the 1<sup>st</sup> layer. The third layer consists of the lossy dielectric host medium – an open region. Finally, the second layer consists of the matter that fills the gap between the probe and the borehole face. In general this matter will be air (free space), but might also be water with given salinity in the case of declined boreholes. The antenna parameters were simulated in a number of host rocks. The probes will be deployed in the norites for the majority of time (see Chapter 6). Only the results for this host rock are discussed in this section. Please refer to Appendix B for simulation results for the other host rocks.

### 3.7.2.1 TX Antenna in Norite

The antenna response and characteristic parameters of a transmitter deployed in an air-filled 48 mm borehole in norite are plotted in Figure 3-38.

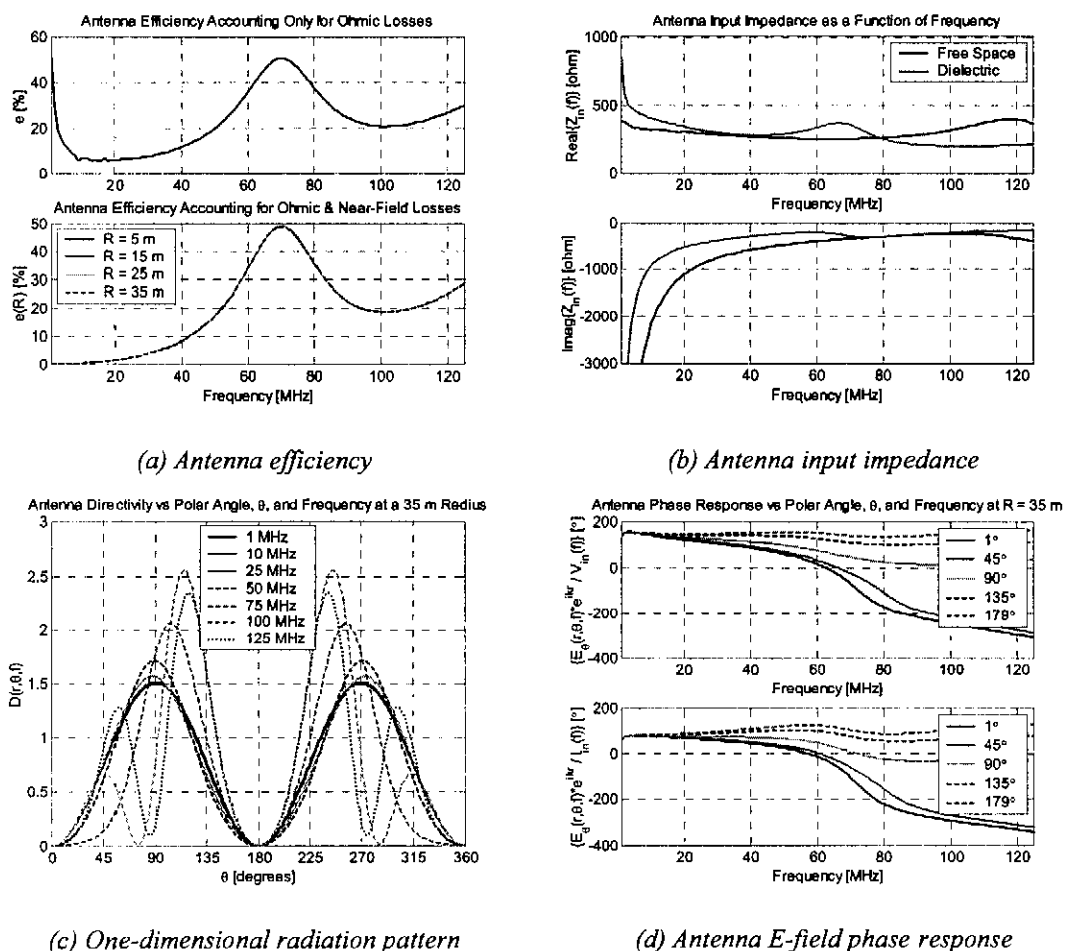


Figure 3-38: GeoMole TX antenna response when deployed in a norite host medium borehole.

When compared to Figure 3-23, it is evident that the antenna response has shifted down in frequency. The quasi-resonance at 130 MHz shifted down to 70 MHz. The

### CHAPTER 3: Characterization of TX and RX Probes

effect of the near field losses on the antenna efficiency is dominant in the lower frequencies. The mean value of the resistive input impedance stays more or less the same, while the equivalent capacitance increases. Unfortunately the host medium degrades the radiation pattern and the phase response of the antenna. The beam starts to squint in the metallic arm's direction at 75 MHz, with a null approaching broadside at 125 MHz. Furthermore, the phase response is only linear up to 60 MHz. If the captured waveform has data above 60 MHz, as can be expected, the pulse shape will be deformed. Knowing the phase response enables removal of this pulse shape distortion by means of inverse processing.

When the TX probe is deployed in a borehole filled with water, the antenna characteristics are modified to an even greater extent. If the salt content is low the effects are mainly due to the high permittivity of the water and when it is high the effects are caused by both the high permittivity and conductivity.

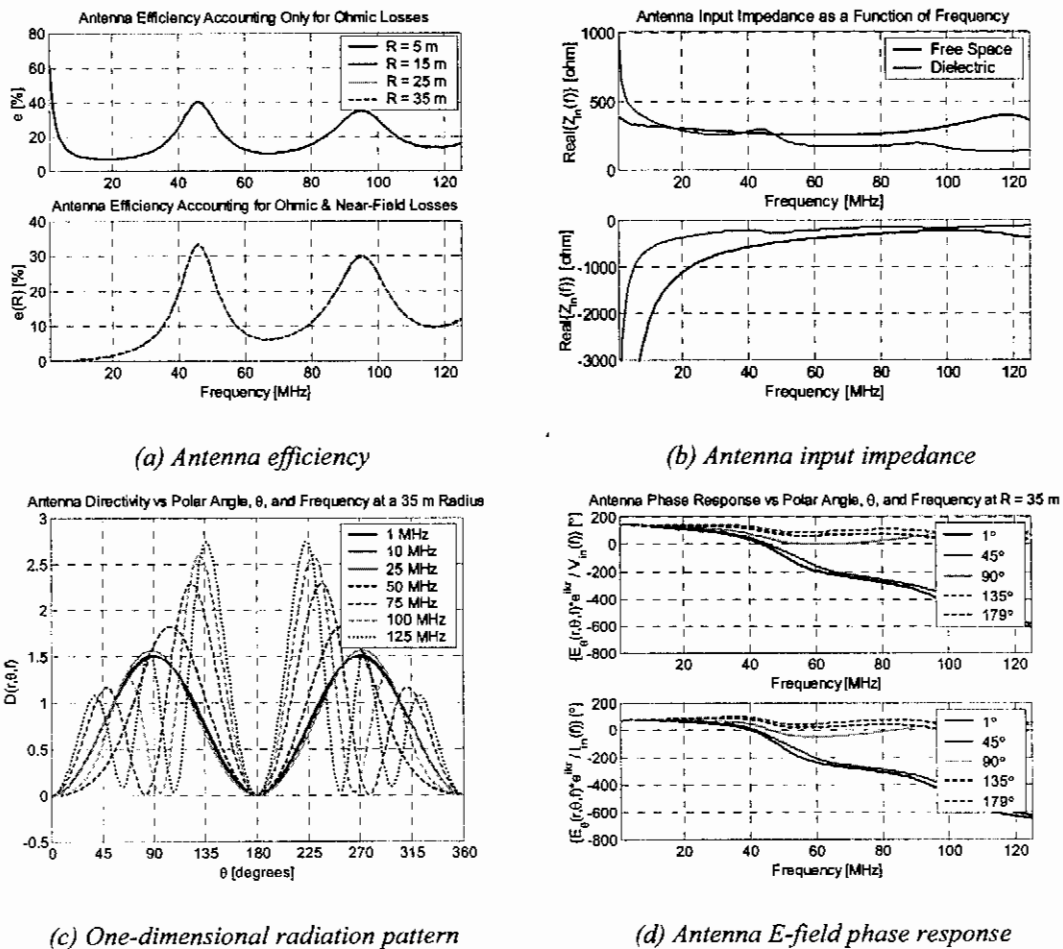


Figure 3-39: GeoMole TX antenna response when deployed in a water-filled (low salt content), norite host medium borehole.

## CHAPTER 3: Characterization of TX and RX Probes

The antenna response and characteristics for water with a low salt content ( $10 \text{ mS}\cdot\text{m}^{-1}$ ) are plotted in Figure 3-39.

The first resonance has been shifted down to a low 46 MHz with the second resonance also in the band of interest at 95 MHz. The mean value of the input impedance stays  $300 \Omega$  from DC to the 1<sup>st</sup> resonance. The radiation pattern is highly modified. It starts to squint below 50 MHz with a null approaching broadside at 75 MHz. The 1<sup>st</sup> sidelobe peaks at broadside at 125 MHz. The phase response is also adversely affected with the linear region narrowed to DC – 40 MHz. Based on the radiation pattern and phase linearity it is clearly not desirable for the holes to be water-filled. It is possible to however, correct for the non-linear phase response of the antennas.

### 3.7.2.2 RX Antenna in Norite

The characteristics and transfer function of the RX antenna deployed in an air-filled 48 mm radius borehole in norite host rock are plotted in Figure 3-40.

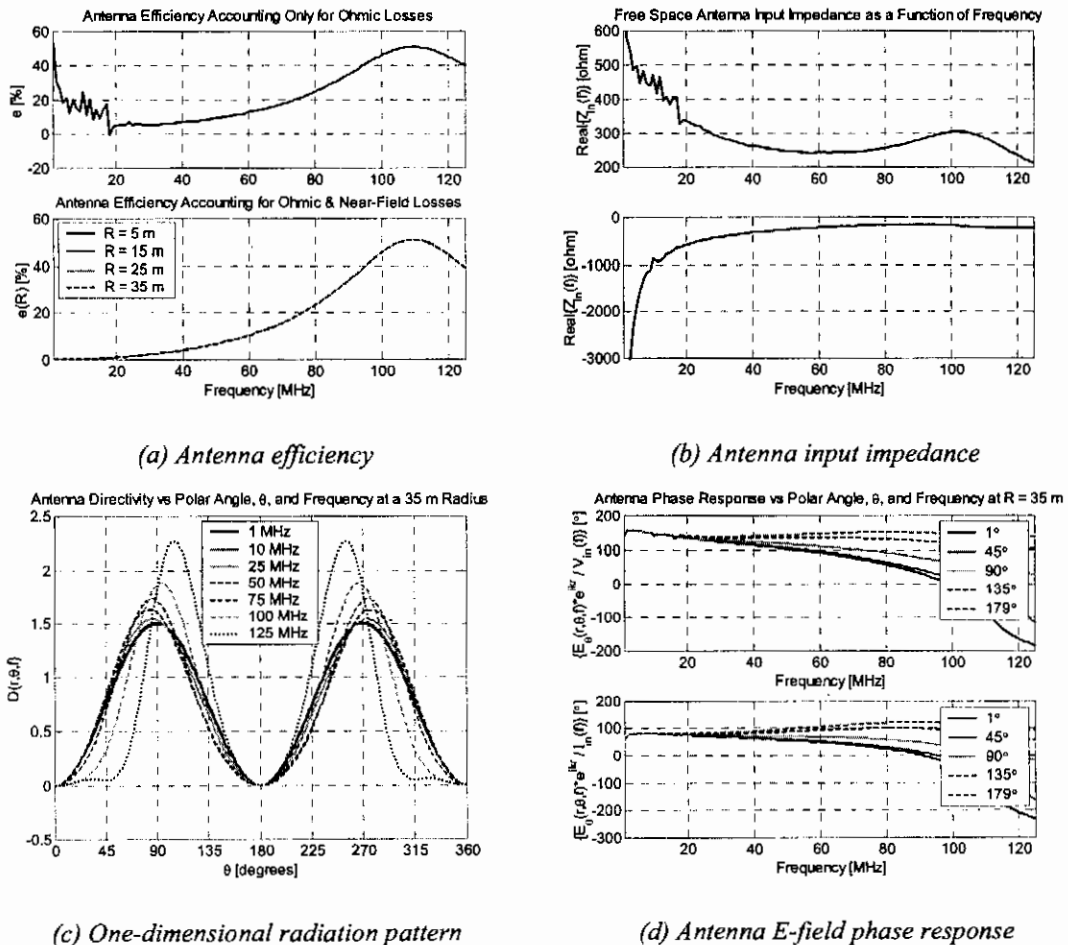


Figure 3-40: GeoMole RX antenna response when deployed in a norite host medium borehole.

The 1<sup>st</sup> resonance is shifted down from 200 MHz to 109 MHz, i.e. at the high side of the frequency range of interest. The beam only starts to squint beyond 100 MHz and the phase response is also relatively linear in this range. Due to the shorter length of the metallic arm, the RX antenna outperforms the TX antenna when the radiation pattern and phase response are considered. When the probe is submerged in a water-filled borehole, the same effects will be observed as with the transmitter. The 1<sup>st</sup> resonance shifts down to 67 MHz, the linear phase response region shrinks accordingly and the beam starts to squint beyond 50 MHz.

### 3.7.3 Power Delivered to TX Antenna

As discussed in Section 3.7.1, the power delivered to the antenna is dependent on the entire antenna structure, i.e. the TX probe, borehole and surrounding medium. Equation (3.19) indicates that the power delivered to the TX antenna in the borehole can be related to the power delivered in free space by a factor dependent on the input impedance in free space and the borehole. The power delivered in free space has been estimated in Section 3.5.3 and the input impedances plotted in Section 3.7.2. The power delivered to the TX antenna in the borehole and the power increment are plotted in Figure 3-41 and Figure 3-42.

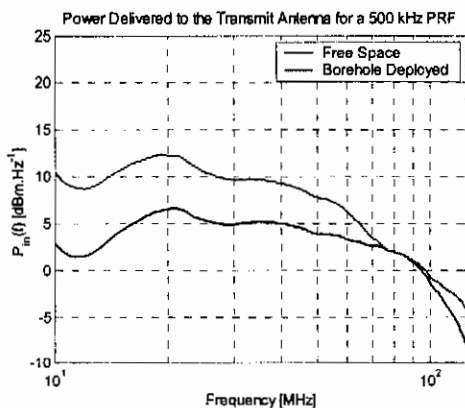


Figure 3-41: Power delivered to TX antenna in free space and borehole deployed (norite rock).

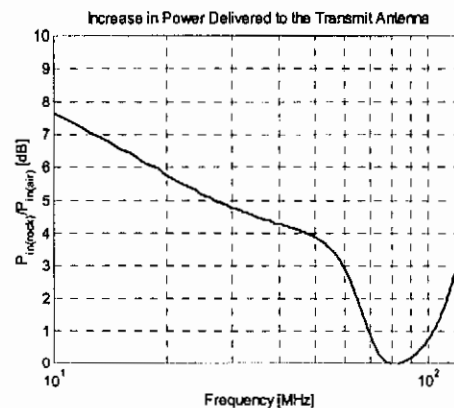


Figure 3-42: Increase in power delivered to TX antenna when borehole deployed.

When comparing Figure 3-41 to Figure 3-28 a 6 dB decrease in the spectral density is observed. This is due to zero padding at the end of the sequence to double the length of the trace to 2  $\mu$ s (a factor of 2). This is necessary so that the spectral densities of the transmitted and digitally stored waveforms (2  $\mu$ s) can be compared 1:1.

Up to 50 MHz, the increase in the power delivered to the TX antenna is more than 4 dB. It decreases to 0 dB at 81 MHz after which it increases once again to a maximum

of 4 dB at 125 MHz. This revised estimation can now be used in power budget calculations.

### **3.8 Concluding Remarks**

In this chapter the characterization and calibration of the GeoMole transmitter and receivers were considered. As a starting point the radiation and interception process was qualitatively and quantitatively formalized. A procedure was developed by which the probes could be characterized. This procedure consisted of numerous numerical simulations (FEKO), theoretical formulations as well as numerous laboratory measurements both in the time- and frequency domain. In the physical realization of the calibration procedure (the RCF), physical structures and a number of electronic instruments (calibration transmitter, calibration receiver, reference receiver and instrumentation SCU) had to be built, tested and characterized.

The power delivered to and radiated by the TX antenna was estimated in its deployed environment by means of adjusting the estimated power values in free space. Furthermore, the transfer functions of both the TX and RX antennas in their deployment environment were numerically simulated. The effect of the specific matter filling the gap between the probes and the borehole interface was also studied.

The characteristics and transfer function of the TX probe will prove to be very valuable in power budgeting, which is discussed in Chapter 4. The characteristics and transfer function of the RX probe will also affect power budgeting, as well as the deconvolution (pulse recompression) process developed in Chapter 5.

# CHAPTER 4

## CHARACTERIZATION OF RECEIVER CHAIN

The GeoMole receiver RF electronics consists of the LNA, 2<sup>nd</sup> stage amplifier, optic modulator, fibre optic link, optic demodulator and the SCU as defined in Chapter 1. The fibre optic link and the SCU are highly configurable for any given radar deployment set-up.

In this chapter a technique is proposed for the accurate characterization of such a configurable RF chain. The outcome of this characterization process is the ability to predict the frequency domain transfer function and noise figure of the entire RF chain. The final subsystem of the borehole radar is the ADC unit also called the data acquisition unit (DAQ). The prediction and measurement of its analogue and digital transfer function is presented.

Having quantified the system transfer function of the radar, this chapter concludes with the extraction of the critical system parameters of which the maximum permissible signal attenuation is the most important.

### 4.1 Quantitative Description of RF Chain

When the GeoMole borehole radar is deployed in an actual mining environment, the system configuration can be extremely complicated. Consider the case where a transmitter- and the first receiver probe, connected with an optic spacer cable, are deployed in one borehole and a second receiver probe is deployed in another borehole.

The transmitter transmits electromagnetic pulses into the rock. The optic trigger pulse travels through the fibre optic patchcord in the transmitter probe. From there it is guided through the optic spacer cable and the receiver probe. It then travels through the second optic fibre of the reinforced optic cable used to deploy the transmitter and first receiver. When the trigger pulse reaches the data acquisition (DAQ) unit, it passes through yet another patchcord before it is converted into an electrical signal. After being amplified, the trigger pulse triggers the ADC to start recording the data

## CHAPTER 4: Characterization of Receiver Chain

converted. The signal received by either of the receiver probes is amplified by the LNA and the 2<sup>nd</sup> amplifier stage after which it is converted into an optical signal by an optic modulator. This optic signal travels through the patchcord in the receiver probe, the first optic fibre of the reinforced optic cable and another patchcord in the DAQ. Thereafter it is demodulated into an electrical signal in the SCU. The final power amplifier amplifies the signal further before the ADC converts it into a binary number, which is stored on the data storage unit.

The signal flow diagram for the first receiver chain is shown in Figure 4-1.

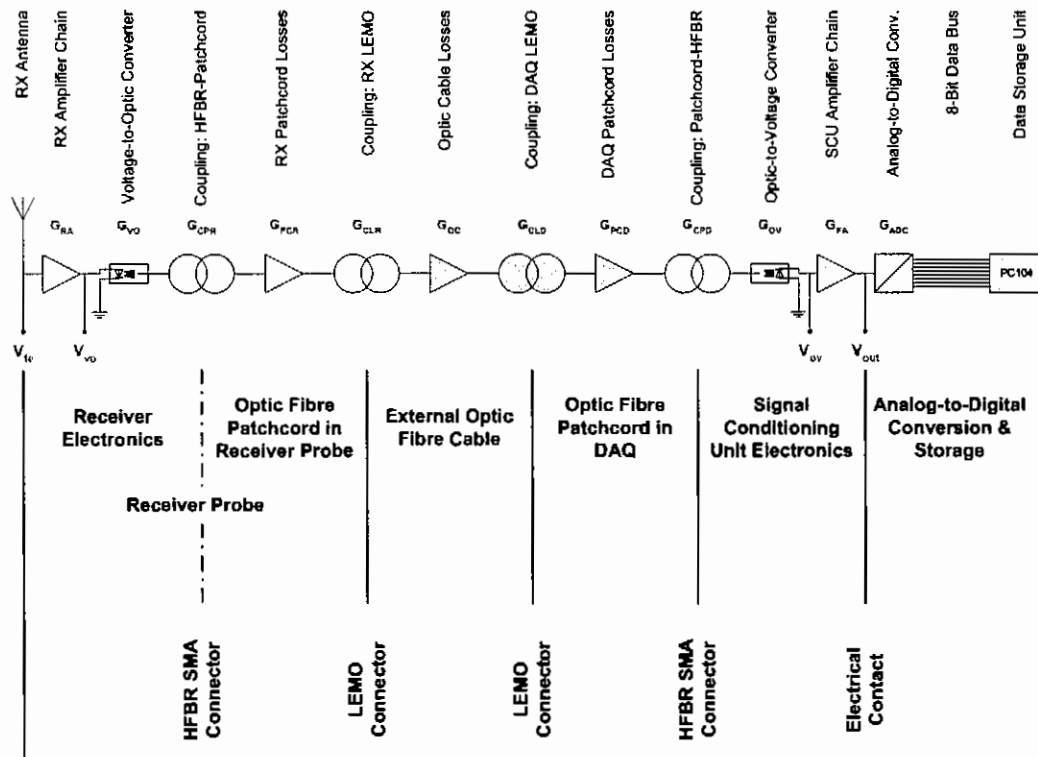


Figure 4-1: Signal flow through the first receiver chain.

The optic link configuration of the second receiver is even more complicated. In general only one reinforced optic cable is deployed on the rotating drum of the GeoMole BHR system. Provision is made for a second optic cable via a fibre optic rotating joint (FORJ) on the axis of the rotating drum. The signal from the receiver stays the same up to the end of the reinforced optic cable. This cable is now connected to a patchcord that is connected to the outside port of the FORJ via a SMA-to-SMA barrel. A final patchcord relays the signal from the inside port of the FORJ to the optic demodulator. The differences in the two paths are indicated in Figure 4-2.

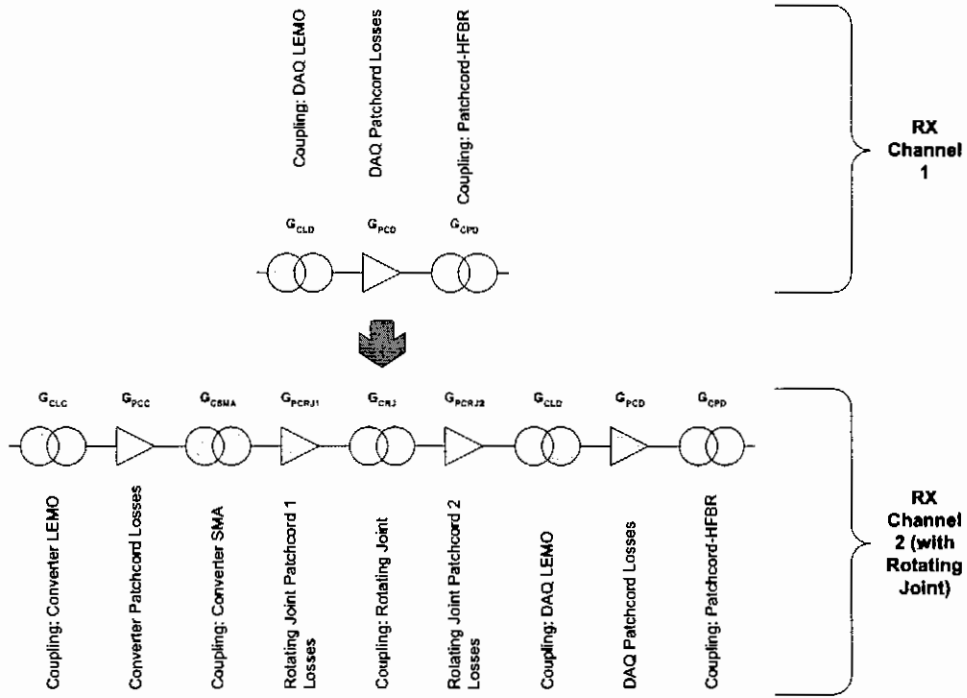


Figure 4-2: Differences in the receiver chain signal flow diagram for the second receiver.

The electrical signal can be probed at four different places in the receiver chain. In order to characterize and calibrate the receiver chain, the voltage and/or power transfer functions between these ports have to be determined. The transfer functions between the four electrical nodes can be written, for the first receiver chain, as

$$\begin{aligned} \frac{V_{vo}}{V_{fe}} &= G_{RA} \\ \frac{V_{ov}}{V_{vo}} &= G_{VO} G_{CPR} G_{PCR} G_{CLR} G_{OC} G_{CLD} G_{PCD} G_{CPD} G_{OV} \\ \frac{V_{out}}{V_{ov}} &= G_{FA} \end{aligned} \quad (4.1)$$

For the second receiver chain, the second equation in (4.1) changes to

$$\begin{aligned} \frac{V_{ov}}{V_{vo}} &= G_{VO} G_{CPR} G_{PCR} G_{CLR} G_{OC} G_{CLC} G_{PCC} G_{CSMA} \times \\ &G_{PCRJ1} G_{CRJ} G_{PCRJ2} G_{CLD} G_{PCD} G_{CPD} G_{OV} \end{aligned} \quad (4.2)$$

In the following section, a technique is proposed by which the abovementioned equations can be simplified significantly.

## 4.2 Definition of a Calibration Standard and Relative Gains

It is possible to measure  $G_{RA}$  and  $G_{FA}$  independently, but it is impossible to single out the other gain blocks as defined in Figure 4-1 and Figure 4-2. To overcome this problem, a reference set of connectors, optic cables and optic patch cords can be chosen. For every reference connector there is an unknown coupling gain for both connectors. The gain of any optic fibre cable consists of three factors. Consider the case of the reinforced optic cable:

$$\begin{aligned}
 G_{OC} &= G_{OCm} G_{OC0} G_{OCr} \\
 G_{OC} (dB) &= G_{OCm} (dB) + G_{OC0} (dB) + G_{OCr} (dB) \\
 G_{OCm} (dB) &= g'_{of} d'_{OC} \\
 &= g'_{of} d'_{OC} + g''_{of} d''_{OC}
 \end{aligned} \tag{4.3}$$

$G_{OC0}$  is the reference gain for the reference optic cable, i.e. the gain of the reference optic cable consisting of losses due to cable damage and coupling to the connectors.  $G_{OCr}$  is the relative gain for the given optic cable and consists of losses relative to the reference optic cable due to cable damage and relative coupling to the two connectors.  $G_{OCm}$  is the gain of the optic cable that is dependant on the length of the cable (per metre losses). In decibels, it can be written as the product of  $g_{of}$  [dB/m] (the average loss per metre) and  $d_{OC}$  (the length of the cable). In the GeoMole radar system, the optic cables are usually partly wound up with a small radius of curvature. The per metre losses,  $G_{OCm}$  is therefore split up in two terms, accounting for the length of cable that is straight  $g'_{of} d'_{OC}$  ( $g'_{of}$  is the per metre losses for a straight optic fibre and  $d'_{OC}$  is the length of the optic fibre that is straight) and the length of cable winded up  $g''_{of} d''_{OC}$  ( $g''_{of}$  is the per metre losses for a wound up optic fibre and  $d''_{OC}$  is the length of the optic fibre that is wound up). For any configuration of optic fibres in the first receiver chain, the transfer function (in decibels) as defined in (4.1) can be rewritten as

$$\begin{aligned}
 V_{ov} &= V_{vo} + G_0 + g'_{of} (d_{PCR} + d'_{OC} + d_{PCD}) + g''_{of} d''_{OC} + G_{PCRr} + G_{OCr} + G_{PCDr} \\
 G_0 &= G_{VO} + G_{CPR0} + G_{PCR0} + G_{CLR0} + G_{OC0} + G_{CLD0} + G_{PCD0} + G_{CPD0} + G_{OV}.
 \end{aligned} \tag{4.4}$$

Using the reference optic fibres the reference gain  $G_0$  can be measured provided that  $g'_{of}$ ,  $g''_{of}$  and the lengths of the various optic fibres are known. The fraction of the

## CHAPTER 4: Characterization of Receiver Chain

optic cable that is wound up also has to be known. With two reference optic fibres and one unknown optic fibre, the relative gain of the unknown optic fibre can easily be calculated by means of vector network analyser measurements.

For the second receiver chain, equation (4.4) has to be altered to accommodate the addition gain blocks as depicted in Figure 4-2:

$$\begin{aligned}
 V_{ov2} &= V_{w2} + G_{02} + g'_{of} (d_{PCR} + d'_{OC} + d_{PCC} + d_{PCRJ1} + d_{PCRJ2} + d_{PCD}) + g''_{of} d''_{OC} \\
 &\quad + G_{PCRr} + G_{OCr} + G_{PCCr} + G_{CSMar} + G_{PCRJ1r} + G_{CRJr} + G_{PCRJ2r} + G_{PCDr} \\
 G_{02} &= G_{VO} + G_{CPR0} + G_{PCR0} + G_{CLR0} + G_{OC0} + G_{CLC0} + G_{PCC0} + G_{CSMA0} \\
 &\quad + G_{PCRJ10} + G_{CRJ0} + G_{PCRJ20} + G_{CLD0} + G_{PCD0} + G_{CPD0} + G_{OV}.
 \end{aligned} \tag{4.5}$$

Equation (4.5) is clearly more comprehensive than (4.4), but can be handled in exactly the same manner to extract the various relative gains. It is impossible to separate the three relative gains associated with the FORJ and they are therefore grouped to form the total relative gain of the FORJ:

$$G_{PCRJr} = G_{PCRJ1r} + G_{CRJr} + G_{PCRJ2r}. \tag{4.6}$$

The final amplification gain,  $G_{FA}$ , is also written in terms of a reference and relative gain, i.e.

$$G_{FA} = G_{FA0} + G_{FAr}. \tag{4.7}$$

Due to practical considerations, the reference optic gain  $G_0$  is grouped together with the reference final amplification gain to form the total reference gain  $G_R$  of the optic link:

$$G_R = G_0 + G_{FA0}. \tag{4.8}$$

The differential gain  $G_D$  is defined as the total of the relative gains and the gain due to the length of the optic cable. For the first receiver it can be written as

$$G_D = g'_{of} (d_{PCR} + d'_{OC} + d_{PCD}) + g''_{of} d''_{OC} + G_{PCRr} + G_{OCr} + G_{PCDr}. \tag{4.9}$$

and for the second receiver chain can be written as

$$\begin{aligned}
 G_D &= g'_{of} (d_{PCR} + d'_{OC} + d_{PCC} + d_{PCRJ1} + d_{PCRJ2} + d_{PCD}) + g''_{of} d''_{OC} \\
 &\quad + G_{PCRr} + G_{OCr} + G_{PCCr} + G_{CSMar} + G_{PCRJr} + G_{PCDr}.
 \end{aligned} \tag{4.10}$$

The total transfer function of the analogue RF chain,  $G_A$ , is therefore defined as

$$\frac{V_{out}}{V_{je}} = G_{RA} G_R G_D G_{FAr}. \tag{4.11}$$

Equations (4.3) - (4.11) can now be used to determine the reference and relative gains of the highly configurable receiver RF chain.

## 4.3 Calibration Standard and Relative Gain Measurements

In this section the loss factor of the wound up optic fibre will be measured and calculated. The total reference gains of the two receiver chain topologies will also be measured and the relative gains of the different optic and electronic components will be measured.

### 4.3.1 Measurement of Fibre Optic Loss Factor

The loss factor per metre of the multimode 100/140  $\mu\text{m}$  optic fibre is 4 dB per kilometre if the fibre is relatively straight. The loss factor for a tightly wound up optic fibre is not known, but can be calculated from two VNA measurements. The physical set up of such an experiment is an optic modulator, patchcord, LEMO connector, reinforced optic fibre cable, LEMO connector, patchcord, optic demodulator and SCU as depicted in Figure 4-3. Since the loss factor is so low, a very long optic cable has to be deployed for accurate measurements. A 200 m cable will only result in a 0.8 dB loss. This is however, sufficiently long for VNA measurements.

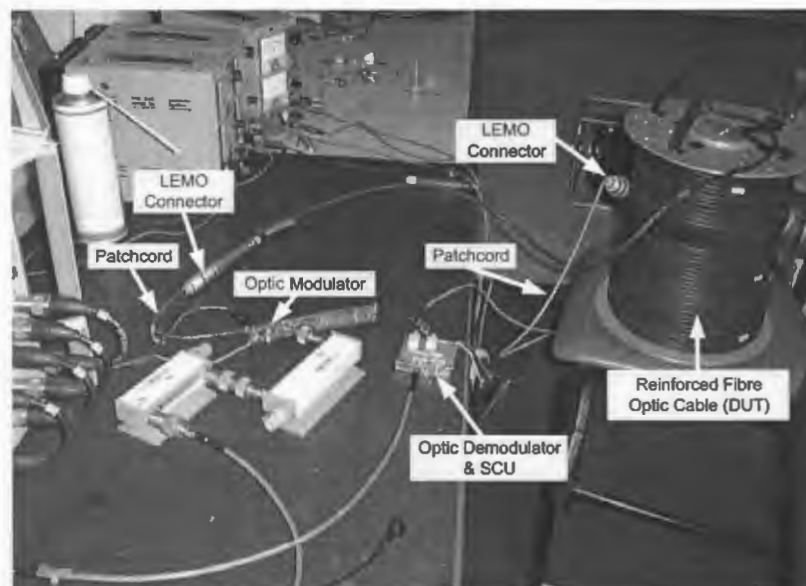


Figure 4-3: Physical configuration for loss factor measurements.

In the first measurement the cable is rolled down and laid straight, i.e.  $d_{OC}'' = 0$ . In the second measurement the cable is wound up on the rotating drum (see Figure 4-3), i.e.

## CHAPTER 4: Characterization of Receiver Chain

$d'_{oc} = 0$  and  $d''_{oc} = 200$  m. Using the results of these two measurements yield one equation with one unknown,  $g''_{of}$ . The estimated and average values of  $g''_{of}$  for the multimode 100/140  $\mu\text{m}$  fibre optic are plotted in Figure 4-4.

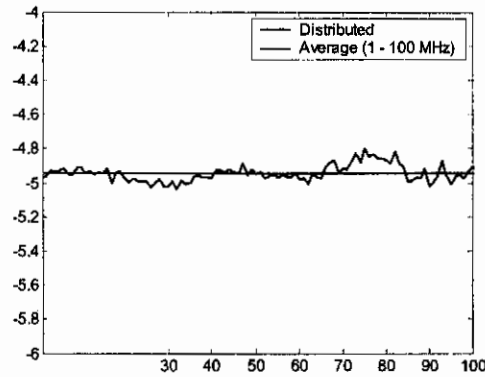


Figure 4-4: Estimated loss factor for a wound up 100/140  $\mu\text{m}$  optic fibre.

The estimated value of  $g''_{of}$  varies by only 0.2 dB over the frequency bandwidth of interest with an average of  $-4.94 \text{ dB.km}^{-1}$ . This implies an additional 0.2 dB loss in the RF chain for a 200 m cable, which is negligible in the light of other loss mechanisms still to be considered.

### 4.3.2 Total Reference Gain of the Two Topologies

The components used in the reference set up of the 1<sup>st</sup> receiver chain configuration are summarized in Table 4-1 and depicted in Figure 4-5.

Table 4-1: Configuration of 1<sup>st</sup> reference receiver chain.

	Optic Modulator	RX Patchcord	Fibre Optic Cable	DAQ Patchcord	SCU
ID	Calibration RX	SMA2	LL1	SMA1	Instr. SCU #1
Fibre Length	N/A	1.005 m	1.41 m	0.875 m	N/A

In Table 4-1 the SMA prefix refers to a patchcord with one SMA and one LEMO female connector, while the LL prefix refers to a patchcord with two LEMO male connectors. The optic modulator of the calibration receiver was used as the instrumentation modulator.

## CHAPTER 4: Characterization of Receiver Chain

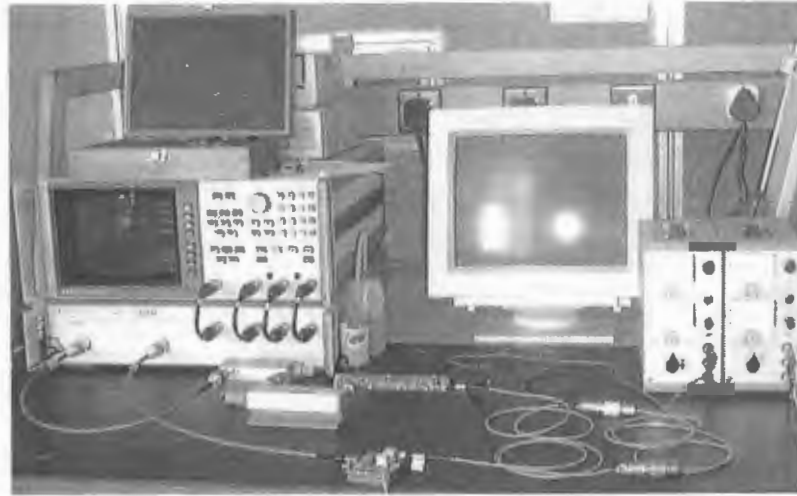


Figure 4-5: Reference fibre optic configuration for 1<sup>st</sup> RF chain.

The measured and calculated total reference gain  $G_R$  for the 1<sup>st</sup> receiver chain is plotted in Figure 4-6, together with the phase response of the reference receiver chain. In the calculation of the phase response, the phase delay due to the optic fibre cables has been removed.

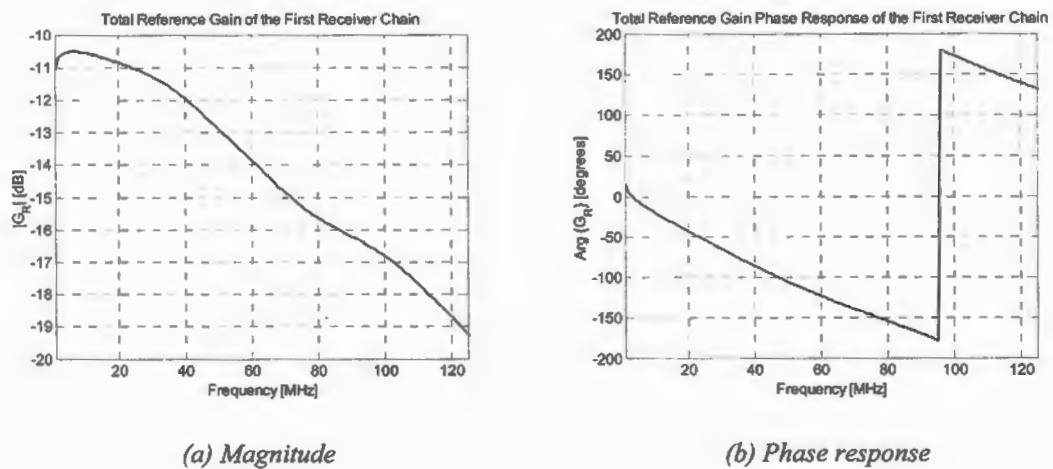


Figure 4-6: Total reference gain of the first receiver chain.

The components used in the reference set up of the 2<sup>nd</sup> receiver chain configuration are summarized in Table 4-2 and depicted in Figure 4-7.

CHAPTER 4: Characterization of Receiver Chain

Table 4-2: Configuration of 2<sup>nd</sup> reference receiver chain.

	Optic Modulator	RX Patchcord	Fibre Optic Cable	Coupling Patchcord	SMA Barrel	FORJ	DAQ Patchcord	SCU
<b>ID</b>	Calibration RX	SMA2	LL1	SMA3	SB1	SMA4	SMA1	Instr. SCU #1
<b>Fibre Length</b>	N/A	1.005 m	1.41 m	0.55 m	N/A	0.25 m	0.875 m	N/A

In the reference configuration the FORJ has been replaced by a standard patchcord, due to unwanted losses inherent to a rotating joint.



Figure 4-7: Reference fibre optic configuration for 2<sup>nd</sup> RF chain.

The measured and calculated total reference gain  $G_R$  for the 2<sup>nd</sup> receiver chain is plotted in Figure 4-8, together with its phase response.

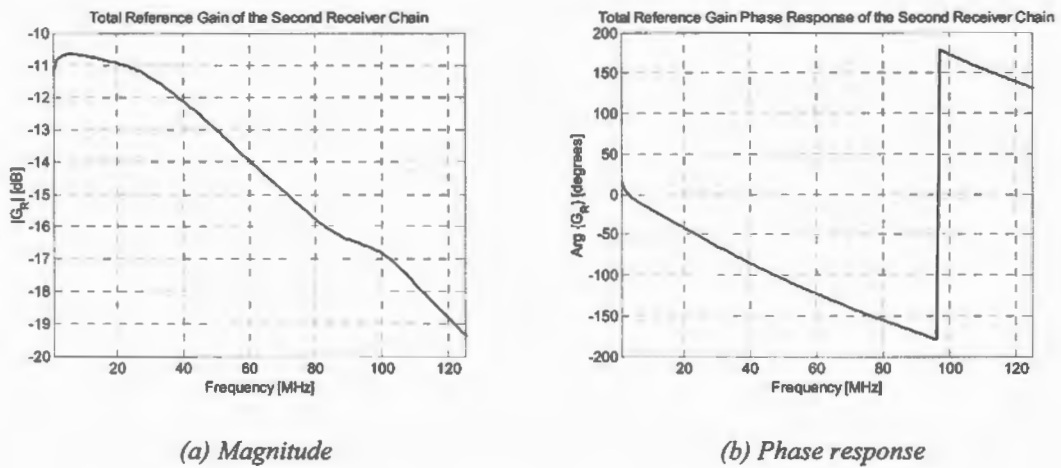


Figure 4-8: Total reference gain of the second receiver chain.

The difference between the gains of the 1<sup>st</sup> and the 2<sup>nd</sup> reference configuration is less than 0.25 dB across the frequency band of interest. These values of  $G_R$  are used in the calculation of the relative gain of the various fibre optic and connector components.

### 4.3.3 Relative Gain of Optic & Electronic Components

In this section the various fibre optic patchcords, reinforced optic cables, connectors (SMA barrels) and SCU's will be characterized with respect to their relative gains as defined in Section 4.2.

The relative gains of the receiver patchcords for the different GeoMole receiver probes have been calculated and plotted in Section 3.6.5. The relative gains  $G_{OCr}$  and non-linear phase responses of the different reinforced optic cables are plotted in Figure 4-9.

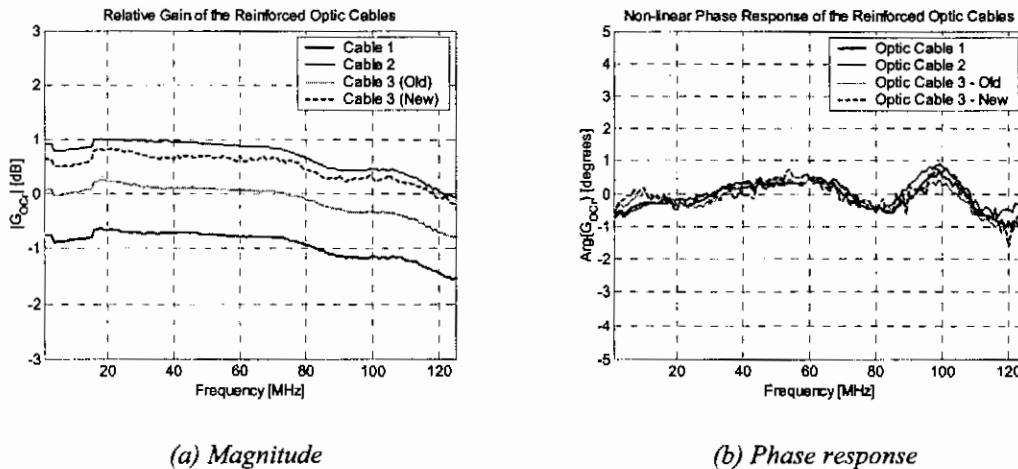


Figure 4-9: Relative gain and phase response of the different reinforced optic cables.

The relative gains of the four optic cables are within 1 dB of the reference optic fibre up to 80 MHz, with a slight decrease in performance for the higher frequencies. It should be noted that these optic cables have been used numerous times in the strenuous mining environment to hoist down and pull up the probes, which in some cases got stuck. Irrespective of this, the performance of these cables are still on par and even better than the laboratory reference optic fibre. The non-linear phase response for these 200 m long cables are less than  $\pm 1^\circ$  across the band of interest. In the relative gain measurements, a slight dip is visible in the DC – 20 MHz region. This anomaly is mainly due to the extreme length of the optic cable and the time it takes for the continuous wave to reach the receiver. The sweep time over the discrete

## CHAPTER 4: Characterization of Receiver Chain

frequency points in the chosen bandwidth was set to 4 seconds. The relative gains of the different DAQ patchcords are plotted in Figure 4-10.

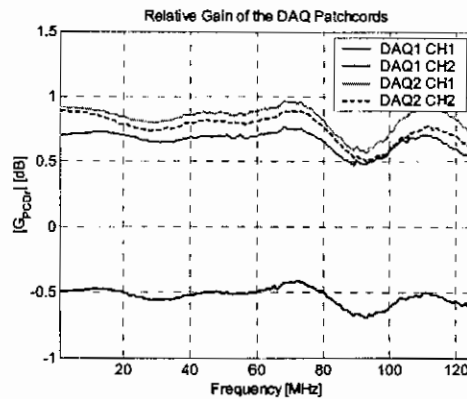


Figure 4-10: Relative gain of the different DAQ patchcords.

Both DAQ #2's (defined in Section 4.5) and the second channel of DAQ #1's patchcords have relative gains in the order of 0.75 dB. DAQ #1's 1<sup>st</sup> channel has a relative gain of only  $-0.5$  dB, i.e. 1.25 dB lower than the others. If SNR is of importance, it might be advisable to change this patchcord, since the first channel is usually regarded as the most important. The relative gains  $G_{FAr}$  and phase responses of the different SCU's are plotted in Figure 4-11 and Figure 4-12.

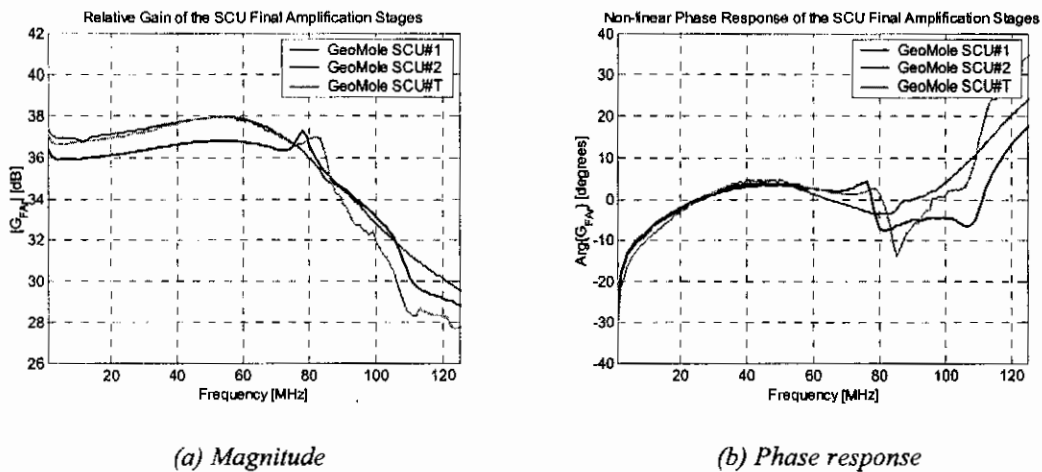


Figure 4-11: Relative gain and phase response of the different SCU's (1).

## CHAPTER 4: Characterization of Receiver Chain

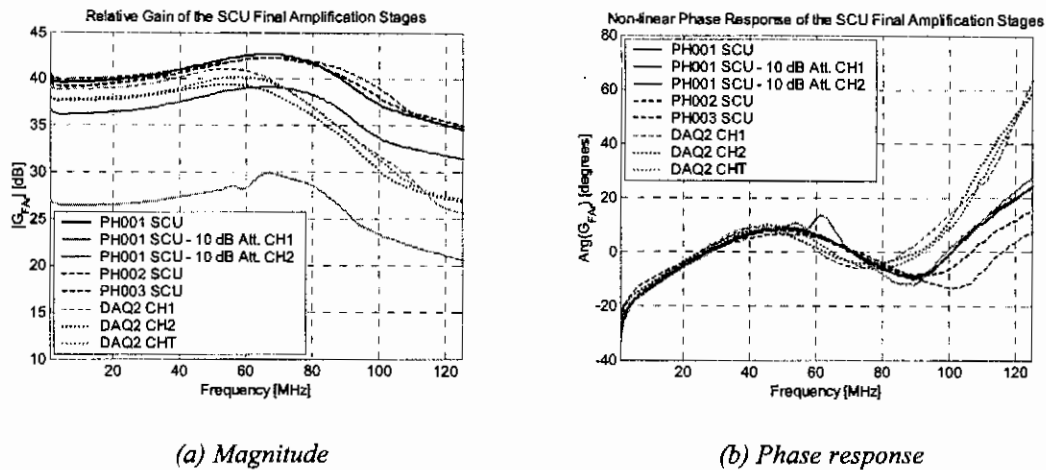


Figure 4-12: Relative gain and phase response of the different SCU's (2).

The cut-off frequency of the GeoMole (DAQ #1) and DAQ #2 SCU's are in the order of 90 MHz. The 1<sup>st</sup> channel of DAQ #1 has a degraded (-2 dB) performance in comparison to the rest, with a glitch at  $\pm 80$  MHz. The gain of the DAQ #2 SCU's are on average 1 dB higher than that of DAQ #1. The phase responses of the channels are closely matched, but not very linear. They are, however within approximately  $\pm \pi/8$  radians over the frequency range of interest. Above 60 MHz, the phase responses of the DAQ #1 channels start to deviate. The overall performance of the DAQ #1 SCU's seems to be deteriorated. A new set of SCU's was therefore built (PH001 – PH003) for deployment in new field experiments. They were used for the first time in the Bleskop II experiments (see Appendix F) and their relative gains and phase responses are plotted above. They have an improved gain and a wider bandwidth of approximately 100 MHz. Their phase responses are closely correlated to that of the DAQ #2 set.

In a number of experiments the output signal of the 1<sup>st</sup> channel is connected to the 1<sup>st</sup> channel of the ADC. In addition, the signal is tapped and connected to the input of the 2<sup>nd</sup> ADC channel via a 10 dB attenuator. In some cases this is desirable when the signal levels are high and saturation of the ADC input has to be avoided. This has the adverse effect of a decrease of the load resistance of the SCU from  $50 \Omega$  to  $25 \Omega$ . Clearly a fraction of the incident power will be lost due to the impedance mismatch. Using basic transmission line theory, the 'gain' of this configuration for the 1<sup>st</sup> and 2<sup>nd</sup> channels of the ADC can be calculated as

CHAPTER 4: Characterization of Receiver Chain

$$G_{ATT}(1) = \frac{2}{3} = -3.52dB$$

$$G_{ATT}(2) = \frac{2}{3\sqrt{10}} = -13.52dB. \tag{4.12}$$

The attenuation levels are observable in the results plotted in Figure 4-12.

The relative gain of the coupling patchcord and the SMA barrels are plotted in Figure 4-13 and Figure 4-14 respectively.

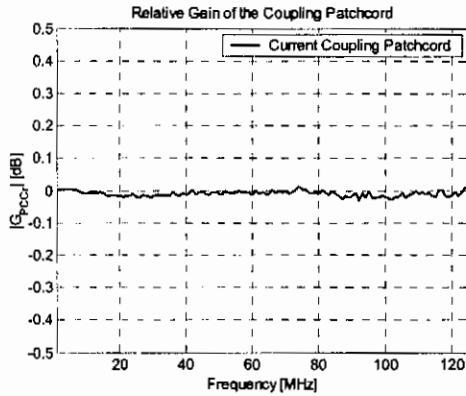


Figure 4-13: Relative gain of coupling patchcord.

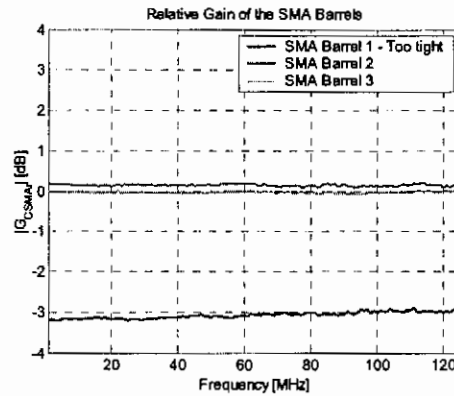


Figure 4-14: Relative gain of the SMA barrels.

The relative gains of the current coupling patchcord (currently deployed in the system) and the SMA barrels are very close to unity – within 0.2 dB. When the SMA connectors are fastened too tight however, the performance degrades and the relative gain can be as low as –3 dB. The relative gains of the different FORJ's are plotted in Figure 4-15.

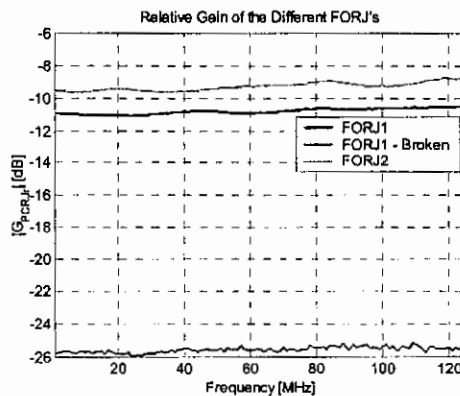


Figure 4-15: Relative gain of the different FORJ's.

The relative gain of the 1<sup>st</sup> FORJ was on average –11 dB and that of the 2<sup>nd</sup> FORJ was –9 dB. The incorporation of a FORJ therefore has an adverse affect on the SNR of the signal and should only be used if the power budget allows it. Unfortunately it was

observed that the 1<sup>st</sup> FORJ had been broken due to exceedingly high stress loads with the relative gain degraded to an unacceptable  $-25.5$  dB.

All the components and fibres currently used in the highly configurable system have been characterized in this section. It is now possible to estimate the total gain of any configuration. The cascaded gain is calculated from the reference gain and the various relative gains of the different fibres and components used in the configuration.

#### **4.3.4 Comments on Repeatable Fibre Optic Measurements**

In the process of calibration, great emphasis was placed on the execution of repeatable measurements. The first step of every calibration routine was to set up the reference configuration and measure its gain. Relative measurements were only made when the gain correlated to within 0.5 dB of the master results. The following key steps were identified as critical in the execution of repeatable fibre optic measurements:

1. Ensure that the faces of the fibre optic contacts are clean. This can be done with an alcohol infused swab and compressed air. Failing to do this resulted in gain errors exceeding 1 dB.
2. Torqueing the SMA connectors is of critical importance in the case of the optic modulator and especially the SMA barrels. It is not that important in the case of the optic demodulator.
3. In some cases the alignment of the optic fibre when connected to the optic modulator plays a critical role. This usually occurs when there is a misalignment between the faces of the modulator and the patchcord.

Adhering to these key steps ensured repeatable measurements with errors of less than 0.5 dB across the band of interest.

### **4.4 Noise Figure Measurements**

The noise figure of the cascaded receiver RF chain (front-end LNA, power amplifier and the 1<sup>st</sup> reference optic receiver chain) was measured. A number of experimental difficulties were encountered. In this section, the problems are examined, methods to solve these inherent problems are discussed and the results obtained are presented.

### 4.4.1 The HP 8970B Noise Figure Meter System

The Hewlett-Packard Model 8970B Noise Figure Meter, together with an appropriate noise source, automatically measures the noise figure and gain of the device to which it is attached [82]. It has a frequency range of 10 to 1600 MHz.



Figure 4-16: HP 8970B noise figure meter.



Figure 4-17: HP 346B noise source.

In essence the noise meter uses the Y-factor method to determine the noise figure of the DUT [14], where two loads at significantly different effective temperatures are connected to the input of the DUT. The 346B noise source is a reverse-biased Schottky diode with a 50  $\Omega$  output impedance. The important measurement parameters of this noise measurement system are summarized in Table 4-3.

Table 4-3: Noise measurement system performance.

Characteristics	Performance Limits
<b>Noise Figure Measurement</b>	
Range	0 to 30 dB
Resolution	0.01 dB
Uncertainty	$\pm 0.1$ dB
<b>Gain Measurement</b>	
Range	-20 to +40 dB
Resolution	0.01 dB
Uncertainty	$\pm 0.15$ dB
<b>Noise Source</b>	
Excess Noise Ratio (ENR)	15.2 dB

The characteristics of the noise meter and the receiver chain (DUT) are examined in the following section to determine whether or not the meter can measure the noise figure of the DUT.

### 4.4.2 Dynamic Range Analysis

The HP 346B noise source can be switched between two effective temperatures. The difference in output power is measured by the 8970B noise figure meter and has to be significant for valid measurements. Consider the block diagram in Figure 4-18.

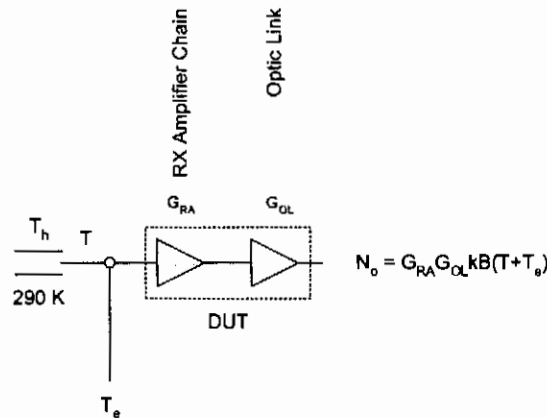


Figure 4-18: Block diagram of noise measurement of DUT.

In Figure 4-18  $T_h$  denotes the ‘hot’ temperature of the noise source,  $290\text{ °K}$  is the ambient room temperature,  $T$  the effective output temperature of the noise source,  $T_e$  the effective temperature of the DUT and  $N_o$  the noise power at the output of the DUT. The effective temperature of a device is the temperature of a matched resistor at the device input that yields the same output noise power [14]. The ‘hot’ temperature of the noise source is calculated as

$$T_h = 290 \left( 10^{\frac{ENR}{10}} + 1 \right) = 9893\text{ °C} \quad (ENR = 15.2). \quad (4.13)$$

The effective temperature of the receiver amplifier chain is

$$T_e = 164\text{ °K}. \quad (4.14)$$

This temperature has been obtained from gain and noise figure measurements of the amplifier chain. The noise contributions from the noise source, at  $50\text{ MHz}$ , at the output of the complete receiver RF chain (amplifier and optic link) are

$$N_o = (1.6793 \cdot 10^7) kB \quad (T = T_h, T_e = 0K). \quad (4.15)$$

The noise contribution of the optics demodulator is crucial. The HFBR 2406 demodulator contains a PIN photodiode and low-noise transimpedance pre-amplifier integrated circuit. The PIN photodiode is a noise source with a high spectral density [79]. At 50 MHz the noise output power can be calculated as:

$$\begin{aligned} N_o(HFBR) &= \frac{(60nV/\sqrt{Hz})^2 B}{50\Omega} \\ &= (5.2174 \cdot 10^6) kB. \end{aligned} \quad (4.16)$$

The noise power contribution from the HFBR is approximately 3 dB less than the noise power generated by the HP 346B noise source. The noise figure meter will not be able to calculate the noise figure accurately, since it will merely detect a change in the output power as the noise source is switched on and off.

### 4.4.3 Dynamic Range Improvement

If an amplifier stage is cascaded at the front of the chain, the noise power contribution of the noise source will be significantly higher than that of the DUT and the noise figure meter should be able to measure the noise figure with a high degree of accuracy. Another important consideration is the maximum gain range of the noise figure meter, as stated in Table 4-3. An Amplifonix TN7101 low-noise amplifier circuit was built. The circuit diagram is shown in Figure 4-19.

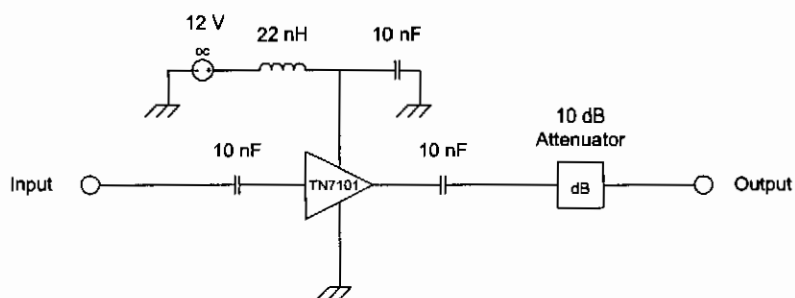


Figure 4-19: Circuit diagram of low noise front-end amplifier.

The 10 dB attenuator is an integral part of the circuit, which has a nominal gain of 16 dB at 50 MHz. Cascaded with the DUT, the total gain is about 48.1 dB at 50 MHz. The maximum gain range of the 8970B noise figure meter is 40 dB. Therefore, an attenuator cascaded at the end of the chain of at least 10 dB is needed. It was decided to use a 20 dB attenuator, since the overall gain of the new chain is higher at lower

frequencies and it is required to stay inside the gain range of the meter at all frequencies of interest.

### 4.4.4 Noise Figure Measurement Results

The noise figure of a two-port system is a measure of the degradation in the signal-to-noise ratio between the input and output of the system. It is defined as

$$F = \frac{S_i/N_i}{S_o/N_o} \geq 1 \quad (4.17)$$

where  $S_i$ ,  $N_i$  are the input signal and noise powers, and  $S_o$ ,  $N_o$  are the output signal and noise powers [14]. By definition, the input noise power is assumed to be the noise power resulting from a matched resistor at  $T_0 = 290$  K; that is  $N_i = kT_0B$ . A cascaded system is used to measure the noise of the DUT. For a cascaded system, each with its associated power gain ( $G_1, G_2, G_3, \dots$ ) and noise figure ( $F_1, F_2, F_3, \dots$ ), the noise figure of the cascaded system is

$$F_{cas} = F_1 + \frac{F_2 - 1}{G_1} + \frac{F_3 - 1}{G_1 G_2} + \dots \quad (4.18)$$

In the derivation of (4.18) it is assumed that the cascaded subsystems are exactly matched – a first order assumption that is not exact, but acceptable. The first step in finding the noise figure of the optic link is to measure the noise figures of the front-end amplifier and the receiver amplifier chain. The noise figures and gain of the front-end amplifier and receiver amplifier chain are plotted in Figure 4-20 and Figure 4-21.

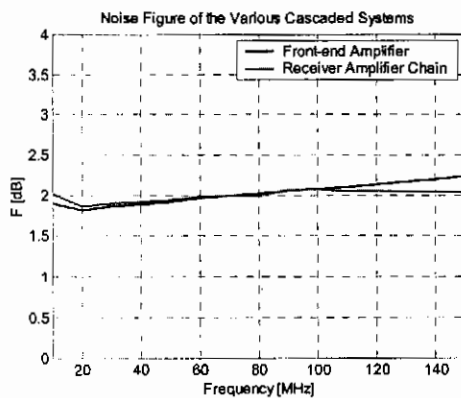


Figure 4-20: Noise figure of various cascaded systems.

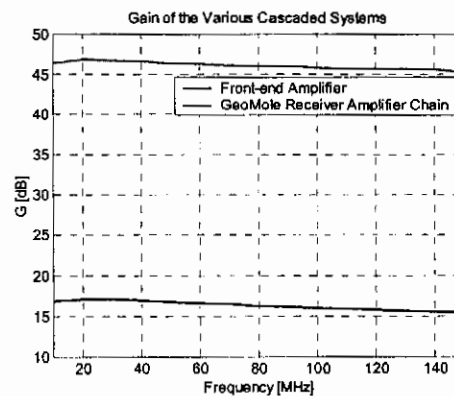


Figure 4-21: Gain of various cascaded systems.

Using the measurement of the noise figure and gain of the cascaded system, the noise figure and gain of the DUT (receiver amplifier chain and optic link) can be calculated.

## CHAPTER 4: Characterization of Receiver Chain

These parameters for the GeoMole receiver amplifier chain cascaded with the optic link are plotted in Figure 4-22 (plotted in Figure 4-23 for the optic link).

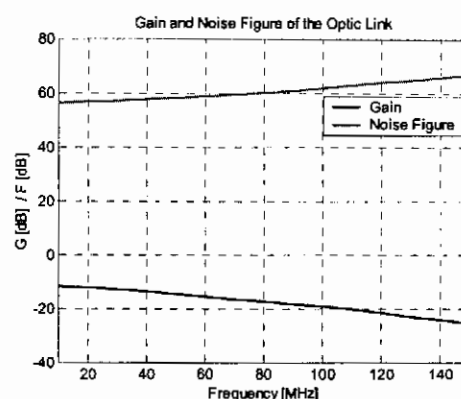
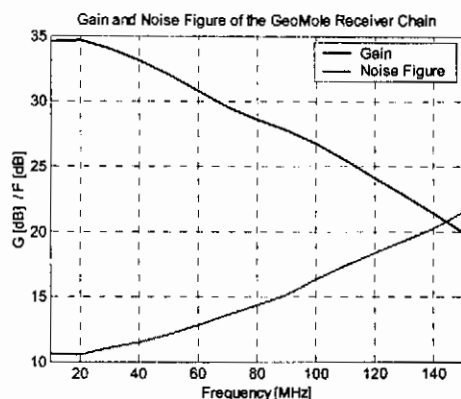


Figure 4-22: Gain and noise figure of GeoMole receiver amplifier cascaded with optic link.

Figure 4-23: Gain and noise figure of optic link.

The noise figure at 50 MHz for the cascaded system is 12.1 dB and 58.1 dB for the optic link. These results are consistent with Hargreaves [4], who estimated the overall noise figure as 15.3 dB and optic link noise figure as 67.1 dB for a slightly older version of the GeoMole system. Hargreaves provides no information on the relevant frequency and measurement technique. The optic link seriously deteriorates the signal-to-noise ratio, as was expected in view of the high noise voltage spectrum of the optic demodulator. The use of a high gain, low noise front-end amplifier improves the performance of the cascaded system. A noise figure of 12.1 dB is still alarmingly high and should be taken into account when dynamic range calculations are made. It should furthermore be clear that the relative gain of the optic fibre configuration has a direct effect on the noise figure of the cascaded receiver chain.

### 4.5 Characterization of Data Acquisition Unit

The current borehole radar uses a two channel, 250 Msps, 100 MHz bandwidth 8-bit Chase CS2250 ADC unit, shown in Figure 4-24.



Figure 4-24: Chase CS2250 analogue-to-digital converter unit.

The Chase CS2250 can digitise a signal with a maximum frequency component of 125 MHz without the introduction of aliasing effects. Since the RF bandwidth of the receiver (final amplifier of SCU) is approximately 100 MHz and the maximum frequency component of a typical borehole radar pulse is less than 80 MHz, the Chase CS2250 ADC unit is suitable to digitise the received waveforms.

Three different experimental measurements were made to characterize the ADC units and are discussed in the following subsections.

#### **4.5.1 Long-Pulse Response Measurement**

The time-domain responses of two channels of three different CS2250 ADC's were measured for a long (125 ns pulsewidth) pulse using the measurement configuration depicted in Figure 4-25. The Tektronix FG504 function generator generates a 484 mV 125 ns pulse, plotted in Figure 4-26. A 1 V trigger signal is also generated. The PRF of the trigger signal is too high for the ADC units and the voltage level is too low to trigger them successfully. Using a 12-bit binary counter and logic level shifter, the PRF can be decreased and the logic level increased to trigger the ADC units. The Tektronix TDS3052B oscilloscope, with a high input impedance probe, probes the voltage at the feed point of the ADC units. When the pulse response of the one channel is measured, the input of the other channel is terminated with a 50  $\Omega$  load.

## CHAPTER 4: Characterization of Receiver Chain

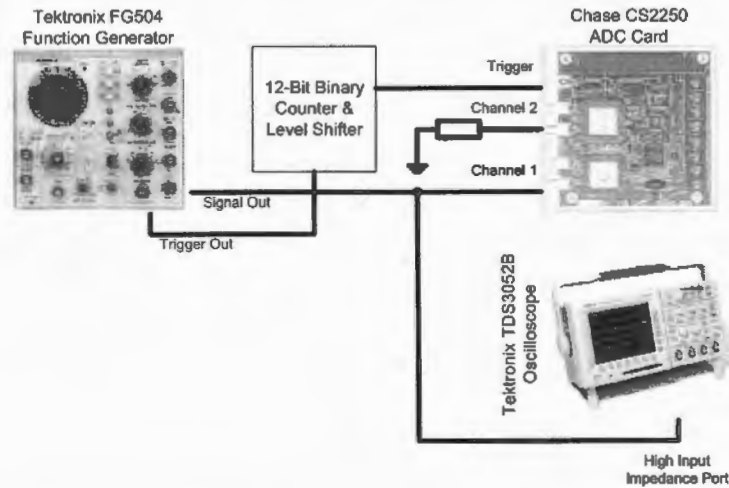


Figure 4-25: Measurement configuration for pulse response measurement.

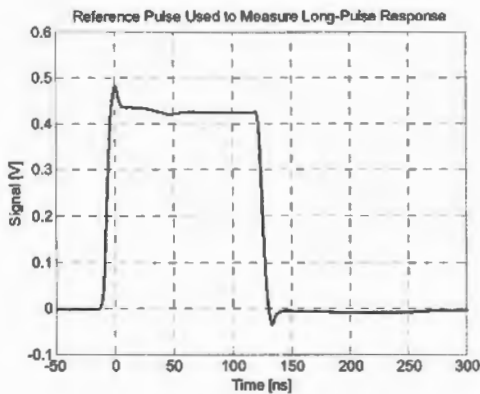


Figure 4-26: Reference pulse for ADC characterization measurements.

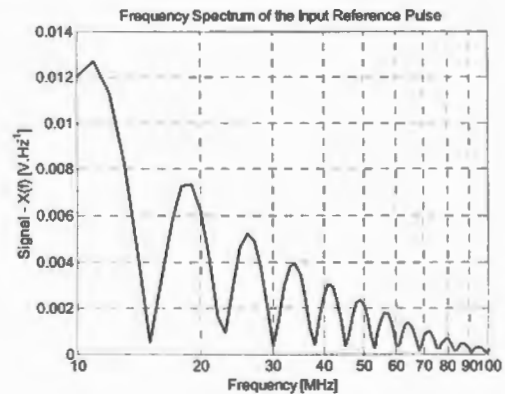


Figure 4-27: Frequency spectrum of input reference pulse.

The frequency spectrum of the reference pulse is plotted in Figure 4-27. The fast rise- and fall times have a high frequency content, while the length of the pulse introduces the sinc-like magnitude response.

The ADC units are controlled with a handheld PSION Workabout computer. Before any digitisation measurement, the clipping value (range) and the amount of stacking have to be set. The input range can be set to  $\pm 0.5$  V,  $\pm 1.25$  V or  $\pm 2.5$  V while the stacking has to be between 128 and 2048 samples. As a complete reference set, the time domain responses of both channels for the 3 DAQ units (2 for field experiments and 1 for laboratory work) at the different clippings and averaging factors are presented in Appendix C. The two field deployable units, DAQ #208 and # 207, are also referred to as DAQ #1 and DAQ #2 respectively. The responses of the two channels of the different ADC units with different clipping settings are compared in Figure 4-28 for a 512 averaging factor.

## CHAPTER 4: Characterization of Receiver Chain

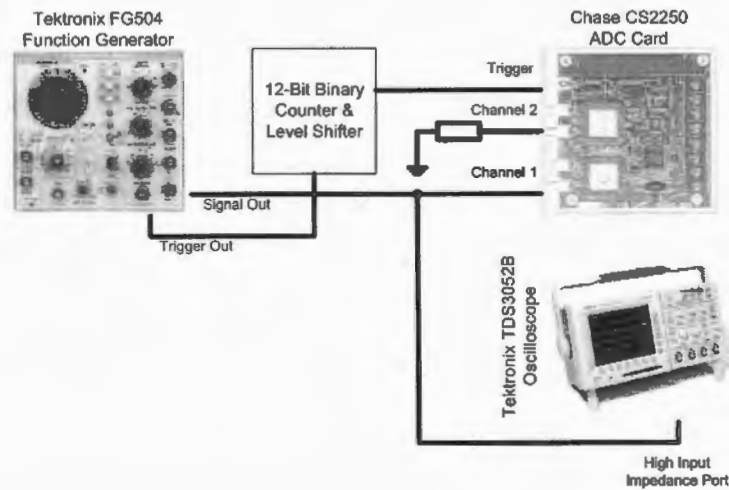


Figure 4-25: Measurement configuration for pulse response measurement.

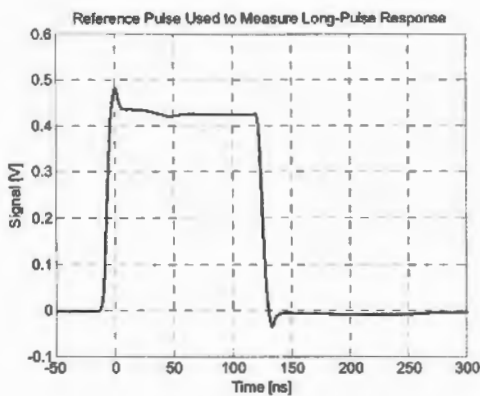


Figure 4-26: Reference pulse for ADC characterization measurements.

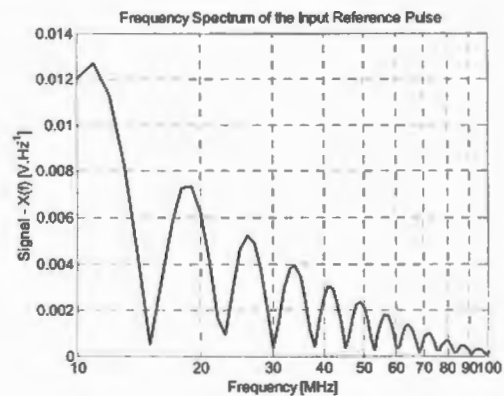


Figure 4-27: Frequency spectrum of input reference pulse.

The frequency spectrum of the reference pulse is plotted in Figure 4-27. The fast rise- and fall times have a high frequency content, while the length of the pulse introduces the sinc-like magnitude response.

The ADC units are controlled with a handheld PSION Workabout computer. Before any digitisation measurement, the clipping value (range) and the amount of stacking have to be set. The input range can be set to  $\pm 0.5$  V,  $\pm 1.25$  V or  $\pm 2.5$  V while the stacking has to be between 128 and 2048 samples. As a complete reference set, the time domain responses of both channels for the 3 DAQ units (2 for field experiments and 1 for laboratory work) at the different clippings and averaging factors are presented in Appendix C. The two field deployable units, DAQ #208 and # 207, are also referred to as DAQ #1 and DAQ #2 respectively. The responses of the two channels of the different ADC units with different clipping settings are compared in Figure 4-28 for a 512 averaging factor.

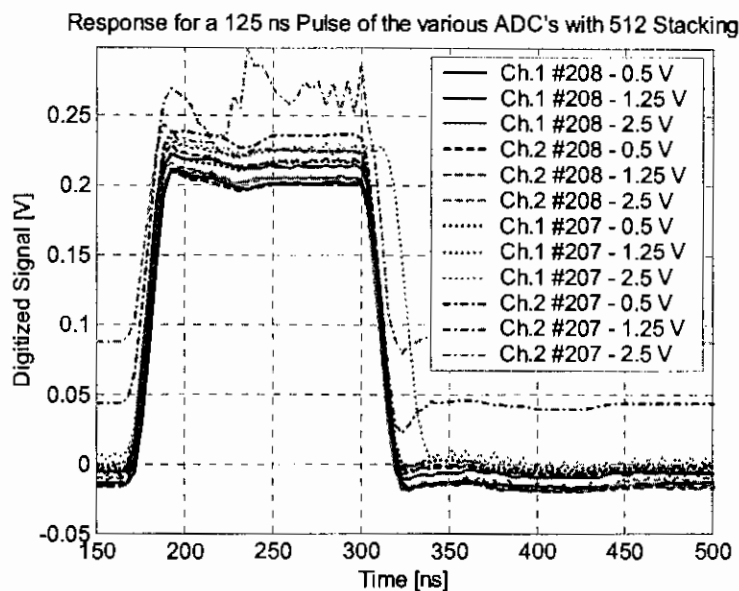


Figure 4-28: Comparison of ADC channel responses to a 125 ns pulse.

With the exception of three, the responses are very closely matched, only differing in the DC offset. The three settings that are deviating notably are:

- ADC serial number #207, Channel 1, 2.5 V Clipping
- ADC serial number #207, Channel 2, 1.25 V Clipping
- ADC serial number #207, Channel 2, 2.5 V Clipping

In Appendix C the irregular response of some of the channels is considered in greater detail. Of great importance is the frequency response of the ADC units. The frequency spectrum of the input reference pulse is presented in Figure 4-27. The frequency spectra of the ADC time domain responses have to be calculated. In order to determine the frequency domain transfer function,  $G_{\text{ADC}}(f)$ , the time scales of the reference and response need to be the same. The reference pulse is measured with the Tektronix TDS3052B Oscilloscope at a sampling interval of 0.2 ns, while the Chase ADC units digitise the signals at a time interval of 4 ns. For adequate frequency resolution and to minimize aliasing effects, a common sampling time interval of 0.8 ns was chosen. The reference pulse can easily be resampled taking every fourth sample. For the responses it is needed to interpolate between the digitised samples by inserting four samples between two adjacent samples.

If the highest frequency contained in an analogue signal  $x_a(t)$  is  $F_{\text{max}} = B$  and the signal is sampled at a rate  $F_s > 2F_{\text{max}} = 2B$ , then  $x_s(t)$  can be exactly recovered from its sample values [9]. When the sampling is performed at the minimum sampling rate  $F_s = 2B$ , the exact reconstruction formula is

$$x_a(t) = \sum_{n=-\infty}^{\infty} x_a \left( \frac{n}{2B} \right) \frac{\sin 2\pi B(t - n/2B)}{2\pi B(t - n/2B)}. \quad (4.19)$$

The actual and resampled response of channel 1 of the ADC serial number #208 at 0.5 V clipping and 128 stacking is plotted in Figure 4-29 together with the resampled input reference pulse.

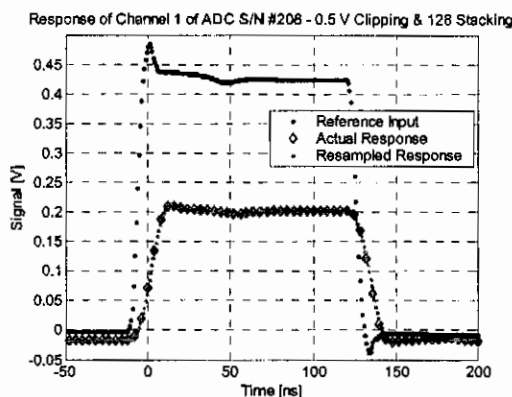


Figure 4-29: Actual and Resampled Response of Channel 1 of ADC serial number #208.

Clearly the rise- and fall time of the ADC unit is slower than that of the input reference pulse, indicating that the bandwidth of the ADC unit is less than the highest frequency component of the reference pulse. The frequency domain transfer functions (magnitude and phase) of channel 1 of ADC serial number # 208 with 0.5 V clipping and 128 stacking are plotted in Figure 4-30 and Figure 4-31.

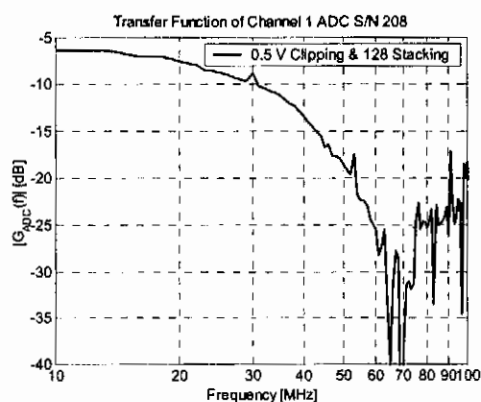


Figure 4-30: Magnitude response for channel 1 of ADC #208 with 0.5 V clipping and 128 stacking.

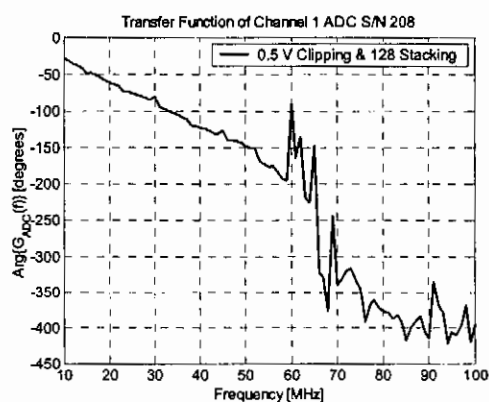


Figure 4-31: Phase response for channel 1 of ADC #208 with 0.5 V clipping and 128 stacking.

The magnitude of the frequency response starts at  $-6$  dB and drops considerably to about  $-25$  dB at 60 MHz after which it deteriorates even more. The cut-off frequency seems to be in the order of about 70 MHz, while the phase response is linear to about 60 MHz. The signal-to-noise ratio beyond 60 MHz is very low. The magnitude responses for different averaging factors are plotted in Figure 4-32, while the

responses for the different channels and clippings of the two ADC units are plotted in Figure 4-33.

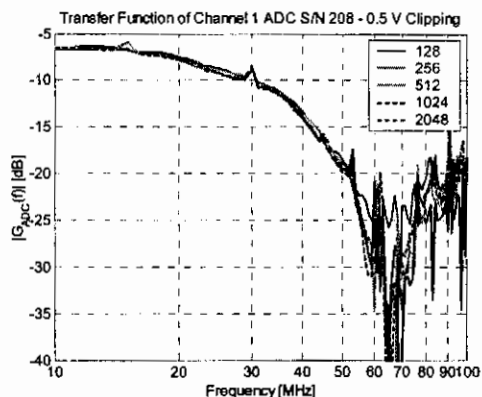


Figure 4-32: Magnitude response for channel 1 of ADC #208 with 0.5 V clipping for different stackings.

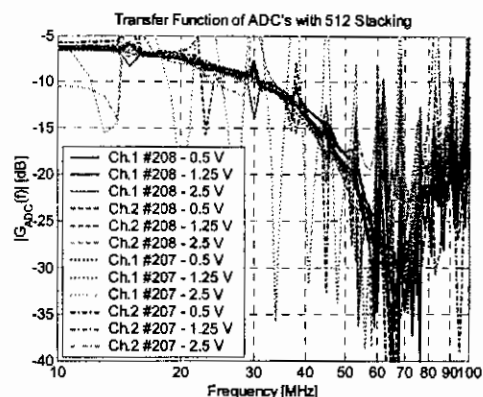


Figure 4-33: Magnitude response for different ADC channels and clippings with 512 stacking.

The increase in SNR as the number of stackings is increased, is not clearly visible. The only difference occurs above 60 MHz where the response signal is very weak and noisy. When the transfer functions of the different clippings and channels are compared, they all seem to correlate quite closely up to 60 MHz, except for the three deviations as pointed out earlier. With a shorter input reference pulse, it might be possible to obtain a higher fidelity transfer function for the upper frequency region above 60 MHz. This is considered in the following section.

### 4.5.2 Short-Pulse Response Measurement

The measurement of Section 4.5.1 was repeated by using a pulse with much shorter duration. If a pulse with a first pseudo null beyond the spectrum of interest can be used, the fidelity of the transfer function will be increased.

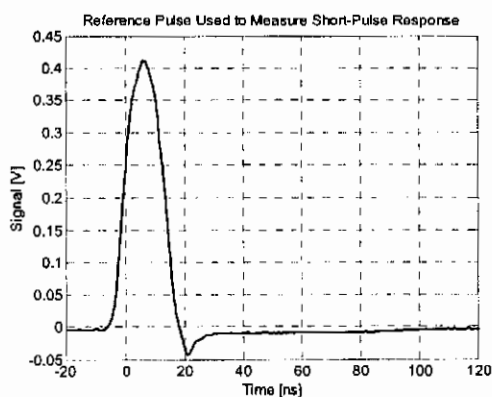


Figure 4-34: Reference pulse used to measure the short-pulse response of the ADC units.

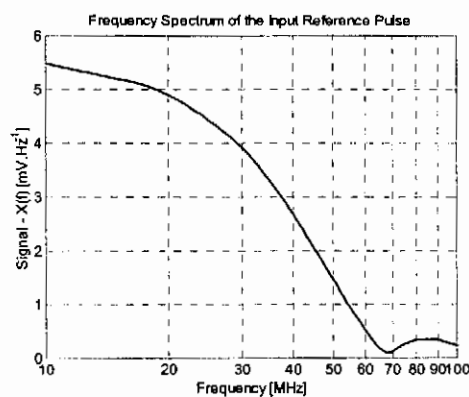


Figure 4-35: Frequency spectrum of the short reference pulse.

## CHAPTER 4: Characterization of Receiver Chain

The reference input short pulse used for this measurement is plotted in Figure 4-34. Its frequency spectrum is plotted in Figure 4-35. The reference pulse has a zero-crossing duration of 24 ns and a PRF of 6.4 MHz. It also has a negative overshoot with a slow recovery time – about 100 ns. The first pseudo null occurs at 68 MHz.

The short pulse measurements were made using 512 stacking. The time domain responses for different clipping settings of the two channels of the two main ADC units are plotted in Figure 4-36.

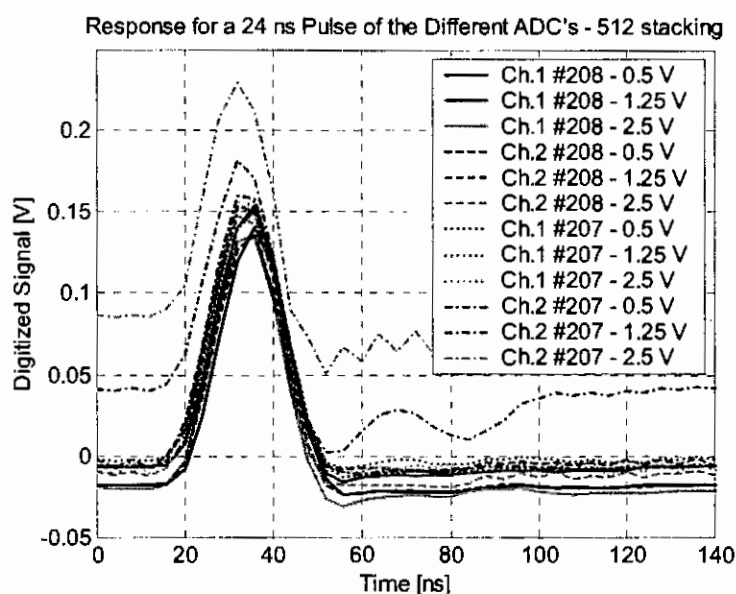


Figure 4-36: Short pulse responses for the two main ADC units (serial numbers #208 and #207).

All the responses, except two, are closely related. The two deviating responses are the same ones that deviated in the long pulse response measurement with the same DC offset. The same broadening of the pulse for channel 1 of ADC serial number #208 at 2.5 V clipping is absent in this measurement. This indicates an error of random nature, if an error at all.

The calculation of the frequency domain transfer function for a short pulse is considerably more difficult. Since the PRF is 6.4 MHz with a corresponding pulse repetition interval of 0.156  $\mu$ s and the desired response length is 1  $\mu$ s, the response will be contaminated with secondary pulse responses that have to be masked. The isolated time section has to include the precursor as well as the tail of the response in order to be accurate. Secondly, the remaining time section has to be set to a DC value equal to the first sample of the isolated sample. Finally, a smooth transition has to be made at the end of the isolated time response to the DC value of the remaining

## CHAPTER 4: Characterization of Receiver Chain

section. The ADC might have a very slow recovery to the exact initial DC value. To avoid anomalies associated with a step function in the response, the tail of the isolated time response is weighted to match the DC value. A time constant was chosen to minimize errors in the spectrum of interest. The actual and resampled response of channel 1 of the ADC serial number #208 at 0.5 V clipping and 512 stacking are plotted in Figure 4-37 together with the resampled input reference pulse.

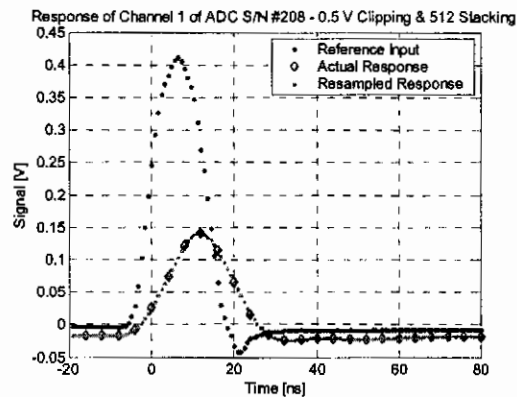


Figure 4-37: Actual and Resampled Response of Channel 1 of ADC serial number #208.

Once again, the slow response of the ADC unit is clear and the negative overshoot is not followed. The magnitude- and phase response of channel 1 of ADC serial number #208 at 0.5 V clipping and 512 stacking are plotted in Figure 4-38 and Figure 4-39.

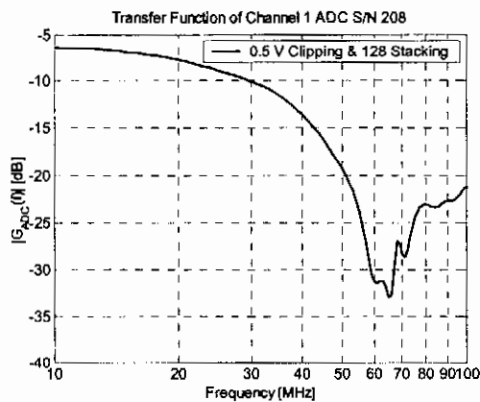


Figure 4-38: Magnitude response of channel 1 of ADC serial number #208 at 0.5 V clipping and 512 stacking for a short pulse.

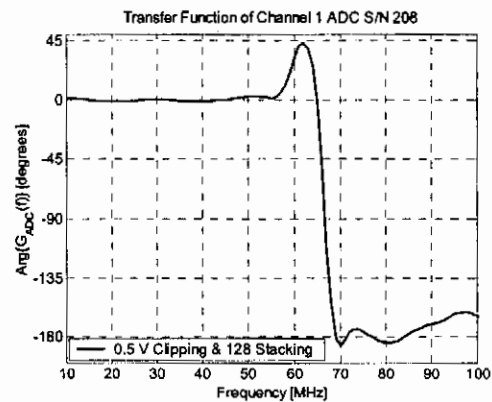


Figure 4-39: Phase response of channel 1 of ADC serial number #208 at 0.5 V clipping and 512 stacking for a short pulse.

The maximum phase deviation is  $4^\circ$  before the phase jump at 62.5 MHz. The phase jump seems to be a discrete  $180^\circ$  associated with a sign reversal. It might be a digital artefact due to asynchronous triggering and stacking, and will be considered subsequently. The local minimum in the magnitude response is also at the same frequency, reconfirming the suspicion of a digital artefact occurring at frequencies including and above 62.5 MHz. This suspicion is raised further when it is realized

that 62.5 MHz is a fourth of the sampling frequency and equal to the master clock on the ADC board.

### 4.5.3 SFCW Response Measurement

The final measurements made on the ADC units are their stepped frequency continuous wave (SFCW) responses. The measurement configuration is depicted in Figure 4-40.

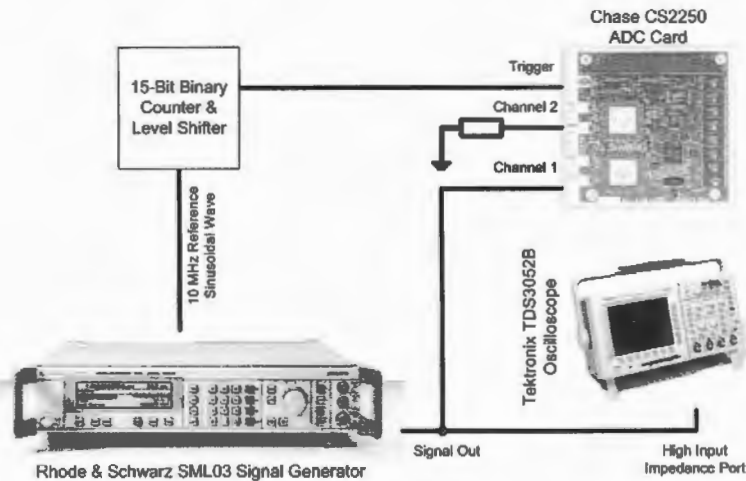


Figure 4-40: Stepped frequency continuous wave response measurement setup.

A Rhode & Schwarz SML03 signal generator is used to excite power-levelled (with respect to a 50  $\Omega$  load) output sinusoidal waves with a digitally controlled frequency. In addition to the RF output, there is also a 10 MHz phase-locked reference output signal. If this signal is used as input to a logic counter, the output will be a square wave with a frequency equal to

$$f_s = \frac{10}{2^n} \text{MHz}. \quad (4.20)$$

A 15-bit counter was used ( $n = 15$ ) yielding a square wave frequency of 305.18 Hz. Since the Chase CS2250 ADC card with the PSION Workabout software can only be operated with a minimum of 128 stacks, the output RF signal has to be phase locked with the trigger pulse. If this does not happen, stacking will produce a severely deteriorated sinusoidal wave because of the random phase of the signal with respect to the trigger. The frequencies at which the RF signal will be phase locked are

$$f_0 = \frac{10}{2^n} m \text{MHz} \quad , \quad n = 15 \quad m = 1, 2, 3, \dots \quad (4.21)$$

## CHAPTER 4: Characterization of Receiver Chain

The magnitude responses of the different ADC unit channels at 2.5 V clipping and 512 stacking are plotted in Figure 4-41 for a 1 V<sub>rms</sub> input signal.

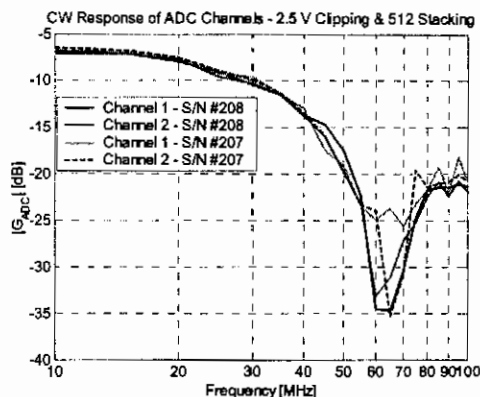


Figure 4-41: SFCW magnitude response of ADC unit channels.

There is a definite pseudo null in the 62.5 MHz region with the typical  $-13$  dB peak sidelobe associated with a rectangular window's spectrum. This phenomenon is investigated in the following section.

Another important effect to bear in mind is the EM cross coupling between the different channels on the ADC units. This was obtained by Fourier transforming the response of a channel with a matched load connected to its input, while the other load was being driven. The results are plotted in Figure 4-42.

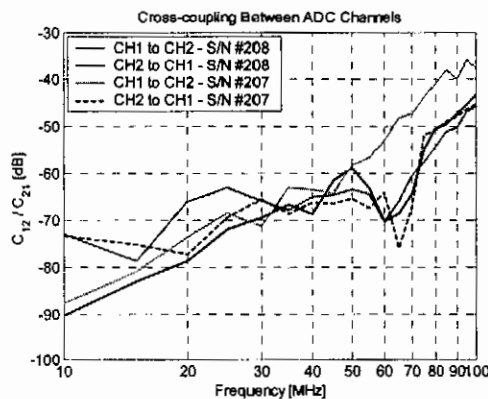


Figure 4-42: EM coupling between different channels on the ADC units.

Cross coupling increases with frequency from an average of  $-80$  dB at 10 MHz to about  $-40$  dB at 100 MHz. This is quite tolerable for a densely populated PCB where both channels are digitised on the same PCB.

### 4.5.4 Theory of Digitisation and Stacking Process

The pseudo null at 62.5 MHz, the approximate  $-13$  dB sidelobes and the abrupt  $180^\circ$  phase change indicated a kind of digital filter. The ADC units are not undersampling,

since the Nyquist criterium is adhered to. The only other process occurring in the analogue-to-digital conversion process is that of stacking. This is investigated in the next section.

#### 4.5.4.1 The Stacking Process

In stacking, a predetermined number of traces are added together and divided by the number of traces stacked – i.e. an averaging process. Stacking improves the SNR in direct proportion to the number of samples, provided the samples are identical and the noise background is uncorrelated. The GeoMole system has been designed so that the thermal noise in the receiver chain is sufficient to toggle the least significant bit of the ADC – a prerequisite when stacking is used to improve the SNR. If the digitised signals from the different traces are exactly aligned, the desired signal samples will add coherently, while the incoherent noise samples will not. If the digitised desired signals do not align however, there will be a deleterious effect on the resultant trace and the stacking process will have an associated transfer function. The alignment of the signals is determined by the triggering technique used in the system. In the GeoMole system, a trigger signal is sent to the ADC unit. This trigger is synchronous with the transmitted pulse, but asynchronous with the digital clock signal of the ADC unit. Consider the diagram in Figure 4-43.

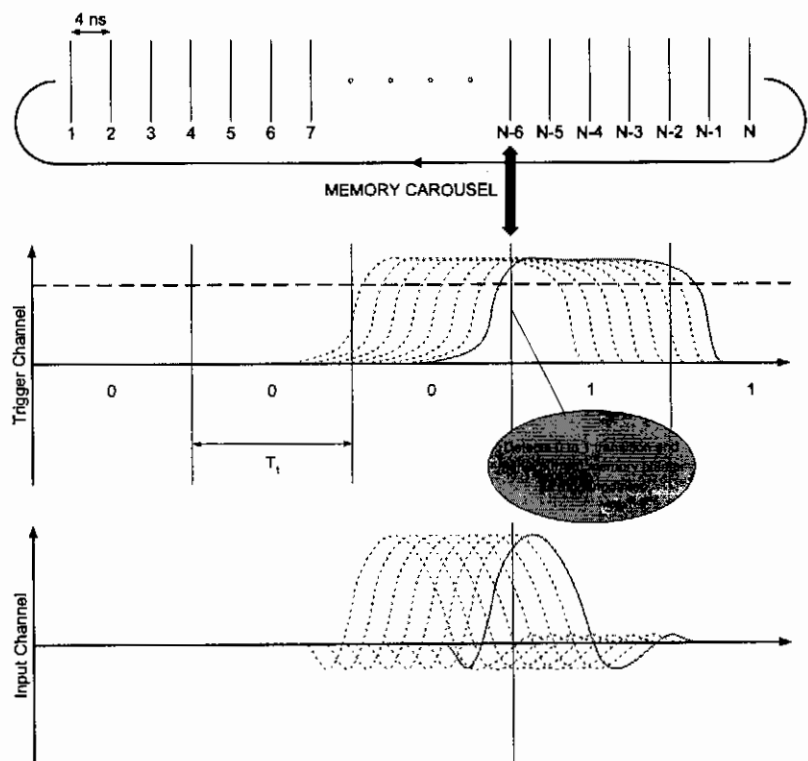


Figure 4-43: Stacking process of the Chase CS2250 ADC units.

When a trigger event (low-to-high or high-to-low) is detected on the trigger channel, the current memory address is marked as the beginning of the trace and the memory data in the trace sequence is exported to the peripheral device. It is possible to store a given amount of samples before the trigger event occurs by a process called pretriggering. The trigger channel is sampled at a given sample period,  $T_t$ , to determine whether or not the signal level exceeds the trigger threshold voltage. The exact time when the signal exceeds this threshold, varies undetected within a given sample period if the trigger signal is not synchronous with the trigger sample clock. The input channel signal is synchronous with the trigger channel. Because of asynchronous triggering, there will be a time offset between different digitised traces of the same input pulse. These traces do not add coherently in the stacking process. The filter function associated with asynchronous triggering is determined by the trigger sample period,  $T_t$ . This is discussed in the next section.

#### 4.5.4.2 Asynchronous Triggering Transfer Function

The frequency domain transfer function associated with the filter action of asynchronous triggering can be determined by a study of continuous wave excitation. Let the input signal,  $x(t)$ , be a cosine with a frequency  $f_0$

$$x(t) = \cos 2\pi f_0 t. \quad (4.22)$$

The digitised output signal  $x_a(n)$  has a time offset  $\zeta$ , because of the asynchronous trigger.  $\zeta$  is bounded within one trigger sample period  $T_t$

$$\begin{aligned} x_a(n) &= \cos 2\pi f_0 (nT_s - \zeta) \\ \zeta &= \{-T_t < \zeta \leq 0\} \end{aligned} \quad (4.23)$$

with  $\zeta$  supposed to be an uncorrelated random variable with a uniform probability density function. The stacking process is easier to understand when using the phasor representation of signals. A graphic representation of the stacking process is shown in Figure 4-44.

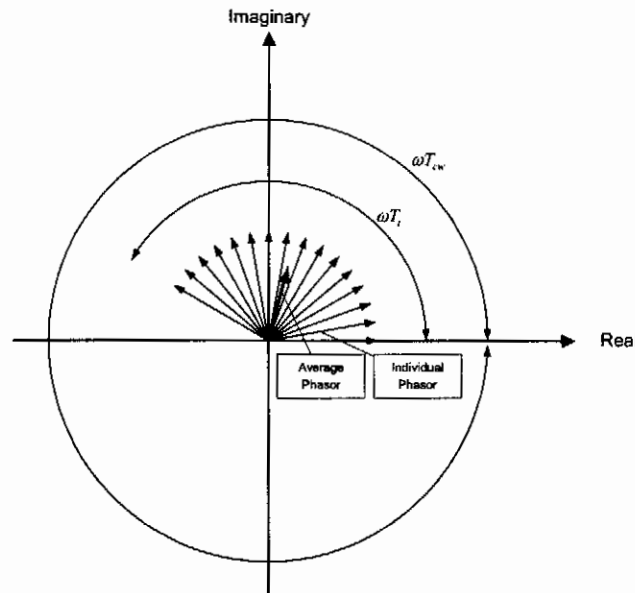


Figure 4-44: Stacking process of phasors in the presence of asynchronous triggering.

The individual phasors have equal magnitudes, but their phases are spread over  $\omega T_i$ . The average phasor has a magnitude smaller than unity with a phase that lags the extreme individual phasor. As  $T_i \rightarrow T_{cw}$ , the magnitude and phase of the average phasor approach 0 and  $180^\circ$  respectively. With  $T_i$  incrementally larger than  $T_{cw}$ , a phase jump of  $180^\circ$  occurs. This phenomenon was clearly visible in the practical measurements. The theoretical predictions of the magnitude- and phase response of the filter associated with asynchronous triggering are plotted in Figure 4-45 and Figure 4-46. The trigger sampling frequency was set to 62.5 MHz. The response was calculated for two cases of time-offset distribution over the range  $\omega T_i$  - equally spaced and as a random process with a uniform distribution function.

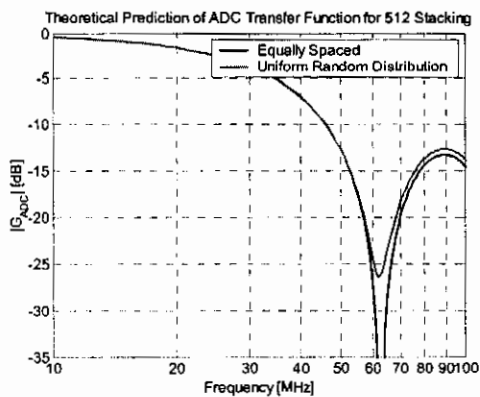


Figure 4-45: Magnitude response of asynchronous trigger filter function.

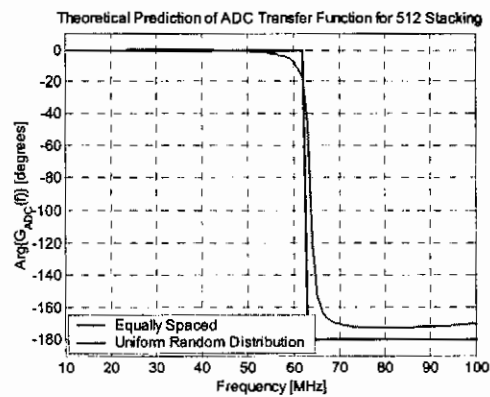


Figure 4-46: Phase response of asynchronous trigger filter function.

The response has the same shape as that of the practical measurements in Sections 4.5.1 to 4.5.3. For the equally spaced phasors there is a null at 62.5 MHz and a pseudo null for the random phasors. Both have a  $-13$  dB sidelobe level as expected and a phase jump of  $180^\circ$  at 62.5 MHz. For the equally spaced phasors, the transition is abrupt, but for the random phasors, it is gradual.

### 4.5.5 Comparing Practical and Theoretical Results

Three different practical measurements were made on the ADC units as summarized in the previous sections. A theoretical prediction was made based on a number of assumptions. Comparing Figure 4-38 and Figure 4-45, it is clear that the form is almost exactly the same, but there is an offset of  $-6$  dB, i.e. half of the voltage. It can therefore be assumed that the transfer function of the ADC units can be divided into an RF and a digital transfer function where the RF transfer function is equal to 0.5 with a linear phase response:

$$G_{ADC}(f) = G_{ADC(rf)}(f)G_{ADC(digital)}(f) \tag{4.24}$$

$$G_{ADC(rf)}(f) = 0.5$$

Taking the RF transfer function into account, the practical measurements of the ADC units' transfer functions are compared with the theoretical prediction in Figure 4-47 and Figure 4-48.

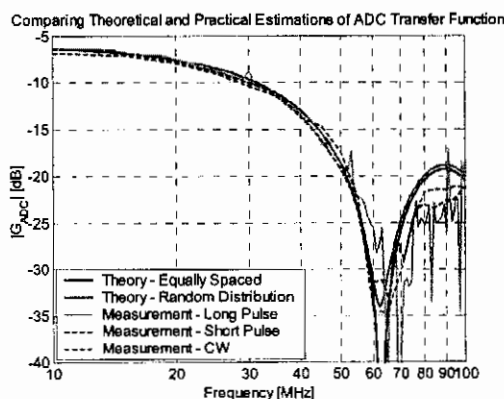


Figure 4-47: Comparison of theoretical and measured magnitude response of the ADC.

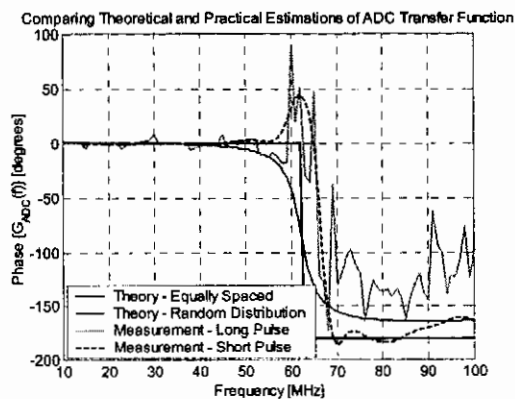


Figure 4-48: Comparison of theoretical and measured phase response of the ADC.

The measured transfer functions are in close agreement with each other and also with the theoretical predictions. The only observable difference is the phase response in the region of 62.5 MHz. The exact shape of the phase jump centred at approximately 62.5 MHz is dependent on the distribution of the phasors within the  $\omega T_i$  window,

which was assumed to be either a random process with a uniform distribution function or equally spaced. Since the SNR is extremely low at 62.5 MHz, there is no use in trying to compensate for the phase response in that region and the exact phase response at 62.5 MHz is of no importance. The theoretical prediction using an equally spaced phasor assumption can be used with a high degree of accuracy in a pulse recompression algorithm.

In the theoretical predictions, the assumption was made that the trigger sampling frequency,  $F_t$ , is 62.5 MHz for the Chase CS2250 ADC units. If this was not the case and it was 125 MHz or even 250 MHz as it was initially assumed, the transfer function would have its first null at 125 MHz or 250 MHz respectively. Since the measured pseudo null occurred at 62.5 MHz, the assumption has to be correct.

## 4.6 System Parameter Extraction

In a radar system, the MDS is a very important parameter. Knowing the transmitter power and the characteristics of the propagating medium, it indicates the amount of signal attenuation allowed before the signal cannot be detected. From the maximum signal attenuation, the maximum detection range of the radar system can be derived.

Another very important parameter in any radar system is the time offset of the recorded waveform, i.e. the elapsed time since the waveform was transmitted until a predefined receiver voltage signal event is captured.

### 4.6.1 Maximum Available Power

In Section 3.7.3 the power delivered to the TX antenna when deployed in a borehole in a host rock was estimated. From this, it is possible to calculate the power delivered to receiver electronics using equation (3.21), rewritten here:

$$P_d = P_{in} \frac{\lambda^2 (1 - |\Gamma_{rx}|^2) e_{rx} e_{tx} D_{rx}(\theta_r, \phi_r) D_{tx}(\theta_t, \phi_t)}{(4\pi r)^2 e^{2\alpha r}} \quad (4.25)$$

This is only exact when the host medium is homogeneous. In (4.25)

$$\frac{D_{rx}(\theta_r, \phi_r) D_{tx}(\theta_t, \phi_t)}{4\pi r^2 e^{2\alpha r}} \quad (4.26)$$

is the fractional factor that is dependent of the spatial configuration of the transmitter and receiver probes. The radial distance dependent factors  $(4\pi r^2)^{-1}$  and  $e^{-2\alpha r}$ , describe

## CHAPTER 4: Characterization of Receiver Chain

the physical processes of geometric spreading and dielectric loss respectively. In power budget calculations it is required to know the attenuation due to spatial separation, which corresponds to the MDS. The maximum available power is therefore defined as the power available to the receiver electronics when the product of the radial distance factors is taken as unity in (4.25) and the directivities are taken as the maximum in the  $4\pi$  solid angle space:

$$P_{av} = P_{in} \frac{\lambda^2 (1 - |\Gamma_{rx}|^2) e_{rx} e_{tx} D_{rx}(\max) D_{tx}(\max)}{4\pi} \quad (4.27)$$

The estimated available power for the USTX 01 transmitter deployed in an air-filled 48 mm borehole in a norite host rock is depicted in Figure 4-49. It is compared to the same deployment configuration for the USTX 03 transmitter, known to have a better high frequency response. Furthermore, it is compared to the available power when the TX is deployed in a water-filled borehole and when the host medium is pyroxenite (PX1).

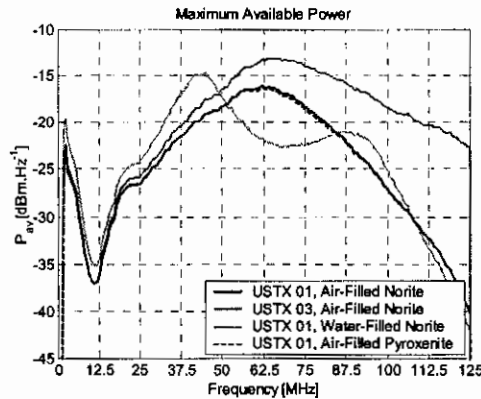


Figure 4-49: Maximum available power for different transmitter configurations.

The USTX 01 transmitter has an inferior performance of about 10 dB at 100 MHz with respect to the USTX 03 transmitter. When the borehole is water-filled, the available power increases in the DC – 50 MHz with a maximum increase of 5 dB at 40 MHz. In the intermediate frequency range (50 – 85 MHz), the available power decreases, but increases once again above about 70 MHz. This behaviour can be ascribed to the lowered 1<sup>st</sup> pseudo resonance and an increased coupling to the host medium in the frequencies below 100 MHz.

### 4.6.2 Noise Figure Estimation

The noise figure of the cascaded receiver chain has been measured in Section 4.4.4. It is heavily dependant however, on the exact configuration of the highly configurable receiver chain.

Consider the cascaded receiver chain depicted in Figure 4-50. The subsystems are identified as the antenna, front-end amplifier chain, optic link (modulator, optic fibres and demodulator), power amplifier and the additional attenuator that is sometimes added.

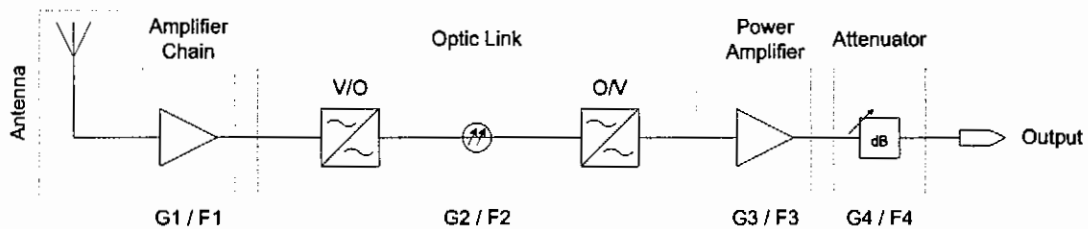


Figure 4-50: Subsystems in the GeoMole receiver RF chain.

In Figure 4-50, the noise figure and power gain of the amplifier chain is the only constant parameter in the entire chain. The noise figure and power gain of the other stages are highly dependent on the exact configuration. From the cascaded noise figure, the equivalent noise temperature of the cascaded system can be found:

$$T_e = (F_{cas} - 1)T_0. \quad (4.28)$$

The effective noise power at the input due to the noise contributions of the antenna and the cascaded receiver electronics is calculated as

$$N_i = k(T_0 + T_e)B + N_a \quad (4.29)$$

where  $N_a$  is the noise power at the input due to the black body radiation intercepted by the receiver antenna. The intercepted noise can be represented by a Thévenin equivalent source connected to the real input impedance of the receiver chain as depicted in Figure 4-51.

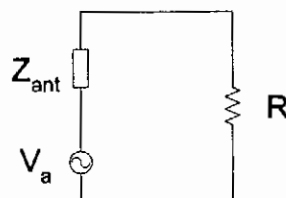


Figure 4-51: Thévenin equivalent of intercepted noise.

## CHAPTER 4: Characterization of Receiver Chain

The antenna impedance  $Z_{ant}$  and the RMS noise voltage  $V_a$  are defined [83] as

$$\begin{aligned} Z_{ant} &= (R_{loss} + R_{rad}) + jX_{ant} \\ V_a &= \sqrt{4kTBR_{rad}}. \end{aligned} \quad (4.30)$$

From (4.30) the black body radiated power intercepted by the antenna and delivered to the load  $N_a$  is calculated as

$$N_a = \frac{4kTBR_{rad}R}{|Z_{ant} + R|^2}. \quad (4.31)$$

The most difficult gain and noise figure to determine in the chain is that of the highly configurable optic link. It has been measured for the 1<sup>st</sup> reference optic link. The optic demodulator has been isolated as the major noise source in the optic link. It can therefore be assumed that the output noise due to the optic link will be the same irrespective of the gain of the optic link, i.e. irrespective of the optic fibre configuration. For a fixed SNR at the input of the optic link, the only power parameter that will change as the fibre optic configuration is changed, is the signal power at the output. The noise figure of the newly configured optic link  $F_2(new)$  can therefore be related to the noise figure of the reference optic link  $F_2(ref)$ :

$$\begin{aligned} F_2(new) &= F_2(ref) \frac{S_0(ref)}{S_0(new)} \\ &= F_2(ref) \frac{G_2(ref)}{G_2(new)}. \end{aligned} \quad (4.32)$$

As the gain of the optic link drops, its noise figure will increase in inverse proportion. The use of the FORJ would therefore increase the noise figure of the optic link by 9 – 11 dB. The equivalent noise power at the input, as defined in (4.29), is reduced by the process of coherent integration in a random, uncorrelated noise background. For an averaging factor of  $n$ , the power is reduced to

$$N'_i = n^{-1}N_i. \quad (4.33)$$

The noise figures of the amplifier chain, optic link and the cascaded receiver chain for two different configurations are plotted in Figure 4-52. The two configurations reflect the two different chains as defined in Section 4.1, i.e. with and without the FORJ. The specific items used in the two configurations are summarized in Table 4-4.

CHAPTER 4: Characterization of Receiver Chain

Table 4-4: Configuration of two optic links for noise figure calculations.

	Optic Modulator	RX Patchcord	Fibre Optic Cable	Coupling Patchcord	SMA Barrel	FORJ	DAQ Patchcord	SCU
Config #1	GM	USRX01	3 (New)	N/A	N/A	N/A	DAQ1 #2	PH001
Config #2	GM	USRX01	3 (New)	Current	Barrel 3	FORJ #1	DAQ1 #2	PH001

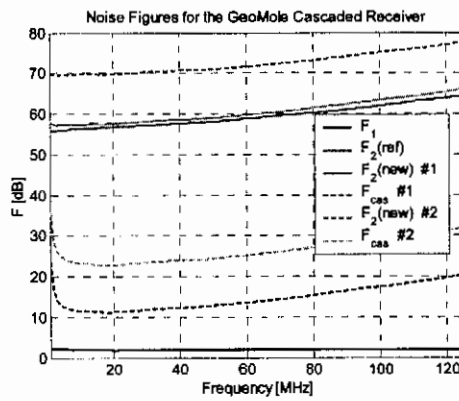


Figure 4-52: Noise figures for 2 cascaded GeoMole receiver chains.

The variable nature of  $F_2$  is evident, especially when the FORJ is incorporated in the optic link. The effect on the cascaded noise figure is also quite severe, as was expected. The equivalent input noise power spectral density for the two configurations in Table 4-4 are plotted in Figure 4-53, with the bandwidth taken as 0.5 MHz.

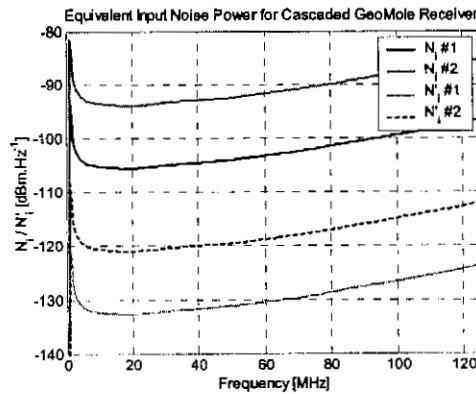


Figure 4-53: Equivalent input noise powers for two GeoMole receiver chain configurations.

The averaging factor was 512 in both configurations, resulting in a 27.1 dB decrease in the noise power density. The use of the FORJ #1 resulted in an increase of 11.7 dB

in the noise power density at 40 MHz. For the 1<sup>st</sup> receiver chain configuration and an averaging factor of 512, the noise power density is in the region  $-130 \text{ dBm.Hz}^{-1}$  across the frequency band of interest.

### 4.6.3 Permissible Signal Attenuation<sup>2</sup>

For a given required SNR, the maximum permissible signal attenuation due to the geometry involved can be calculated from the maximum available power and the input noise power by the mathematical relation

$$A_{\max} = \frac{N_i \cdot \text{SNR}}{P_{av}} \quad (4.34)$$

The maximum attenuation for the two configurations in Table 4-4 are plotted in Figure 4-54 for a SNR = 1.

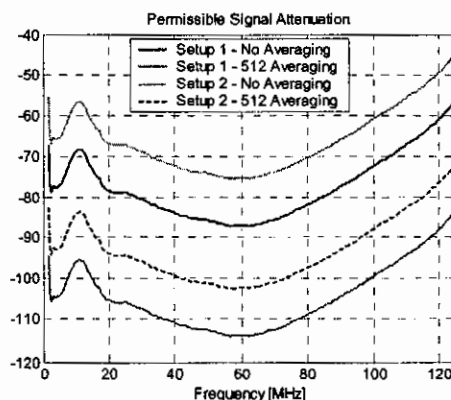


Figure 4-54: Maximum permissible signal attenuation for SNR = 1.

The average permissible attenuation for the 1<sup>st</sup> configuration with 512 averaging is  $-110 \text{ dB}$  (a power factor of  $1 \times 10^{11}$ ) over the frequency range 20 MHz – 100 MHz. The permissible attenuation decreases by 40 dB when the FORJ is included in the optic link and when no averaging is performed. The maximum permissible attenuation for a given radar system is a well-defined figure of merit by which different systems can be benchmarked. It is necessary to keep in mind the pulse shape characteristics of different systems as well.

<sup>2</sup> This is not the dynamic range, but rather the maximum signal attenuation due to the geometry and propagating medium of the MDS for a given SNR – it ties down the floor of the dynamic range.

### 4.6.4 Time-offset Estimation

In the GeoMole BHR system a procedure had to be developed by which the timing characteristics can be predicted accurately for a given configuration.

The transmitter generates a trigger signal at the instant that the transient current is initiated on the antenna structure, i.e. when the antenna radiates the pulse. The trigger signal is modulated on an optic carrier and relayed via the optic fibre link to the SCU and the ADC unit where it triggers the sampling and storage of the received signal. The received signal is also modulated on an optic carrier and relayed to the SCU and one of the ADC unit's channels. The exact configurations of both optic links determine the timing of the received signal as well as the pre-triggering used by the ADC unit itself (see Section 4.5.4.1 ). Consider the timing diagram of the trigger and signal channels of the ADC unit as depicted in Figure 4-55 together with Figure 4-56 that explains the timing nomenclature.

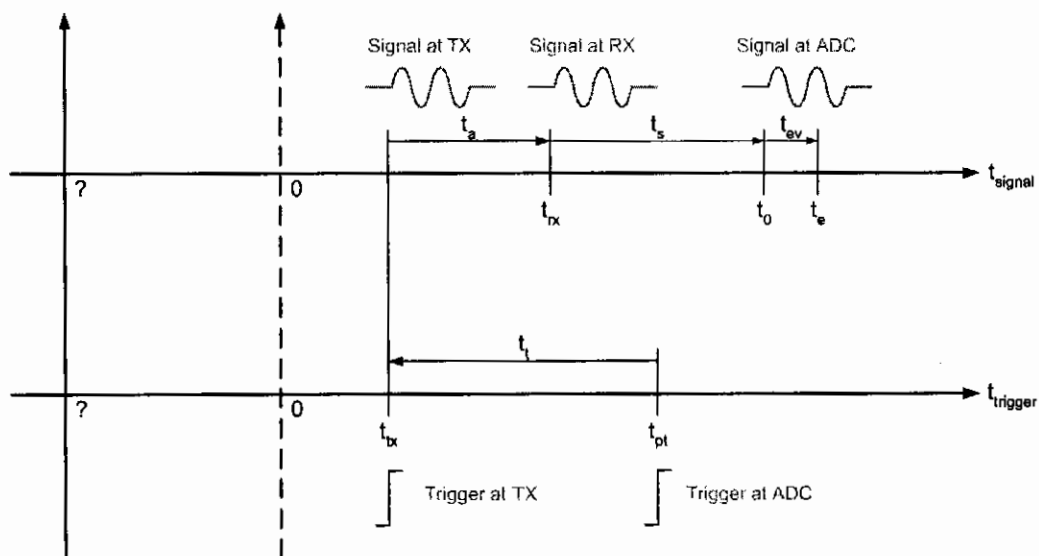


Figure 4-55: Timing diagram for the trigger and signal channels.

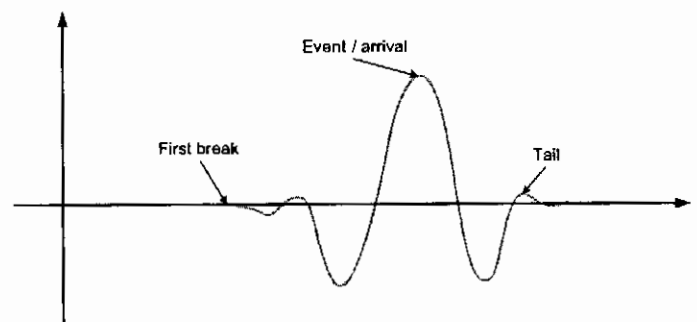


Figure 4-56: Illustrative definition of timing nomenclature.

The trigger channel of the ADC is triggered by a positive edge event and in the case of pre-triggering, marks a certain pointer in the memory carousel as the time zero, i.e.  $t = 0$ . The time of triggering is the pre-triggering time  $t_{pt}$ . The velocity of the optic waves in the optic fibres has been measured as

$$v_{optic} = 2 \times 10^8 \text{ m.s}^{-1}. \quad (4.35)$$

The time delay of the trigger through the optic fibres is dependent on their exact length:

$$t_i = \frac{d_i}{v_{optic}}. \quad (4.36)$$

The same relationship exists between the time delay of the signal  $t_s$  and the total length of the fibre optics for the received signal,  $d_s$ . The transmit time  $t_{tx}$  is the instant at which both the trigger and the pulse are transmitted by the TX probe. The RF signal propagates through a given medium for a finite time  $t_a$  that depends on the geometry and properties of the medium. Upon arrival, the signal is amplified and modulated on an optic carrier and relayed to the SCU. It eventually arrives at the input of the ADC at the time  $t_0$ . If  $t_0$  is subtracted from the recorded time for a given trace, the time axes will reflect the time delay  $t_a$ . It should be clear that  $t_0$  refers to the time-offset of the first-break of the transmitted pulse. It is usually better to use the time-offset of a well-defined and high fidelity event  $t_e$ , especially in the presence of noise. In a controlled laboratory environment, it might be possible to measure the time increment between the first break and the identified event. In Figure 4-55 the second peak was identified as the event of choice. No attention was given to the time delays inherent to the electronics. Due to the difficulty involved in their precise measurement, it was decided to include these terms in the pre-triggering time  $t_{pt}$ , thus yielding an effective pre-triggering time. This effective pre-triggering time should be constant for any given configuration.

A laboratory experiment was designed in which the pre-triggering time could be measured. The physical configuration is depicted in Figure 4-57.

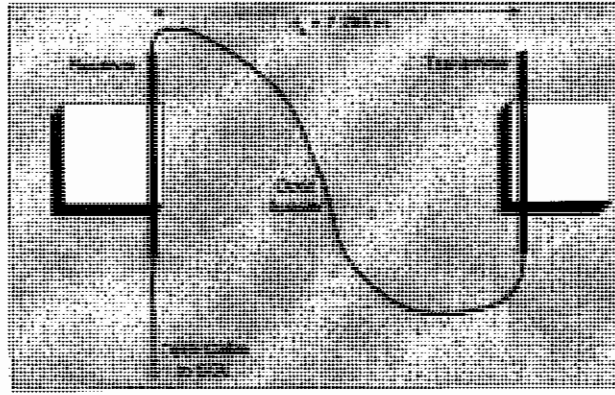


Figure 4-57: Configuration of experiment to measure the pre-triggering time.

The effective pre-triggering time can be calculated from the measured value of  $t_0$  as

$$t_{pt} = t_0(\text{meas}) - t_a + \Delta t_{ts} \quad (4.37)$$

$$\Delta t_{ts} = t_t - t_s = \frac{d_t - d_s}{v_{optic}}$$

For the configuration as depicted in Figure 4-57, the length of the optic spacer and the optic patchcord connecting the optic cable and spacer in the RX probe determine the incremental time of the trigger relative to the signal  $\Delta t_{ts}$ , which is

$$d_t - d_s = (1.45 + 8.73)m \quad (4.38)$$

$$= 10.18m$$

for the experimental configuration. A single captured trace for this configuration is plotted in Figure 4-58.

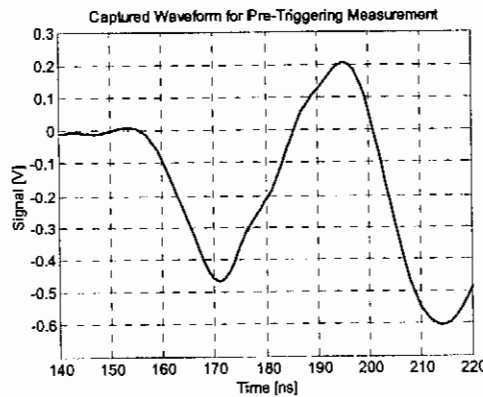


Figure 4-58: Captured trace for the measurement of the pre-triggering time.

From Figure 4-58  $t_0$  is taken as

$$t_0 = 0.1573 \mu s \quad (4.39)$$

and finally  $t_{pt}$  is calculated as

$$t_{pt} = 0.1839 \mu s. \quad (4.40)$$

## CHAPTER 4: Characterization of Receiver Chain

The first break offset time  $t_0$  can be calculated for any configuration using the following three steps:

- Calculate the total optic fibre length for the trigger  $d_t$ .
- Calculate the total optic fibre length for the signal  $d_s$ .
- Calculate the time  $t_0$  using

$$t_0 = t_{pt} - \Delta t_{ts}. \quad (4.41)$$

The time increment between the first break and the chosen event,  $t_{ev}$ , depends on a number of parameters. An average value of

$$t_{ev} = 28 \text{ ns} \quad (4.42)$$

has been measured for a moderate travelling distance of 30 m in a norite host medium without any signal processing. The first break and event time offsets for the first configuration in Table 4-4 are given in Table 4-5 for a 3.1 m optic spacer.

Table 4-5: First break and event time offsets with a 3.1 m optic spacer.

	$t_0$ [ns]	$t_e$ [ns]
Config. #1	160.9	188.9

Pulse recompression algorithms will inevitably modify the first-break time offset, as well as the abovementioned time increment of the event. These parameters have to be recalculated for any pulse recompression algorithm.

## 4.7 Concluding Remarks

In this chapter the highly configurable receiver chain (RF and digital) of the GeoMole BHR system was discussed, quantitatively described and characterized to a high degree of accuracy.

Since absolute measurements are impossible for every stage of the RF chain, a system of reference and relative gains was defined and implemented. This allows the calculation of the absolute gain of any receiver chain by the addition of the relative gains of the configurable items to the reference gain of the specific topology.

A noise figure measurement configuration was designed to adhere to the dynamic range constraints of the HP8970B noise figure meter for the accurate measurement of the gain and noise figure of the optic link. The noise figure of the optic link is

## CHAPTER 4: Characterization of Receiver Chain

extremely high, but the high gain, low noise front-end amplifier improves the overall performance of the system.

The frequency domain transfer function of the Chase CS2250 ADC units was measured by using three time domain techniques and predicted theoretically. It was established that the RF magnitude response of the signal conditioning front-end electronics of the ADC is  $-6$  dB with a linear phase response. As stated in Section 4.5.5, the theoretically developed transfer function can be used in the development of signal processing algorithms.

In conclusion, the basic system parameters of the GeoMole system were defined and characterized. The maximum power available for spatial losses was defined and calculated, as well as the minimum detectable signal, which is coupled to the cascaded noise figure of the system. Precise timing is of crucial importance in the delineation of geometry with radar. The different timing parameters were defined, the fixed parameters were measured and an algorithm was developed to calculate the variable parameters.

# CHAPTER 5

## PULSE RECOMPRESSION

The different subsystems of the GeoMole BHR system were characterized quantitatively and comprehensively in the frequency domain in Chapters 3 and 4. Knowing the exact transfer function of each subsystem, it is now possible to deconvolve the measured response with the system transfer functions to estimate the response at various stages in the radar system.

The excitation waveform at the TX antenna is a crisp pulse associated with the time derivative of the voltage step function. The different systems convolve this waveform with their impulse responses. They effectively spread the waveform over time at every intermediate stage. The digitally captured waveform is therefore a time-spread version of the excitation. The process of deconvolution in this specific case, inherently performs pulse recompression. In this dissertation, the terms deconvolution and pulse recompression are used interchangeably.

The different processes in the pulse recompression algorithm developed are discussed in the subsequent sections. Examples of the performance of this algorithm are presented for laboratory and field measurements. This algorithm has been modified for the batch processing of field experiment data. The basic modifications and some of the results obtained will also be presented.

### 5.1 Literature Review

Only one relevant publication on the pulse recompression of pulsed radar signals has been found. Chernokalov *et al.* [66] developed time and frequency domain techniques to increase the probability of detecting objects with weak contrast. The authors corrected for both the magnitude and phase response to suppress the finite damping of the antenna transient response, reverberations and coupling of antennas in air.

The development of the pulse recompression algorithm in this dissertation was built on basic engineering principles.

## 5.2 Inferring the Input Voltage of the RX Chain

Consider the cascaded receiver chain as depicted in Figure 4-1. If the received voltage at the input of the ADC,  $V_{out}$ , was sampled by at least the Nyquist frequency, the voltages at the different electrical interfaces can be inferred with a high degree of accuracy. If the different RF circuit elements are operated in their linear region, the only errors in the calculated voltages will be due to the irreversible effect of quantisation in the ADC and band-limiting filtering. The following steps summarize the algorithm developed to calculate the voltage at the front-end of the receiver,  $V_{fe}$ :

1. Use the interpolation scheme as in Section 4.5.1 to resample the digitally stored voltage sequence with a time increment of 1 ns to yield a digital voltage sequence  $v_d(t_n)$ , where  $t_n = nT$ . Crop this sequence to have a PRF of 0.5 MHz.
2. Calculate the phasor frequency domain representation of this sequence,  $V_d(f)$ , by using the discrete Fourier transform (DFT).
3. Calculate the Fourier series coefficients of the voltage at the input of the ADC

$$V_{out}(f) = \frac{V_d(f)}{G_{ADC}(f)}. \quad (5.1)$$

4. Determine the total analogue gain for the given radar configuration.
5. Calculate the Fourier series coefficients of the voltage at the front-end of the receiver chain

$$V_{fe}(f) = \frac{V_{out}(f)}{G_{RA}(f)G_R(f)G_D(f)G_{FAr}(f)}. \quad (5.2)$$

6. Calculate the time domain equivalent series of the voltage at the front-end of the receiver chain,  $v_{fe}(t_n)$ , using the inverse discrete Fourier transform (IDFT).

The poles of (5.1) and (5.2) have been replaced with zeros for the moment, but will be dealt with at a later stage. The results of this algorithm are presented in Section 5.5.

## 5.3 Estimating the Electric Field at the Receiver Antenna

The next step in the pulse recompression / deconvolution algorithm is the estimation of the plane wave electric field incident upon the receiver antenna. The following

steps summarize the algorithm developed to calculate the electric field from the voltage at the front-end of the receiver chain:

1. Calculate the discrete double-sided power spectral density (DPSD) of the power delivered to the front-end of the receiver

$$P_d(f) = \frac{|V_{fe}(f)|^2}{R_{in}} \quad (5.3)$$

with  $R_{in}$  assumed to be  $50 \Omega$ .

2. Calculate the DPSD of the power received by the antenna

$$P_{rec}(f) = \frac{P_d(f)}{e_{rx}(f) [1 - |\Gamma_{rx}(f)|^2]}. \quad (5.4)$$

3. Estimate the DPSD of the time-averaged radial power flux density at the feedpoint with the assumption that the antenna is illuminated uniformly with a normally incident plane wave

$$S_{r(avg)}(f) = \frac{4\pi P_{rec}(f)}{\lambda^2 D_{rx}(0,0)}. \quad (5.5)$$

4. Estimate the magnitude of the discrete Fourier series representation of the co-polarized (with the axial direction of the antenna) electric field at the feedpoint of the antenna

$$|E_\theta(f)| = \left[ \frac{2S_{r(avg)} |\eta|^2}{\text{Re}\{\eta\}} \right]^{1/2} \quad (5.6)$$

where  $\eta$  is the intrinsic (characteristic) impedance of the host medium as defined in Section 6.5.

In steps 1 to 4 attention was only given to the magnitudes of the various physical variables. Since these variables have been described in the frequency domain and inference of the equivalent time domain response is required, their phases are crucially important. Before the steps of the algorithm are continued, the important phase relationships should be discussed.

Consider a transmitter antenna with an input impedance  $Z(f)$  excited by a perfect voltage source,  $V(f)$ . There exists a deterministic phase relationship between the

## CHAPTER 5: Pulse Recompression

excitation voltage and the electric field at any point in space. When the probed E-field is in the far-field of the antenna, the following phase relationship exists:

$$\angle E(f, r, \theta, \phi) = \angle H_{ev}(f, \theta, \phi) + \beta r + \angle V(f). \quad (5.7)$$

In (5.7) the  $e^{-i\omega t}$  time convention is used,  $\beta$  is the propagation constant as defined in Section 6.5 and  $H_{ev}(f, \theta, \phi)$  is a unity gain transfer function accounting for the phase response in addition to the spatially dependant phase delay. This latter is equivalent to the theoretical phase relationship between the far-field E-field at the transmitter and the excitation voltage. There exists a simple relationship between the phase of the excitation voltage and the associated feed current

$$\angle V(f) = \angle Z(f) + \angle I(f). \quad (5.8)$$

The phase relationship between the 'zero radial distance' far field E-field and the excitation current is therefore

$$\begin{aligned} \angle E(f, 0, \theta, \phi) &= \angle H_{ei}(f, \theta, \phi) + \angle I(f) \\ \angle H_{ei}(f, \theta, \phi) &= \angle H_{ev}(f, \theta, \phi) + \angle Z(f). \end{aligned} \quad (5.9)$$

In (5.9)  $H_{ei}(f, \theta, \phi)$  is a unity gain transfer function relating the phase of zero radial distance near field E-field to the excitation current's phase. In the case of the receiver antenna, the incident co-polarized (with the axis of the antenna) E-field induces a current on the feed segment when terminated with a load. Due to reciprocity, the phase relationship between the induced current and the incident E-field at the feedpoint of the antenna can be derived from (5.9) as

$$\angle I_{ind}(f) = \angle E_{rec}(f, 0, \theta, \phi) + \angle H_{ei}(f, \theta, \phi). \quad (5.10)$$

Consider the Norton equivalent circuit of the antenna connected to a load resistor  $R_{load}$ , Figure 5-1.

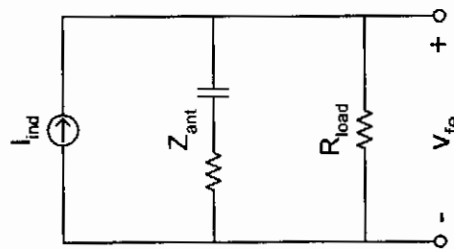


Figure 5-1: Norton equivalent circuit of receiver antenna connected to a resistive load.

Finally, the phase relationship between the voltage at the front-end of the receiver can be related to the incident E-field at the feedpoint

$$\angle V_{fe}(f) = \angle E_{rec}(f, 0, \theta, \phi) + \angle H_{ei}(f, \theta, \phi) + \angle \frac{R_{load} Z_{ant}(f)}{R_{load} + Z_{ant}(f)}. \quad (5.11)$$

The final steps of the algorithm to estimate the electric field from the voltage at the front-end of the receiver chain follow:

5. Calculate  $H_{ev}(f, \theta, \phi)$  using an analysis tool like FEKO and (5.7). This is done by the evaluation of the E-field at a known position in the far-field of the antenna.
6. Infer  $H_{ei}(f, \theta, \phi)$  from (5.9).
7. Calculate the phase of the discrete Fourier series representation of the co-polarized (with the axial direction of the antenna) electric field at the feedpoint of the antenna,  $\angle E_{\theta}(f, 0, \theta, \phi)$ , using (5.11).
8. Combine the magnitude and phase of the discrete Fourier series representation. Use the IDFT to find the time domain equivalent series of the co-polarized E-field at the feedpoint of the receiver,  $E_{\theta}(t_n)$ .

The results of this algorithm are presented in Section 5.5.

## 5.4 Windowing the Inferred and Estimated Responses

In the algorithm to estimate the electric field at the feedpoint of the receiver a number of multiplications with inverse transfer functions were carried out. The transmitted pulse has a limited bandwidth. If only the transfer function of the optic link, which has a degraded high frequency (> 200 MHz) response is considered, it is clear that the algorithm will attempt to raise the amplitude of the high frequency Fourier series coefficients. If these coefficients are merely noise, the time domain representation of the E-field will be contaminated with high-frequency noise. It is therefore necessary to filter the calculated coefficients of the E-field Fourier series. The proposed filter function is plotted in Figure 5-2.

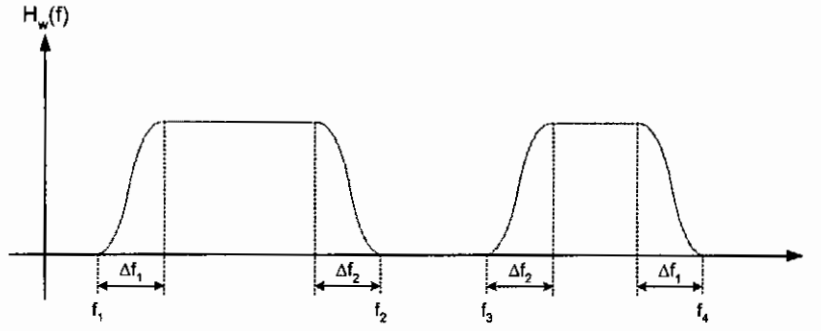


Figure 5-2: Window function in pulse recompression algorithm.

The digital filter is a zero phase, single bandpass filter combined with a notch filter that yields two bandpass filters. The rising and falling edges are realized as Hanning window functions with a given frequency span. The first cut-off frequency  $f_1$  is determined by the existence and relative amplitude of the unwanted low-frequency anomalies due to saturation of the amplifiers. The fourth cut-off frequency  $f_4$  is determined by the highest frequency with a given SNR. In Chapter 4 it was established that the ADC has a pseudo null in its digital transfer function at 62.5 MHz. The notch filter cut-off frequencies  $f_2$  and  $f_3$  are centred on this null. The width of the Hanning window's rising and falling edges,  $\Delta f_1$  and  $\Delta f_2$ , are determined by the depth of the pseudo null and the slope of the overall transfer functions respectively. When the pulse recompression algorithm is used, it is important to fine-tune these parameters to suit the specific configuration and SNR.

Knowing the system transfer function and the uncorrelated noise power spectral density, the Wiener filter can be used to reconstruct the input of the system. The Wiener filter is classified as an optimum linear system that minimizes the mean-squared error between the desired input signal and the actual input signal, which consists of the desired signal and noise [84], [85] - [87]. The sum of the signal and noise is denoted as

$$W(t) = X(t) + N(t) \quad (5.12)$$

and the optimal Wiener filter is given as

$$H_{opt}(\omega) = \frac{S_{XX}(\omega)}{S_{XX}(\omega) + S_{NN}(\omega)} \quad (5.13)$$

where  $S_{xx}(\omega)$  and  $S_{NN}(\omega)$  are the power spectral densities of  $X(t)$  and  $N(t)$  respectively. When the system transfer function  $G(\omega)$  is known, the Wiener filter yielding the optimal input signal to the system is given as

$$H_{opt}(\omega) = \frac{G^*(\omega)S_{XX}(\omega)}{|G(\omega)|^2 S_{XX}(\omega) + S_{NN}(\omega)}. \quad (5.14)$$

From (8.14) it can be seen that the Wiener filter is actually the inverse filter function  $G(\omega)^{-1}$  when  $|G(\omega)|^2 S_{XX}(\omega) \gg S_{NN}(\omega)$  and the matched filter  $k(\omega)G^*(\omega)$  when  $|G(\omega)|^2 S_{XX}(\omega) \ll S_{NN}(\omega)$ . The matched filter is also an optimum linear system that maximizes the signal-to-noise ratio [85]. It is clear that the pulse recompression algorithm described in Sections 5.2 to 5.3 is indeed the inverse filter function performed by the Wiener filter when  $|G(\omega)|^2 S_{XX}(\omega) \gg S_{NN}(\omega)$ . In the application of the Wiener filter to BHR, the processing has to be done as a function of range. This is due to the strong dependency of the SNR on range and frequency. However, this falls outside the scope of this dissertation and will not be discussed.

## 5.5 Preliminary Results

### 5.5.1 Laboratory Experiment

In the RCF, the calibration transmitter and reference receiver were deployed to estimate the power delivered to the TX antenna by the calibration transmitter (see Section 3.6.1). The resampled and time-gated digital voltage  $v_d$  and the estimated E-field, which illuminates the RX antenna,  $E_\theta$ , are plotted in Figure 5-3.

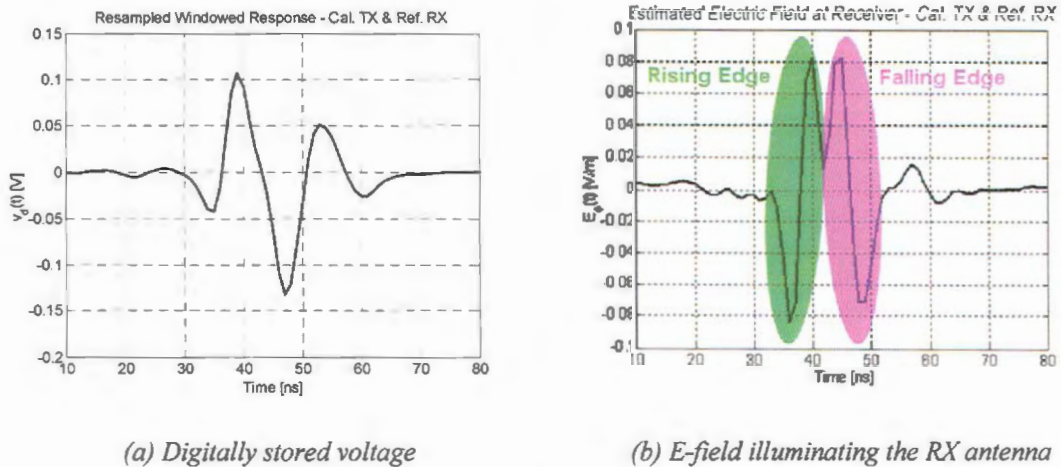


Figure 5-3: Deconvolution results for calibration transmitter and reference receiver.

The frequency domain window function parameters for these calculations and estimations were

$$f_1 = 20 \text{ MHz}, f_2 = 250 \text{ MHz}, \Delta f_1 = 5 \text{ MHz}. \quad (5.15)$$

## CHAPTER 5: Pulse Recompression

The digital notch parameters  $f_2$ ,  $f_3$  and  $\Delta f_2$  were omitted since the laboratory ADC did not have a transfer function null.

The digitally stored voltage in (a) closely resembles the 3<sup>rd</sup> time derivative of a Gaussian pulse. In this association the final tail is ignored, which might be artificial and due to secondary reflections in the RCF. When the E-field response was examined at first, the dip in the middle of the response seemed counterintuitive. Upon closer examination it was established that the response as a matter of fact is the E-field response of two distinct excitations. The first response (negative and positive peaks of equal amplitudes) is due to the rising edge of the voltage pulse at the input of the transmit antenna, while the second response (the inverse of the first) is due to the falling edge. These two responses are very close to the ideal response when a voltage pulse with finite rise and fall times excites a vertical electrical dipole (VED) – derivable from Ishimaru [43]. In this specific laboratory case, the pulse recompression algorithm resolved the responses of two excitations that were unresolved in the digitally stored voltage.

Consider another example of the results obtained with the pulse recompression algorithm where the calibration receiver was used to intercept the pulse radiated by one of the GeoMole transmitters (USTX 03). The frequency domain window function parameters for this example were

$$f_1 = 5\text{MHz} , f_4 = 250\text{MHz} , \Delta f_1 = 5\text{MHz}. \quad (5.16)$$

The results are plotted in Figure 5-4.

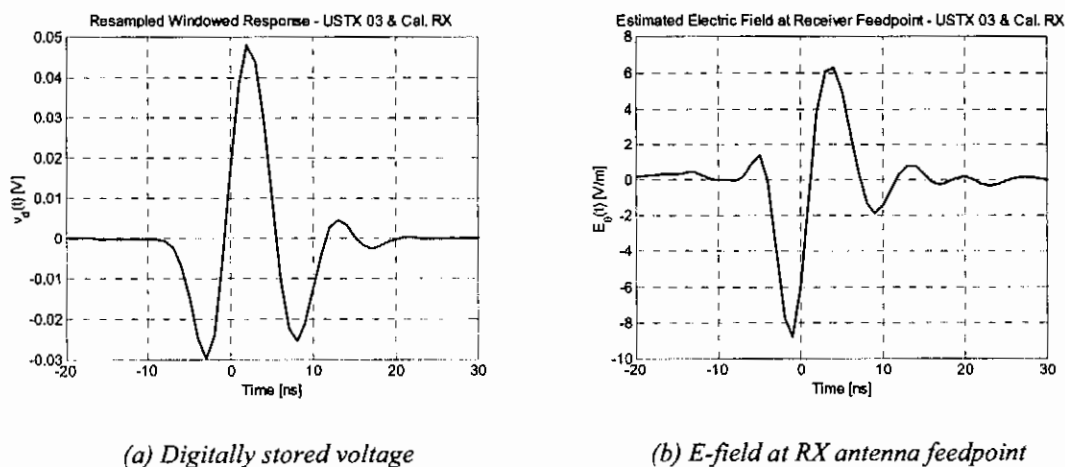


Figure 5-4: Deconvolution results for USTX 03 transmitter and reference receiver.

The captured waveform closely resembles the Ricker wavelet (second derivative of the Gaussian pulse). The estimated E-field has a shape very close to the first derivative of the Gaussian pulse or a monocycle. It is also close to the expected signal for a VED when excited by a voltage step of finite rise or fall time – similarly derivable from Ishimaru [43]. A very important observation is that the significant instantaneous power in the recompressed signal has a significantly shorter time span.

### 5.5.2 Field Experiment

The application of the pulse recompression algorithm to laboratory (controlled) measurements was described in the previous section. The real value of the algorithm lies in the application thereof to real-life field experiment data. A preliminary example of the results of this algorithm on field experimental data is presented in this section.

Consider the 1<sup>st</sup> cross-hole survey between holes 46 and 48 at Bleskop, 13 Level West Haulage (see Appendix F). The USTX 03 transmitter probe was located in hole 46 (air-filled) and the USRX 02 receiver probe was located in hole 48 (air-filled). The configuration of the optic link is given in Table 5-1.

Table 5-1: Optic link configuration for cross-hole survey between holes 46 and 48.

	Optic Modulator	RX Patchcord	Fibre Optic Cable	Coupling Patchcord	SMA Barrel	FORJ	DAQ Patchcord	SCU
ID	GM	USRX02	2	Current	Barrel 3	FORJ #2	None	DAQ2 CH2

The results of the algorithm are presented in Figure 5-5. The frequency domain window function parameters for this example are

$$\begin{aligned}
 f_1 = 5\text{MHz} , f_2 = 60\text{MHz} , f_3 = 65\text{MHz} , f_4 = 110\text{MHz} \\
 \Delta f_1 = 5\text{MHz} , \Delta f_2 = 5\text{MHz}.
 \end{aligned}
 \tag{5.17}$$

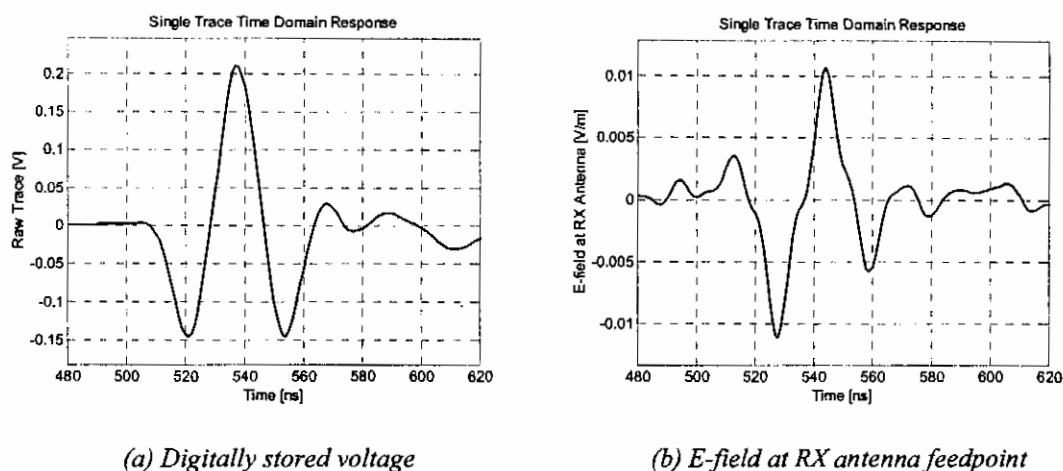


Figure 5-5: Deconvolution results for USTX 03 transmitter and USRX 02 receiver in a cross-hole configuration in a norite host medium.

The digitally stored voltage once again shows good correlation with the Ricker wavelet with equal negative sidelobes and a single main lobe. The estimated E-field has a stronger noise component than the digitally stored voltage, but clearly has a better resolution. It has the characteristic equal positive and negative lobes of the first derivative of a Gaussian pulse.

It is impossible however, to get an exact estimate of the E-field due to the complexity of the deployment and the unknown variables at play. A relatively small positive and a moderate negative sidelobe artefact are visible at the start and end of the estimated response. Even though these artefacts are created, the pulse recompression algorithm can play a significant role in the enhancement of the resolution of field experimental data, which has a positive impact on the accuracy of geometry delineation. It is also important to remember that this algorithm accentuates data of previously insignificant amplitude from the digitally stored voltage sequence. In essence it adds information not previously visible to the interpreter.

## 5.6 Field Experiment Pulse Recompression

Due to the series of convolutions inherent to the system, the recorded echoes are smeared in the time domain. These smeared time domain echoes have been used in the past for the delineation of the geometry in the BIC with specific attention to the UG1 – UG2 stratigraphy introduced in Chapter 6. Accurately mapping the geological defects, as defined in Section 6.2.4, is of crucial importance. The accuracy of mapping is ultimately determined by the resolution and SNR of the echoes.

In this section the developed pulse recompression algorithm is adapted for the batch processing of field experiment data.

### **5.6.1 Batch Pulse Recompression Algorithm**

In a field experiment a vast amount of data is captured. In a single profile of a 100 m borehole, more than 300 traces can be captured with an averaging factor of 512. As this factor decreases, the number of traces increases inversely proportional. It is therefore important to adapt the algorithm for operation on a matrix of data rather than on a single vector.

Fortunately MATLAB, the computing platform used, has been optimised for matrix operation and the algorithm was easily modified for matrix operations. The data field is fed in as a matrix with one dimension as the traces and the other dimension as time. The algorithm operates on the matrix and outputs the E-field matrix.

Furthermore, in a field experiment however the system is highly configurable. The system transfer function depends on the chosen radar configuration, the host rock, the media that fills the boreholes, the diameter of the boreholes and the specific set of components used for the experiment.

The pulse recompression algorithm developed, has to be modified to allow for a highly configurable system. In Chapter 4 the concept of reference and relative gain measurement was introduced and in Chapter 3 the transfer functions of the antennas in different deployment configurations were determined. This was combined in a graphic user interface (GUI) console to allow the operator to select the exact configuration used for the experiment. The underlying signal processor automatically calculates the system transfer function.

This GUI-based pulse recompression algorithm allows the user to import the captured data field. It resamples the data and stores it in a two-dimensional matrix. The next step is for the user to interactively set up the configuration of the experiment. The final step is to set up the parameters of the windowing function. The recompressed E-field can then be viewed, analysed or exported for use in other software packages. An added function of the GUI is the real-time update and display of the system transfer function, as well as the time or frequency domain response of a single trace in the data field. This allows for the interactive set-up of the filter and system parameters. The batch-processing pulse recompression GUI is briefly presented in Appendix G.

## 5.6.2 Field Experiment Results

The batch-processing algorithm introduced in the previous section and presented in Appendix G has been tested and applied to field experiment data with great success. A brief pictorial summary of the results obtained at different experimental sites is presented in this section.

### 5.6.2.1 Bleskop II Profiles

The estimated E-field data field for the GBH46 profile scan is plotted in Figure 5-6, while the configuration of the receiver chain in this experiment is given in Table 5-2.

Table 5-2: Receiver chain configuration for the GBH46 profile.

	Optic Modulator	RX Patchcord	Fibre Optic Cable	Coupling Patchcord	SMA Barrel	FORJ	DAQ Patchcord	SCU
ID	GM	USRX03	3 (New)	N/A	N/A	N/A	DAQ1 CH1	PH001

A 5 – 80 MHz digital zero-phase bandpass filter with 10 MHz Hanning window edges was used to form the reference data set, while the parameters for the window function in the pulse recompression algorithm was set to

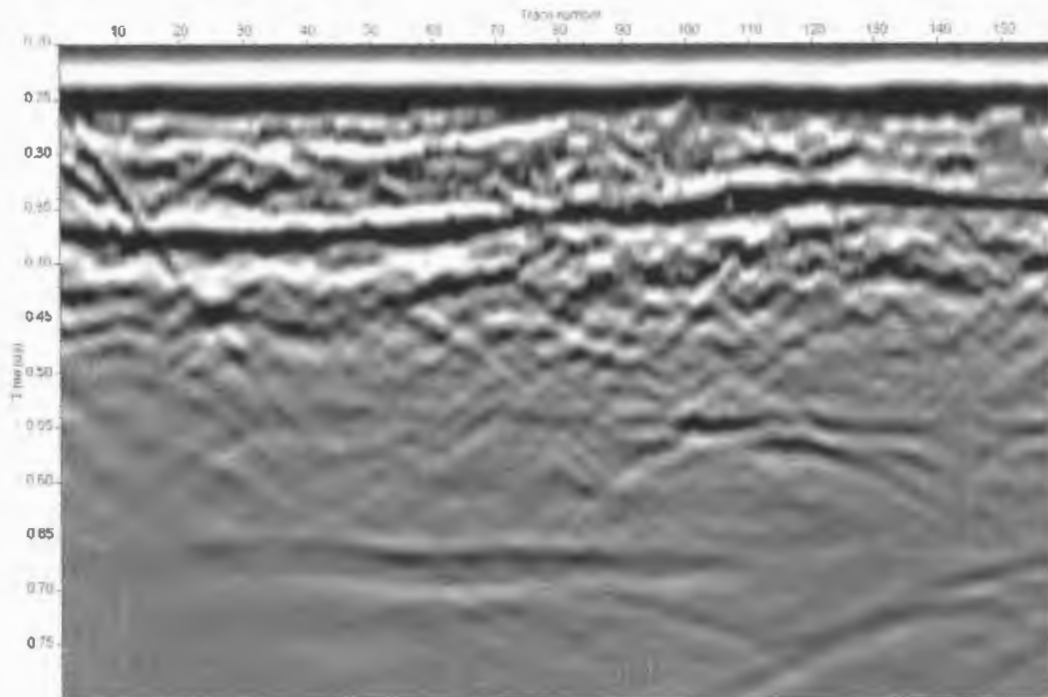
$$f_1 = 5 \text{ MHz} , f_2 = 60 \text{ MHz} , f_3 = 65 \text{ MHz} , f_4 = 100 \text{ MHz} \quad (5.18)$$

$$\Delta f_1 = 5 \text{ MHz} , \Delta f_2 = 5 \text{ MHz}.$$

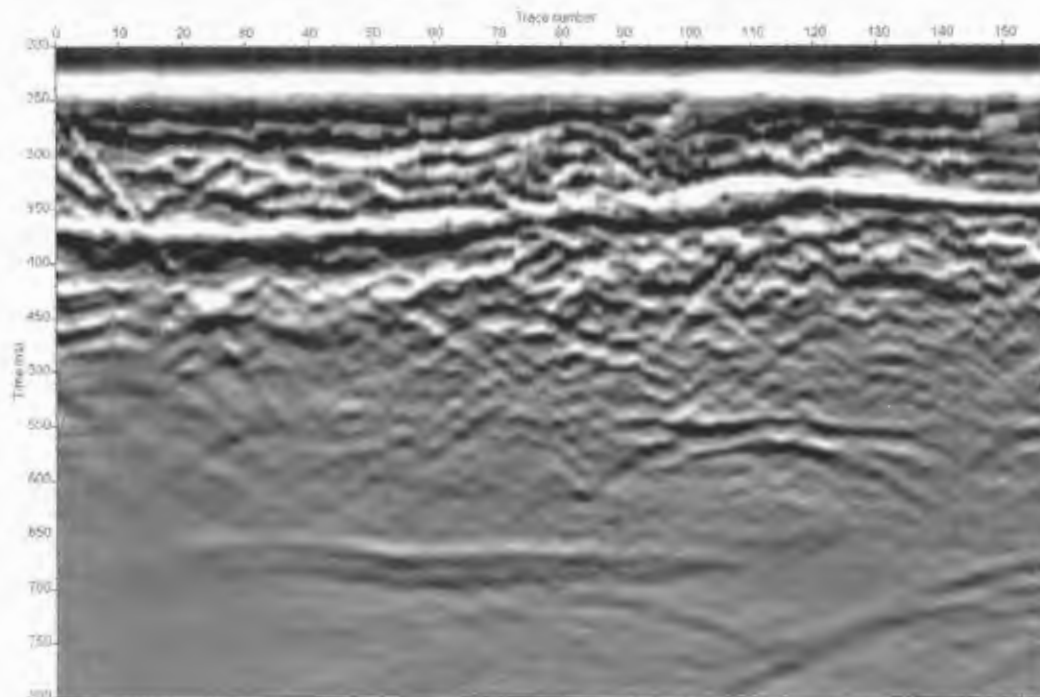
When the two data sets are compared the following observations can be made:

- The resolution of the echoes is more vivid and the pulse shape also changed from a Ricker wavelet to that of a monocycle wavelet (as defined in Section 8.2).
- More information is available to the interpreter, especially for the lower amplitude echoes. The larger echoes in the conventional signal processing algorithms, i.e. AGC and zero-phase filters, generally smear these echoes out. The pulse recompression algorithm resolves these echoes.
- The inherent bandpass filter in the algorithm removes the effects of saturation. This has to be done explicitly in standard processing algorithms.

## CHAPTER 5: Pulse Recompression



(a) Frequency domain bandpass filtered - GBH46 profile.



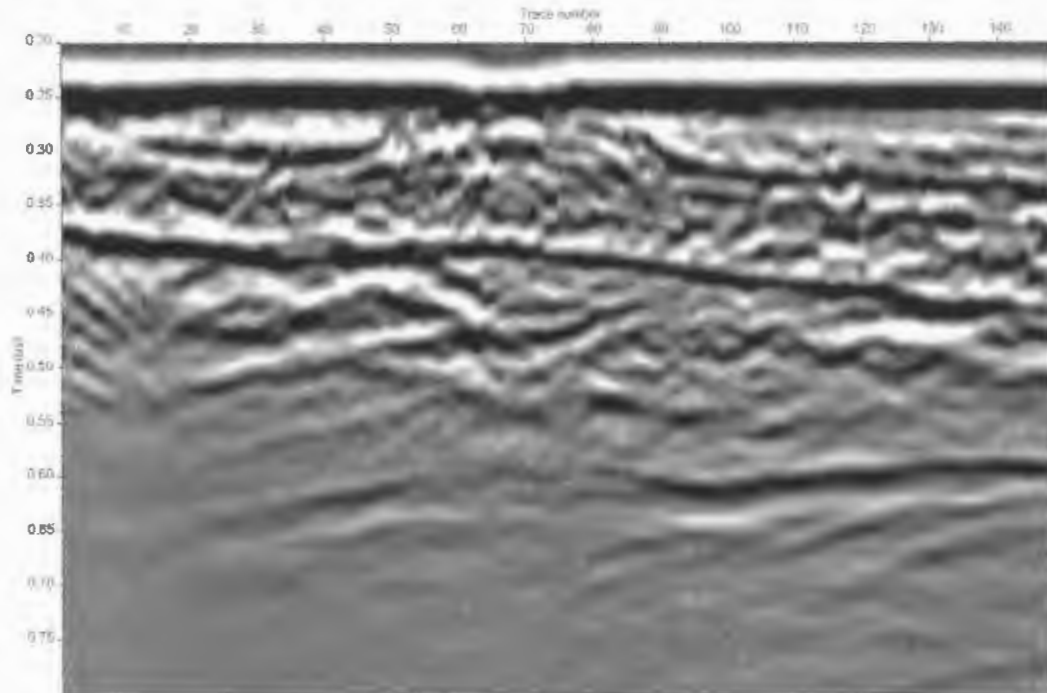
(b) E-field as estimated with pulse recompression algorithm - GBH46 profile.

Figure 5-6: Comparison of estimated E-field with bandpass filtered data – GHB46 profile.

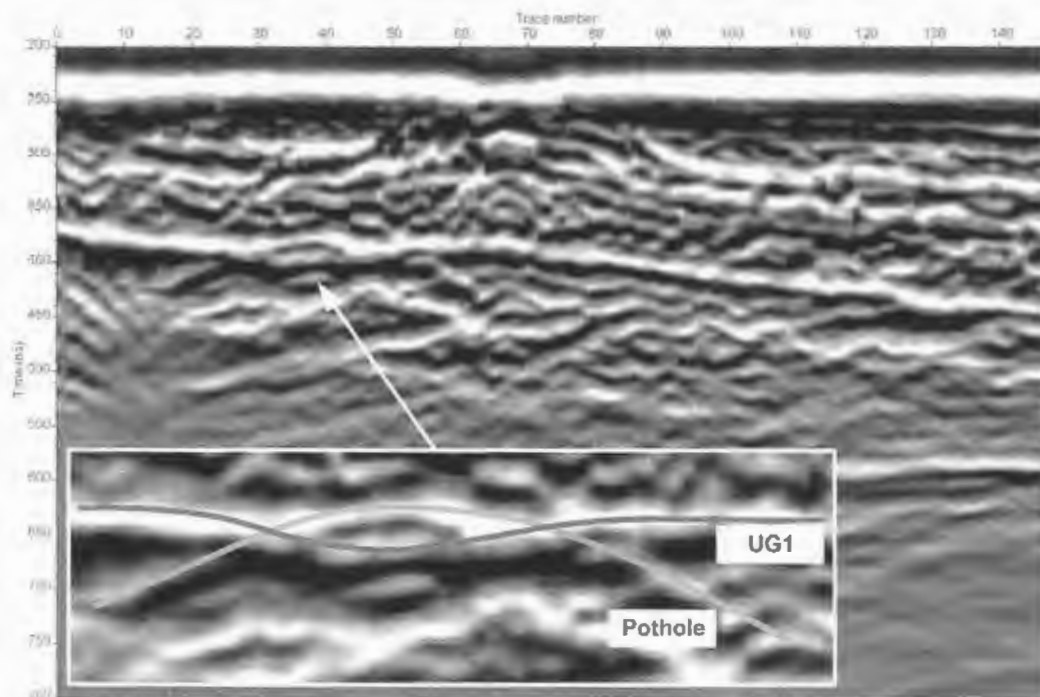
The estimated E-field data field for the GBH47 profile scan is plotted in Figure 5-7. The configuration of the receiver chain is the same as in Table 5-2 and the parameters of both processing techniques are the same as for the previous example. The same basic observation is made when the two data fields are compared. One significant example of the increased resolution and added information is highlighted in Figure

## CHAPTER 5: Pulse Recompression

5-7 (b). In the original data a smearing effect is clearly visible in the UG1 echo in the region about trace 40. In the recompressed data field, it is clear that this smeared echo is indeed the superposition of two echoes, which are resolved in the recompressed data. The one echo is that of the UG1 interface, while the other echo has the typical signature of a pothole or point-like target.



(a) Frequency domain bandpass filtered - GBH47 profile.

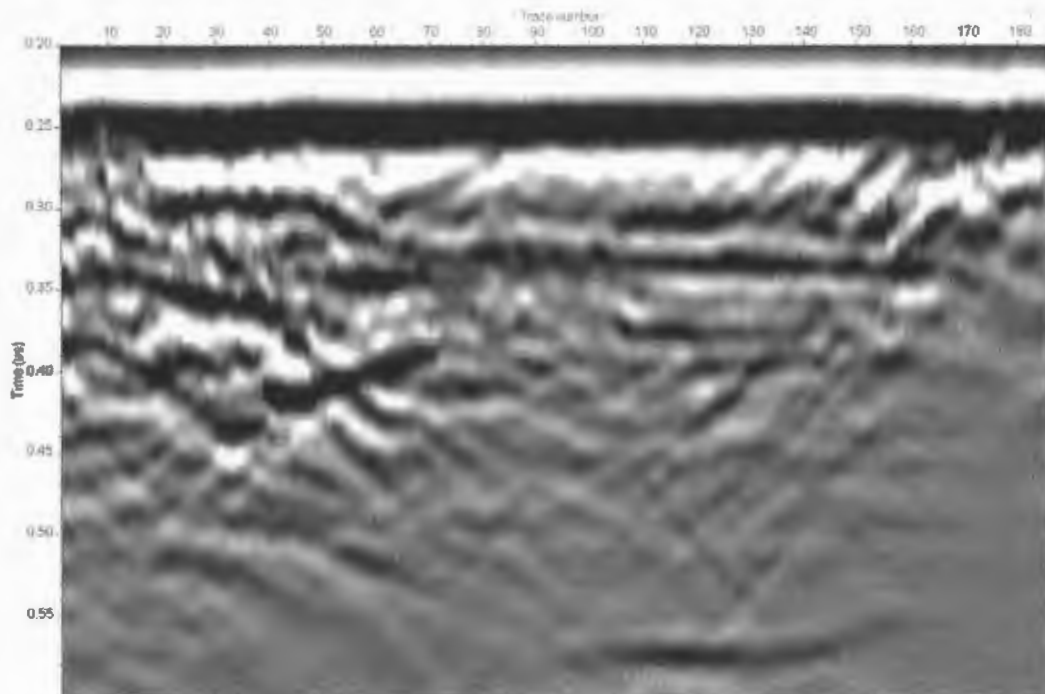


(b) E-field as estimated with pulse recompression algorithm - GBH47 profile.

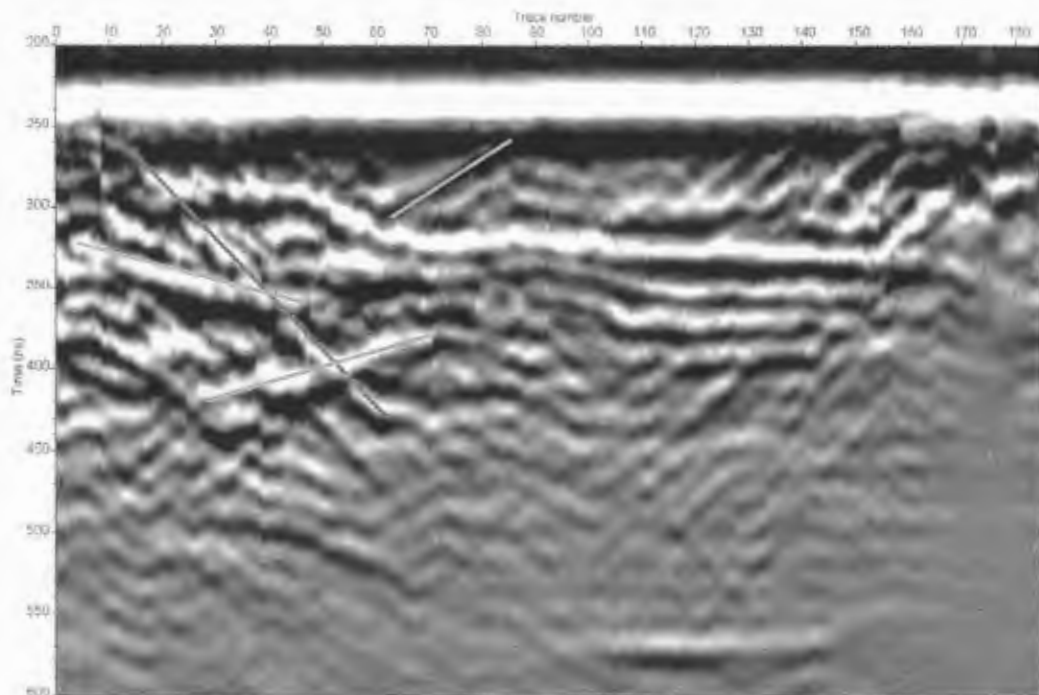
Figure 5-7: Comparison of estimated E-field with bandpass filtered data – GHB47 profile.

### 5.6.2.2 Brakspruit I Profile

The estimated E-field data field for the GBH2 profile scan at the Brakspruit I experiment (Appendix E) is plotted in Figure 5-8.



(a) Frequency domain bandpass filtered - GBH2 profile.



(b) E-field as estimated with pulse recompression algorithm - GBH2 profile.

Figure 5-8: Comparison of estimated E-field with bandpass filtered data – GHB2 profile. The configuration of the receiver chain in this experiment is given in Table 5-3.

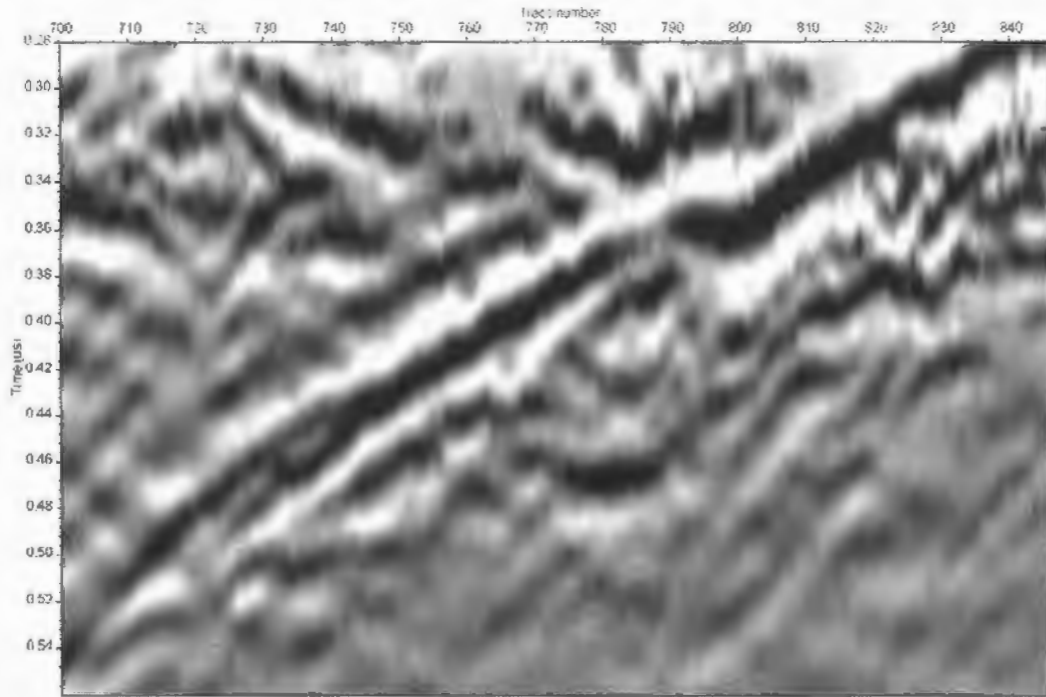
Table 5-3: Receiver chain configuration for the GBH2 profile.

	Optic Modulator	RX Patchcord	Fibre Optic Cable	Coupling Patchcord	SMA Barrel	FORJ	DAQ Patchcord	SCU
ID	GM	USRX01	?	N/A	N/A	N/A	DAQ1 CH1	GM CH1

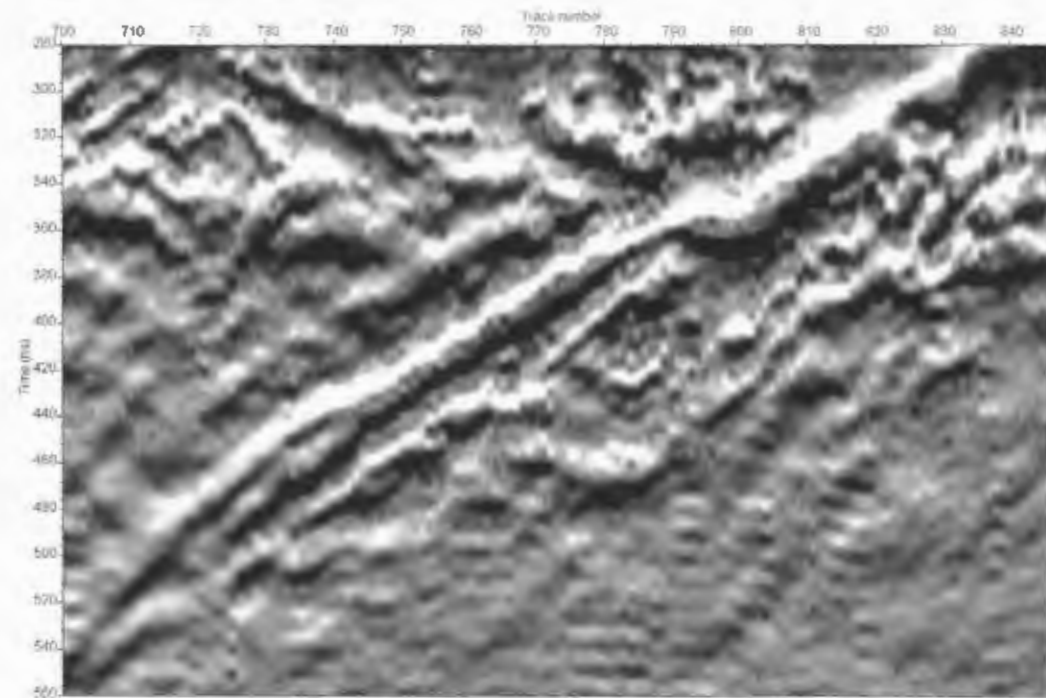
The parameters of both processing techniques are the same as for the previous two examples. The echoes in the E-field data field are more vivid than the original data and a number of echo signatures have been resolved. These signatures have been highlighted in the data field, Figure 5-8 (b).

### 5.6.2.3 Mponeng VCR Profile

Based on the significant results obtained with the pulse recompression algorithm on field experiment data in the BIC, it was decided to investigate the possible application of the algorithm in other geological settings. The GeoMole BHR system gained international recognition after the results obtained at the now famous LIB19B survey at the Mponeng gold mine in the Witwatersrand Basin, South Africa [5],[6] were published. The geological setting of the experiment can be approximated as a three layered system. The hanging wall consisted of the Venterspost lava, the footwall of quartzite and the sandwiched layer was the Ventersdorp Contact Reef (gold bearing). A long inclined borehole (LIB) was drilled in the footwall below the VCR. The E-field data field for a section of the profile of LIB19B is plotted in Figure 5-9. The RX antenna characteristics and transfer function had to be determined for this setting and were based on the measured dielectric properties of the footwall [38]. A generic configuration was chosen for the receiver chain, because the actual configuration was not logged. The pulse recompression algorithm focussed the echo signature of the VCR significantly. This sparked a renewed interest in the processing of the data obtained at this famous survey.



(a) Frequency domain bandpass filtered - LIB19B profile.



(b) E-field as estimated with pulse recompression algorithm - LIB19B profile.

Figure 5-9: Comparison of estimated E-field with bandpass filtered data – LIB19B profile.

## 5.7 Concluding Remarks

In this chapter an algorithm was proposed to reconstruct the voltage at the front-end of the receiver and to estimate the E-field at the feedpoint of the RX antenna from the digitally stored voltage sequence.

## CHAPTER 5: Pulse Recompression

This algorithm was tested on data from a number of laboratory experiments and the results obtained confirmed the validity of the algorithm. The estimated E-fields correlated with the expected E-fields for the different excitations. The algorithm was also tested on data from field experimental data. The algorithm succeeded in the compression of the received pulse and the estimation of the actual E-fields.

Based on the results presented in this chapter, it is evident that the batch-processing GUI-based pulse recompression algorithm can be used effectively in geometry delineation in the BIC and other geological settings, i.e. the Witwatersrand Basin. In the case of the BIC it was shown that the algorithm is not exclusive to a specific setting, but can be applied at the different mines in the Anglo Platinum Rustenburg Section.

The algorithm effectively recompresses the smeared echoes. The resolution of a single echo is increased, while the pulse shape is returned to its original form. The algorithm also has the capability to resolve echoes that have been superimposed on one another and appear smeared in the original data field.

One of the adverse effects of this algorithm is the addition of artefacts in the estimated E-field time domain trace. The positive traits (pulse recompression and pulse shape alteration) of the algorithm however justify the applicability of this algorithm as a tool for geometry delineation. Best results should be obtained if the estimated E-field data is used in conjunction with the digitally stored data.

# CHAPTER 6

## PROPAGATION IN THE ROCK STRATA OF THE UG1 – UG2 SYSTEM OF THE BUSHVELD IGNEOUS COMPLEX

The BIC of South Africa “... is host to one of the richest platinum group metals (PGM) deposits in the world,” [7]. It holds 75% of the world’s known PGM resources and produces 75% of the world’s platinum, 35% of the palladium as well as 75% of the rhodium. The enormous financial, political and environmental impact of this resource speaks for itself and sound management is of unprecedented importance.

A thorough knowledge base is an important prerequisite. The discovery, geological setting, ore-forming events of the BIC and the stratigraphical variations of it have been discussed extensively in the literature, e.g. [28]-[31]. This first part of this chapter briefly introduces layered complexes and gives an overview of the BIC, in particular the stratigraphy sandwiched between the upper group 1 (UG1) and upper group 2 (UG2) economic horizons.

Proper knowledge of the propagation of EM radiowaves at VHF frequencies in a homogeneous, isotropic and linear lossy medium is a prerequisite for the study of radiowave propagation in a stratified system like the BIC.

This latter part of this chapter is dedicated to the study of propagation conditions in the host media in the BIC. The most important parameters of a propagating EM wave in a lossy dielectric are its propagation velocity and rate of attenuation due to dielectric loss mechanisms. These parameters have been measured for core samples of the various rock layers, but will be determined on a macroscopic level from actual recorded data obtained from various field experiments.

### 6.1 Literature Review

Before propagation in a specific environment can be studied, it has to be understood. Cawthorn [28] presents a very good overview of the discovery of the platiniferous Merensky reef in the BIC. Schweitzer *et al.* [31] discuss the economic potential of the

Rooiberg Group (volcanic rocks in the floor and roof of the BIC), giving detailed attention to the different mineralising events. Viring *et al.* [29] carried out a detailed study on the geology and stratigraphy of the BIC from the UG1 footwall to the Bastard Reef. These authors also performed a primary, secondary and tertiary classification of potholes in the BIC. Lomberg *et al.* [30] presents an in-depth study on the morphology of potholes in the UG2 chromitite layer and Merensky reef. Useful information with regard to this was also found at a variety of internet websites of high integrity [7],[32] - [34]. These websites are mastered by platinum producing or processing companies and research institutes (e.g. University of Witwatersrand, South Africa).

Hollender and Tillard [35] state the importance of knowing the dielectric properties of the propagating medium before making any predictions on the propagation itself. A variety of models can be found on the dielectric properties of media. Jonscher [36] presents a formulation that accurately models dielectric properties in the frequency range and geology of interest. Olhoeft [37] summarizes the important electric and magnetic properties that govern the performance of GPR. Rütshlin [38], [39] did pioneering work on the measurement of the dielectric properties of rocks found in the BIC.

## **6.2 Geology of the BIC UG1 – UG2 Stratigraphy**

The BIC has been classified as one of eight known layered chromium-platinum igneous complexes on earth. The basic geology of this complex will be discussed in this section.

### **6.2.1 Layered Cr-Pt Complexes**

Layered chromium-platinum complexes ... *occur in a plutonic igneous setting and appear to be intruded into a more or less stable craton* [32]. The economically important ones are mostly Proterozoic (1.9 gigayears) in age. Viewed in cross-section, the majority of them appear as inverted funnels, are massive in size and easily cover thousands of square kilometres. Eight layered igneous (formed by the solidification of magma) complexes have been identified in the world, of which three

have economically significant chromium. Only the Great Dyke (Zimbabwe) and the BIC are mined for chromium, while platinum is only mined in the latter.

These geological systems ... *seem to have been intruded into tectonically stable portions of the crust of the earth with little synkinematic or postkinematic deformation* [32]. Peridotites, dunites and anorthosites are found at the base of the complexes, ... *grading upward in gabbro and occasionally diorite* [32]. On the topside of the complexes, granite that is significantly younger is usually found. Chromite is only found in the bottom section, while platinum is associated with a few sulphide-rich chromite bands.

Two different types of rock layering are found. The repetitious oscillation from rock type to rock type is defined as rhythmic layering, while the systematic variation of certain elements (e.g. magnesium) is defined as cryptic layering.

## **6.2.2 Bushveld Igneous Complex**

The BIC ...*can be compared to an enormous, irregularly-shaped saucer 370 kilometres across, with its centre buried deep underground, but its rim exposed* [33]. It is a ... *composite body intruding into the Proterozoic sedimentary rocks of the Transvaal Supergroup and overlying Rooiberg Lavas, which themselves lie on a basement of Archean granite and gneiss* [32]. Younger sediments of the Paleozoic Karoo Supergroup overlie the central portion of the complex, which consists of the lower mafic/ultramafic group and the overlying Bushveld Granites. The lower mafic/ultramafic series is a composite of four intrusives (mineralising events) [31],[32]. Figure 6-1 is a simplified geological map of the BIC, including the mafic (Rustenburg Layered Suite) and felsic phases (Lebowa Granite Suite).

The mafic/ultramafic rocks host all chromite-platinum horizons and can be subdivided into four zones. Interlayered peridotite and pyroxenite are found in the lower Basal Zone. A chromitite layer defines the transient to the overlying Critical Zone, which consists of ... *repetitive thin layers of dunite, pyroxenite, anorthosite and chromite as well as several platinum-bearing horizons* [32]. The Merensky Reef tops the Critical Zone that is succeeded by the overlying Main Zone and the Upper Zone. Platinum is closely associated with chromite seams and appears to be concentrated beneath anorthosite layers. The Merensky and UG2 reefs (both in the Critical Zone) that

occur around the eastern and western sides of the BIC are deemed to be the principal PGM-bearing reefs.

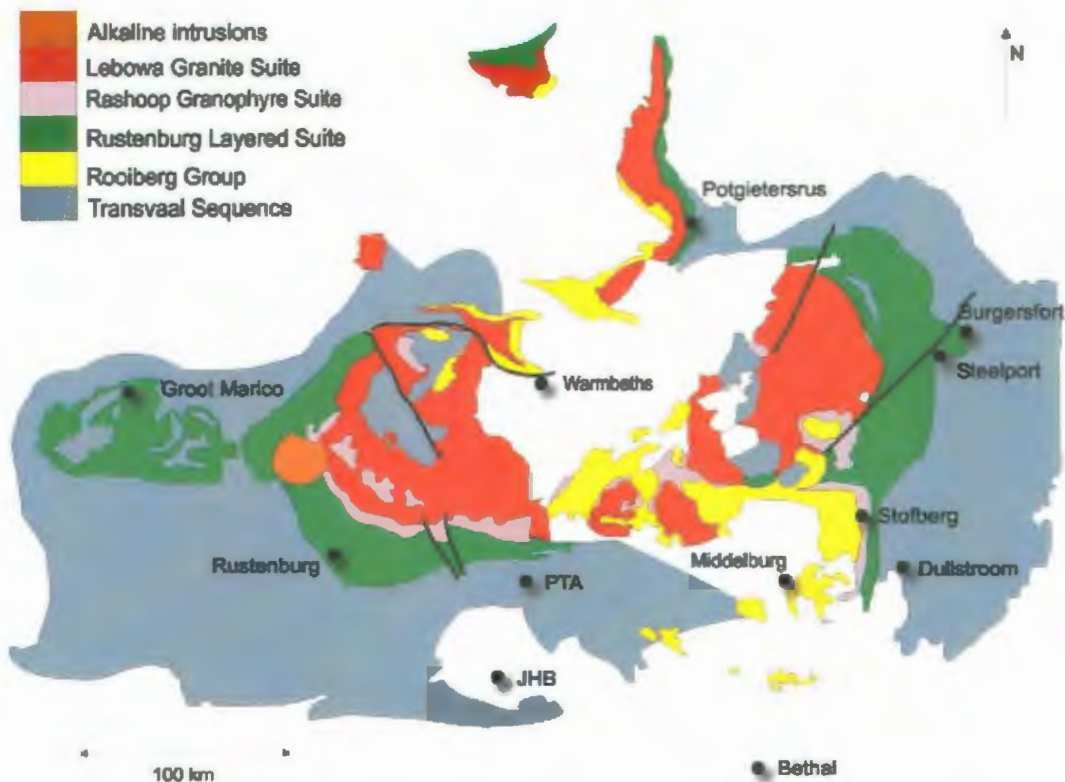


Figure 6-1: Geological map of the Bushveld Igneous Complex [34].

Until 1970, the Merensky Reef was by far the principal source of PGM since its discovery in 1925 by Lombaard and Merensky [28]. The other reefs, however, have grown considerably in importance. In the 1970's the exploitation of the UG2 began and increased steadily to produce 42% of the ore processed in 1999 [33].

### 6.2.3 Generalization of UG1 – UG2 Stratigraphy

For delineation of the UG2 chromitite reef by borehole radar, the important section of the critical zone is the stratigraphy between the UG1 chromitite layers and the UG2 chromitite reef<sup>3</sup>. In general, boreholes (whether for cover, exploration or specifically for BHR) are drilled into the rock from haulages, raises, winzes and stopes. The collars of these boreholes are usually within the UG1 - UG2 column with the

<sup>3</sup> Under certain circumstances it may be advantageous to deploy borehole radar in the hangingwall, i.e. above the UG2 reef. However, this dissertation deals exclusively with deployment between the UG1 and UG2. The relatively homogeneous host rock between these two reefs is semi-translucent to radiowaves in the HF/VHF range [94].

CHAPTER 6: Propagation in the Rock Strata of the UG1 – UG2 System

trajectory in a upwards, horizontal or downwards direction. The entire borehole is generally within this column, but sometimes intrudes into the layers immediately above or below.

Even though some of the layers might vary considerably in occurrence and thickness from site to site, the general UG1 – UG2 stratigraphy of the sites used for the field experiments discussed in this dissertation is depicted in Figure 6-2.

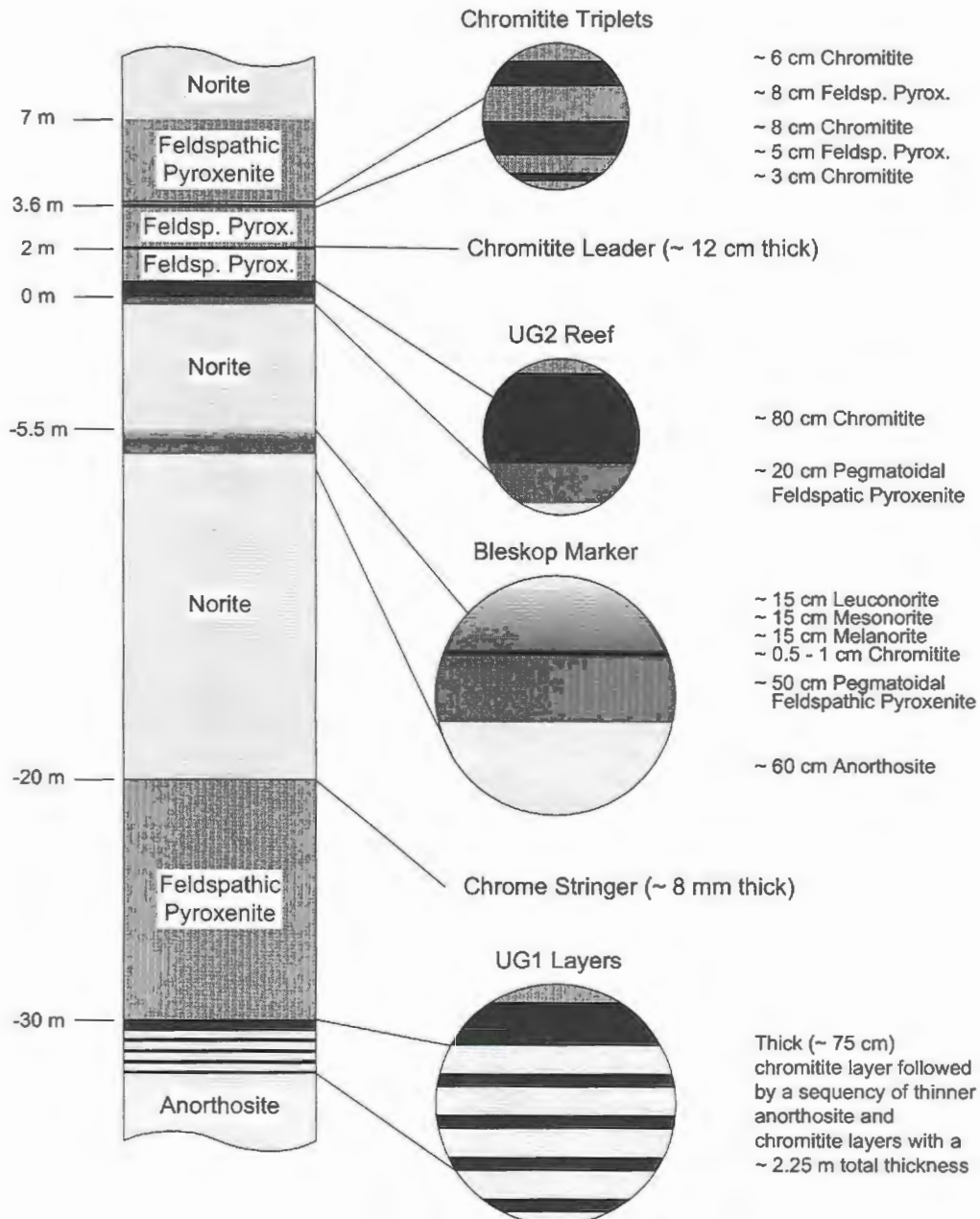


Figure 6-2: Stratigraphic column of UG1 - UG2 layering at RPM's Bleskop Mine<sup>4</sup>.

<sup>4</sup> At the adjacent Brakspruit mine the Bleskop Marker is absent and the UG1 – UG2 spacing is  $20 \pm m$ .

CHAPTER 6: Propagation in the Rock Strata of the UG1 – UG2 System

Below the UG1 layers we have a thick layer of anorthosite. The UG1 chromitite layers consist of between 4 to 8 chromitite layers of variable thickness. In general, the top layer is approximately 75 cm with the other layers relatively thin, approximately 10 cm. Anorthosite layers are sandwiched between these layers, as depicted in Figure 6-3. A 10 m layer of homogeneous feldspathic pyroxenite caps the top UG1 layer. Above this pyroxenite layer is a 13 m layer of norite. Between these two layers is a very thin (approximately 8 mm) layer of chromitite, as shown Figure 6-4, which is not always present. This layer is not an economically viable source of chromitite.

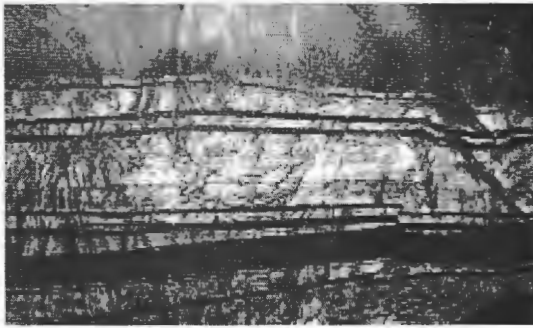


Figure 6-3: UG1 chromitite layers (Courtesy of K. Chotoki, Anglo Platinum).



Figure 6-4: Single chromitite stringer (Courtesy of K. Chotoki, Anglo Platinum).

Above the 13 m of norite we find the Bleskop marker, a unique sequence of layers approximately 1.5 m thick [88], Figure 6-5.

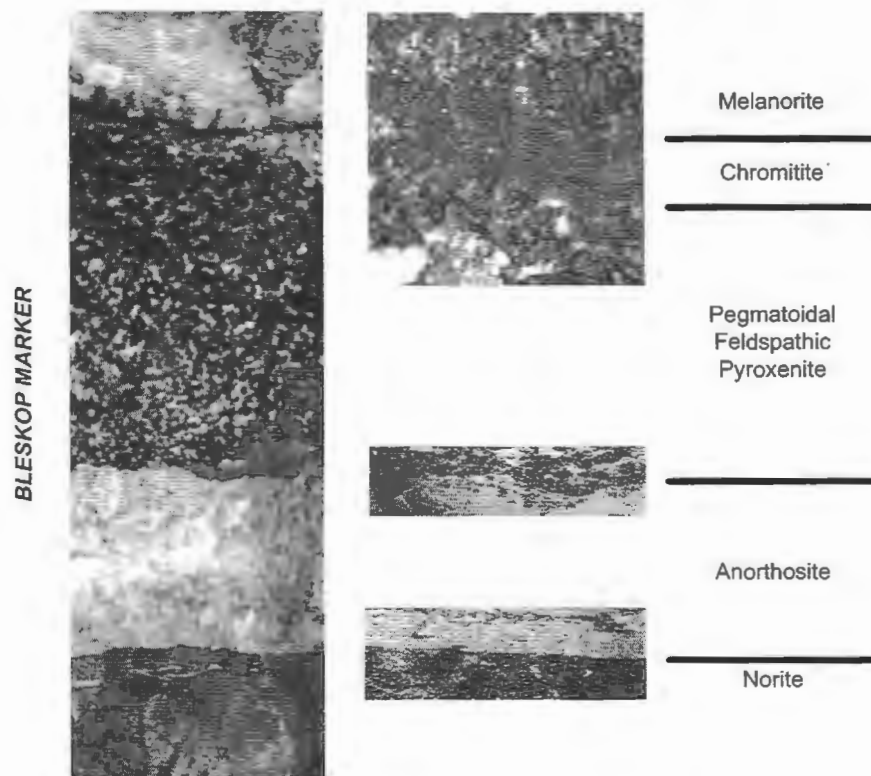
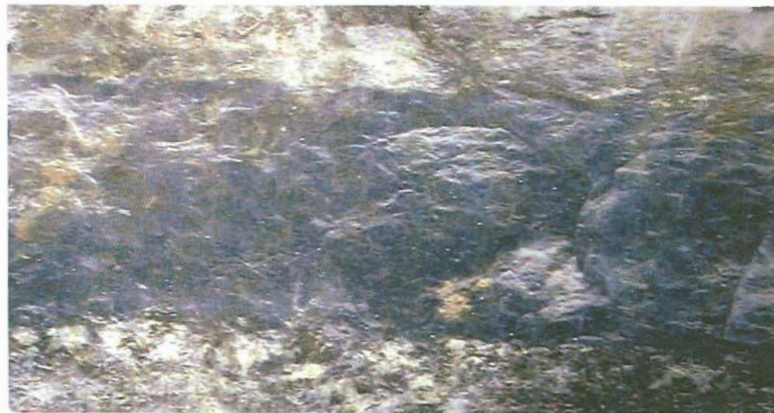


Figure 6-5: Bleskop marker sequence.

## CHAPTER 6: Propagation in the Rock Strata of the UG1 – UG2 System

It is highly variable, both in the thickness of the layers and in the presence or absence of certain rock strata. At the Bleskop shaft of Anglo Platinum's Rustenburg Platinum Mines (RPM)<sup>5</sup>, the pegmatoidal feldspathic pyroxenite is in direct contact with the anorthosite. At other sites however, there is an additional norite layer of 4 m between these two layers. At the bottom of the Bleskop marker is a 60 cm layer of anorthosite (whitish rock), topped by a 50 cm layer of pegmatoidal feldspathic pyroxenite (gray rock with white inclusions). A very thin 5 – 10 mm chromitite seam follows. A 45 cm layer of norite tops the Bleskop marker with 80 % pyroxenite at the base (melanorite – dark in colour), gradually becoming a 90 % anorthosite (leuconorite – whitish in colour). The transitional zone is called mesonorite.

Above the Bleskop marker is a 4 – 6 m thick norite layer, forming the base of the UG2 chromitite reef. At the base of the UG2 reef is a thin (20 cm, but up to 50 cm), highly variant layer of pegmatoidal feldspathic pyroxenite. The UG2 chromitite layer is rather stable with the exception of potholes, rolls, etc. as discussed in Section 6.2.4. It is approximately 80 cm thick, but can reach a thickness of 110 cm.



*Figure 6-6: UG2 chromitite reef.*

Above the UG2 chromitite reef is a 6 – 7 m thick layer of feldspathic pyroxenite. In this layer we find another 12 cm thick chromitite layer, the leader, as well as the chromitite triplets consisting of three thin layers of chromitite. The height of the leader and triplets above the UG2 reef is highly variable.

---

<sup>5</sup> Now known as Rustenburg Section, but for convenience the abbreviation RPM will be used.



Figure 6-7: Chromitite leader.

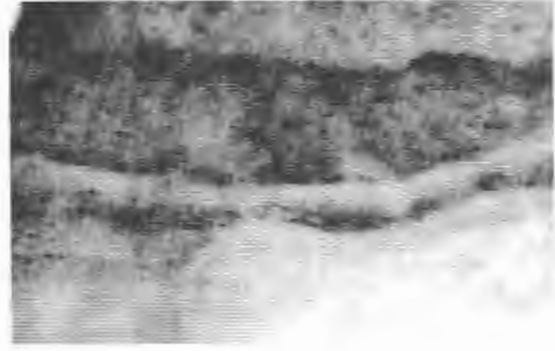


Figure 6-8: Chromitite triplets.

It should be noted that this is a generalized UG1 – UG2 stratigraphy and highly variable from site to site [30],[88].

### 6.2.4 Geometry of Perturbations

Generally the UG2 chromitite layer is regular with respect to dip, strike and thickness [30]. Local changes in dip, strike and thickness occur and are associated with rolls, potholes and xenoliths as indicated in Figure 6-9.

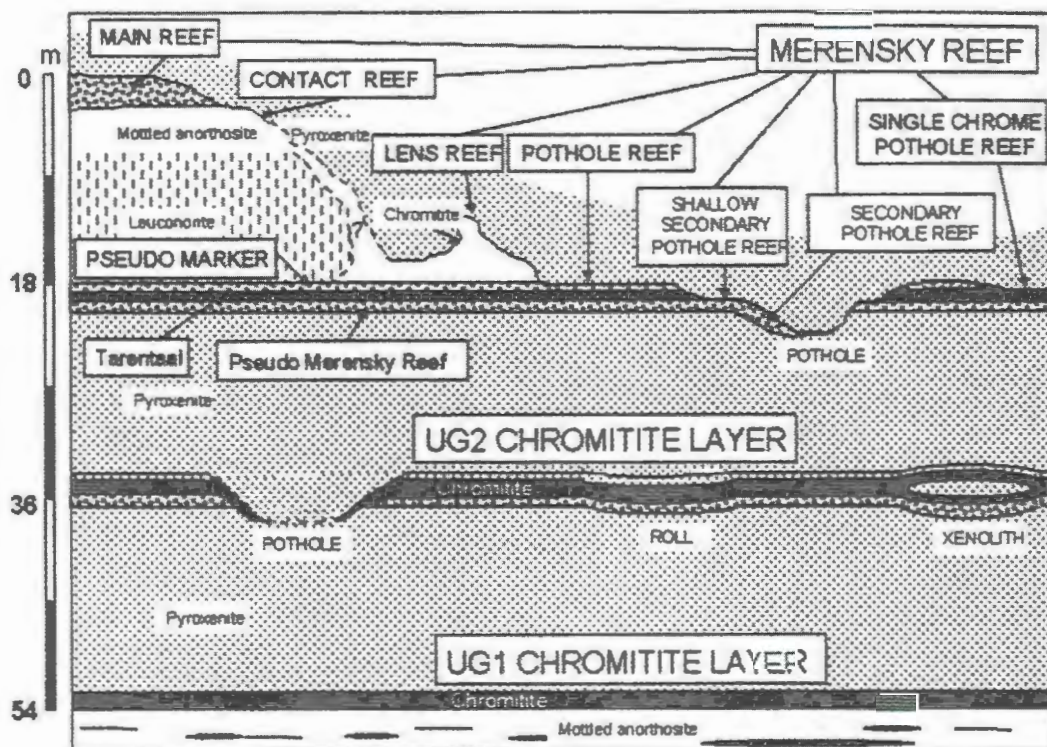


Figure 6-9: Schematic dip section demonstrating local changes in dip, strike and thickness [30].

In these local areas the leader chromitites and the main seam form wavelike structures. A roll is a feature where there is a small change in the dip and strike angle and may take on the form of a monocline or a depression. The roll may be as much as 1 m deep with an extent of 10 – 30 m in general [30]. Potholes are truly fascinating

structures and more disruptive than rolls [91]. They are characterized by the ... *upper leader chromitite suddenly transgressing the lower leader chromitites and then transgressing the whole main chromitite and cutting sharply into the underlying feldspathic pyroxenite* [30]. The lateral extent of these transgressions is 2 – 5 m. Inside a pothole the UG2 chromitite seam is poorly developed with an average thickness of  $\pm 20$  cm. The base of these potholes can drop several metres below the normal reef elevation. Potholes in the UG2 are usually circular or almost circular in plan and  $\pm 30$  m in diameter. In some cases the disruption of the underlying Bleskop marker has also been noted. This is a very simplistic description. Vos [91] thoroughly investigated the different types of potholes and divided UG2 potholes in two basic categories – shallow and carrot-like deep potholes. The distribution of these potholes is highly irregular, but they are frequently concentrated in clusters. UG2 potholes cannot be mined because of their lateral extent, sharp transgression and poor reef development.

### **6.3 Simplified Planar Model Approximation**

The UG1 – UG2 stratigraphy can be simplified for basic theoretical predictions and numerical simulations of radiowave propagation by a first order planarly layered approximation. In general, all the layers encountered are planar on the scale of wavelengths at VHF frequencies. They generally have the same dip and strike angle, where the dip angle is the elevation angle and the strike angle is perpendicular to the compass direction of the dip. Deviations from planarity occur mainly when local disturbances are encountered, macroscopic scale migration of layers occurs, layers are terminated or a combination of these mechanisms are encountered. In the absence of local disturbances it is possible to approximate the stratigraphy locally by a planar model, i.e. a finite sequence of planar slabs of finite thickness. Since their dip and strike angles are similar, the axis can be rotated so that they are horizontally planar.

Based on the generalized UG1 – UG2 stratigraphy in Figure 6-2 (also [90]) and the dielectric property measurements in Section 6.4, the following sequence of layers is used to approximate the UG1 – UG2 stratigraphy:

CHAPTER 6: Propagation in the Rock Strata of the UG1 – UG2 System

Table 6-1: Simplified planar UG1 - UG2 stratigraphy at Bleskop.

Horizon	Rock Type	Dielectric Properties	Thickness	
Hanging Wall	Norite	Approx. as Norite	$\infty$	
Hanging Wall	Feldspathic Pyroxenite	Approx. as PX2	3.1 m	
	Chromitite	Approx. as Leader	0.06 m	
	Feldspathic Pyroxenite	Approx. as PX2	0.08 m	
	Chromitite	Approx. as Leader	0.08 m	
	Feldspathic Pyroxenite	Approx. as PX2	0.05 m	
	Chromitite	Approx. as Leader	0.03 m	
Host	Feldspathic Pyroxenite	Measured as PX 2	1.48 m	
	Chromitite	Measured as Leader	0.12 m	
Host	Feldspathic Pyroxenite	Measured as PX 1	1.2 m	
	Chromitite	Measured as UG2 Top	0.4 m	
	Chromitite	Measured as UG2 Bottom	0.4 m	
	Pegm. Feldsp. Pyroxenite	Approx. as PX 1	0.2 m	
Host	Norite	Measured as Norite	5.3 m	
Bleskop Marker	Leuconorite	Approx. as Norite	0.15 m	
	Mesonorite	Approx. as Norite	0.15 m	
	Melanorite	Approx. as PX 1	0.15 m	
	Chromitite	Approx. as UG2 Top	0.01 m	
	Pegm. Feldsp. Pyroxenite	Approx. as PX 1	0.5 m	
	Anorthosite	Approx. as Norite	0.6 m	
Host	Norite	Approx. as Norite	12.94 m	
	Chromitite	Approx. as UG2 Top	0.008 m	
Host	Feldspathic Pyroxenite	Approx. as PX 1	10 m	
	Chromitite	Approx. as UG2 Top	0.75 m	
	4 X	Anorthosite	Approx. as Norite	30 cm
		Chromitite	Approx. as UG2 Top	10 cm
Footwall	Anorthosite	Approx. as Norite	$\infty$	

This approximated planar model, consisting of 31 layers and two half-spaces, can now be used for theoretical predictions and numerical simulations.

## 6.4 Dielectric Properties of Rocks

Radiowave propagation in any medium is governed by its electromagnetic properties. These determine the propagation velocity, attenuation and dispersion of an EM wave. Any host to EM wave propagation can be classified as either magnetic or non-magnetic. Furthermore it can be classified as being lossy or lossless. For a homogeneous, isotropic, linear and non-magnetic material, the dielectric permittivity determines all radiowave propagation properties. It is therefore essential to find the dielectric permittivity of the different layers in a stratified system before any predictions can be made on propagation in the stratified system [35],[38],[48].

In the generalized UG1 – UG2 stratigraphy of the BIC, there are in essence only eight distinctive rock types. It is important to find accurate estimates of the propagation properties of these different rocks. Fortunately the eight layers in the UG1 – UG2 column are essentially non-magnetic and only the dielectric permittivity of these rocks needs to be found.

Rütschlin measured the dielectric permittivities of the norites, pyroxenites and chromitites using a Marconi measurement device [38], [39]. A parallel plate capacitor technique was used to accurately (less than 5% error margin) measure the propagation and attenuation constants in the 1 – 30 MHz frequency range. These measurements were done on thinly sliced core samples extracted while drilling the boreholes. Accurate radiowave propagation predictions for a baseband radar with 100 MHz bandwidth can only be made if the propagation properties of the host media in the frequency range of interest is known. Since the measured properties are only known up to 30 MHz, an extrapolation model has to be used to accurately predict the propagation properties up to 100 MHz. Various models can be found in the literature [35]. In the megahertz frequency range and for rock types such as those encountered in the BIC, the Jonscher formulation approximates the electromagnetic behaviour of a non-magnetic material quite accurately [35], [36]. The empirical model only needs three real, constant parameters ( $\epsilon_0$ ,  $\epsilon_\infty$  and  $\chi_r$ ) to completely model the EM behaviour. The complex permittivity is expressed in terms of these three variables

$$\tilde{\epsilon}(\omega) = \epsilon_0 \chi_r \left( \frac{\omega}{\omega_r} \right)^{n-1} \left[ 1 + i \cot \left( \frac{n\pi}{2} \right) \right] + \epsilon_\infty \quad (6.1)$$

CHAPTER 6: Propagation in the Rock Strata of the UG1 – UG2 System

where  $\omega_r = 2\pi f_r$  is an arbitrary radial frequency constant. Equation (6.1) is not valid as  $\omega \rightarrow 0$  due to the singularity at  $\omega = 0$  and an imaginary term with another singularity at  $\omega = 0$  that have been omitted in (6.1) [35]. With the complex permittivity known at a number of frequency points, the three parameters can be found using a least square error numerical method. These parameters have been found [39] for the norites, pyroxenites and chromitites and are summarized in Table 6-2.

Table 6-2: Jonscher parameters for BIC rocks [39].

Rock Type	Location	Frequency (MHz)	$\alpha$	$\beta$	$\tau$
Norite	Beneath UG2	20 MHz	0.49	0.29	6.81
Pyroxenite	Between triplets and leader	20 MHz	0.52	0.35	5.7
Pyroxenite	Between leader and UG2	20 MHz	0.48	0.47	7.05
Chromitite	Leader	20 MHz	0.43	0.37	9.43
Chromitite	Top part of UG2	20 MHz	0.53	1.6	10.16
Chromitite	Bottom part of UG2	20 MHz	0.52	0.72	8.31

Two pyroxenite and three chromitite samples were measured. It was found that the dielectric properties of the UG2 chromitite layer are not constant across the entire seam and it was therefore split up in a bottom and top section. It has been confirmed that the base of the UG2 chromitite reef is usually more feldspathic [29]. There is a clear distinction between the properties of the chromitite-bearing layers and the other layers. The extrapolated complex permittivity for these layers was calculated using (6.1) and Table 6-2. The real part of the complex permittivity mainly determines (under certain conditions) the propagation velocity of EM waves in the host medium. In Figure 6-10 and Figure 6-11, the real parts of the complex permittivity and the propagation velocities are plotted as a function of frequency for the different rock types.

## CHAPTER 6: Propagation in the Rock Strata of the UG1 – UG2 System

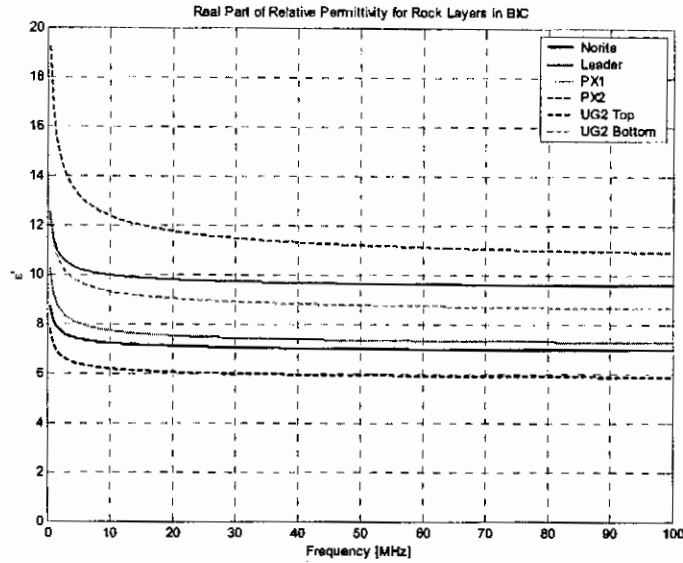


Figure 6-10: Real part of normalized dielectric permittivity for BIC rocks.

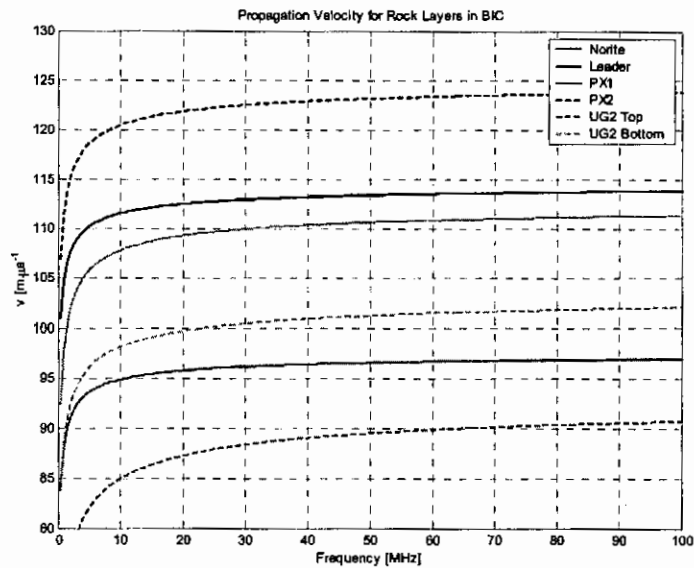


Figure 6-11: Propagation velocity for rock layers in BIC.

From these plots it is clear that the chromitite layers are electromagnetically denser than the pyroxenites and norites, where the propagation velocity for the chromitites are approximately  $96 \text{ m.}\mu\text{s}^{-1}$  and approximately  $113 \text{ m.}\mu\text{s}^{-1}$  for the norites and pyroxenites. The pyroxenite between the triplets and the leader is the least dense medium with a propagation velocity of  $123 \text{ m.}\mu\text{s}^{-1}$  – assuming the measured data [39] to be correct.

The quality factor of a dielectric medium is a measure of the opacity of the medium for EM radiowaves at the given frequency and is the mathematical quotient of the real

and imaginary parts of the complex permittivity (see Section 7.2). The quality factor for the various rock layers in the BIC is plotted as a function of frequency in Figure 6-12.

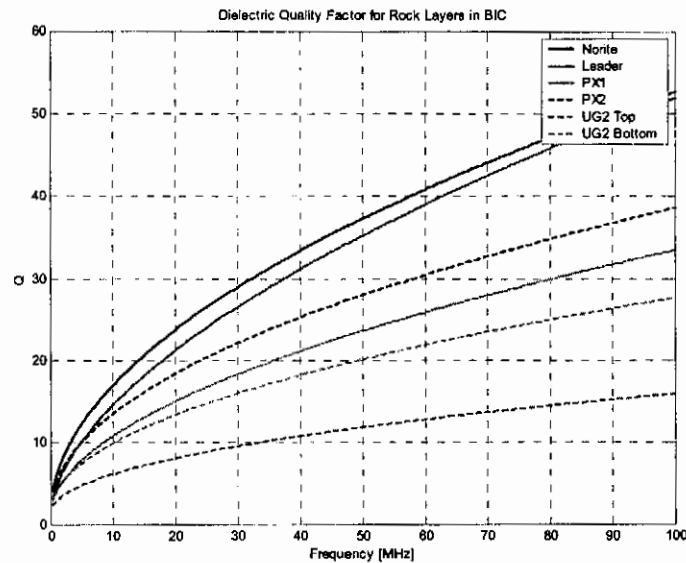


Figure 6-12: Quality factor for rock layers in BIC.

The quality factor of the UG2 chromitite is visibly the lowest, i.e. the most attenuating media. Norite, on the other hand, has the highest Q and is the best medium for radiowave propagation in the VHF frequency range. The pyroxenites have a relatively high Q, slightly less than norite, but still regarded as good propagating media. The Q-curves of all measured media have a distinctively similar shape. They rise sharply at the lower frequency with the tangent dropping and settling almost to a constant value at the higher VHF frequencies. This low-frequency response of dielectric media with conduction losses is mathematically intuitive [41],[43].

The dielectric properties of the other rocks encountered in the UG1 – UG2 stratigraphy (i.e. the anorthosites, pegmatoidal feldspathic pyroxenites and the leuco-, meso- and melanorites) were not available at the time of the research presented in this dissertation. Rütshlin [39] is currently busy developing a technique to measure the dielectric properties of all the rocks up to 30 MHz. Preliminary results have since been presented [89]. Predictions can be made however on the behaviour of these five rock layers. Norite is composed mainly of anorthosite with speckles of pyroxenite, while leuconorite is composed of 90 % anorthosite and 10 % pyroxenite [88]. The dielectric properties of the anorthosites and pyroxenites are closely matched. The likelihood that the dielectric properties of the anorthosites, leuco- and mesonorites are

similar to the norites is very good. The pegmatoidal feldspathic pyroxenites and melanorites, on the other hand, have a similar mineral composition (high pyroxenite contents) as the feldspathic pyroxenites and their dielectric properties should be closely matched.

## 6.5 Radiation in a Lossy Homogeneous Medium

The basic mathematical expression for radiation from an electrical dipole is equivalent for either a lossless or a lossy encapsulating medium [43]. There are a number of subtle differences, however, in the physical interpretation of these mathematical equations. Consider a relatively short (to the wavelength)  $z$ -directed electric dipole located at the origin and fed at the centre, with a current  $I_0$  and effective length  $L_0$ . The Hertz vector [43] due to this dipole is given by

$$\vec{\pi} = \hat{z} \frac{iI_0 L_0}{\omega \tilde{\epsilon}} \frac{e^{ikr}}{4\pi r} \quad (6.2)$$

where  $k = \omega \sqrt{\mu_0 \tilde{\epsilon}}$  is the wave number and  $\mu_0$  and  $\tilde{\epsilon}$  are the dielectric permeability and effective permittivity. Since we assume non-magnetic material, the permeability equals the free space permeability. In general the permittivity is complex and hence also the wave number [37], [41], [43]. The angle,  $\delta$ , of the complex permittivity phasor is of extreme importance when EM propagation in lossy media is considered. The consequences of this are discussed in Chapter 7, but for the moment the need is only to realize that the wave number  $k = \beta + i\alpha$  is complex, with  $\beta$  the propagation constant and  $\alpha$  the attenuation constant. A relationship exists between  $\alpha$  and the quality factor  $Q$  of the dielectric medium. It can be derived from (7.2), (7.3) and (7.10) that

$$\alpha = \frac{\omega \sqrt{\tilde{\epsilon}''}}{2cQ} \quad (6.3)$$

whenever  $Q \gg 1$ . In the far field zone of the dipole, i.e.  $|kr| \gg 1$ , the spherical field components are given by

$$E_{\theta} = -i(I_0 L_0) \omega \mu_0 \frac{e^{-\alpha r}}{4\pi r} e^{i\beta r} \sin \theta$$

$$H_{\phi} = -i(I_0 L_0) k \frac{e^{-\alpha r}}{4\pi r} e^{i\beta r} \sin \theta.$$
(6.4)

From (6.4), it is evident that the electric and magnetic fields are perpendicular to one another and also perpendicular to the direction of wave propagation  $\hat{r}$ . Furthermore, the ratio of  $E_{\theta}$  to  $H_{\phi}$  is the characteristic impedance of the medium

$$\frac{E_{\theta}}{H_{\phi}} = \eta = \sqrt{\frac{\mu_0}{\epsilon}}$$
(6.5)

which is a complex number for lossy media. The most significant implication of the fact that  $k$  is complex for lossy media is that, in addition to the  $(4\pi r)^{-1}$  geometric spreading losses, there is an exponential decay  $e^{-\alpha r}$  due to dielectric losses in the magnitudes of both the electric and magnetic fields. The dielectric losses can be separated in two separate loss mechanisms, i.e. conduction losses due to the ohmic conductivity of the medium and polarization losses due to the lag of the polarization response with respect to the incident field [41], [37]. In general the conduction losses dominate at lower frequencies, while the polarization losses dominate at higher frequencies. The exact mechanism of dielectric losses is not important for the scope of this dissertation and will therefore not be separated. It is intuitive from (6.3) that  $\alpha$  is constant if  $Q$  is proportional to  $\omega$  and proportional to  $\omega$  when  $Q$  is constant.

We can find a radial distance,  $r_{\alpha}$ , from the antenna where the geometric losses will dominate the dielectric losses if  $r < r_{\alpha}$  and where the dielectric losses will dominate whenever  $r > r_{\alpha}$ . This can be seen when we take the natural logarithm of both losses together:

$$\ln \frac{e^{-\alpha r}}{4\pi r} = -\alpha r - \ln(4\pi r).$$
(6.6)

Clearly the magnitude of  $\alpha$  plays a very important role in wave propagation in lossy media, since it determines the distance  $r_{\alpha}$ . In a BHR environment the ideal is that  $r_{\alpha}$  will be larger than the maximum distance of the targets under survey. This is not always possible and  $r_{\alpha}$  is usually of the same order, or sometimes even less, than the target distance,  $r_t$ . The dielectric properties of the host media for a deployed borehole radar (or ground penetrating radar) therefore determines the maximum range at which

the radar will be able to detect targets and is highly variable for different deployment sites. It has been proven that the GeoMole BHR is able to detect a planar interface, the Ventersdorp Contact Reef (VCR), up to 60 m away with a lava hanging wall host medium [5], [6]. The maximum target detection distance for a BHR system deployed in the BIC host media (pyroxenites and norites) is to be found. This is considered in the following section.

## **6.6 Possible Detection Range in BIC**

Knowing the dynamic range of a given BHR system and also the dielectric properties of the host media, makes it possible to determine the maximum detection range for a target of a known radar cross section or with a known reflectivity profile. On the other hand it is possible to get an estimated maximum detection range for a known target by the evaluation of experimental data.

The first GeoMole borehole radar trial in the UG1 – UG2 stratigraphy of the BIC was conducted at Anglo Platinum's Bleskop mine in the vicinity of Rustenburg during the last week of September 2001. The purpose of this survey was to determine whether or not the system that hosts the UG2 reef is indeed sufficiently transparent to enable the GeoMole borehole radar to detect economically important geological features like potholes, rolls and faults in the UG2 reef [94]. In view of the stratigraphic column depicted in Figure 6-2 on page 124, the maximum detection range of reef features (like potholes) in the UG1 and UG2 reefs has to be in the order of 30 m if the radar is deployed within the UG1 – UG2 stratigraphy. The second purpose of the first radar experiment was to investigate whether there is adequate dielectric contrast between the reef seams and the host media for good radar reflectivity. The essence of the first Bleskop radar trial is summarized in Appendix D. From the work done at Bleskop it was established that the host media of the UG1 – UG2 stratigraphy adequately support radiowave propagation over at least 60 m in cross-hole mode, translated to a maximum radar detection range in the order of 30 m (as was required).

## 6.7 Propagation Velocity Estimates

The propagation velocity of an EM pulse is of extreme importance in the interpretation of radar scans and inverse imaging techniques (e.g. synthetic aperture processing).

Papoulis [10] defines the quantities phase, group and signal front velocity –  $v_{ph}(\omega)$ ,  $v_{gr}(\omega)$  and  $v_{fr}$  respectively. These quantities are regularly used to describe the propagation of waves in a linear system, which might be the propagating medium (host rock) under consideration [10], [42], [43]. For a narrow-band signal these quantities describe the propagation velocity of the signal envelope, carrier and the beginning (front) of the signal [10]. In wideband systems such as the GeoMole BHR, where the signal has a multi-octave bandwidth and no fixed carrier frequency, these quantities have a more vague meaning, if any.

Consider a pulse recorded during a field experiment (e.g. Figure 5-5). This pulse has a finite bandwidth with a dominant frequency. Unless  $\alpha$  is constant as a function of frequency, this dominant frequency will depend on the distance travelled through the medium. If  $\alpha$  increases as a function of frequency, the dominant frequency will decrease as the travelling distance increases. A variable  $\alpha$  will also change the shape of the pulse and its envelope, as will a frequency-dependant phase velocity. With a range-dependant envelope it becomes rather complicated to define its velocity. It is also no longer associated with the group velocity at the carrier frequency.

The measurement of phase and group velocity for a broadband signal in a medium where  $\alpha$  and  $v_{ph}$  are both frequency dependent, is clearly very complicated. For the purpose of signal processing, only the velocity of the signal event being traced is of real importance. The velocity with which the peak (absolute maximum) of the pulse propagates is therefore defined as the pulse peak velocity  $v_{pp}$  and will be the desired quantity to estimate. In the special case where  $\alpha$  and  $v_{ph}$  are constant, the phase and group velocity will both be equal to the pulse peak velocity.

In order to get a good estimate of the pulse peak velocity of a pulse propagating through a given medium, the distance travelled must be known to a high degree of accuracy, as well as the time it took the pulse to propagate the given distance. The most obvious BHR deployment configuration for velocity estimates is a cross-hole

configuration where the transmitter is at a fixed, known position and the receiver is at a spatially separated position. The host rock between the transmitter and receiver has to be relatively homogeneous for accurate estimates. The time-offset for that specific event from zero time (the time the DAQ starts recording),  $t = 0$ , also has to be known.

### **6.7.1 Bleskop I Propagation Velocity Estimate**

The first velocity estimate of the host media in the BIC was made during the first radar trial at Bleskop, as discussed in Appendix D. The transmitter and receiver were deployed in boreholes in the host rock immediately below the UG2 chromitite reef. It can be seen in Figure D-3 that the host medium between the transmitter and receiver included both the norites underneath the UG2 reef as well as the Bleskop marker. The transmitter and receiver were very close to the main seam as well as the tunnel (both very good reflectors) and the received signal had to be a superposition of the direct wave and a number of reflected waves. The only undisturbed signal event was the first-break and it was therefore chosen as the event to calculate the pulse peak velocity. The time-offset for the first-break was measured experimentally by placing the transmitter and receiver feedpoints next to each other and analysing the acquired trace. The pulse peak velocity was estimated using three different surveys and the average pulse peak velocity was calculated as

$$v_{pp} = 104 \text{ m}\cdot\mu\text{s}^{-1} \quad (6.7)$$

which is within 9 % of the velocity of norite calculated from the measured dielectric properties. One possible explanation for this error margin (if it is indeed an error) include the fact that the geometry was not known to a high degree of accuracy. The trajectories of the boreholes have to be known as well as the coordinates of the collars of the boreholes. It was unfortunately not possible to obtain these. A second possible explanation is because of the choice of signal event. The first-break of a pulse is a very difficult event to pick, especially in the presence of noise. Finally, it should be noted that the host medium between the transmitter and receiver was not homogeneous at all and consisted of a mixture of pyroxenites, norites, anorthosites and chromitite layers. None the less, (6.7) gives a relatively good approximation for the pulse peak velocity in the host media of the BIC.

### **6.7.2 Bleskop II Propagation Velocity Estimate**

Because of the restrictions of the first velocity estimate (geometry, homogeneity and signal event), a second experiment was designed to obtain an improved velocity estimate. The key characteristics of such an experiment can be summed up as follows:

- Accurate time-offset calculation
- High fidelity signal event
- Minimum reflection interference
- Homogeneous host medium

A borehole radar experiment was conducted at the RPM Bleskop mine over five days from 10 to 14 June 2002 [95]. This was the second radar field experiment at Bleskop. An extensive summary of the Bleskop II field experiment is presented in Appendix F. Five 48 mm boreholes of approximately 100m were drilled into the UG2 footwall. The holes were drilled southernly in a fan-like shape. Three holes, spaced 30° in plan, were inclined upwards and two were drilled down along the bisecting angles. All the boreholes were confined within the UG2 reef and the UG1 layers. The boreholes were drilled from a common point with the collars closely grouped, about 8 m below the UG2. The collars were either just below the Bleskop marker or drilled within the marker. At Brakspruit (see Appendix E) a GeoMole three-axis magnetometer and accelerometer were used for the first time to find the trajectories of BHR boreholes. The five boreholes at the Bleskop II experiment were also surveyed with the GeoMole rotational sensor, yielding the trajectories of the holes with a high degree of accuracy [96]. The cartesian coordinates of the borehole collars were surveyed by the mine surveyors and tied to the mine maps. It is therefore possible to adhere to the four requirements stated at the beginning of this section, provided that the BHR deployment is controlled with a high degree of accuracy with regard to the positioning of the transmitter and receiver and also the fibre optic chain determining the time-offset.

The two declining boreholes, H49 and H50, enter the BIC stratigraphy below the Bleskop marker with their end-of-hole (EOH) points above the UG1 layers. The host rock between the transmitter and the receiver is therefore norites for the majority of the borehole lengths – a favourable site for velocity estimation. The trajectories of the boreholes are calculated with 0.1 m intervals between stations. In this specific

experiment the transmitter was located in H50 and the transmitter in H49. They were pulled at the exact same speed from the collars to the EOH while acquiring traces. A zero trace (trace with 0 V at each time sample) was inserted in the data after every 5 m of movement up to the EOH. The zero traces can be used to interpolate the positions of the probe feedpoints at each trace using the boreholes trajectories. The five borehole trajectories are plotted in three dimensions in Figure 6-13 with the transmitter and receiver feedpoints marked for each trace.

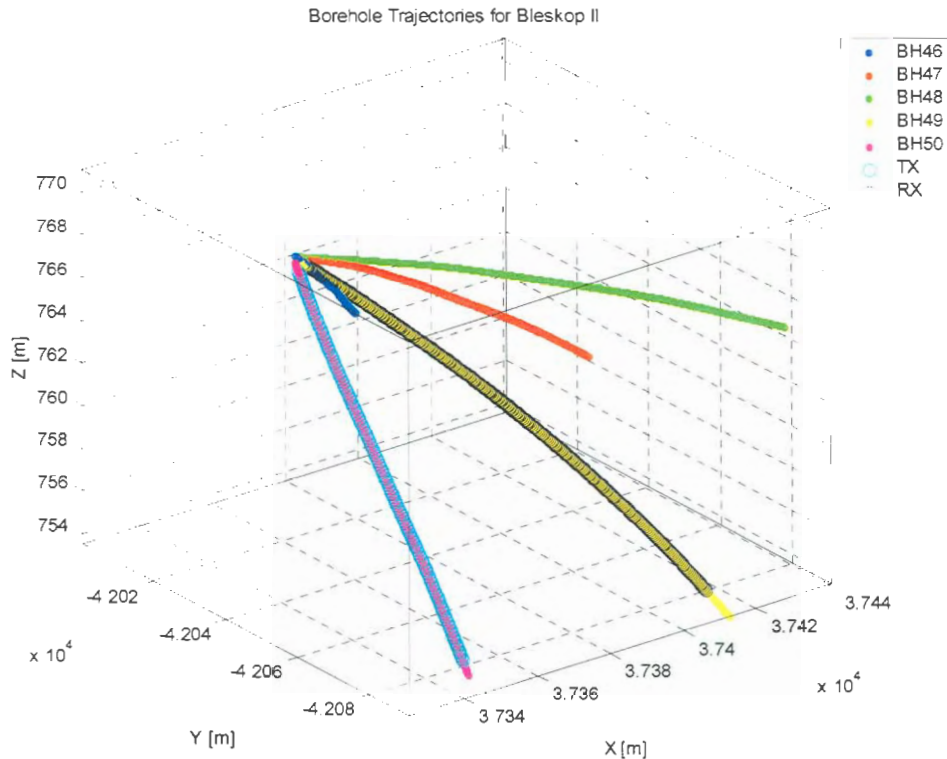


Figure 6-13: Borehole trajectories with TX and RX feedpoints used for velocity estimation.

The recorded radar scan was evaluated and the highest fidelity signal event was found to be the first trough of the pulse, Figure 6-14. The radar/seismic signal processing and imaging software package SeisWin was used to automatically pick this event for every trace. The tomographic picking procedure was used with an offset time of 0.2  $\mu$ s and a median filter length of 5 traces to automatically pick the first trough. The auto picking for trace 240 is graphically depicted in Figure 6-14. The result for the entire scan is depicted in Figure 6-15.

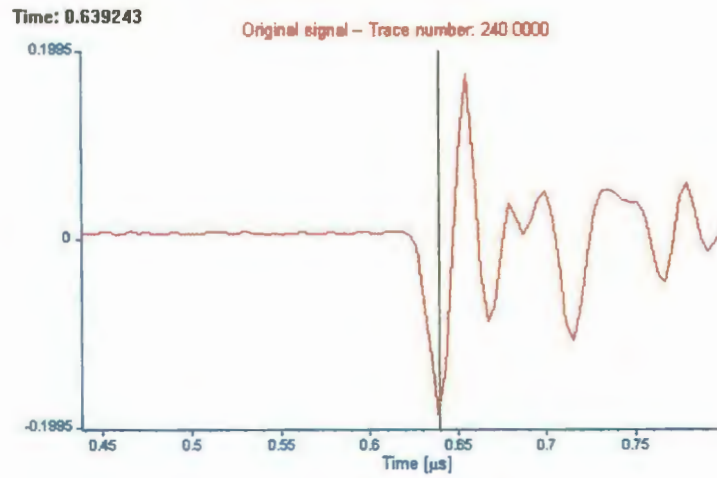


Figure 6-14: Automatic picking of first trough signal event.

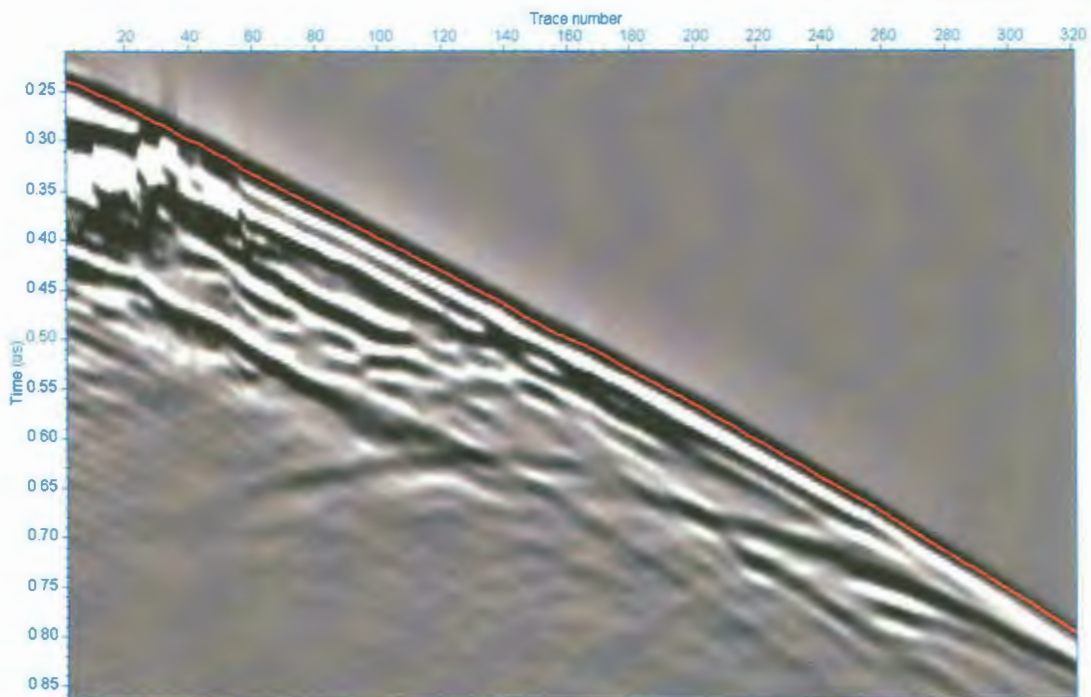


Figure 6-15: First trough auto picking for the entire radar scan.

The time-offset for the given event,  $t_e$ , was calculated from the exact fibre optic chains used in conjunction with the laboratory measurements in Section 4.6.4 as

$$t_e \approx 218 \text{ ns.} \quad (6.8)$$

The pulse peak velocity of the transmitted pulse can be estimated using the simple equation

$$v_{\text{norite}} = \frac{r}{t - t_e}. \quad (6.9)$$

The estimated pulse peak velocities are plotted for each trace in Figure 6-16. The first 99 traces are omitted because of the saturation of the front-end amplifier visible in the raw data.

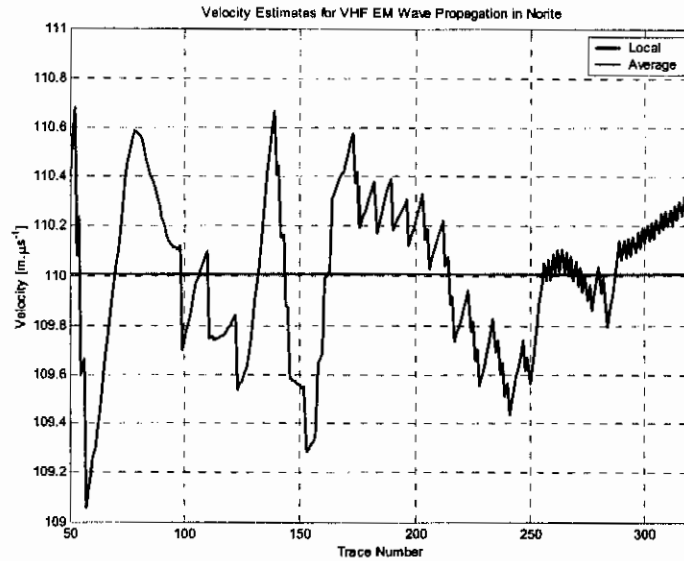


Figure 6-16: Local and average estimated pulse peak velocity.

The average pulse peak velocity is calculated as

$$v_{norite} = 110 \text{ m.}\mu\text{s}^{-1}, \quad (6.10)$$

with a maximum and standard deviation of  $0.95 \text{ m.}\mu\text{s}^{-1}$  and  $0.32 \text{ m.}\mu\text{s}^{-1}$  respectively. The estimated pulse peak velocity is within 3 % of the average phase velocity calculated in Section 6.4. The fidelity of this estimate is assumed to be very high, since the standard deviation is less than 0.3 % over the survey length of approximately 90 m.

## 6.8 Quality Factor Estimates

The second property of EM wave propagation in the BIC host media with equal, or even greater importance than the pulse peak velocity, is the attenuation due to dielectric losses as a function of distance – determined by the quality factor of the media. The quality factors for the pyroxenites and norites were summarized in Section 6.4. These calculations were based however, on microscopic measurements of small circular discs cut from borehole cores [39]. The macroscopic quality factor of the host media is the determining factor of radar performance and the only way to get an estimate is by the interpretation or exploitation of experimental data. The

restrictions for accurate quality factor estimates from an experimental survey, are considerably more stringent than those imposed for velocity estimates.

An attempt was made to obtain an initial estimate of  $Q$  for the norites from the Bleskop I field experiment (Appendix D). This experiment was ill-conditioned for  $Q$  estimates and yielded very poor and erratic results – first arrivals were cluttered by reflections from nearby strata. In addition to the restrictions for velocity estimates, the direct wave travelling the shortest distance between the two feedpoints has to be separated from any reflections or secondary effects. This is necessary since the power density spectrum of the received pulse needs to be calculated and this is only possible if the direct wave can be time-gated. Studying the cross-hole radar scans of the Bleskop II field experiment, two cross-hole scans satisfied the requirements for  $Q$  estimation:

- Cross-hole scan with transmitter in H46 and receiver in H48,
- Cross-hole scan with transmitter in H50 and receiver in H49.

Firstly, consider the cross-hole scan between H46 and H48. The direct wave pulse is spatially separated from any reflections with the markings on the optic cables between 20 m and 30 m, i.e. a 10 m length of scan. A total of 38 traces have been recorded over this length of scan, with the raw data shown in Figure 6-17.

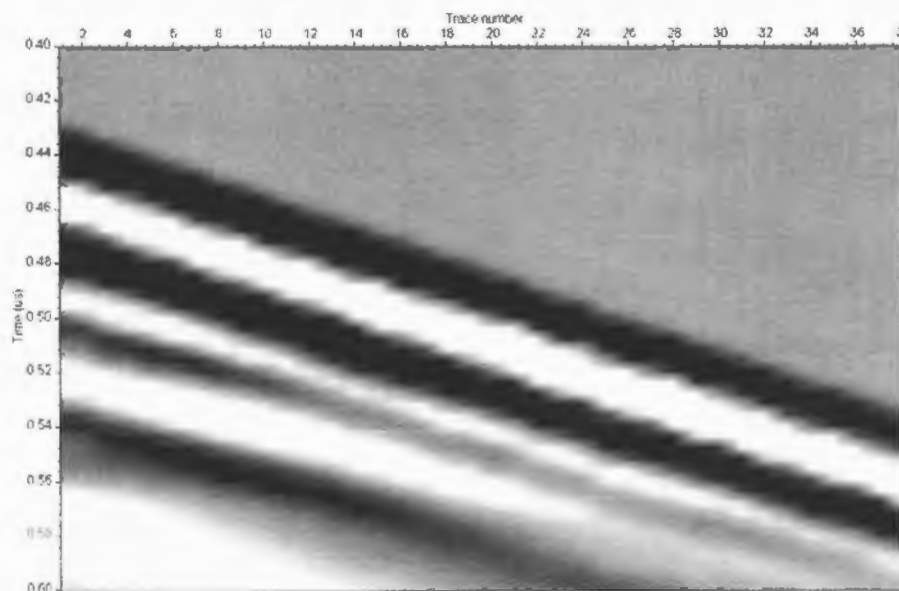


*Figure 6-17: Section of raw radar data where direct wave is spatially separated.*

With the definition of the available power,  $P_{av}$ , as given in Section 4.6.1  $P_d$  (the power delivered to the RF chain) can be calculated as

$$P_d = P_{av} \frac{D_{rx}(\theta_r) D_{tx}(\theta_t)}{D_{rx(max)} D_{tx(max)}} p \frac{e^{-2\alpha r}}{4\pi r^2} \quad (6.11)$$

where  $\theta_r$  is the angle that the receiver makes with the line connecting the TX and RX feedpoints in the plane of the transmitter.  $\theta_t$  is the angle that the transmitter makes with the same connecting line and  $p$  is the polarization efficiency [11]. With  $\alpha$  as the only unknown, we can find  $\alpha$ , as well as  $Q$ , since  $\beta$  can be approximated from the pulse peak velocity estimate. The available power is a function of the BHR deployment configuration. This is plotted in Figure 6-19 for the given cross-hole scan. The power delivered,  $P_d$ , has to be calculated from each trace. The pulse recompression (deconvolution) technique discussed in Chapter 5 was used to find the electric field at the receiver feedpoint for every trace. The frequency domain bandpass and notch filter had the following parameter settings:

$$\begin{aligned} f_1 = 5 \text{ MHz} , f_2 = 60 \text{ MHz} , f_3 = 65 \text{ MHz} , f_4 = 110 \text{ MHz} \\ \Delta f_1 = 5 \text{ MHz} , \Delta f_2 = 5 \text{ MHz}. \end{aligned} \quad (6.12)$$

The resulting waveform now has to be time-gated to retain only the direct wave pulse. A time domain window function was set up with a total width of 80 ns and Hanning window rising- and falling edges of 20 ns each resulting in a 40 ns unity passband. The original and time-gated E-fields for trace 30 are plotted in Figure 6-18. The power delivered to the RF chain is calculated from the time-gated E-field using the power transfer function of the antenna. This is plotted in Figure 6-19 for trace 30, together with the calculated noise floor.

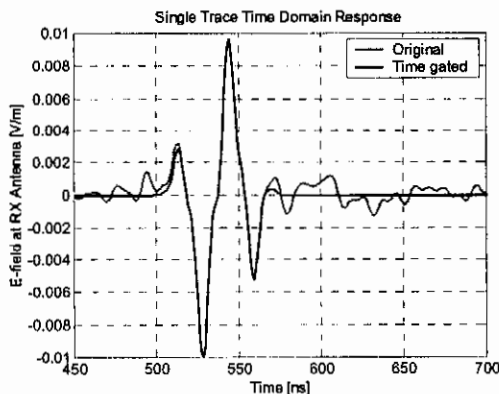


Figure 6-18: Reconstructed incident E-field for trace 30.

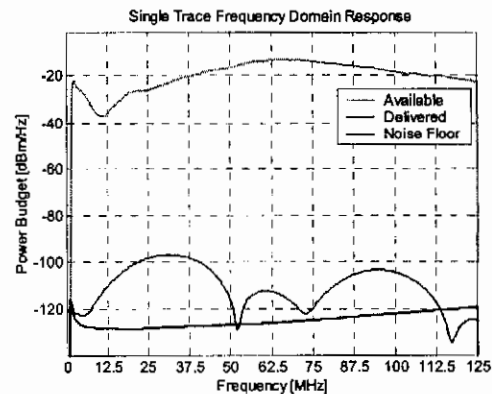


Figure 6-19: Power budget for trace 30.

The remaining unknown parameters depend on the geometry of the transmitter and receiver probes. The exact locations of the transmitter and receiver feedpoints are calculated in the same way as described in Section 6.7.2 and plotted in Figure 6-20.

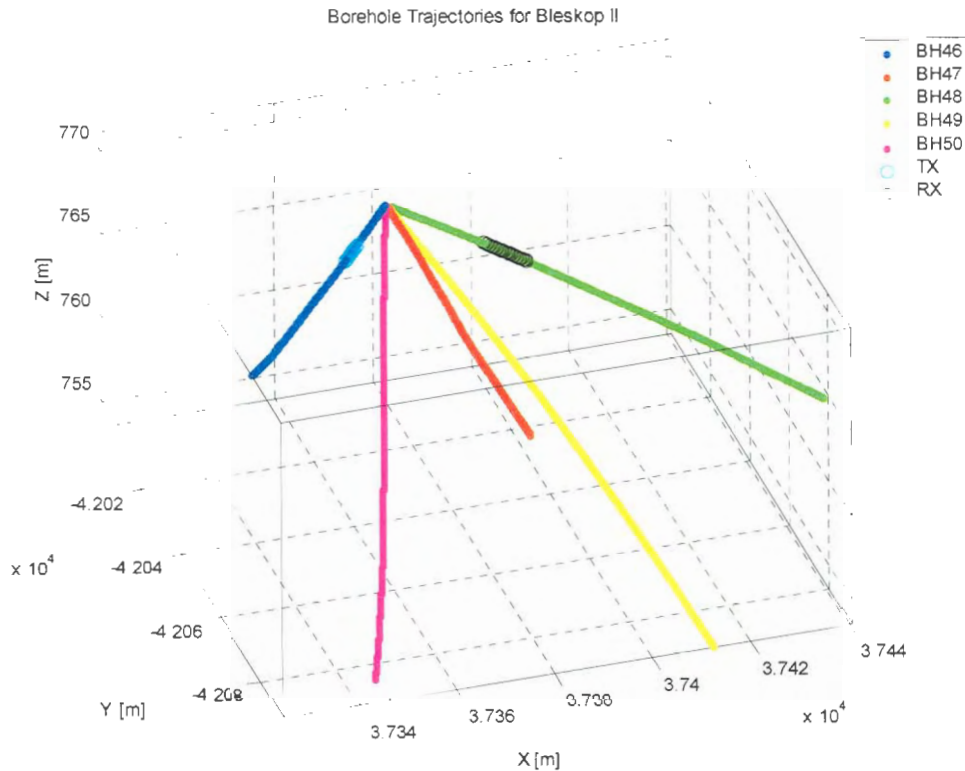


Figure 6-20: Borehole trajectories with transmitter and receiver locations for  $Q$  estimation.

In addition to this, two new coordinates were introduced, which represent the endpoints of the transmitter and receiver. This was necessary because the relative orientations of the transmitter and receiver need to be known. The coordinate system is now translated so that the transmitter feedpoints for every trace lie at the origin, yielding the coordinates  $\bar{r}_{i1} = 0$ ,  $\bar{r}_{i2}$ ,  $\bar{r}_{r1}$  and  $\bar{r}_{r2}$  associated with the transmitter feedpoint, transmitter endpoint, receiver feedpoint and receiver endpoint respectively. Next, the coordinate system is rotated about the  $z$ -axis and then about the  $y$ -axis so that the TX-RX feedpoint lines lie on the  $x$ -axis. This yields the coordinates  $\bar{r}'_{i2}$ ,  $\bar{r}'_{r1}$  and  $\bar{r}'_{r2}$  as plotted in Figure 6-21.

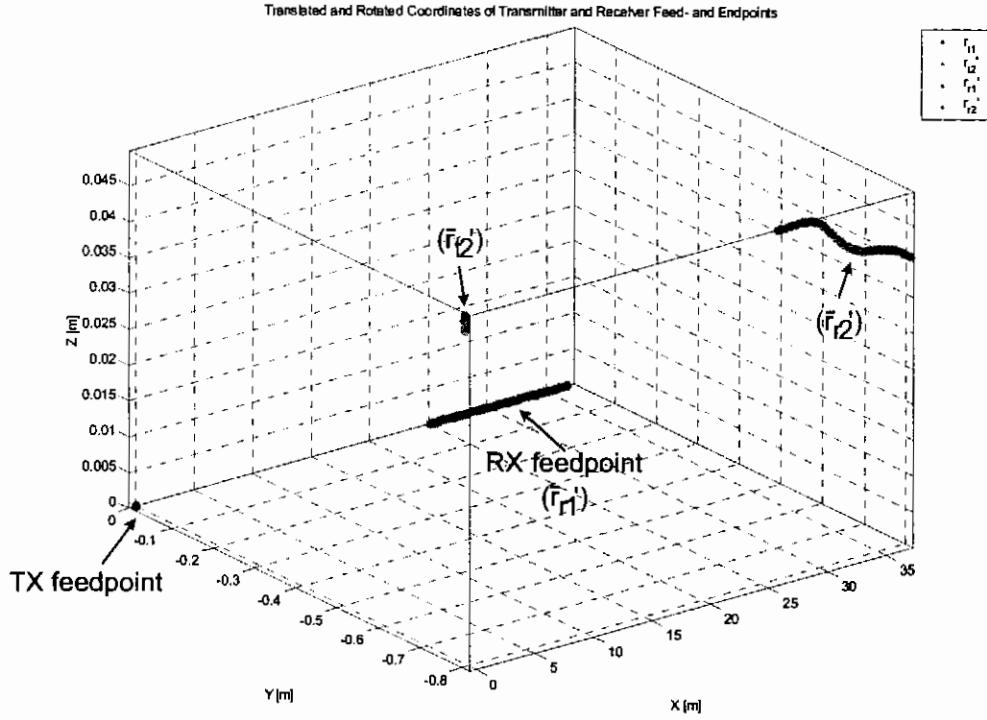


Figure 6-21: Translated and rotated coordinates of TX/RX feed- and endpoints for  $Q$  estimation.

The final step is to rotate the coordinate system about the  $x$ -axis so that the vector  $\bar{r}'_{12} - \bar{r}_{11}$  lies only in the  $x$ - $z$  plane and yields the coordinates  $\bar{r}''_{12}$ ,  $\bar{r}''_{r1}$  and  $\bar{r}''_{r2}$ . The angle that the vector  $\bar{r}''_{12} - \bar{r}_{11}$  makes with the  $x$ -axis,  $\theta_t$ , is used to find the directivity of the transmitter, while the angle that the vector  $\bar{r}''_{r2} - \bar{r}_{r1}$  makes with the negative  $x$ -axis,  $\theta_r$ , is used to find the directivity of the receiver. These angles are plotted in Figure 6-22 for the different traces. The rotational angle of the vector  $\bar{r}''_{r2} - \bar{r}_{r1}$  about the  $x$ -axis is the polarization angle used to find the polarization efficiency

$$p = \cos^2 \chi_r \quad (6.13)$$

and is also plotted in Figure 6-22. The maximum directivities of the transmitter and receiver, as well as the directivities in the given directions, can be found from the numerical simulations as discussed in Chapter 4. The attenuation constant,  $\alpha_{norite}$ , can be found using (6.11) and the propagation constant,  $\beta$ , can be found using (6.10) and the equation

$$\beta_{norite} = \frac{\omega}{v_{norite}} \quad (6.14)$$

From these two parameters,  $Q_{norite}$  can be found from (7.3) and (7.10) as

$$\begin{aligned} \delta_{norite} &= \angle(\beta_{norite} + i\alpha_{norite})^2 \\ Q_{norite} &= (\tan \delta_{norite})^{-1}. \end{aligned} \tag{6.15}$$

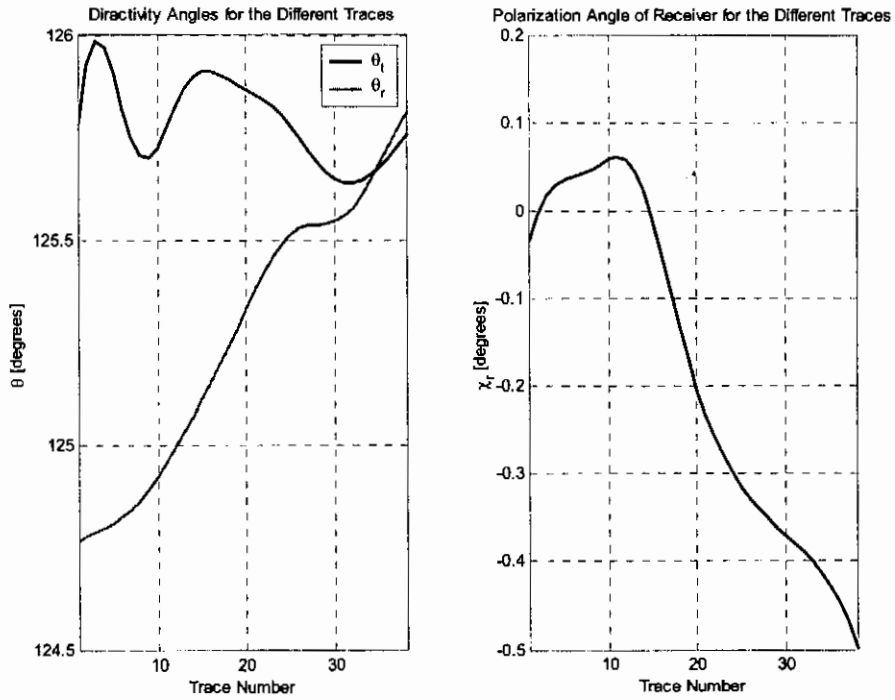


Figure 6-22: Directivity and polarization angles for the different traces used in  $Q$  estimation.

The estimated  $Q_{norite}$  as a function of frequency for the different traces together with the averaged value of  $Q_{norite}$  are plotted in Figure 6-23.

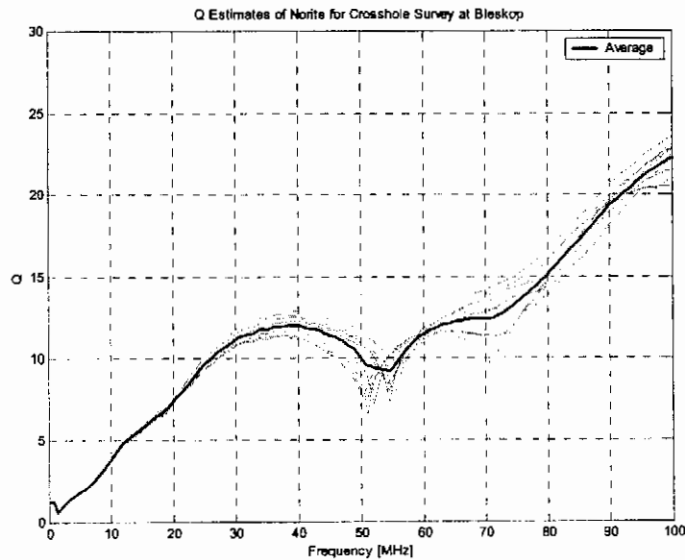


Figure 6-23: Individual and average  $Q_{norite}$  estimates as a function of frequency.

$Q_{\text{norite}}$  has a definite, almost linear, trend in the lower frequency range up to about 35 MHz. This linear trend in the low frequency region is expected from a medium characterised by a finite conductivity with  $\omega \ll \omega_c$  (see Section 7.2). In this region the losses due to ohmic conduction dominate the polarization losses. Two dips in the estimate of  $Q_{\text{norite}}$  occur at approximately 50 and 70 MHz and can be associated with the squint of the transmitter and receiver antennas at those particular frequencies.  $Q_{\text{norite}}$  still rises as a function of frequency to reach a maximum of 22.3 at 100 MHz. A quadratic fitting of  $Q_{\text{norite}}$  was done in the frequency range of interest, yielding the polynomial

$$Q'_{\text{norite}} \approx -1.8213 \times 10^{-3} f^2 + 3.9672 \times 10^{-1} f + 2.4651^{-1} \quad (6.16)$$

where  $f$  is the frequency in MHz. The quadratic polynomial approximation,  $Q_{\text{norite}}$  is plotted together with the average  $Q_{\text{norite}}$  in Figure 6-24.

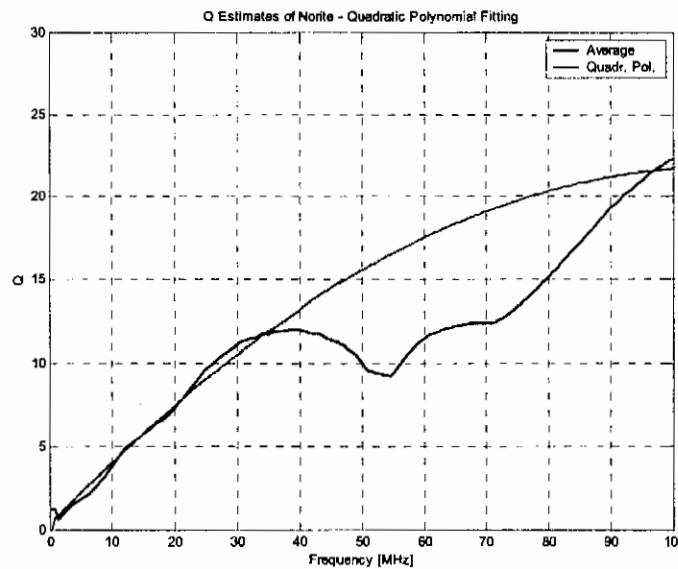


Figure 6-24:  $Q_{\text{norite}}$  approximated by a quadratic polynomial.

The basic shape of  $Q$  as a function of frequency is quite intuitive. The initial linear rise is typical of a dielectric with dominant ohmic conduction losses. The tapering off at the higher frequencies can be ascribed to either polarization losses starting to play a significant role, or macroscopic inhomogeneities causing scattering of the higher (> 50 MHz) frequencies. When compared with the Jonscher-model calculated  $Q$  of norite, based on the measurements by Rütshlin [39], as depicted in Figure 6-12, it is clear that the macroscopic estimations are notably lower than the microscopic values. This might be due to a number of factors, e.g. microscopic measurement inaccuracies,

## CHAPTER 6: Propagation in the Rock Strata of the UG1 – UG2 System

microscopic measurements that were only done up to 30 MHz, inaccurate modelling of deployed antennas, system transfer function errors, incorrect geometry, etc.

Borehole H46, in which the transmitter was deployed, traversed through the various layers of the Bleskop marker from the collar to the EOH. This is evident from both the radar profile data and the borehole core logs. For the section used in  $Q$  estimation, the transmitter feedpoint was between 21.15 – 31.15 m from the collar. The transmitter feedpoint was therefore just below the Bleskop marker with the host medium feldspathic pyroxenite or norite. Borehole H48, in which the receiver was deployed, on the other hand traversed below the Bleskop marker for its entire length. The section used for  $Q$  estimation was either located in pyroxenites (in the beginning) or norites (at the end). The host rock between the transmitter and receiver feedpoints were therefore a mixture of pyroxenites and norites and the  $Q$  estimate is approximately an average of the  $Q$  values of the norites and pyroxenites.

Consider the second cross-hole experiment with transmitter in H50 and receiver in H49. The direct wave pulse is spatially separated from any reflections with the markings on the optic cables between 45 m and 55 m, i.e. a 10 m length of scan. A total of 37 traces have been recorded over this length of scan. This is plotted in Figure 6-25.

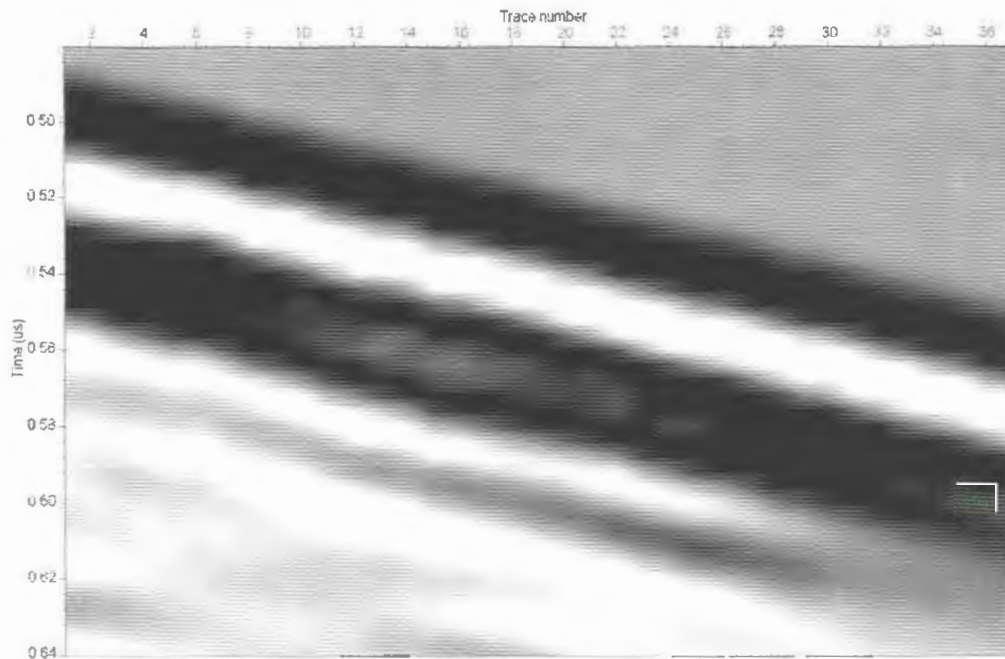


Figure 6-25: Section of raw radar data where direct wave is spatially separated for 2<sup>nd</sup>  $Q$  estimate.

In Figure 6-25 it actually seems as though there is interference of a secondary pulse at the end of the direct wave pulse. However, after the pulse recompression algorithm has been applied, the direct wave pulse is spatially separated from any secondary pulse interference. The original voltage signal with the interference and the recompressed E-field are plotted in Figure 6-26 and Figure 6-27 for trace 25 as an example.

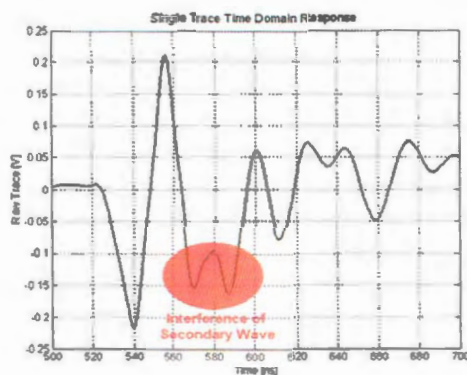


Figure 6-26: Interference of secondary pulse for trace 25.

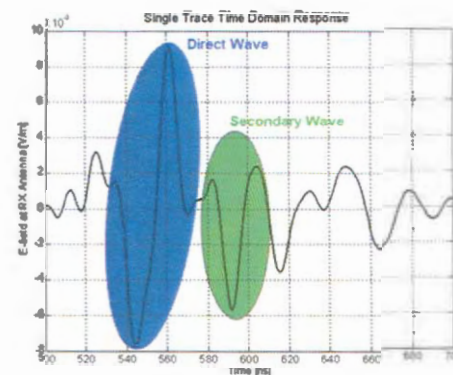


Figure 6-27: Spatially separated direct wave and secondary pulses for trace 25.

It should be noted that the boreholes H49 and H50 were filled with water with a low salt content, whereas the boreholes H46 and H48 were dry. The antenna transfer functions therefore had to be calculated for a water-filled borehole in norite with a low salt content. The negative effect of a water-filled borehole is that the bandwidth of the received signal is decreased by approximately 10 % with a maximum frequency content of  $\pm 95$  MHz.

The estimate of  $Q$  for the host media between H49 and H50 is done in exactly the same manner as it was done for the cross-hole scan between H46 and H48. It was found that a cubic polynomial fitted the  $Q_{\text{norite}}$  curve better than a quadratic polynomial, yielding the polynomial

$$Q'_{\text{norite}} \approx 1.375 \times 10^{-5} f^3 - 3.306 \times 10^{-3} f^2 + 4.035 \times 10^{-1} f + 8.254 \times 10^{-1}. \quad (6.17)$$

The average and cubic polynomial approximation of  $Q_{\text{norite}}$  for the evaluated section are plotted in Figure 6-28, together with the quadratic approximation for the first  $Q_{\text{norite}}$  estimate (6.16).

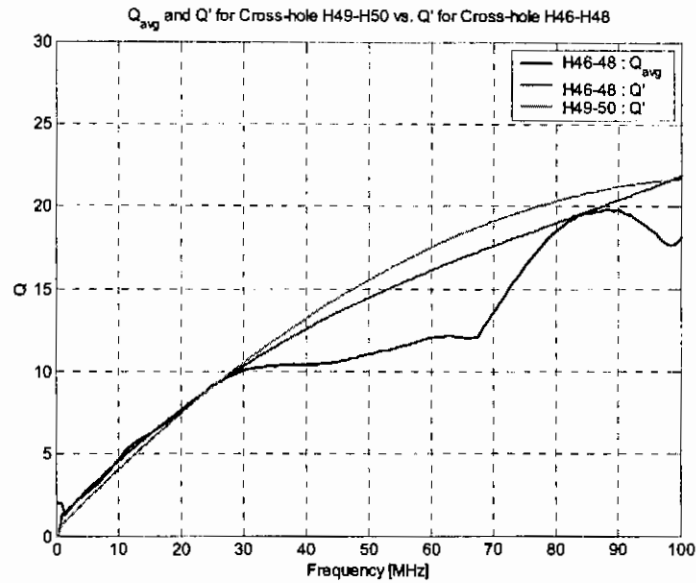


Figure 6-28: Second  $Q_{norite}$  estimate approximated by a cubic polynomial and compared to the first estimate approximation.

The two polynomial fittings for  $Q_{norite}$  are in reasonable close correlation considering the complexity of the geometric deployment of the radar and the host media between the probes.

## 6.9 Concluding Remarks

In this chapter a quantitative description of EM wave propagation in the rock strata of the UG1 – UG2 system in the BIC, i.e. the pyroxenites and norites, was established.

The approximate pulse peak velocity in the host media, consisting mainly of norites with pyroxenite layers of lesser thickness sometimes present, was found to be approximately  $110 \text{ m} \cdot \mu\text{s}^{-1}$ , while the  $Q$  of the host media closely fits a quadratic polynomial.  $Q$  rises almost linearly to 12.5 at 35 MHz after which the tangent drops with a maximum of 22.5 at 100 MHz.

Finally, it was established that detection ranges of +30 m are possible with the UG2 and UG1 reefs as targets. Given the empirically calculated quality factor of the host rock, the anticipated maximum detection range of a known target, i.e. the UG2 reef, will be estimated in Chapter 8. In order to do this, a good approximation of the average target reflectivity is necessary, which in turn requires a thorough understanding of radiowave propagation in stratified lossy matter.

# CHAPTER 7

## THEORY OF PLANE WAVE PROPAGATION IN STRATIFIED LOSSY MATTER

Radiowave propagation in stratified media has been studied comprehensively [43], [45] - [49]. Despite the fact that the theory is generalized for a medium with polarization and conductive losses, only King, Owens and Wu [49] thoroughly consider the case where one of the layers in a two-layered system has conductive losses. They briefly discuss the case where both layers have conductive losses. Since the BIC consists of numerous layers with conductive losses, a clear understanding of radiowave propagation in stratified lossy media is very important.

### 7.1 Literature Review

Haus and Melcher [40], [41], Ramo *et al.* [42], Ishimaru [43] and Lindell [44], to name a few, lay a solid EM propagation theory foundation. Most of the EM derivations and developments in this dissertation are based on this foundation.

The work of Ishimaru [43] and Felsen and Marcuvitz [45] on advanced EM propagation has also been studied. Wait [46] studied very comprehensively the propagation in and above stratified media. He frequently introduced the concept of impedance matching in the propagation in stratified media. Brekhovskikh [47] also compiled a very good study on propagation in layered media. Chew [48] gained worldwide recognition for his formulation and solution of plane wave propagation in stratified media. The formulation presented by him is used in this dissertation.

Ishimaru [43] presents a concise summary on the different propagating modes of plane waves in stratified layers. King *et al.* [49] consider the reflection and transmission of plane waves incident on the interface between half-spaces where either or both have dielectric losses and provide a very good formulation and treatment of inhomogeneous plane waves. Du Toit and Cloete [50] also consider the specular reflection of plane waves incident on stratified lossy dielectric media.

Literature on specific propagation issues was also considered. Born and Wolf [51] present a historic overview of the principles of optic propagation. Of specific interest is the treatment of the principle of Fermat. In the same line Oliner [52] presents historical perspectives of microwave field theory. Of specific interest are the perspectives on the controversy that raged about the existence of leaky waves. Brekhovskikh [47] gives an excellent treatment on the Goos-Hanchen effect, albeit for scalar sound waves. Haus [53] also presents useful mathematical and illustrative descriptions of this physical phenomenon of lateral shift at a boundary.

## 7.2 Electromagnetic Preliminaries

In this chapter, it is assumed that the field is time harmonic and the  $e^{-i\omega t}$  time convention is used. Maxwell's equations, together with the constitutive relations, mathematically describe the electromagnetic behaviour of matter [40].

Chapter 6 showed that the stratigraphically complex environment in which the borehole radar is deployed could be approximated as being planarly layered. In a specific layer the rock is assumed to be an isotropic, homogeneous, linear and non-magnetic medium.

Under the abovementioned assumptions Ampere's law, with the added displacement current, can now be rewritten as

$$\begin{aligned}\nabla \times \bar{H}(\bar{r}, \omega) &= -i\omega\epsilon(\bar{r}, \omega)\bar{E}(\bar{r}, \omega) + \sigma(\bar{r}, \omega)\bar{E}(\bar{r}, \omega) + \bar{J}_s(\bar{r}, \omega) \\ &= -i\omega\tilde{\epsilon}(\bar{r}, \omega)\bar{E}(\bar{r}, \omega) + \bar{J}_s(\bar{r}, \omega),\end{aligned}\quad (7.1)$$

where  $\bar{E}$  is the electric field (V/m),  $\bar{H}$  the magnetic field (A/m),  $\epsilon$  the dielectric permittivity (F/m),  $\sigma$  the conductivity (S/m) of the medium and  $\bar{J}_s$  the externally maintained or impressed electric current (A/m<sup>2</sup>) in localized regions occupied by sources such as electric dipoles or antennas embedded in the ambient medium. The complex permittivity  $\tilde{\epsilon}$  includes the permittivity and the conductivity, which are in general complex due to polarization and conduction lag [43],[49],[41]. Hence

$$\begin{aligned}\epsilon &= \epsilon' + i\epsilon'' \quad ; \quad \sigma = \sigma' + i\sigma'' \\ \tilde{\epsilon} &= \epsilon + i\sigma/\omega \\ \tilde{\epsilon}_r &= \tilde{\epsilon}/\epsilon_0 = \tilde{\epsilon}' + i\tilde{\epsilon}''.\end{aligned}\quad (7.2)$$

The ratio  $\tilde{\epsilon}''/\tilde{\epsilon}'$  is called the loss tangent

$$\tan \delta = \tilde{\epsilon}''/\tilde{\epsilon}' = Q^{-1}. \quad (7.3)$$

This inverse of the loss tangent is equal to the quality factor  $Q$  of the medium, which is  $2\pi$  times the quotient of energy stored and the energy dissipated per cycle. Rewritten as

$$Q = \frac{\epsilon'}{\epsilon'' + \frac{\sigma}{\omega}} \quad (7.4)$$

it is clear that a corner frequency  $\omega_c$  exists where the losses due to ohmic conduction and polarization lag are equal. For  $\omega \ll \omega_c$

$$Q \approx \frac{\omega\epsilon'}{\sigma} \quad (7.5)$$

and the losses are predominantly due to ohmic conduction, while for  $\omega \gg \omega_c$

$$Q \approx \frac{\epsilon'}{\epsilon''} \quad (7.6)$$

and the losses are predominantly due to the polarization lag as depicted in Figure 7-1.  $Q$  is approximately proportional to  $\omega$  below  $\omega_c$ , while it is asymptotically constant above  $\omega_c$  under the assumption that  $\epsilon'$  is nearly constant.

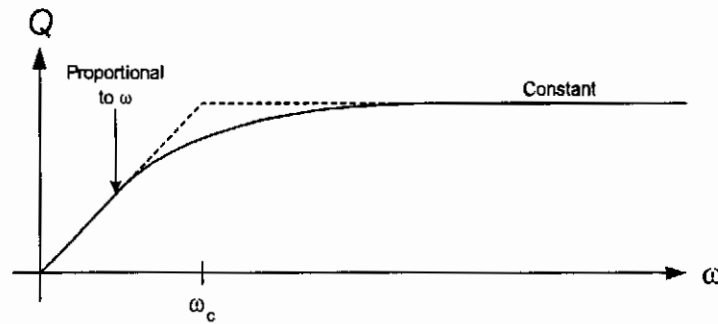


Figure 7-1:  $Q$  as a function of frequency.

### 7.2.1 Vector Wave Equation for Isotropic Media

The general time harmonic vector wave equation for isotropic media can be described mathematically as:

$$\mu_0^{-1} \nabla \times \nabla \times \bar{E}(\vec{r}) - \omega^2 \epsilon \bar{E}(\vec{r}) = i\omega \bar{J}(\vec{r}). \quad (7.7)$$

For a time-varying field, this equation describes the solution of an electromagnetic field in an inhomogeneous, isotropic medium where  $\epsilon$  is assumed to be a function of position and does not commute with the  $\nabla$  operator.

### 7.2.2 **Scalar Wave Equations for One-Dimensional Planar Inhomogeneity**

Due to the planarly layered media approximation, the dielectric properties are only varying in one dimension. Without loss of generality, the  $z$ -axis is chosen as the axis of dielectric properties variation. The mathematical beauty of this assumption is that the vector wave equation (7.7) need not be solved in its full form. For the source-free case, the vector wave equations reduce to two decoupled scalar equations, characterizing two different types of waves – transverse electric (TE) and transverse magnetic (TM).

The E-field is directed in the  $x$ - $y$  plane for TE waves. Assuming that the E-field is linearly polarized, the coordinates can be rotated about the  $z$ -axis to force the E-field to point only in the  $y$  direction,  $\vec{E} = \vec{E}_y$ . For this rotation, the TM wave's magnetic field will also be  $y$ -directed. Since the magnetic field of the TE wave and the electric field of the TM wave can be found from Maxwell's equations, the EM field solution will only be described in terms of the  $y$ -components of the electric and magnetic fields.

Because of the  $\partial^2/\partial x^2$  terms embedded in (7.7), the solutions must have the form

$$\begin{bmatrix} E_y \\ H_y \end{bmatrix} = \begin{bmatrix} e_y(z) \\ h_y(z) \end{bmatrix} e^{\pm ik_x x} \quad (7.8)$$

for all  $z$  [48], where  $k_x$  is the  $x$ -directed wave number. The phase matching condition has to be satisfied in the  $x$  direction and the solution for all  $z$  must have the same phase variation,  $e^{\pm ik_x x}$ . The solutions for  $e_y$  and  $h_y$  are two decoupled scalar one-dimensional differential equations:

$$\begin{aligned} \left[ \frac{d^2}{dz^2} + \omega^2 \mu_0 \tilde{\epsilon} - k_x^2 \right] e_y &= 0 \\ \left[ \tilde{\epsilon} \frac{d}{dz} \tilde{\epsilon}^{-1} \frac{d}{dz} + \omega^2 \mu_0 \tilde{\epsilon} - k_x^2 \right] h_y &= 0 \end{aligned} \quad (7.9)$$

where

$$\begin{aligned} k &= \omega \sqrt{\mu_0 \tilde{\epsilon}} \\ &= \beta + i\alpha \end{aligned} \quad (7.10)$$

is the medium wave number with  $\beta$  and  $\alpha$  the propagation and attenuation constants respectively.

A given characteristic of the stratified media in which this study is performed, is that the different rock layers are relatively homogeneous with respect to dielectric properties. If assumed that these layers are completely homogeneous, (7.8) and (7.9) can be solved in each layer. A unique solution can be obtained by matching the boundary conditions across the discontinuities at the interfaces of the layers. For a given layer  $\tilde{\epsilon}$  is constant. The solution of (7.9) is a linear superposition of  $e^{\pm ik_z z}$ , where  $k_z = (\omega^2 \mu_0 \tilde{\epsilon} - k_x^2)^{1/2}$ . At the interface between two regions, 1 and 2, the boundary conditions for TE waves are

$$e_{1y} = e_{2y}, \quad \frac{d}{dz} e_{1y} = \frac{d}{dz} e_{2y}. \quad (7.11)$$

For TM waves, the following boundary conditions apply:

$$h_{1y} = h_{2y}, \quad \tilde{\epsilon}_1^{-1} \frac{d}{dz} h_{1y} = \tilde{\epsilon}_2^{-1} \frac{d}{dz} h_{2y}. \quad (7.12)$$

### 7.3 Reflection from a Half-Space

A half-space with two piecewise constant regions is the simplest example of a planar, one-dimensional inhomogeneity. Firstly a TE wave incident on a half-space will be considered.

Both layers are allowed to have conduction and polarization losses. It is inevitable that the plane wave will attenuate as it propagates – the characteristic of an inhomogeneous plane wave. In general, a plane wave with the form

$$e^{i\bar{k} \cdot \vec{r}} = e^{i(k_x x + k_y y + k_z z)} \quad (7.13)$$

is an inhomogeneous plane wave when  $k_x$ ,  $k_y$  and  $k_z$  are complex. This wave has two characteristic directions - the direction of increasing phase  $\hat{n}$  and the direction of decreasing amplitude  $\hat{n}'$  [49]. With

$$\begin{aligned} \bar{k} &= \hat{x}k_x + \hat{y}k_y + \hat{z}k_z \\ k_j &= \beta_j + i\alpha_j, \quad j = x, y, z \end{aligned} \quad (7.14)$$

and  $\alpha_j > 0$ , it follows that

$$e^{i\vec{k}\cdot\vec{r}} = e^{-(\alpha_x x + \alpha_y y + \alpha_z z)} e^{i(\beta_x x + \beta_y y + \beta_z z)}. \quad (7.15)$$

The directions cosines of the two characteristic directions are

$$\hat{n} = \frac{(\beta_x, \beta_y, \beta_z)}{(\beta_x^2 + \beta_y^2 + \beta_z^2)^{1/2}} \quad (7.16)$$

$$\hat{n}' = \frac{(\alpha_x, \alpha_y, \alpha_z)}{(\alpha_x^2 + \alpha_y^2 + \alpha_z^2)^{1/2}}.$$

The angle between these two directions is limited to be less than  $\pi/2$  for all lossy media. The real angle of transmission is the angle  $\psi$  between the normal  $\hat{n}$  to the plane of constant phase and the  $z$ -axis, while the real angle of attenuation is the angle  $\phi$  between the normal  $\hat{n}'$  to the plane of constant amplitude and the  $z$ -axis:

$$\psi = \sin^{-1} \frac{\beta_x}{(\beta_x^2 + \beta_z^2)^{1/2}} \quad (7.17)$$

$$\phi = \sin^{-1} \frac{\alpha_x}{(\alpha_x^2 + \alpha_z^2)^{1/2}}.$$

In this study, the assumption is made that the incident pulse has a planar phase front and the amplitude is equal across the phase front. In the frequency domain, this amounts to a sequence of inhomogeneous plane waves with their directions of increasing phase and decreasing amplitude coinciding, i.e.

$$\theta \equiv \psi = \phi. \quad (7.18)$$

This physical problem is depicted in Figure 7-2 with an inhomogeneous plane wave incident from region 1 on a planar interface between regions 1 & 2.

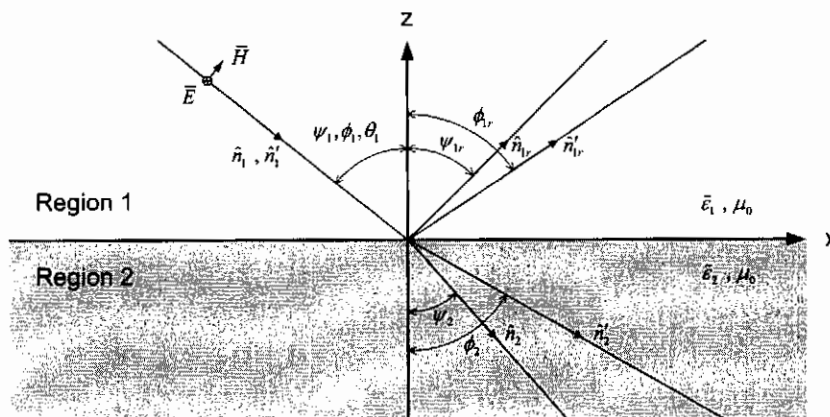


Figure 7-2: Reflection and transmission of a TE inhomogeneous plane wave at an interface.

### 7.3.1 Incident Field

For the physical problem studied in this section, (7.18) holds true that the directions of increasing phase and decreasing amplitude coincide. Furthermore, it can be derived from (7.9) that

$$k^2 = k_x^2 + k_z^2. \quad (7.19)$$

The wave numbers  $k$ ,  $k_x$  and  $k_z$  are in general complex. Equating the real and imaginary parts yields

$$\begin{aligned} \beta^2 - \alpha^2 &= \beta_x^2 + \beta_z^2 - \alpha_x^2 - \alpha_z^2 \\ \beta\alpha &= \beta_x\alpha_x + \beta_z\alpha_z. \end{aligned} \quad (7.20)$$

Using (7.17), (7.18) and (7.20), the fourth order polynomial

$$\beta_x^4 - [(\beta^2 - \alpha^2)\sin^2 \theta] \beta_x^2 - \beta^2 \alpha^2 \sin^4 \theta = 0 \quad (7.21)$$

is found. Since, by definition,  $\beta$ ,  $\alpha$ ,  $\beta_x$  are real and positive and  $\theta$  is limited to range

$$\theta \in [\{0^\circ \leq \theta \leq 90^\circ\}, \mathbb{R}] \quad (7.22)$$

the following elegant and intuitive solution is obtained:

$$\beta_x = \beta \sin \theta. \quad (7.23)$$

From (7.23), the solutions for  $\beta_z$ ,  $\alpha_x$  and  $\alpha_z$  are found:

$$\begin{aligned} \beta_z &= \beta \cos \theta \\ \alpha_x &= \alpha \sin \theta \\ \alpha_z &= \alpha \cos \theta. \end{aligned} \quad (7.24)$$

In the limiting case where  $\alpha$  equals zero, i.e. zero medium losses, (7.23) and (7.24) still holds true for  $\beta_x$  and  $\beta_z$ , but  $\alpha_x$  and  $\alpha_z$  are forced to be zero.

### 7.3.2 Reflected and Transmitted Fields

To reduce the problem to a one-dimensional space for TE waves, the E-field is expanded as

$$E_y = e_y(z) e^{ik_x x} = e_y(z) e^{j\beta_x z} e^{-\alpha_x x} \quad (7.25)$$

in both regions. In the upper half-space the solution for  $e_y(z)$  is a linear superposition of the incident wave travelling in the  $-z$  direction and the reflected wave travelling in the  $+z$  direction, i.e. a superposition of  $e^{\pm ik_z z}$ , written as

$$e_{1y}(z) = e_0 e^{-ik_{1z}z} + R^{TE} e_0 e^{ik_{1z}z} \quad (7.26)$$

where  $R^{TE}$  is the ratio of the amplitude of the reflected wave to that of the incident wave. In the lower half-space there is only a transmitted wave travelling in the  $-z$  direction, with the general expression

$$e_{2y}(z) = T^{TE} e_0 e^{-ik_{2z}z} \quad (7.27)$$

where  $T^{TE}$  is the ratio of the amplitude of the transmitted wave to that of the incident wave at  $z = 0$ . For TM waves the attention is on the behaviour of the  $y$ -directed magnetic field,  $H_y$ . In the upper half-space the total solution is once again a linear superposition of two travelling wave travelling in opposite  $z$ -directions

$$h_{1y}(z) = h_0 e^{-ik_{1z}z} + R^{TM} h_0 e^{ik_{1z}z} \quad (7.28)$$

while there is only a transmitted wave travelling in the  $-z$  direction in the lower half-space

$$h_{2y}(z) = T^{TM} h_0 e^{-ik_{2z}z}. \quad (7.29)$$

From the scalar wave equations (7.9), the following is found:

$$k_{iz} = \beta_{iz} + i\alpha_{iz} = (k_i^2 - k_{ix}^2)^{1/2}, \text{ where } k_i^2 = \omega^2 \mu_0 \tilde{\epsilon}_i. \quad (7.30)$$

In (7.30), the variables lie in the complex number plane. Care should be taken when deciding on the sign of the square root. The two solutions are called branches and they meet at the branch point. For complex or negative numbers the branches of the square root is represented by different complex planes, called Riemann surfaces [10], [43]. On each Riemann surface, the function is single-valued and deterministic. For (7.30), there are two branch points  $k_1 = k_{1x}$  and  $k_1 = -k_{1x}$ . The one Riemann surface of (7.30) yields a non-physical solution, while the other yields the physical solution. This idea of the physical solution will be returned to.

With  $k_{1z}$  on the correct Riemann surface, the boundary conditions [43] are solved, yielding the Fresnel reflection and transmission coefficients for TE waves

$$\begin{aligned} R^{TE} &= \frac{k_{1z} - k_{2z}}{k_{1z} + k_{2z}} \\ T^{TE} &= \frac{2k_{1z}}{k_{1z} + k_{2z}}. \end{aligned} \quad (7.31)$$

The Fresnel coefficients for TM waves

$$\begin{aligned}
 R^{TM} &= \frac{\tilde{\epsilon}_2 k_{1z} - \tilde{\epsilon}_1 k_{2z}}{\tilde{\epsilon}_2 k_{1z} + \tilde{\epsilon}_1 k_{2z}} \\
 T^{TM} &= \frac{2\tilde{\epsilon}_2 k_{1z}}{\tilde{\epsilon}_2 k_{1z} + \tilde{\epsilon}_1 k_{2z}}
 \end{aligned} \tag{7.32}$$

can be found using the same principle. A number of interesting propagation phenomena are encountered in different regions of the  $k_{1x}$  complex space (i.e. different incident angles – in this case real and coinciding). In lossless media the two main phenomena encountered are total internal reflection ( $k_1 > k_2$  and the magnitude of  $R^{TE}$  equals 1) and the Brewster effect (no reflected wave). The Brewster effect is observed only when  $\mu_1/\mu_2 \neq 1$  for TE waves and  $\epsilon_1/\epsilon_2 \neq 1$  for TM waves. For lossy media the Brewster effect and total internal reflection is observed only in special cases, but the more common pseudo-Brewster effect is frequently observed. The latter is defined as the angle at which the modulus of the reflection coefficient is a minimum [65]. In general there will not be total internal reflection, since both propagation coefficients in the  $z$ -direction are complex (have real components).

It has been stated that (7.30) yields two solutions for  $k_{2z}$  – the propagation constant in the second medium in the  $z$ -direction. The chosen solution is to obey the laws of physics. These can be summarized as follows:

- i. The incident-, reflected- and transmitted waves have to be causal. This implies that the direction of time averaged power flow (Poynting vector) has to be in positive  $x$ -direction for all waves, in the negative  $z$ -direction for the incident- and transmitted waves and in the positive  $z$ -direction for the reflected wave.
- ii. The total time averaged power in the reflected- and transmitted waves has to be equal to or smaller than the time averaged power in the incident wave, i.e. energy conservation.

### 7.3.3 Branch Choice for TE Waves

For the incident wave, using (7.25), (7.26), Faraday's law and the identity  $\nabla \times \vec{E} = i\vec{k} \times \vec{E}$  for plane waves, the real part of the complex Poynting vector (equal to the time averaged power flux density) is

$$\text{Re} \left\{ \vec{S}_{incident} = \frac{1}{2} \vec{E} \times \vec{H}^* \right\} = \frac{|e_0|^2}{2\omega\mu_0} e^{-2(\alpha_1 x - \alpha_1 z)} (\beta_{1x} \hat{x} - \beta_{1z} \hat{z}). \tag{7.33}$$

For the incident wave to be causal and with the real power flow in the positive  $x$ - and negative  $z$ -direction, both phase constants  $\beta_{1x}$  and  $\beta_{1z}$  must be positive. In the same way the real part of the complex Poynting vectors of the reflected and transmitted waves are

$$\begin{aligned} \operatorname{Re}\{\bar{S}_{\text{reflected}}\} &= \frac{|R^{TE}|^2 |e_0|^2}{2\omega\mu_0} e^{-2(\alpha_{1x}x + \alpha_{1z}z)} (\beta_{1x}\hat{x} + \beta_{1z}\hat{z}) \\ \operatorname{Re}\{\bar{S}_{\text{transmitted}}\} &= \frac{|T^{TE}|^2 |e_0|^2}{2\omega\mu_0} e^{-2(\alpha_{1x}x - \alpha_{2z}z)} (\beta_{1x}\hat{x} - \beta_{2z}\hat{z}). \end{aligned} \quad (7.34)$$

Once again, for the reflected- and transmitted waves to be causal and for their average real power to flow in the correct direction, the phase constants  $\beta_{1x}$ ,  $\beta_{1z}$  and  $\beta_{2z}$  have to be positive.

The second physical constraint implies that the magnitude of the reflection coefficient has to be less than (or equal to) unity. The square of the magnitude of the reflection coefficient can also be considered. This can be rewritten in terms of the phase- and attenuation constants in the two regions:

$$|R^{TE}|^2 = 1 - 4 \frac{\beta_{1z}\beta_{2z} + \alpha_{1z}\alpha_{2z}}{(\beta_{1z} + \beta_{2z})^2 + (\alpha_{1z} + \alpha_{2z})^2}. \quad (7.35)$$

For a reflection coefficient smaller than unity, the branch has to be chosen such that

$$\beta_{1z}\beta_{2z} + \alpha_{1z}\alpha_{2z} \geq 0 \quad (7.36)$$

or alternatively

$$\operatorname{Re}\{k_{1z} \cdot k_{2z}^*\} \geq 0. \quad (7.37)$$

Rewriting  $k_{1z}$  and  $k_{2z}$  in phasor notation, i.e.

$$k_{1z} = r_1 e^{i\chi_1} \quad \text{and} \quad k_{2z} = r_2 e^{i\chi_2} \quad (7.38)$$

the constraints in (7.36) and (7.37) are equal to

$$\cos(\chi_1 - \chi_2) \geq 0. \quad (7.39)$$

Since the one branch of (7.30) is the negative of the other, the reflection coefficient of the one is the inverse of the other and will be larger than unity if the other is smaller. Assuming that one of the solutions is proper (i.e. can be excited by a physical source, albeit at infinity), it will be causal with a reflection coefficient smaller than unity.

The  $k_{2z}^2$  space in the complex plane maps to two different regions in the  $k_{2z}$  space. Depending on the location of  $k_{2z}^2$  in the complex plane, different observations can be made of the behaviour of the reflected and transmitted waves. The  $k_{2z}^2$ -complex plane can be divided into four different regions with different physical properties and interpretations, as will be discussed.

### 7.3.3.1 Region A with $\text{Im}\{k_{2z}^2\} \geq 0$

The mapping of the complex space where  $\text{Im}\{k_{2z}^2\} \geq 0$  is depicted in Figure 7-3.

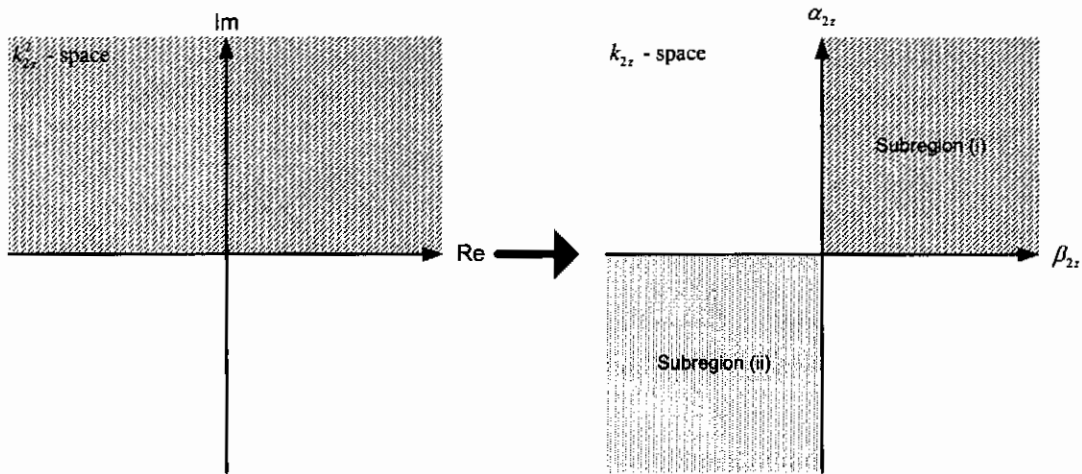


Figure 7-3: Mapping of  $k_{2z}^2$  for  $\text{Im}\{k_{2z}^2\} \geq 0$  to the  $k_{2z}$  space.

Two subregions (i) and (ii) are associated with the two branches. Considering subregion (i), it is noted that both  $\alpha_{2z}$  and  $\beta_{2z}$  are positive. According to (7.34) this solution is causal and according to (7.36) it is also the solution with a reflection coefficient smaller than unity, since for homogeneous, isotropic media  $\alpha_1 \geq 0$  and  $\beta_1 > 0$ . For real incident angles  $\theta_1$ , the following is found:

$$\begin{aligned}\beta_{1z} &= \beta_1 \cos \theta_1 \geq 0 \\ \alpha_{1z} &= \alpha_1 \cos \theta_1 \geq 0.\end{aligned}\tag{7.40}$$

For subregion (ii) it can be shown that the solution is non-causal. It yields a reflection coefficient larger than unity and is associated with the improper mode.

In Region A, subregion (i) is associated with the proper inhomogeneous plane wave whose average real energy is moving in the positive  $x$ - and negative  $z$ -direction in the lower half-space.

### 7.3.3.2 Region B with $\text{Im}\{k_{2z}^2\} \leq 0$ and $\text{Re}\{k_{2z}^2\} \geq 0$

The mapping of the complex space where  $\text{Im}\{k_{2z}^2\} \leq 0$  and  $\text{Re}\{k_{2z}^2\} \geq 0$  is depicted in Figure 7-4.

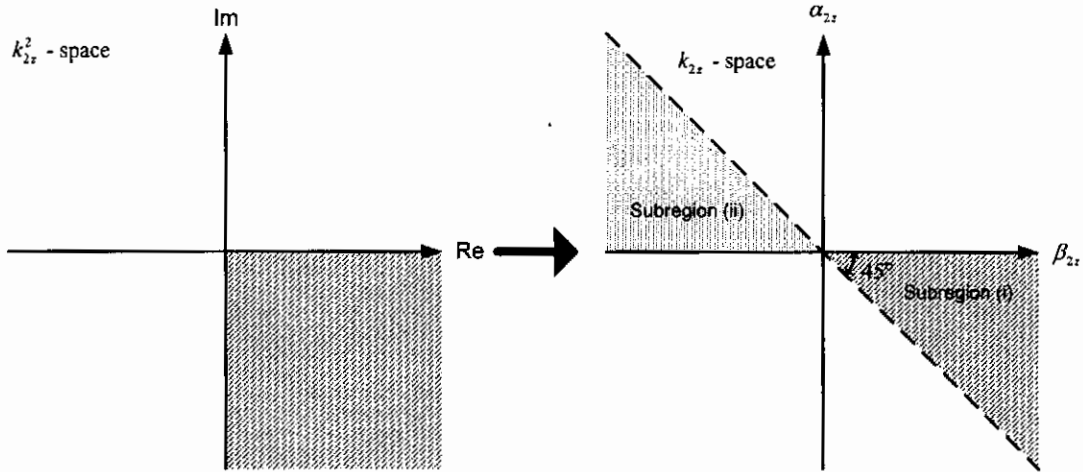


Figure 7-4: Mapping of  $k_{2z}^2$  for  $\text{Im}\{k_{2z}^2\} \leq 0$  and  $\text{Re}\{k_{2z}^2\} \geq 0$  to the  $k_{2z}$  space.

In subregion (i) it can be noted that  $\beta_{2z} \geq 0$ ,  $\alpha_{2z} \leq 0$  and  $|\beta_{2z}| \geq |\alpha_{2z}|$ . For a homogeneous, isotropic medium  $\beta_1 \geq \alpha_1$  and for  $\theta_1$  real

$$\beta_{1z} \geq \alpha_{1z}. \quad (7.41)$$

From this it is clear that the condition for a reflection coefficient smaller than unity (7.36) is met and the solution in subregion (ii) is causal. However, there is once again the controversy where  $\alpha_{2z}$  is negative, but the resultant waves seem to adhere to the law of energy conservation. It has been stated in the beginning of Section 7.3 that the angle between the directions of increasing phase increase and decreasing amplitude is less than  $\pi/2$ . The projection of  $\hat{n}'$  onto  $\hat{n}$  is therefore greater than zero, implying that the signal is attenuated in the direction of propagation (i.e the direction of increasing phase). After careful consideration it is clear that this is an analogy of the improper leaky wave observed in leaky wave slot antennas [52],[43]. Since the leaky wave is an improper wave, it cannot exist by itself, but it can exist within a portion of space.

In subregion (ii) the solution is non-causal and the reflection coefficient is larger than unity, therefore the solution is an improper mode.

In region B, both subregions (i) and (ii) yield improper modes. The solution of subregion (i), however is proper within a portion of space, yielding a leaky plane

wave whose average real energy is moving in the positive  $x$ - and negative  $z$ -direction in the lower half-space.

### 7.3.3.3 Region C with $\text{Im}\{k_{2z}^2\} \leq 0$ , $\text{Re}\{k_{2z}^2\} \leq 0$ and $\delta_2 < \delta_1$

For both regions C and D there is the constraint that  $\text{Im}\{k_{2z}^2\} \leq 0$  and  $\text{Re}\{k_{2z}^2\} \leq 0$ , which can be rewritten (when expanded) as

$$\begin{aligned} \varepsilon_1' \tan \delta_1 \sin^2 \theta_1 &\geq \varepsilon_2' \tan \delta_2 \\ \varepsilon_1' \sin^2 \theta_1 &\geq \varepsilon_2'. \end{aligned} \quad (7.42)$$

For  $\theta_1$  real, this implies also that

$$\begin{aligned} \varepsilon_1' \tan \delta_1 &\geq \varepsilon_2' \tan \delta_2 \\ \varepsilon_1' &\geq \varepsilon_2'. \end{aligned} \quad (7.43)$$

The behaviour of  $k_1^2$ ,  $k_1^2 \sin^2 \theta_1$  and  $k_2^2$  for the region where  $\delta_1 < \delta_2$  in the complex plane can be studied with the help of Figure 7-5.

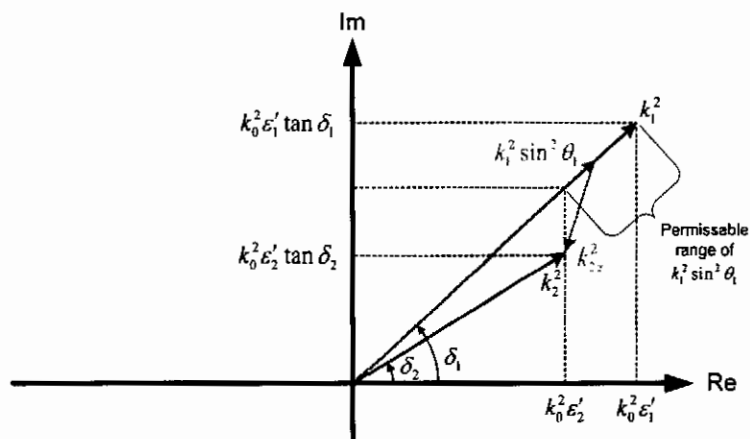


Figure 7-5: The behaviour of the squares of  $k_1$ ,  $k_1 \sin \theta_1$ ,  $k_2$  and  $k_{2z}$  in the complex plane for  $\delta_2 < \delta_1$ .

A careful study of Figure 7-5 reveals that  $k_{2z}^2$  lies in the 3<sup>rd</sup> quadrant of the complex plane with a minimum angle of  $\pi + \delta_1$  and a maximum angle of  $3\pi/2$ . Therefore the mapping occurs as shown in Figure 7-6.

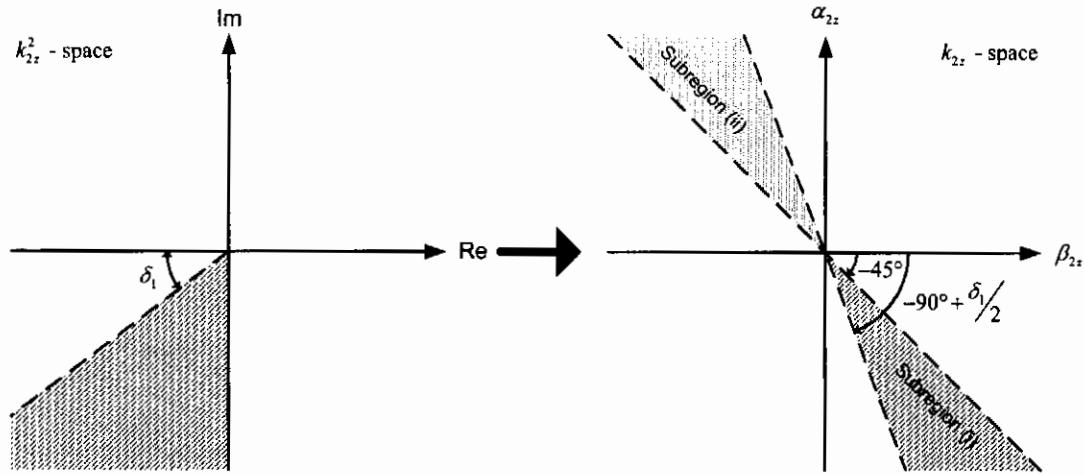


Figure 7-6: Mapping of  $k_{2z}^2$  for  $\text{Im}\{k_{2z}^2\} \leq 0$ ,  $\text{Re}\{k_{2z}^2\} \geq 0$  and  $\delta_2 < \delta_1$  to the  $k_{2z}$  space.

In subregion (i) once again  $\alpha_{2z} \leq 0$  and  $\beta_{2z} \geq 0$ , but now the attenuation constant is larger than the phase constant  $|\alpha_{2z}| \geq |\beta_{2z}|$ . It is not clear from (7.36) that this solution yields a reflection coefficient smaller than unity. Looking at the angles  $\chi_1$  and  $\chi_2$  as defined in (7.38), the following mutually inclusive constraints for region C are found:

$$\begin{aligned} 0^\circ &\leq \chi_1 \leq 45^\circ \\ -90^\circ + \frac{\delta_1}{2} &\leq \chi_2 \leq -45^\circ \\ 45^\circ + \chi_1 &\leq \chi_1 - \chi_2 \leq 90^\circ. \end{aligned} \quad (7.44)$$

From (7.44) it is clear that the constraint for passivity as stated in (7.39) is met. Therefore, the solution in subregion (i) is once again improper ( $\alpha_{2z} \leq 0$ ) in general, but proper in a portion of space. The solution is causal, yields a reflection coefficient smaller than unity and attenuates in the direction of propagation.

The solution in subregion (ii) on the other hand is non-causal with a reflection coefficient larger than unity and therefore an improper mode.

#### 7.3.3.4 Region D with $\text{Im}\{k_{2z}^2\} \leq 0$ , $\text{Re}\{k_{2z}^2\} \leq 0$ and $\delta_2 > \delta_1$

The behaviour of  $k_1^2$ ,  $k_1^2 \sin^2 \theta_1$  and  $k_2^2$  for the region where  $\delta_1 < \delta_2$  in the complex plane can be studied by way of Figure 7-7. Studying this graphical representation of the vectors reveals that  $k_{2z}^2$  lies in the 3<sup>rd</sup> quadrant of the complex plane with a minimum angle of  $\pi$  and a maximum angle of  $\pi + \delta_1$ . Therefore the mapping occurs as shown in Figure 7-8.

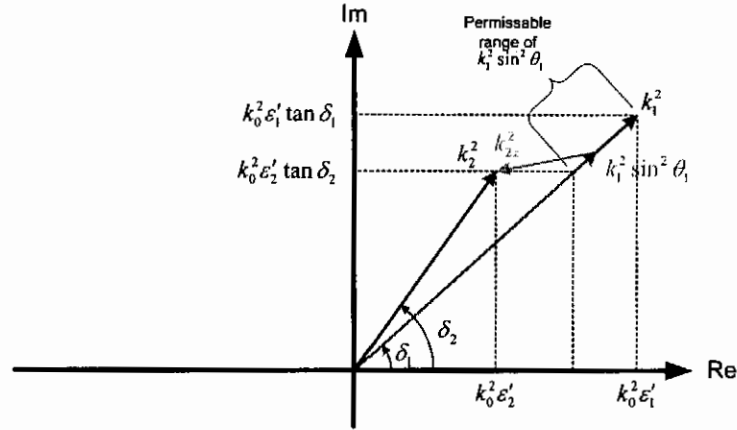


Figure 7-7: The behaviour of the squares of  $k_1$ ,  $k_1 \sin \theta_1$ ,  $k_2$  and  $k_{2z}$  in the complex plane for  $\delta_2 > \delta_1$ .

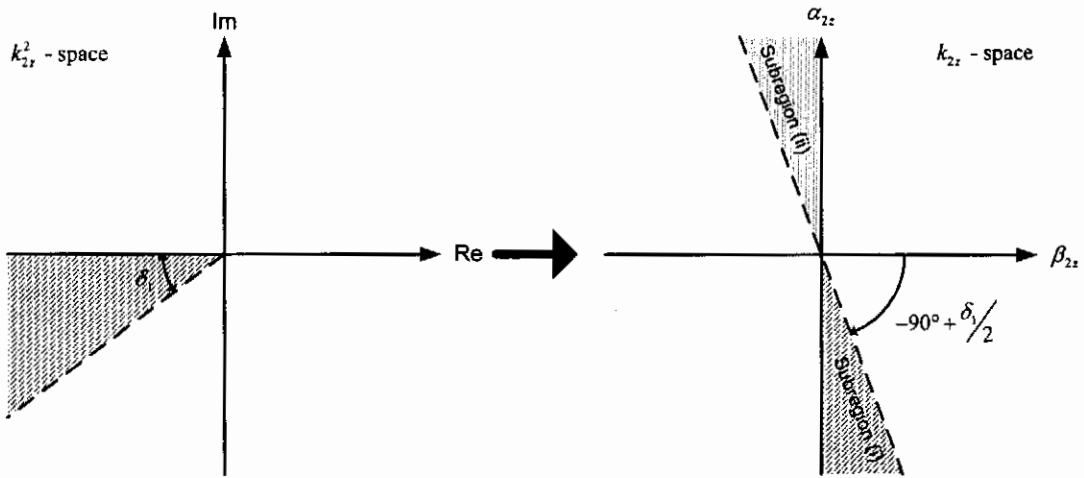


Figure 7-8: Mapping of  $k_{2z}^2$  for  $\text{Im}\{k_{2z}^2\} \leq 0$ ,  $\text{Re}\{k_{2z}^2\} \geq 0$  and  $\delta_2 > \delta_1$  to the  $k_{2z}$  space.

As in region C, it is found in subregion (i) that  $\alpha_{2z} \leq 0$ ,  $\beta_{2z} \geq 0$  and also  $|\alpha_{2z}| \geq |\beta_{2z}|$ .

The restriction, in subregion (i) of region D, on the angles  $\chi_1$  and  $\chi_2$  are that

$$\begin{aligned} 0^\circ &\leq \chi_1 \leq 45^\circ \\ -90^\circ &\leq \chi_2 \leq -90^\circ + \frac{\delta_1}{2} \\ 90^\circ &\leq \chi_1 - \chi_2 \leq 90^\circ + \chi_1. \end{aligned} \tag{7.45}$$

From (7.45), it is found that the solution in subregion (i) yields a reflection coefficient larger than unity while the solution is causal and attenuates in the direction of propagation. The solution in subregion (ii) will subsequently yield a reflection coefficient smaller than unity, but is non-causal. Once again, there is a controversy about the existence of either of the two solutions.

Let us consider a numeric example at a centre frequency of 50 MHz with the following media parameters:

$$\varepsilon_1' = 6, \quad \tan \delta_1 = 0.05$$

$$\varepsilon_1'' = 4, \quad \tan \delta_1 = 0.06.$$

The incident angle  $\theta_1$  is taken as  $70^\circ$  in order to satisfy (7.42). With these input parameters, the solution in subregion (i) yields the following output parameters:

$$k_{1,x} = 2.4128 + 0.0603i$$

$$k_{2,z}^2 = -1.4255 - 0.0274i$$

$$k_{2,z} = 0.0115 - 1.1940i$$

$$R^{TE} = -0.3021 + 0.9688i$$

$$|R^{TE}| = 1.0148.$$

Clearly the magnitude of the reflection coefficient is larger than unity. This should not be possible, but is it?

Looking at the numerical example, it is evident that the wave number in the  $z$ -direction is mainly imaginary. The transmitted wave is therefore mostly attenuating in the negative  $z$ -direction, while it is propagating in the positive  $x$ -direction. The transmitted wave therefore has the same characteristics as the evanescent transmitted wave when the incidence angle is greater than the critical angle for lossless media. The physical behaviour of the reflected and transmitted wave in lossless media, when the incidence angle is larger than the critical angle, is called the Goos-Hanchen effect [43]. In essence the reflected beam is proportional to the beam from the image point with a lateral shift. In the definition of the reflection coefficient, we assume that the source of the reflected wave is the incident wave at the same  $x$ -location on the boundary, i.e. a localized reflection point. When the Goos-Hanchen effect is at play however, the source of the reflected wave is the incident wave at a different position on the  $x$ -axis. The condition for a reflection adhering to the law of energy conservation when the Goos-Hanchen effect is observed, should therefore be reformulated as follows:

***The power in the reflected wave should be less than or equal to the power in the source of the reflected wave (the incident wave), which is laterally shifted.***

In order to prove that solution in subregion (i) is valid, it has to be shown that the abovementioned condition is met. This will be considered in the following sections.

### 7.3.4 TE Beam Wave Incident on Planar Inhomogeneity

The reflection coefficient for a plane wave incident on a planar inhomogeneity might be a complex number. The reflected wave is therefore shifted in space, or time, due to the additional phase in the reflection coefficient. It is however difficult to understand the physics of this phase change by only considering plane waves. Greater physical insight is gained when a beam wave (similar to the plane wave) incident on the planar inhomogeneity is considered.

Consider a beam wave incident on a planar inhomogeneity at an incidence angle of  $\theta_1 = \theta_0$  as depicted in Figure 7-9.

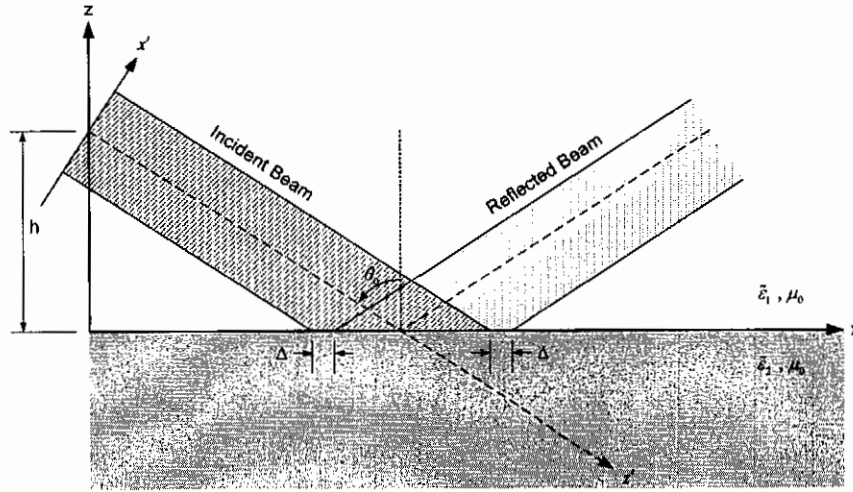


Figure 7-9: Beam wave incident on planar inhomogeneity

The incident beam,  $u_i(x', z')$ , can be written as

$$u_i(x', z') = A(x') e^{ik_1 z'} \quad (7.46)$$

with the coordinate transformation

$$\begin{bmatrix} x' \\ z' \end{bmatrix} = \begin{bmatrix} \cos \theta_0 & \sin \theta_0 \\ \sin \theta_0 & -\cos \theta_0 \end{bmatrix} \begin{bmatrix} x \\ z - h \end{bmatrix}. \quad (7.47)$$

The incident beam wave can be reconstructed from the spectral representation of the incident beam wave at  $z = h$  using the inverse Fourier transform [43].

$$u_i(x, z) = \frac{1}{2\pi} \int_{-\infty}^{\infty} U(k_x - k_{0x}) e^{ik_x x - ik_{1z}(z-h)} dk_x, \quad k_{1z}^2 = k_1^2 - k_x^2 \quad (7.48)$$

The reflected- and transmitted waves,  $u_r(x, z)$  and  $u_t(x, z)$ , can be written as

$$\begin{aligned}
 u_r(x, z) &= \frac{1}{2\pi} \int_{-\infty}^{\infty} R(k_x) U(k_x - k_{0x}) e^{ik_x x + ik_{1z}(z+h)} dk_x \\
 u_t(x, z) &= \frac{1}{2\pi} \int_{-\infty}^{\infty} T(k_x) U(k_x - k_{0x}) e^{ik_x x - ik_{2z}z + ik_{1z}h} dk_x.
 \end{aligned} \tag{7.49}$$

In (7.49),  $R(k_x)$  and  $T(k_x)$  are the reflection and transmission coefficients. The reflected field will be examined for two different cases in the following subsections.

### 7.3.4.1 Lossless Media with $\theta_0 > \theta_c$

When  $\theta_0$  is larger than the critical angle for total internal reflection, the wave number in the lower half-space in the  $z$ -direction becomes purely imaginary

$$k_{2z} = i\alpha_{2z}. \tag{7.50}$$

From this it is clear that the reflection coefficient will be a complex number with unity magnitude and can be rewritten as a phasor

$$\begin{aligned}
 R(k_x) &= \exp[-i\phi(k_x)] \\
 \phi(k_x) &= 2 \tan^{-1} \left( \frac{\alpha_{2z}}{k_{1z}} \right).
 \end{aligned} \tag{7.51}$$

It is possible to expand  $\phi(k_x)$  in a 2-term Taylor's series about  $k_{0x}$ , because the major contribution to the integral (7.49) comes from the neighbourhood of  $k_x = k_{0x}$ :

$$\phi(k_x) = \phi(k_{0x}) + (k_x - k_{0x}) \phi'(k_{0x}). \tag{7.52}$$

The reflection coefficient now takes on the form

$$R(k_x) = R(k_{0x}) e^{ik_{0x} \phi'(k_{0x})} e^{-ik_x \phi'(k_{0x})} \tag{7.53}$$

yielding the reflected beam wave

$$u_r(x, z) = R(k_{0x}) e^{ik_{0x} \phi'(k_{0x})} u_{r,0}(x - \phi'(k_{0x}), z). \tag{7.54}$$

The reflected beam is proportional to the source's image with a lateral shift of  $\Delta = \phi'(k_{0x})$ . This shift is called the Goos-Hanchen effect [43]. The phase derivative (i.e. lateral shift) has been derived in terms of the incidence angle and the attenuation constant in the lower half-space:

$$\phi'(k_x) = \frac{2 \tan \theta_1}{\alpha_{2z}}. \tag{7.55}$$

The shift increases as the incidence angle approaches the critical angle, striving towards infinity. It also has a singularity at  $\theta_0 = 90^\circ$ . As  $\theta_0$  approaches the critical angle however, the higher order terms of the Taylor series become significant and the reflected rays form what is known as a caustic [43].

### 7.3.4.2 Lossy Media

When the media in the two half-spaces are allowed to have dielectric losses, the reflection coefficient is complex for any arbitrary incidence angle. There is even a subset of solutions (region D) where the magnitude of the reflection coefficient is not bound to be less than or equal to unity. Clearly, the reflection coefficient is therefore a phasor with a given magnitude and phase response

$$R(k_x) = |R(k_x)| e^{-i\phi(k_x)}. \quad (7.56)$$

In order to simplify (7.49), it may first be assumed that the magnitude of the reflection coefficient can be approximated as the magnitude of the reflection coefficient at  $k_x = k_{0x}$ . The second assumption is that the phase can be approximated as a Taylor's series about  $k_x = k_{0x}$  with only two terms:

$$\begin{aligned} |R(k_x)| &\sim |R(k_{0x})| \\ \phi(k_x) &= \phi(k_{0x}) + (k_x - k_{0x})\phi'(k_{0x}). \end{aligned} \quad (7.57)$$

Under the abovementioned assumptions, the reflection coefficient takes on the same form as in (7.53). The reflected beam wave can be expressed as

$$\begin{aligned} u_r(x, z) &= \left[ R(k_{0x}) e^{-\alpha_{0x}\phi'(k_{0x})} \right] e^{i\beta_{0x}\phi'(k_{0x})} u_{r0}(x - \phi'(k_{0x}), z) \\ &= R'(k_{0x}) e^{i\beta_{0x}\phi'(k_{0x})} u_{r0}(x - \phi'(k_{0x}), z) \\ R'(k_{0x}) &= R(k_{0x}) e^{-\alpha_{0x}\phi'(k_{0x})}. \end{aligned} \quad (7.58)$$

The reflected beam wave is therefore proportional to the beam from the image point with the lateral shift of  $\Delta = \phi'(k_{0x})$ . We note that the magnitude of the modified reflection coefficient  $R'(k_{0x})$  has to be less than or equal to unity. It is therefore possible that, when  $\phi'(k_{0x})$  is positive, the magnitude of the standard reflection coefficient is larger than unity with the restriction that

$$|R(k_{0x})| \leq e^{\alpha_{0x}\phi'(k_{0x})}. \quad (7.59)$$

In order to show that the solution in subregion (i) of region D is proper, we have to show that (7.59) is satisfied. In the derivation of (7.59) however, a number of assumptions were made. The validity of these assumptions has to be verified. It should also be noted that in (7.57) and (7.58) it is assumed that the derivative of  $\phi(k_x)$  (a complex variable function), exists (it has to be analytical) and is a real quantity. This is not proved in this section, since the purpose of this section is merely to explain the phenomenon of beam shift at the planar interface between two lossy media.

### 7.3.5 Energy Conservation for TE Waves

One of the basic laws of electromagnetics is that of energy conservation in a finite volume [41]. In a given volume  $V$ , the energy is distributed through space with an energy density  $W(\vec{r}, t)$  ( $J/m^3$ ) and the power is dissipated locally at a rate per unit volume  $P_d(\vec{r}, t)$  ( $W/m^3$ ). The power flows with a density  $\vec{S}(\vec{r}, t)$ . The law of energy conservation [41] states that power flowing into a volume  $V$ , enclosed by the surface  $S$ , must be given as:

$$-\oint_S \vec{S}(\vec{r}, t) \cdot d\vec{a} = \frac{d}{dt} \int_V W(\vec{r}, t) dv + \int_V P_d(\vec{r}, t) dv. \quad (7.60)$$

Considering steady state sinusoidal excitation and integrating the energy conservation law over the period  $T$ , the time averaged energy conservation law then becomes

$$-\left\langle \oint_S \vec{S}(\vec{r}, t) \cdot d\vec{a} \right\rangle = \left\langle \int_V P_d(\vec{r}, t) dv \right\rangle \quad (7.61)$$

where  $\langle \rangle$  indicates the time averaging of the operand. (7.61) states that the time average of the power flowing into the volume  $V$  equals the time average of the power dissipated in the volume  $V$ . With a fixed volume, the time averaging operator can be taken inside the integrals. Using the time averaging theorem [41] the time average of the power flux density is given as:

$$\begin{aligned} \langle \vec{S}(\vec{r}, t) \rangle &= \text{Re} \{ \vec{S}(\vec{r}, \omega) \} \\ \vec{S}(\vec{r}, \omega) &= \frac{1}{2} [ \vec{E}(\vec{r}, \omega) \times \vec{H}^*(\vec{r}, \omega) ]. \end{aligned} \quad (7.62)$$

It has been derived [41] that the time averaged electrical dissipation density is

$$\langle P_d(\vec{r}, t) \rangle = \frac{\omega \epsilon_0 \tilde{\epsilon}' \tan \delta | \vec{E}(\vec{r}, \omega) |^2}{2}. \quad (7.63)$$

Using (7.25)-(7.27) and writing the reflection coefficient as a phasor

$$R^{TE} = |R^{TE}| e^{i\phi_R} \quad (7.64)$$

the time averaged power dissipation densities in the two half-spaces are given by

$$\langle P_{d1} \rangle = \frac{\omega \epsilon_0 \tilde{\epsilon}'_1 \tan \delta_1 |e_0|^2}{2} e^{-2\alpha_1 x} \left[ 2 |R^{TE}| \cos(\phi_R + 2\beta_{1z} z) + e^{2\alpha_1 z} + |R^{TE}|^2 e^{-2\alpha_1 z} \right] \quad (7.65)$$

$$\langle P_{d2} \rangle = \frac{\omega \epsilon_0 \tilde{\epsilon}'_2 \tan \delta_2 |T^{TE}|^2 |e_0|^2}{2} e^{-2(\alpha_1 x - \alpha_2 z)}. \quad (7.66)$$

The first term on the right hand side of (7.65) is due to the cross product of the incident and the reflected waves. The time averaged power densities for both half-spaces are

$$\begin{aligned}
 \langle \bar{S}_1 \rangle &= \langle S_{1x} \rangle \hat{x} + \langle S_{1z} \rangle \hat{z} \\
 \langle S_{1x} \rangle &= \frac{|e_0|^2 \beta_x}{2\omega\mu_0} e^{-2\alpha_x x} \left[ e^{2\alpha_{1z} z} + 2|R^{TE}| \cos(\phi_R + 2\beta_{1z} z) + |R^{TE}|^2 e^{-2\alpha_{1z} z} \right] \\
 \langle S_{1z} \rangle &= -\frac{|e_0|^2}{2\omega\mu_0} e^{-2\alpha_x x} \left[ \beta_{1z} \left( e^{2\alpha_{1z} z} - |R^{TE}|^2 e^{-2\alpha_{1z} z} \right) \right. \\
 &\quad \left. + 2\alpha_{1z} |R^{TE}| \sin(\phi_R + 2\beta_{1z} z) \right] \\
 \langle \bar{S}_2 \rangle &= \frac{|e_0|^2 |T^{TE}|^2}{2\omega\mu_0} e^{-2(\alpha_x x - \alpha_{2z} z)} (\beta_x \hat{x} - \beta_{2z} \hat{z}).
 \end{aligned} \tag{7.67}$$

Using (7.65) - (7.67) it is possible to determine whether or not the energy conservation law is satisfied for any arbitrary closed volume in either, or both, half-spaces. Of specific interest is energy conservation when a TE wave is incident on a planar interface between two media with the magnitude of the reflection coefficient is larger than unity as discussed in Section 7.3.3.4 .

Consider the rectangular volume  $V$  with planes parallel to the main axes depicted in Figure 7-10.

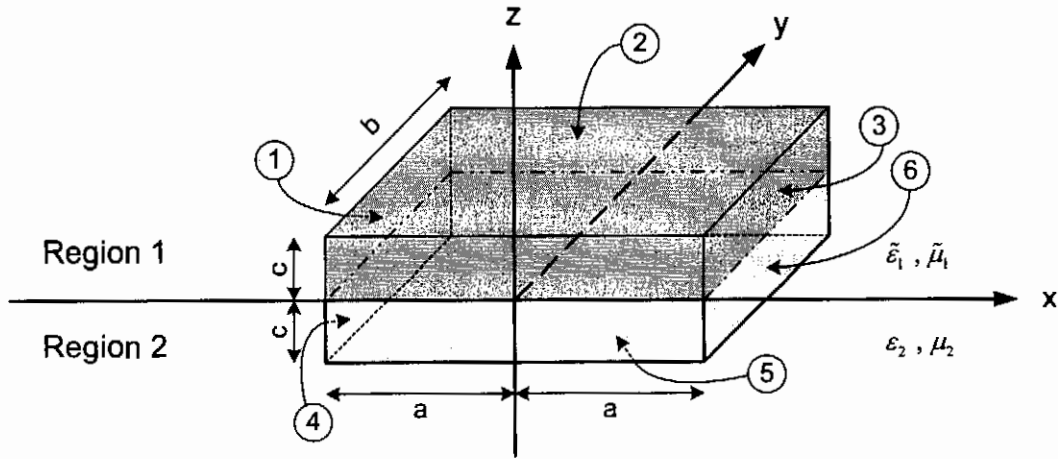


Figure 7-10: Closed volume  $V$  for energy conservation calculations.

Since the power flux densities in both half-spaces are only  $x$ - and  $y$ -directed, the only contributions to the surface integral (7.61) are from surfaces 1 to 6. Using (7.67), the surface integral can be calculated for each surface and then added to find the time averaged power flowing into the volume:

$$\begin{aligned}
 -\oint_S \langle \bar{S} \rangle \cdot d\bar{a} &= \frac{b|e_0|^2 \beta_x}{2\omega\mu_0} (e^{2\alpha_x a} - e^{-2\alpha_x a}) f_1(k_{1z}, k_{2z}, c) \\
 &+ \frac{b|e_0|^2}{4\omega\mu_0 \alpha_x} (e^{2\alpha_x a} - e^{-2\alpha_x a}) f_2(k_{1z}, k_{2z}, c) \\
 &+ \frac{b|e_0|^2 |T^{TE}|^2}{4\omega\mu_0} (e^{2\alpha_x a} - e^{-2\alpha_x a}) \left[ \frac{\beta_x}{\alpha_{2z}} (1 - e^{-2\alpha_{2z} c}) - \frac{\beta_{2z}}{\alpha_x} e^{-2\alpha_{2z} c} \right] \quad (7.68) \\
 f_1(k_{1z}, k_{2z}, c) &= \frac{1}{2\alpha_{1z}} (e^{2\alpha_{1z} c} - 1) + \frac{|R^{TE}|^2}{2\alpha_{1z}} (1 - e^{-2\alpha_{1z} c}) \\
 &+ \frac{|R^{TE}|}{\beta_{1z}} [\sin(\phi_R + 2\beta_{1z} c) - \sin(\phi_R)] \\
 f_2(k_{1z}, k_{2z}, c) &= \beta_{1z} (e^{2\alpha_{1z} c} - |R^{TE}|^2 e^{-2\alpha_{1z} c}) + 2\alpha_{1z} |R^{TE}| \sin(\phi_R + 2\beta_{1z} c).
 \end{aligned}$$

The time averaged power dissipation in volume V are calculated using (7.65) and (7.66):

$$\begin{aligned}
 \int_V \langle P_d \rangle dv &= \frac{b|e_0|^2 \omega \epsilon_0 \tilde{\epsilon}'_1 \tan \delta_1}{4\alpha_x} (e^{2\alpha_x a} - e^{-2\alpha_x a}) f_1(k_{1z}, k_{2z}, c) \\
 &+ \frac{b|e_0|^2 |T^{TE}|^2 \omega \epsilon_0 \tilde{\epsilon}'_2 \tan \delta_2}{8\alpha_x \alpha_{2z}} (e^{2\alpha_x a} - e^{-2\alpha_x a}) (1 - e^{-2\alpha_{2z} c}). \quad (7.69)
 \end{aligned}$$

It can be derived that the energy conservation law equation (7.61) is independent of  $c$  for TE waves. The first step in doing so is to realize that the energy conservation law has to apply to plane waves in a homogeneous medium. Therefore, for the transmitted wave it is found that

$$-\int_{S_4+S_5+S_6} \langle \bar{S}_{transmitted} \rangle \cdot d\bar{a} - \int_{S_0} \langle \bar{S}_{transmitted} \rangle \cdot d\bar{a} = \int_{V_2} \langle P_{d(transmitted)} \rangle dv \quad (7.70)$$

where  $S_0$  is the surface in the  $xy$ -plane with  $z = 0$ . If the energy conservation law equation is independent of  $c$ , the sum of all terms dependant on  $c$  has to be a constant (independent off  $c$ ):

$$K_1 = \left( \frac{\beta_x}{4\omega\mu_0 \alpha_{1z}} + \frac{\beta_{1z}}{4\omega\mu_0 \alpha_x} - \frac{\omega \epsilon_0 \tilde{\epsilon}'_1 \tan \delta_1}{8\alpha_x \alpha_{1z}} \right) \left[ \frac{2\alpha_{1z}}{\beta_{1z}} |R^{TE}| \sin(\phi_R + 2\beta_{1z} c) \right] \left[ +e^{2\alpha_{1z} c} - |R^{TE}|^2 e^{-2\alpha_{1z} c} \right] \quad (7.71)$$

where  $K_1$  is constant. Parametric manipulation shows that

$$\omega^2 \mu_0 \epsilon_0 \tilde{\epsilon}'_1 \tan \delta_1 = 2\beta_{1z} \alpha_{1z}. \quad (7.72)$$

Using (7.72) yields  $K_1$  to be constant and also equal to zero. For the energy conservation law to hold, the sum of the terms in (7.61) that are independent of  $c$  has to be zero. This restriction can be simplified with the use of (7.72):

$$\beta_{1z} \left(1 - |R^{TE}|^2\right) + 2|R^{TE}| \sin(\phi_R) \alpha_{1z} = |T^{TE}|^2 \beta_{2z}. \quad (7.73)$$

If the definitions of  $R^{TE}$  and  $T^{TE}$  are expanded in terms of the real and imaginary parts of  $k_{1z}$  and  $k_{2z}$ , and realizing that

$$|R^{TE}| \sin \phi_R = \text{Im} \{ R^{TE} \} \quad (7.74)$$

it is easy to show that (7.73) and therefore also the energy conservation law holds true in general for TE plane waves incident on a planar interface between two lossy dielectric media.

The very important consequence of this derivation is that the plane wave propagation solution with a magnitude of greater than unity is proper, provided that the direction of average real power flow is in the correct direction. The TE wave solution in subregion (i) of region D in the  $k_{2z}^2$  space is therefore proper, since the direction of average real power flow is in the positive  $x$ - and negative  $z$ - direction and the energy conservation law is satisfied. In other words, energy is neither created nor destroyed at the interface between the two media.

### 7.3.6 Branch Choice for TM Waves

For the incident wave field, using Ampere's law with the added displacement current, (7.8) and (7.28), the time averaged, real part of the Poynting vector

$$\text{Re} \{ \bar{S}_{incident} = \bar{E} \times \bar{H}^* \} = \frac{\beta_1 \omega \mu_0 |h_0|^2}{2|k_1|^2} e^{-2(\alpha_x x - \alpha_{1z} z)} (\sin \theta_1 \hat{x} - \cos \theta_1 \hat{z}) \quad (7.75)$$

directs into the positive  $x$ -direction and the negative  $z$ -direction for any real incidence angle in the range  $0^\circ$  to  $90^\circ$  and the Poynting vector condition is satisfied. For the reflected wave, the following is found:

$$\text{Re} \{ \bar{S}_{reflected} = \bar{E} \times \bar{H}^* \} = \frac{\beta_1 \omega \mu_0 |R^{TM} h_0|^2}{2|k_1|^2} e^{-2(\alpha_x x + \alpha_{1z} z)} (\sin \theta_1 \hat{x} + \cos \theta_1 \hat{z}). \quad (7.76)$$

The direction of real power flow is in the positive  $x$ - and  $z$ -direction for any real incidence angle in the range  $0^\circ$  and  $90^\circ$ . Therefore the Poynting vector condition is

also satisfied for the reflected wave. For the transmitted wave, using (7.29), it is found that:

$$\operatorname{Re}\left\{\bar{S}_{\text{transmitted}} = \bar{E} \times \bar{H}^*\right\} = \frac{|T^{TM} h_0|^2}{2\omega} e^{-2(\alpha_x x - \alpha_{2z} z)} \left( \operatorname{Re}\left\{\frac{k_x}{\tilde{\epsilon}_2}\right\} \hat{x} - \operatorname{Re}\left\{\frac{k_{2z}}{\tilde{\epsilon}_2}\right\} \hat{z} \right). \quad (7.77)$$

For the direction of power flow to be in the positive  $x$ - and negative  $z$ -direction (i.e. satisfying the Poynting vector condition), two subsequent equations have to be satisfied:

$$\operatorname{Re}\left\{\frac{k_x}{\tilde{\epsilon}_2}\right\} \geq 0 \quad ; \quad \theta \in [\{0^\circ \leq \theta \leq 90^\circ\}, \mathbb{R}] \quad (7.78)$$

$$\operatorname{Re}\left\{\frac{k_{2z}}{\tilde{\epsilon}_2}\right\} \geq 0. \quad (7.79)$$

Restrictions (7.78) and (7.79) can be rewritten in terms of the arguments of the phasors

$$-90^\circ \leq \angle k_x - \angle \tilde{\epsilon}_2 \leq 90^\circ \quad (7.80)$$

$$-90^\circ \leq \angle k_{2z} - \angle \tilde{\epsilon}_2 \leq 90^\circ. \quad (7.81)$$

The angular regions of the two phasors are well defined

$$\begin{aligned} 0^\circ \leq \angle k_x \leq 45^\circ \\ 0^\circ \leq \angle \tilde{\epsilon}_2 \leq 90^\circ \end{aligned} \quad (7.82)$$

and satisfy the restriction in (7.80). It is not that simple to prove (7.81) in general. The region of  $k_{2z}^2$  in the complex plane will once again be divided into 4 subregions to simplify the choice of branch to ensure solutions on the correct Riemann surface.

The second condition that has to be met is that of energy conservation. The full derivation of energy conservation for TE waves was discussed in Section 7.3.5. The derivation of energy conservation for TM waves will not be discussed in this section. It is possible to do it using the exact same method as was used in the derivation for TE waves and it will intuitively be assumed that it is once again independent of the magnitude of the reflection coefficient.

### 7.3.6.1 Region A with $\operatorname{Im}\{k_{2z}^2\} \geq 0$

The exact mapping of Figure 7-3 applies for this region. In subregion (i)

$$0^\circ \leq \angle k_{2z} \leq 90^\circ. \quad (7.83)$$

Using (7.82), restriction (7.81) is satisfied and the Poynting vector condition is also satisfied. Thus the solution using the branch of subregion (i) is the proper solution. It can easily be shown that (7.81) is not satisfied in subregion (ii).

### 7.3.6.2 Region B with $\text{Im}\{k_{2z}^2\} \leq 0$ and $\text{Re}\{k_{2z}^2\} \geq 0$

The exact mapping of Figure 7-4 applies for this region. In subregion (i)

$$-45^\circ \leq \angle k_{2z} \leq 0^\circ. \quad (7.84)$$

In all the rock layers encountered in the BIC UG1 – UG2 stratigraphy it is known that  $\tan \delta < 1$ , which implies

$$0^\circ \leq \angle \tilde{\epsilon}_2 \leq 45^\circ. \quad (7.85)$$

Restriction (7.81) is therefore satisfied in subregion (i) and also the Poynting vector condition, implying that the solution is proper. It can once again be shown that the solution in subregion (ii) does not satisfy the Poynting vector condition necessary for a proper solution.

### 7.3.6.3 Region C with $(180^\circ + 2\delta_2) \leq k_{2z}^2 \leq 270^\circ$

The mapping of  $k_{2z}^2$  to  $k_{2z}$  for region C is depicted in Figure 7-11.

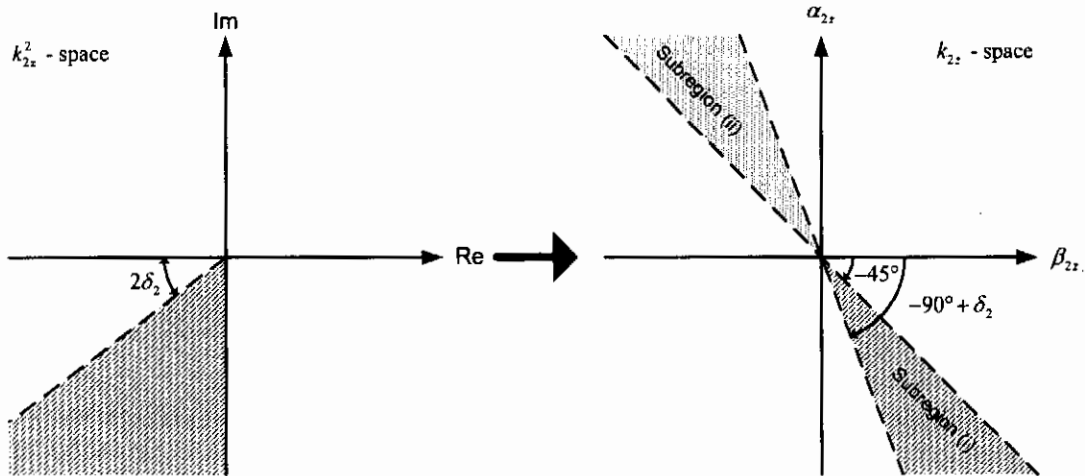


Figure 7-11: Mapping of  $k_{2z}^2$  to the  $k_{2z}$  space for region C.

In subregion (i), with  $\delta_2 < 45^\circ$ , the phase of  $k_{2z}$  is restricted to the range

$$-90^\circ + \delta_2 \leq \angle k_{2z} \leq -45^\circ \quad (7.86)$$

and restriction (7.81) is satisfied. The solution in subregion (i) is therefore proper and it can be shown that the solution in subregion (ii) is improper.

### 7.3.6.4 Region D with $180^\circ \leq k_{2z}^2 \leq (180^\circ + 2\delta_2)$

The mapping of  $k_{2z}^2$  to  $k_{2z}$  for region D is depicted in Figure 7-12.

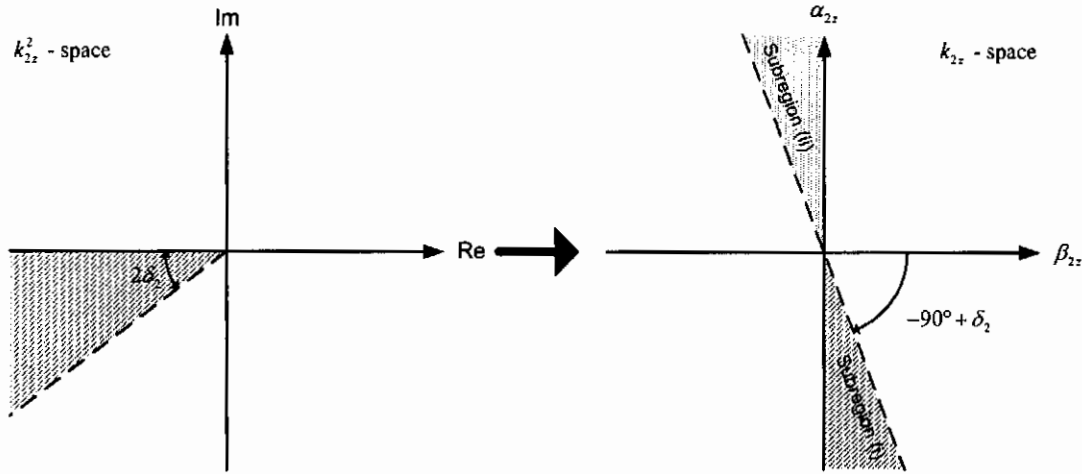


Figure 7-12: Mapping of  $k_{2z}^2$  to the  $k_{2z}$  space for region D.

In regions A-C, subregion (i) yielded the proper solution. If assumed that in region D subregion (i) yields the proper solution, it is found that

$$-(90^\circ + \delta_2) \leq \angle k_{2z} - \angle \tilde{\epsilon}_2 \leq -90^\circ \quad (7.87)$$

which does not satisfy the Poynting vector condition. Looking at subregion (ii) however, it is found that

$$90^\circ - \delta_2 \leq \angle k_{2z} - \angle \tilde{\epsilon}_2 \leq 90^\circ. \quad (7.88)$$

In region D, subregion (ii) satisfies the Poynting vector condition and therefore yields the proper solution. In subregion (ii) we find that  $\beta_{2z} < 0$ , which implies that the solution yields a backward propagating wave. Even though the phase velocity is negative (in the negative  $z$ -direction), the direction of energy flow is positive. It should be noted however that  $|\alpha_{2z}| < |\beta_{2z}|$  and the wave can be described as mostly attenuating, i.e. an evanescent wave.

## 7.4 Reflection and Transmission in a Multilayered Planar System

In Section 7.3 a thorough theoretical treatment was given to transmission and reflection from a single planar inhomogeneity. A number of interesting phenomena were encountered, i.e. reflections coefficients that are larger than unity with an associated lateral shift of waves at planar inhomogeneities. In the BIC stratigraphy however, there is a system of planar inhomogeneities, i.e. layers. A number of these layers are platiniferous and of economical interest, while some of the layers are

merely host media. In order to understand radiowave propagation in the BIC UG1-UG2 stratigraphy, we have to understand propagation (reflection and transmission) in a multilayered system of planar inhomogeneities.

Reflection and transmission in a multilayered system are discussed in almost every major textbook on EM radiation and propagation, each with a unique approach based on physical insight. In this section, the theory as developed by Chew [48] is briefly discussed. Attention is given to the complications due to the presence of lossy media.

Consider the multilayered system depicted in Figure 7-13.

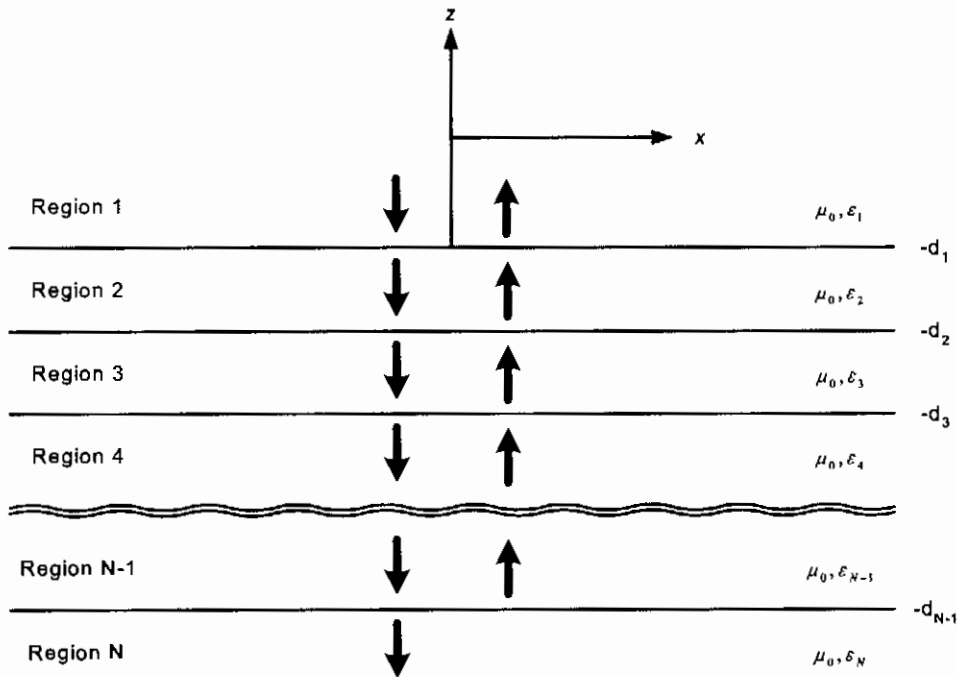


Figure 7-13: Reflection and transmission in a multilayered system.

The wave, for TE polarization, in the  $i$ -th region has the form

$$e_{iy} = A_i \left( e^{-ik_{iz}z} + \tilde{R}_{i,i+1} e^{2ik_{iz}d_i + ik_{iz}z} \right) \quad (7.89)$$

where  $\tilde{R}_{i,i+1}$  is the generalized reflection coefficient that relates the amplitude of the upgoing wave to the amplitude of the downgoing wave in the region. The generalized reflection coefficient includes the combined effects of the reflection from the first interface and the subsurface reflections. The additional phase term ensures that the generalized reflection coefficient is properly defined at the boundary. The TM polarized wave has the exact form of equation (7.89) for the  $y$ -directed magnetic field. It should be noted that the generalized reflection coefficient is zero in region N.

Using constraint conditions at the interfaces, a recursive relation is found, expressing  $\tilde{R}_{i,i+1}$  in terms of  $\tilde{R}_{i+1,i+2}$ :

$$\tilde{R}_{i,i+1} = \frac{R_{i,i+1} + \tilde{R}_{i+1,i+2} e^{2ik_{i+1,z}(d_{i+1}-d_i)}}{1 + R_{i,i+1} \tilde{R}_{i+1,i+2} e^{2ik_{i+1,z}(d_{i+1}-d_i)}}. \quad (7.90)$$

There is also a recursive relation expressing  $A_i$  in terms of  $A_{i-1}$ :

$$A_i e^{ik_{iz}d_{i-1}} = \frac{T_{i-1,i} A_{i-1} e^{ik_{i-1,z}d_{i-1}}}{1 - R_{i,i-1} \tilde{R}_{i,i+1} e^{2ik_{iz}(d_i-d_{i-1})}} = A_{i-1} e^{ik_{i-1,z}d_{i-1}} S_{i-1,i} \quad (7.91)$$

$$S_{i-1,i} = \frac{T_{i-1,i}}{1 - R_{i,i-1} \tilde{R}_{i,i+1} e^{2ik_{iz}(d_i-d_{i-1})}}.$$

In (7.91),  $S_{i-1,i}$  is known for all the regions and we can derive  $A_i$  for all the regions since  $A_1$  is known in region 1:

$$A_i e^{ik_{iz}d_{i-1}} = A_1 e^{ik_{1z}d_1} \prod_{j=1}^{i-1} e^{ik_{jz}(d_j-d_{j-1})} S_{j,j+1} \quad (7.92)$$

where it is assumed that  $d_0 = d_1$ . Once  $A_i$  and  $\tilde{R}_{i,i+1}$  are known in all the regions, the fields can be calculated using (7.89). In (7.90) and (7.91), the superscript of the reflections and transmission coefficients have been omitted to keep them general. For TE waves, they will be of the TE type with

$$R_{i,i+1}^{TE} = \frac{k_{iz} - k_{i+1,z}}{k_{iz} + k_{i+1,z}}, \quad T_{i,i+1}^{TE} = \frac{2k_{iz}}{k_{iz} + k_{i+1,z}}. \quad (7.93)$$

For TM waves, they will be of the TM type with

$$R_{i,i+1}^{TM} = \frac{\tilde{\epsilon}_{i+1} k_{iz} - \tilde{\epsilon}_i k_{i+1,z}}{\tilde{\epsilon}_{i+1} k_{iz} + \tilde{\epsilon}_i k_{i+1,z}}, \quad T_{i,i+1}^{TM} = \frac{2\tilde{\epsilon}_{i+1} k_{iz}}{\tilde{\epsilon}_{i+1} k_{iz} + \tilde{\epsilon}_i k_{i+1,z}}. \quad (7.94)$$

The final step of the analysis of reflection and transmission in a multilayered system is to ensure that the correct branch in each region is dealt with. In the following two sections the choice of the correct branch are discussed for the two polarizations.

### 7.4.1 Branch Choice for TE Waves

The time averaged power flux density vector for the downgoing wave in region  $i$  can be calculated as:

$$\text{Re} \{ \bar{S}_{down}(\vec{r}, \omega) \} = \frac{|A_i|^2}{2\omega\mu_0} e^{-2(\alpha_x x - \alpha_{iz} z)} (\beta_x \hat{x} - \beta_{iz} \hat{z}). \quad (7.95)$$

For the upgoing wave in region  $i$  it can be calculated as:

$$\operatorname{Re}\{\bar{S}_{up}(\bar{r}, \omega)\} = \frac{|A_i|^2 |\tilde{R}_{i,i+1}|^2}{2\omega\mu_0} e^{-4\alpha_{iz}d_i} e^{-2(\alpha_x x + \alpha_{iz}z)} (\beta_x \hat{x} + \beta_{iz} \hat{z}). \quad (7.96)$$

For the time averaged power flow to be in the correct direction, i.e. in the positive  $x$  and negative  $z$  direction for the downgoing wave and in the positive  $x$  and  $z$  direction for the upgoing wave, the restrictions on the wave numbers are

$$\beta_x \geq 0, \quad \beta_{iz} \geq 0. \quad (7.97)$$

It has been shown that  $\beta_x$  is always greater or equal to zero. Therefore the only restriction for TE waves is that, in a given region, the propagation constant in the  $z$ -direction has to be greater or equal to zero.

## 7.4.2 Branch Choice for TM Waves

The time averaged power flux density vector for the downgoing wave in region  $i$  can be calculated as follows:

$$\operatorname{Re}\{\bar{S}_{down}(\bar{r}, \omega)\} = \frac{|A_i|^2}{2\omega_0} e^{-2(\alpha_x x - \alpha_{iz}z)} \left( \operatorname{Re}\left\{\frac{k_x}{\tilde{\epsilon}_i}\right\} \hat{x} - \operatorname{Re}\left\{\frac{k_{iz}}{\tilde{\epsilon}_i}\right\} \hat{z} \right). \quad (7.98)$$

For the upgoing wave in region  $i$  it can be calculated as:

$$\operatorname{Re}\{\bar{S}_{up}(\bar{r}, \omega)\} = \frac{|A_i|^2 |\tilde{R}_{i,i+1}|^2}{2\omega} e^{-4\alpha_{iz}d_i - 2(\alpha_x x + \alpha_{iz}z)} \left( \operatorname{Re}\left\{\frac{k_x}{\tilde{\epsilon}_i}\right\} \hat{x} + \operatorname{Re}\left\{\frac{k_{iz}}{\tilde{\epsilon}_i}\right\} \hat{z} \right). \quad (7.99)$$

For the time averaged power flow to be in the correct direction, i.e. in the positive  $x$  and negative  $z$  direction for the downgoing wave and in the positive  $x$  and  $z$  direction for the upgoing wave, the restrictions on the wave numbers are

$$\operatorname{Re}\left\{\frac{k_x}{\tilde{\epsilon}_i}\right\} \geq 0 \quad (7.100)$$

$$\operatorname{Re}\left\{\frac{k_{iz}}{\tilde{\epsilon}_i}\right\} \geq 0. \quad (7.101)$$

It has been shown in Section 7.3.6 that (7.100) is always true. Therefore, the only restriction for TM waves is that, in a given region, (7.101) holds true.

## 7.5 Concluding Remarks

The theory of plane wave propagation in stratified lossy media was formalised in this chapter. Even though the basic theory has been presented in every major EM textbook, the details for layers with dielectric losses have not been widely published.

Reflection and transmission of a plane wave incident on the interface between two half-spaces have been generalised as such that both half-spaces may be lossy dielectrics. It was shown that a number of different wave phenomena are encountered under this generalisation, the most profound being a local reflection coefficient larger than unity. It was proved that the latter is a solution abiding by the laws of physics. In essence the reflected wave experiences a lateral shift at the boundary and the localised reflection coefficient does not relate the reflected wave to its actual source. A theory is developed by which the correct branch choice can be made.

Reflection and transmission in a multilayered system have also been generalised for lossy layers, with specific attention to the selection of the correct branch (Riemann surface).

# CHAPTER 8

## PROPAGATION AND DETECTION IN THE STRATIFIED UG1 – UG2 SYSTEM

The simplified planar model approximation of the BIC (Section 6.3) is used together with the measured (Section 6.4) and estimated (Sections 6.7 and 6.8) dielectric properties of the stratified layers to predict various wave propagation phenomena encountered in the BIC. This is based on the theory developed in Chapter 7. The time domain reflections of pulses incident on a single planar dielectric interface will be considered for any incidence angle. The study is expanded to include a sandwiched layer bound by two half-spaces. The theory developed in Section 7.4 is slightly modified to do this. The first part of this chapter is concluded with a study of the transmission and reflection of a pulse normally incident on a sequence of layers as found in the BIC. This study sheds light on the transmissivity and reflectivity of given layers in the BIC stratigraphy, i.e. the Bleskop Marker and the UG1/UG2 reef structures.

The second part of this chapter includes the estimation of maximum detection range of a pulse reflected by the UG1/UG2 reefs based on practical measurements and theoretical predictions, as well as the estimation of the UG2 reflectivity profile from practical field experiment measurements.

### 8.1 Literature Review

Xu and McMechan [54] present an algorithm to simulate GPR attenuation in 2.5 dimensions. They solve Maxwell's equation in 2 dimensions using a FDTD technique and then superimpose the results for different horizontal wavenumbers (the 3<sup>rd</sup> dimension). Ellefsen [55] simulates the propagation of a guided wave in a sandwiched layer structure where the layer and half-spaces are allowed to have finite conductivity.

Mason and Simmat [56],[57] have modelled the propagation of EM waves in a homogeneous lossy medium, while Claassen [3] did constant  $Q^*$  (derived from the

quality factor) modelling of propagation in a lossy dielectric. The constant  $Q^*$  model for subsurface radar pulse attenuation was developed by Turner and Siggins [58]. The  $Q^*$  parameter was defined to characterize the slope of the attenuation constant as a function of frequency in its linear region. Irving and Knight [59] confirmed the constant  $Q^*$  model and developed an inverse-Q filter to compensate for the frequency-dependant attenuation. In the modelling of GPR propagation the Ricker wavelet is often used as the excitation, even though it originates from seismic propagation studies.

A series of publications by Ricker [60] - [64] develop the concept of an ideal seismic pulse for signal processing purposes. Ricker proposed a number of wavelets based on recorded seismic data. The Ricker wavelet (2<sup>nd</sup> derivative of a gaussian pulse), as it is commonly known today, yielded the best correlation with the recorded data.

## 8.2 Pulse Shape Approximation for Theoretical Predictions

A prerequisite for time domain pulse reflection analysis is a time domain source signal with a physical foundation. The most basic time domain signal is the sinc

$\left(\frac{\sin \pi x}{\pi x}\right)$  function associated with a zero-phase unity bandpass frequency spectrum

[12]. The sinc function is however, a non-causal and non-physical source signal. The Gaussian pulse has the unique property that its Fourier spectrum is also a Gaussian distribution, either at baseband or centred at a carrier frequency. This waveform is strictly also non-causal, because it's described mathematically by an exponential decay in the positive and negative time direction. A source signal is needed with a pulse shape approximately that of actual recorded pulses. The Gaussian pulse modulated with a carrier frequency might be used in some cases [57], provided that the time constant is chosen correctly to simulate the rise and fall times of the signal properly. In seismics (acoustic waves) recorded pulses can be approximated very accurately by the Ricker wavelet [60] - [64]. This wavelet, as it is commonly used today, is one of a series of wavelets derived by Norman Ricker to approximate mechanically and electrically obtained seismic traces [60]-[64]. According to Ricker, *... a sharp seismic disturbance gives rise to a travelling wavelet, of shape determined by the nature of the earth's absorption spectrum for elastic waves* [60]. Two of the

electrical type wavelets proved to yield the best correlation with actual traces. They are the velocity-type wavelet near the shot point (near field region) and the velocity-type wavelet at larger distances from the shot point (far field region) [63]. The latter is a symmetric function expressed analytically as

$$f(t) = \frac{\sqrt{\pi}}{4} \left( 2 \frac{\pi t^2}{\tau^2} - 1 \right) e^{-\frac{\pi t^2}{\tau^2}} \quad (8.1)$$

commonly referred to as the Ricker wavelet (even though Ricker derived a series of wavelets). It should be noted that this wavelet is also the second derivative of a standard Gaussian pulse. Even though this wavelet has its origin in seismics, it has been used effectively to model EM GPR pulse propagation [54], [55]. In light of the successful use of the Ricker wavelet in GPR, the possibility that the digitally stored pulses received by the GeoMole BHR can be approximated by it, was investigated.

Consider the cross-hole radar scan between holes H46 and H48 at the Bleskop II field experiment (discussed in Appendix F). The direct wave in trace 30 is spatially separated from any secondary reflections. This is the ideal pulse for the fitting of an analytical wavelet, and is plotted in Figure 8-1.

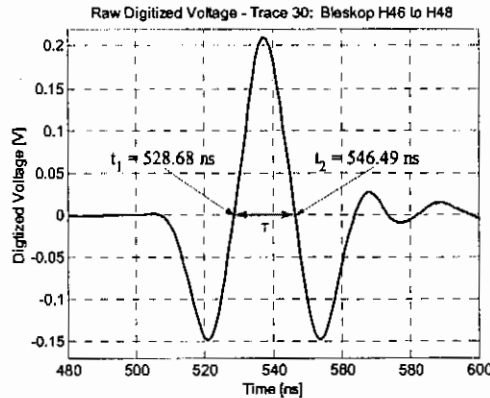


Figure 8-1: Digitally stored direct wave pulse for GeoMole BHR.

Supposing that the Ricker wavelet and the actual measured pulse have coinciding zero crossings, the characteristic time,  $\tau$ , of the wavelet has to be set to

$$\tau = \sqrt{2\pi} \frac{T}{2} = \sqrt{2\pi} \frac{(t_2 - t_1)}{2} = 22.32 \text{ ns.} \quad (8.2)$$

The wavelet (amplitude scaled and inverted) is graphically compared with the actual pulse in Figure 8-2 in the time domain. Their frequency spectra are compared in Figure 8-3.

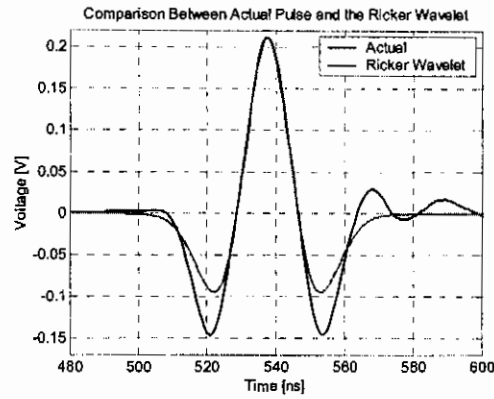


Figure 8-2: Time domain comparison of Ricker wavelet to actual pulse.

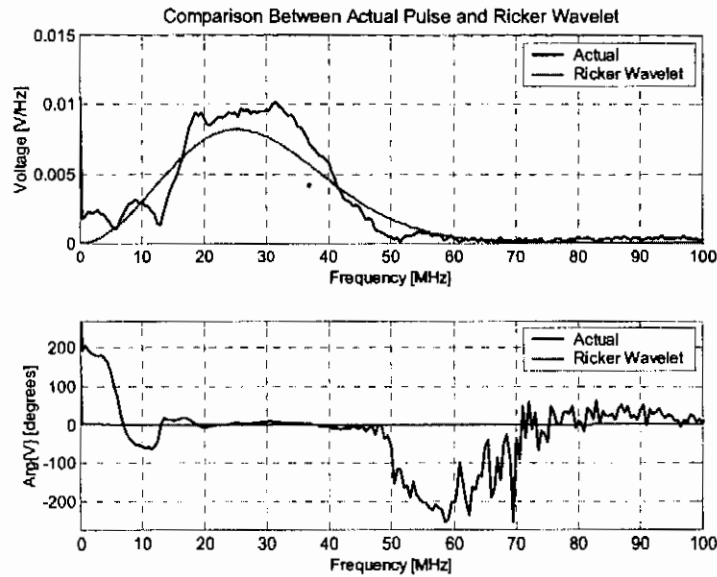


Figure 8-3: Frequency domain comparison of Ricker wavelet to actual pulse.

Clearly the wavelet approximates the actual pulse with a high degree of accuracy in both time and frequency domain. The main lobe is almost an exact replica while the two negative sidelobes are slightly smaller with a slower decay in the wavelet approximation. The phase response deviates only at the lower ( $< 15$  MHz) frequencies and in the frequency range from 50 MHz to 70 MHz. In the latter frequency range, the deviation of the actual pulse is  $180^\circ$  associated with a sign reversal. In the  $Q$  estimates of Section 6.8 it was observed that for this specific radar scan, the transmitter antenna squinted at about 50 MHz and the receiver only at 70 MHz. Above 50 MHz, the transmitter polarization rotates  $180^\circ$ , while the receiver polarization rotates  $180^\circ$  above 70 MHz. Therefore a polarity change could be expected in the acquired signal in the frequency range considered. The Ricker

wavelet can therefore be used effectively as a source signal in the study of radiowave propagation in the BIC with specific application to the GeoMole BHR.

It has been stated in Chapter 5 that the digitally stored voltage in Figure 8-1 may be deconvolved to find the associated E-field at the receiver feedpoint. This time domain wavefield is plotted in Figure 8-4.

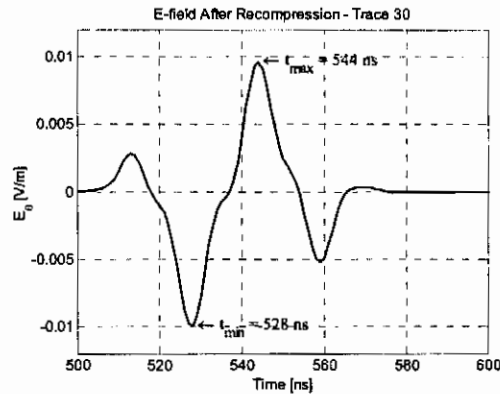


Figure 8-4: Deconvolved E-field for trace 30.

Disregarding the precursor and the tail, this waveform is quite similar to the first derivative of Gaussian pulse

$$f(t) = -\frac{2\pi A_0}{\tau^2} t e^{-\frac{\pi t^2}{\tau^2}}. \quad (8.3)$$

This wavelet is a good approximation of the monocycle wavelet, which is defined as one cycle of a sinusoid, and will be referred to as a monocycle wavelet. Choosing the maximum and minimum points of both waveforms to be coincident,  $\tau$  has to be

$$\tau = \sqrt{2\pi} \frac{(t_{\max} - t_{\min})}{2} = 20.05 \text{ ns}. \quad (8.4)$$

The wavelet is graphically compared with the deconvolved E-field in Figure 8-5 in the time domain, while their frequency spectra (magnitude and phase response) are compared in Figure 8-6.

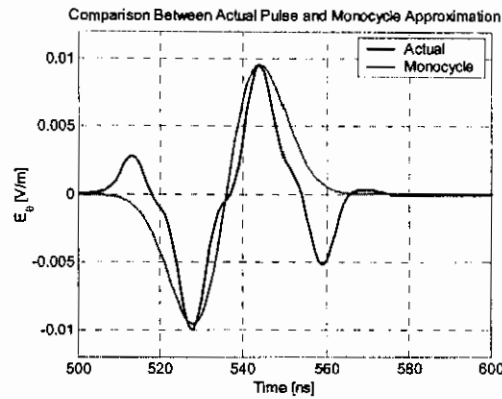


Figure 8-5: Time domain comparison of monocycle wavelet to deconvolved E-field.

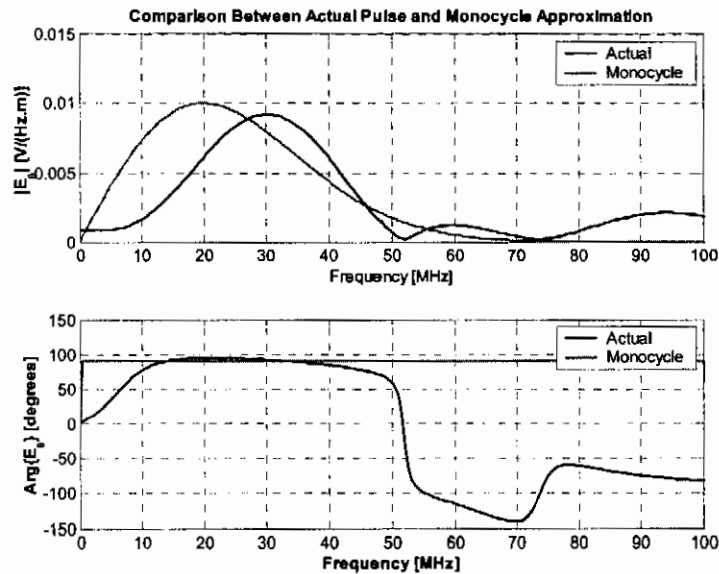


Figure 8-6: Frequency domain comparison of monocycle wavelet to deconvolved E-field.

The time response approximation correlates relatively well with the transient response between the two extremes, but decays to  $+\infty$  and  $-\infty$  a little slower than the actual pulse. The actual pulse has a complex frequency response, with a main lobe below 50 MHz, a secondary lobe between 50 MHz and 70 MHz, and another lobe above 70 MHz. These secondary lobes give rise to the quicker transients and also the precursor and tail. Once again the polarity change between 50 MHz and 70 MHz is visible in the phase response of the actual pulse.

There are now two wavelets, with their respective frequency spectra, to use as stimuli in pulse propagation studies in stratified media.

### 8.3 Planar Interface Pulse Reflection

Consider a source and observation point at a given distance,  $h_1$ , above the planar interface between two half-spaces spatially separated a distance  $d$  as depicted in Figure 8-7.

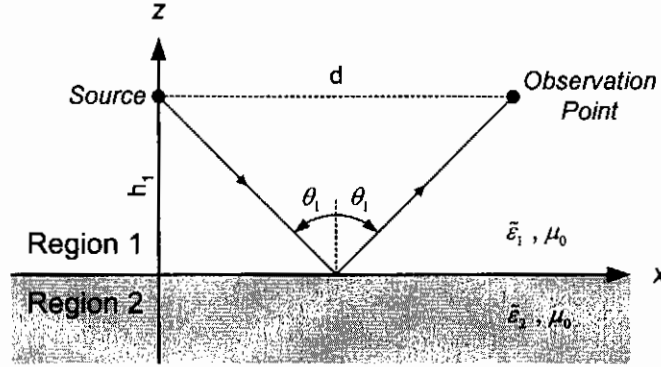


Figure 8-7: Geometry for planar interface pulse reflection.

Equation (7.26) describes Figure 8-7 where the downgoing wave at the Cartesian coordinate  $(0, 0, h_1)$  is taken as the excitation source, i.e. for TE polarization

$$\begin{aligned} e_0(\omega) &= e_{1y}^{down}(\omega, h_1) e^{ik_{1z}h_1} \\ &= F(\omega) e^{ik_{1z}h_1} \end{aligned} \quad (8.5)$$

where  $F(\omega)$  is the frequency spectrum of the source signal  $f(t)$  as defined in either (8.1) for a Ricker wavelet or (8.3) for a monocycle wavelet. From (7.26) the reflected upgoing wave at  $(d, 0, h_1)$  can be found as

$$E_{1y}^r = F(\omega) R^{TE} e^{i(k_x d + 2k_{1z} h_1)}. \quad (8.6)$$

The same applies for the y-directed H-field for TM polarization, with the exception that  $R^{TM}$  is used instead of  $R^{TE}$ . Equation (8.6) holds true only when there is no lateral shift (Goos-Hanchen effect). It is therefore important to investigate the magnitude and phase behaviour of the reflection coefficient as a function of the incidence angle,  $\theta_1$ , to determine whether or not the Goos-Hanchen effect is encountered. It is possible to approximate this lateral shift using (7.55) when the incidence angle is between, but not equal to, the critical angle and oblique ( $90^\circ$ ) incidence and both regions are lossless. Whenever either of the layers are lossy, it is considerably more difficult and beyond the scope of this dissertation to determine the lateral shift.

### 8.3.1 Interface Reflections for TE Polarized Pulses

For TE polarized pulses, region 1 is taken as norite and region 2 as chromitite (UG2 Top), the reflection coefficient as a function of incidence angle for different frequencies is plotted in Figure 8-8. It is plotted as a function of frequency for different incidence angles in Figure 8-9.

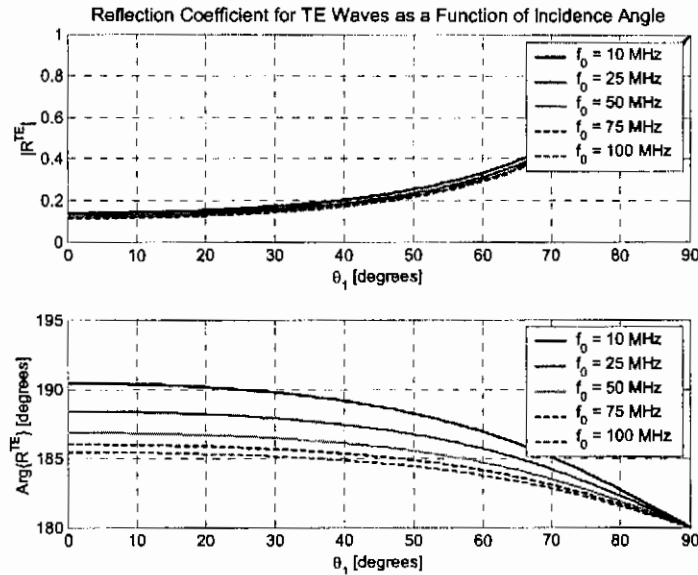


Figure 8-8: Reflection coefficient for TE polarized pulses with norite and chromitite half-spaces as a function of incidence angle.

For each frequency component in the spectrum, the amplitude increases from approximately 0.12 at  $0^\circ$  to unity at  $90^\circ$ . The phase decreases from a maximum value of  $190.4^\circ$  at 10 MHz and  $185.4^\circ$  at 100 MHz for normal incidence to  $180^\circ$  as the incidence angle approaches  $90^\circ$ . The total phase response of the reflection coefficient is the sum of  $180^\circ$  associated with a polarity change and an additional phase term,  $\phi'$ , associated with a time delay of the response of the interface reflection

$$\phi = 180^\circ + \phi'. \quad (8.7)$$

If the interface reflection is viewed as an infinite distribution of Huygens' sources, the implication is that there is a time delay between the excitation of these sources and their reradiation of the energy. The phase delay decreases as a function of incidence angle.

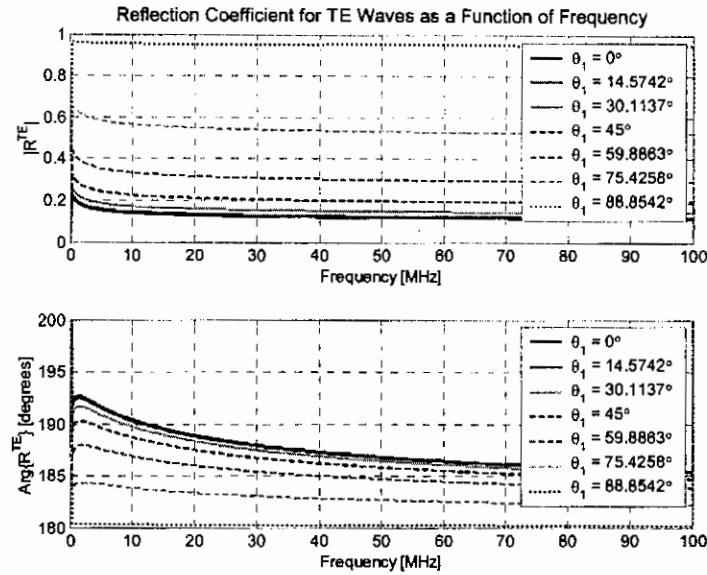


Figure 8-9: Reflection coefficient for TE polarized pulses with norite and chromitite half-spaces as a function of frequency.

From Figure 8-9 it is further clear that both the amplitude and phase of the reflection coefficient decreases monotonically as a function of frequency for all incidence angles. The observed increase in path length due to the finite duration of the pulse response of the interface,  $\Delta R$ , can be related to the additional phase term  $\phi'$  and the propagation constant in the top half-space as

$$\Delta R = \frac{\phi'}{\beta_1}. \quad (8.8)$$

This distance, in turn, leads to an increase  $\Delta h$  in the observed (effective) depth of the interface

$$\Delta h = \left\{ \left[ \left( h_1^2 + \left( \frac{d}{2} \right)^2 \right)^{1/2} + \frac{\Delta R}{2} \right]^2 - \left( \frac{d}{2} \right)^2 \right\}^{1/2} - h_1. \quad (8.9)$$

The increase in effective path length and observed interface depth are plotted as a function of frequency for different incidence angles in Figure 8-10 and Figure 8-11. It should be noted that the height  $h_1$  was kept constant for  $\theta_1 \leq 45^\circ$  and the separation distance  $d$  was kept constant for  $\theta_1 > 45^\circ$ .

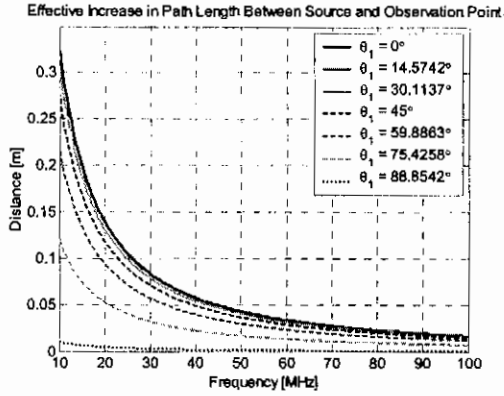


Figure 8-10: Effective path length increase for TE pulses as a function of frequency.

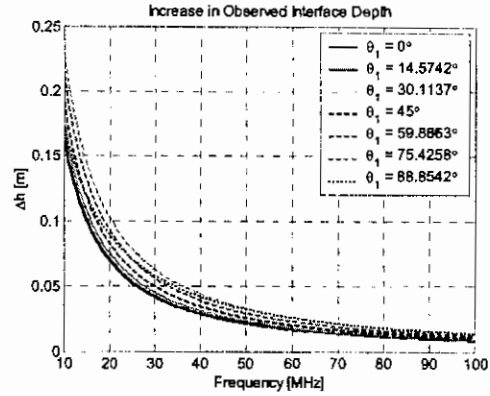


Figure 8-11: Observed interface depth increase for TE pulses as a function of frequency.

Studying the spectrum of the synthetic Ricker wavelet as plotted in Figure 8-3, it is clear that the weight is centred at about 25 MHz. The increase in effective path length decreases monotonically from 105 mm at normal incidence to only 3 mm at 88.85°. This converts to an increase in the observed interface depth of between 52.6 mm and 78.5 mm. With an average velocity of  $110 \text{ m} \cdot \mu\text{s}^{-1}$  a single range cell is 55 mm long for the traces resampled at 1 ns time intervals and 220 mm long for the raw data sampled at 250 Msps. In the raw data this additional delay is less than a range cell and not easily resolvable, especially in the presence of noise. In the resampled data however, the increase is at least one range cell and should be resolved.

The time domain reflected field for the given source excitation can be calculated using the Fourier transform pair for the phasors in (8.6). It has been stated that the travel distance of the reflected wave between the source and observation point is variable and a function of the incidence angle and either the vertical height  $h_1$  or the lateral distance  $d$ . To compare the reflected field for various incidence angles, a fixed travelling distance

$$R = \sqrt{4h_1^2 + d^2} \quad (8.10)$$

is required. Choosing a convenient reference distance  $R_{\text{ref}}$ , it is possible to modify the reflected field's phasor with the multiplication factor  $e^{ik(R_{\text{ref}}-R)}$  so that the effective travel distance is constant for all incidence angles. The reflected fields for  $R_{\text{ref}} = 20 \text{ m}$  and a range of incidence angles between  $0^\circ$  and  $90^\circ$  are plotted in Figure 8-12.

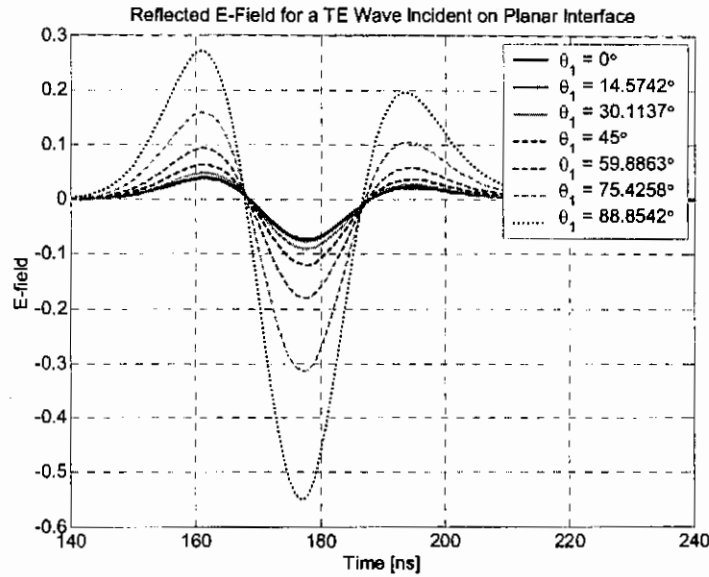


Figure 8-12: Modified time domain reflected E-fields for TE waves incident on planar interface.

The increase in reflection coefficient as a function of incidence angle is obvious. It should be noted that even though the reflected field is the largest as the incidence angle approached  $90^\circ$ , the polarity is inverted. When the difference in pathlength for the direct and reflected waves are negligible, these two waveforms interfere destructively. In Figure 8-13 the reflected wave for normal incidence is plotted together with a reflected wave with the same geometric configuration, but with a frequency independent, zero-phase reflection coefficient. The magnitude of the reflection coefficient is chosen so that the peak values of both waveforms are equal in amplitude.

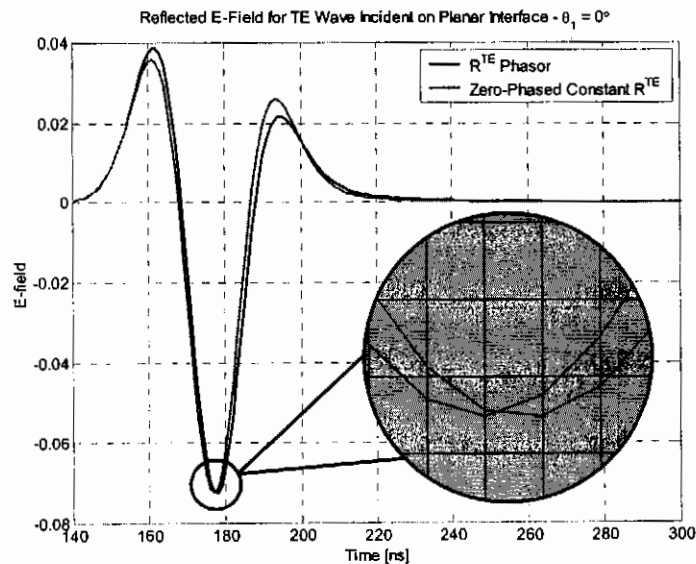


Figure 8-13: Time domain reflected TE wave for normal incidence indicating time retardation.

The waveform with a uniform, zero phase reflection coefficient is closely correlated with the actual reflected field waveform. The additional retardation of the lower frequency components (below 25 MHz) accounts for the smaller front and bigger back lobes. In the zoomed view of the peaks it is clear that there is an additional delay of approximately 1 ns (110 mm at  $110 \text{ m}\cdot\mu\text{s}^{-1}$ ). This agrees within 5% of the predicted delay of 105 mm.

### 8.3.2 Interface Reflections for TM Polarized Pulses

For TM polarized pulses (H-field is perpendicular to plane of incidence), with region 1 taken as norite and region 2 as chromitite (UG2 Top), the reflection coefficient as a function of incidence angle for different frequencies is plotted in Figure 8-14. It is plotted as a function of frequency for different incidence angles in Figure 8-15.

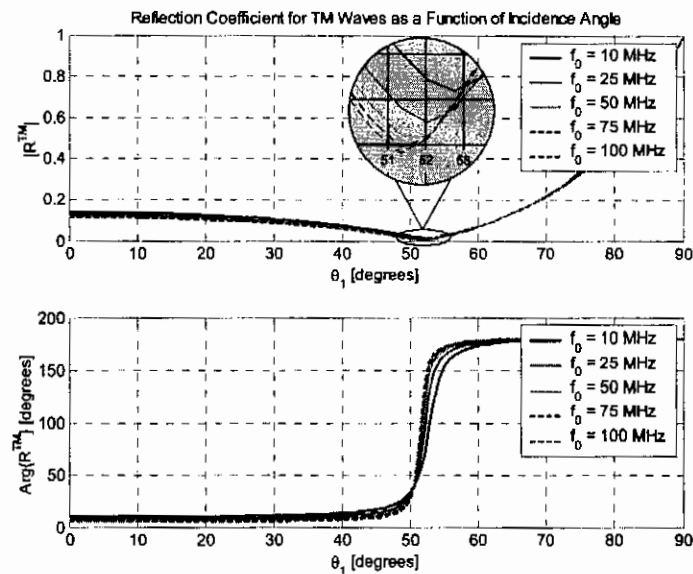


Figure 8-14: Reflection coefficient for TM polarized pulses with norite and chromitite half-spaces as a function of incidence angle.

From Figure 8-14 it can be seen that  $|R^{\text{TM}}|$  decreases from approximately 0.12 at  $\theta_1 = 0^\circ$  to a local minimum at the pseudo Brewster angle, after which it increases monotonically to unity as  $\theta_1$  approaches  $90^\circ$ . The pseudo Brewster angle  $\theta_b$  decreases from  $52.77^\circ$  at 10 MHz to  $51.34^\circ$  at 100 MHz (visible in the magnified portion of Figure 8-14). The phase response of  $R^{\text{TM}}$  is more complicated than that for  $R^{\text{TE}}$  because of the Brewster effect. The phase response at  $\theta_1 = 0^\circ$  varies between  $10.43^\circ$  at 10 MHz and  $5.43^\circ$  at 100 MHz. The phase response increases gradually as a function of  $\theta_1$  up to  $\theta_1 = 45^\circ$  (less than  $20^\circ$  phase delay). In the incidence angle range

of  $45^\circ < \theta_1 < 60^\circ$  the phase response has a rapid increase of approximately  $180^\circ$  associated with the Brewster effect. If both half-spaces were lossless the phase reversal would have been abrupt at the Brewster angle, but since both half-spaces are lossy the phase reversal is a continuous function of incidence angle. From  $\theta_1 = 73.5^\circ$  the phase response decreases from a slight “overshoot” (less than  $1^\circ$  above  $180^\circ$ ) to  $180^\circ$  as  $\theta_1$  approaches  $90^\circ$ .

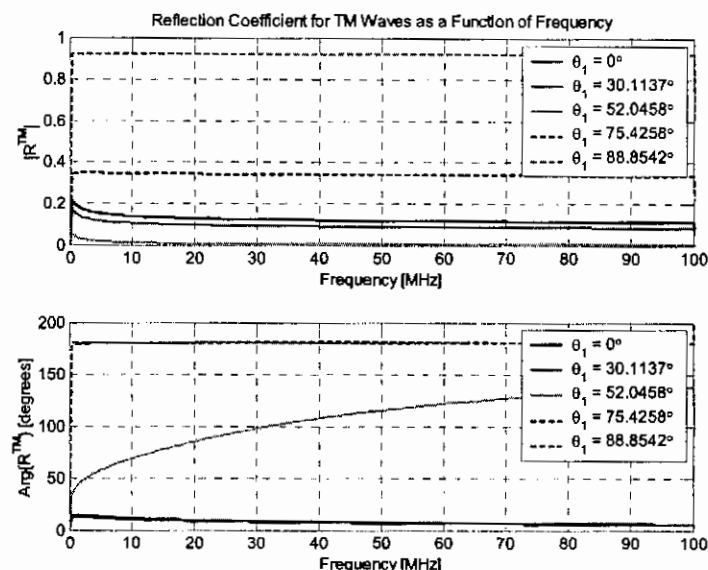


Figure 8-15: Reflection coefficient for TM polarized pulses with norite and chromitite half-spaces as a function of frequency for different incidence angles.

Plotting the reflection coefficient for TM polarized pulses as a function of frequency reveals the intricate nature of the reflection of this polarization for lossy half-spaces. For  $\theta_1 \ll \theta_b$ , the phase response consists mainly of the retardation term  $\phi'$  introduced in (8.7). For  $\theta_1 \gg \theta_b$ , the phase response consists of the  $180^\circ$  phase reversal and the retardation term  $\phi'$ . With  $\theta_1 \approx \theta_b$  (within 10%) however, the phase response will vary between approximately  $0^\circ$  and  $180^\circ$ . This will seriously affect the pulse shape. If the phase response is linear it will only imply additional time retardation, but whenever it becomes severely non-linear, the pulse shape will be affected.

To compare the pulse reflections for various incidence angles, it is once again necessary to choose a reference travelling distance  $R_{ref}$  and modify the returns for the various incidence angles so that the travelling distance are equal for all incidence angles. The time domain reflections are plotted for a number of incidence angles in Figure 8-16 with  $R_{ref} = 20$  m.

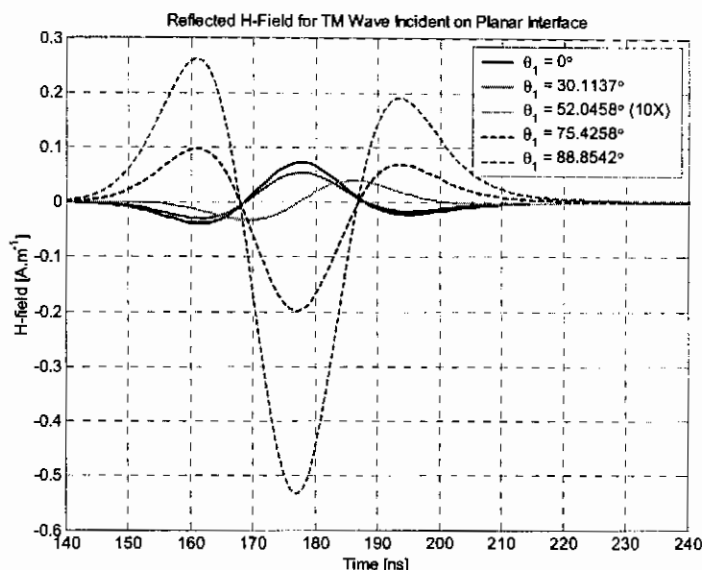


Figure 8-16: Modified time domain reflected H-fields for TM waves incident on planar interface.

The behaviour of the reflection coefficient magnitude as a function of incidence angle is clearly visible. Note that the reflected pulse for  $\theta_1 \approx 52^\circ$ , as plotted in Figure 8-16, is approximately 26 dB below the reflected pulse for normal incidence. The pulse shape is also quite different than for the incidence angles more than 10% away from the Brewster angle. For this specific case it seems to be an integrated version of the other pulses (associated with a  $90^\circ$  phase change). Clearly, interface pulse reflections for TM polarized pulses and lossy half-spaces reveal interesting physical radiowave propagation phenomena.

## 8.4 Sandwiched Layer Pulse Reflection

Consider the physical configuration where a rock layer of finite thickness is sandwiched between two semi-infinite half-spaces, e.g. a chromitite stringer sandwiched between norite (on top) and feldspathic pyroxenite (bottom) as depicted in Figure 6-4 on page 125. When the thickness of the sandwiched layer is taken as the variable  $h_2$  and the interfaces between the half-spaces and the layer are assumed to be planar, the geometry in Figure 8-17 applies.

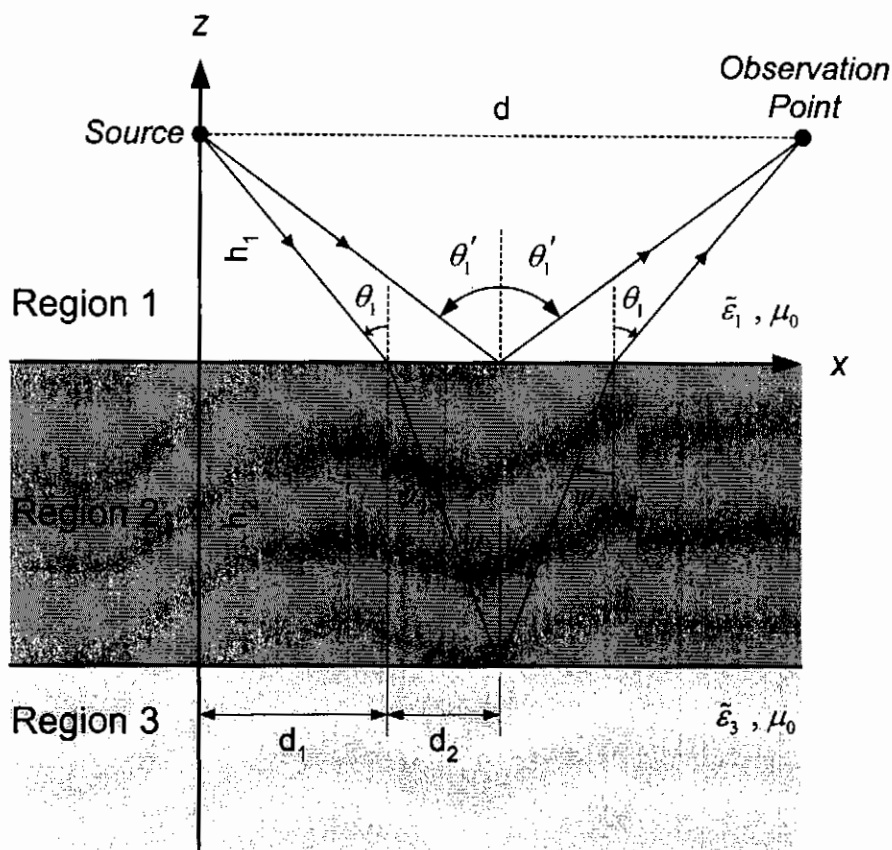


Figure 8-17: Geometry for sandwiched layer pulse reflection.

In the derivation for a multi-layered system, Section 7.4, we assumed a plane wave source at infinity with a given direction of propagation and attenuation (coinciding for homogeneous plane waves). In general, when the source is not infinitely (or approximately infinitely) far from the interface and a multi-layered system is illuminated, the field solution consists of a spectrum of incident field propagation vectors. If we only consider the reflection from the interface between regions 1 and 2 and the first reflection from the interface between regions 2 and 3, the spectrum will consist of a minimum of 2 directions of propagation. The spectrum will consist of 2 when no total internal reflection or lateral beam shifting occurs. This is the specific case study in this section.

Whenever regions 1 and 2 are lossy dielectrics (finite  $Q$ ), the plane wave in region 2 will be inhomogeneous and the directions of propagation and attenuation will not be coinciding. This is regardless of whether these two directions coincided for the incident plane wave. In Section 7.3 the real angles of transmission (propagation) and attenuation,  $\psi$  and  $\phi$ , have been defined. In this section the angle of importance is  $\psi_2$  – the real angle of propagation of the transmitted wave in region 2. As the transmitted

(from region 1) wave propagates through region 2, the sandwiched layer, it gets reflected back by the interface between regions 2 and 3. This wave then propagates upwards through region 2 with the same angle of propagation  $\psi_2$ . This can be proved by invoking the derivation for lossless dielectric using the phase matching condition [43]. As this upwards propagating wave reaches the interface between regions 2 and 1 it gets partially reflected back into region 2 and transmitted up into region 1. The latter eventually adds up with the wave directly reflected back from the interface between regions 1 and 2. Even though the total solution consists of an infinite series of reflected waves (reflected up and down in region 2), the concern of this study is with the directly reflected wave from the interface between regions 1 and 2 and the wave reflected from the interface between regions 2 and 3 as a first order approximation. The major contributions to the total solution come from these two waves. There is not a severe contrast in the dielectric properties of the various layers. It was shown in Section 8.3 that the magnitude of the reflected coefficients are relatively small. The magnitude of the  $n^{\text{th}}$  secondary reflected wave would decrease by a factor of at least  $(R_{23}R_{21})^n$  relative to the first wave reflected from the interface between regions 2 and 3.

The approximated reflected E-field for TE polarized plane waves can be written as

$$E'_{1y} = F(\omega) e^{i(k_x d + 2k_{1z} h_1)} \left[ R_{12}^{TE} + T_{21}^{TE} R_{23}^{TE} T_{12}^{TE} e^{i2k_{2z} h_2} \right] \quad (8.11)$$

where  $F(\omega)$  is the frequency spectrum of the source signal  $f(t)$  as defined in either (8.1) for a Ricker wavelet or (8.3) for a monocycle wavelet. The angle  $\psi_2$  can be calculated using (7.17). Equation (8.11) is only an accurate solution if

- the dielectric contrast between region 2 and regions 1 and 3 is not too severe,
- the plane wave approximation is valid, and
- no total internal reflection occurs at either of the two interfaces.

The latter restriction is of critical importance, since its violation will imply that a lateral shift occurs at either or both of the interfaces and the basic plane wave approximation will no longer be accurate.

Consider the specific case where region 1 is taken as norite (simulated as norite), region 2 as a chromitite layer (simulated as UG2 Bottom) and region 3 as feldspathic pyroxenite (simulated as PX2). This is a common sequence in the BIC, i.e. the UG2 reef when viewed from below. The reflection coefficients (magnitude and phase)  $R_{12}^{TE}$

CHAPTER 8: Propagation and Detection in the Stratified UG1 – UG2 System

and  $R_{23}^{TE}$  are plotted in Figure 8-18 and Figure 8-19 as a function of the incidence angle  $\theta_1$ .

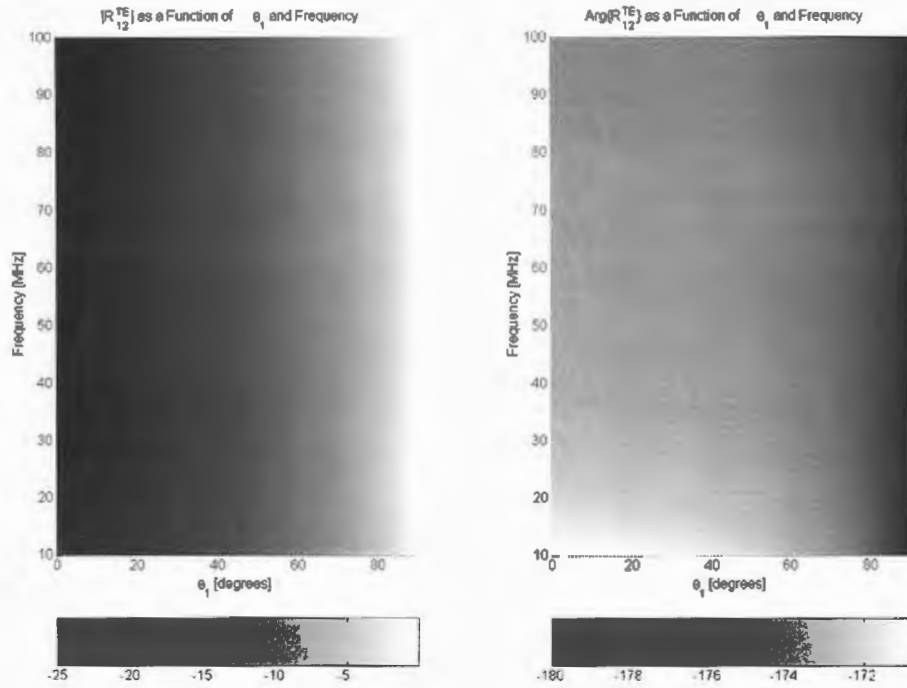


Figure 8-18: Reflection coefficient for interface between regions 1 and 2 as a function of frequency and incidence angle.

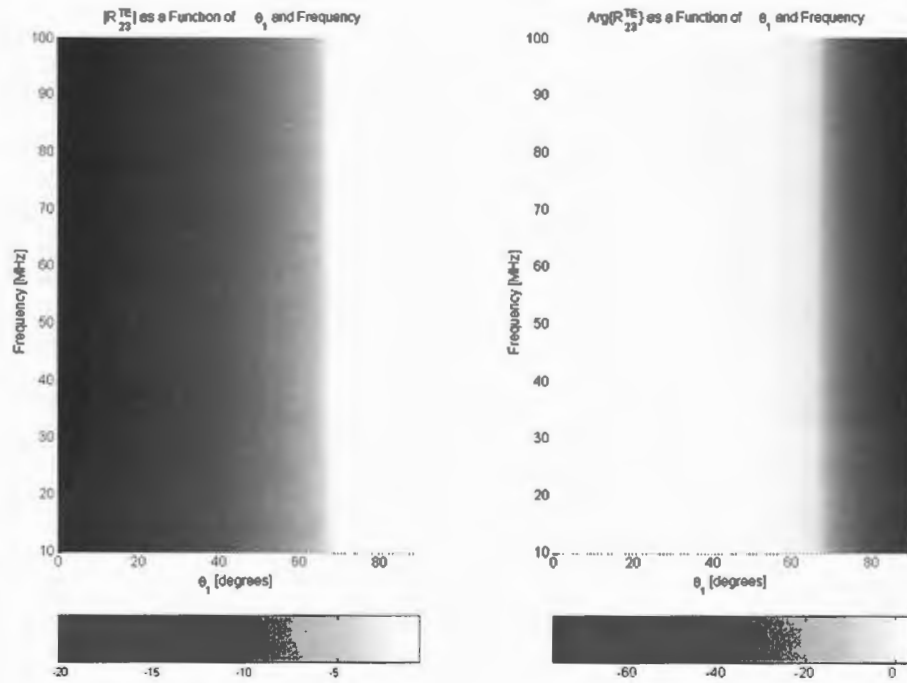


Figure 8-19: Reflection coefficient for interface between regions 2 and 3 as a function of frequency and incidence angle.

From Figure 8-18 it can be seen that the reflection coefficient for the interface between regions 1 and 2 is regular with the phase approaching  $-180^\circ$  as  $\theta_1$  approaches  $90^\circ$ . There is no apparent lateral shift for any real incidence angle between  $0^\circ$  and  $90^\circ$ . This is not the case for the reflection coefficient  $R_{23}^{TE}$ . From Figure 8-19 it is apparent that critical angle for total internal reflection is reached at approximately  $67^\circ$ . The magnitude of the reflection coefficient approaches unity and the phase response has the typical negative slope as a function of incidence angle when  $\theta_1 > \theta_c$ . The phase response is  $0^\circ$  when

$$\theta_1 = 56.34^\circ \quad (8.12)$$

and this will be used as the maximum incidence angle for the plane wave study. Whenever  $\theta_1 > 56.34^\circ$  a lateral shift at the second interface is expected and the plane wave approximation will not yield an accurate answer. For  $h_1 = 10$  m and  $h_2 = 0.7$  m (the approximate thickness of the UG2 chromitite reef) the reflections of the first and second interface (as well as the total reflected field) are plotted in Figure 8-20 for normal incidence.

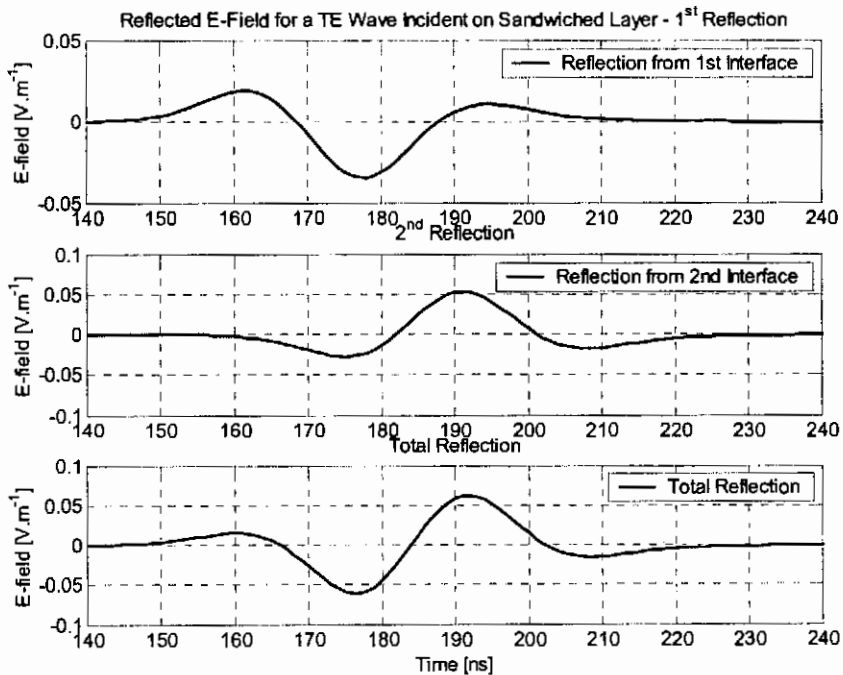


Figure 8-20: The time domain reflections from the two interfaces yielding the total reflection of the sandwiched layer.

For this specific case, the reflection from the first interface is smaller than the reflection from the second interface. They are almost  $180^\circ$  out of phase. Constructive

interference between the peaks and side lobes of the Ricker wavelet yields a total reflected field larger than either of the two. The pulse shape also changed from a Ricker wavelet to a monocyte-like pulse with a positive and negative peak of equal amplitudes and much smaller side lobes – also the typical shape of the Ricker derivative. The total reflected fields as a function of the incidence angle for a fixed thickness  $h_2 = 0.7$  m are plotted in Figure 8-21, while they are plotted as a function of the sandwich thickness  $h_2$  for normal incidence in Figure 8-22.

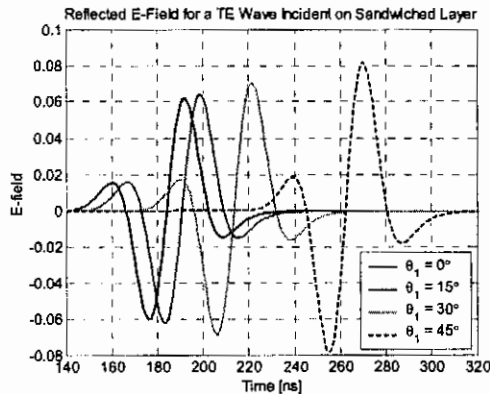


Figure 8-21: Total time domain reflected field as a function of incidence angle.

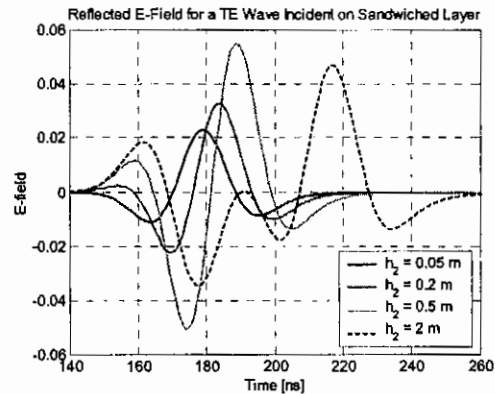


Figure 8-22: Total time domain reflected field as a function of the sandwich thickness  $h_2$ .

It should be noted that change in propagation time in Figure 8-21 is mainly due to the increase in the distance from the source (at a height  $h_1 = 10$  m) to the first interface as a function of incidence angle. The first observation is that the magnitude of the reflected pulses increases as a function of incidence angle. This is due to the increase of the reflection coefficient for TE waves as a function of  $\theta_1$ . The pulse shape for a moderate thickness ( $h_2 = 0.7$  m) does not vary much as a function of incidence angle as long as  $\theta_1 < \theta_c$ . The thickness of the sandwiched layer plays a very important role, however, in the magnitude and shape of the reflected pulse. For thin layers ( $h_2 < 0.1$  m), the reflected pulse has a Ricker wavelet shape and a magnitude smaller than either of the two reflections. For layers of moderate thickness ( $0.1$  m  $< h_2 < 1$  m), the magnitude increases with thickness and the pulse shape changes from a Ricker wavelet to a pulse reminiscent of the Ricker wavelet derivative. For thick layers ( $h_2 > 1$  m), the reflected pulse resolves into the two individually reflected pulses. For an unresolved pulse, the peak will be associated with a position between the two interfaces, depending on the relative magnitudes of the two reflection coefficients. For a dominant second reflection, the effective reflection position might even be below the second interface. This is due to the retarded reflections associated with

lossy dielectric media. It is therefore an intricate and sometime impossible process to resolve the exact position of the first interface. This is due to the dependence thereof on the exact thickness of the layer – a more than often unknown variable.

## **8.5 Multiple Layer Pulse Reflection and Transmission**

In a typical borehole radar survey in the BIC, the transmitter and receiver pair will both be located in the norites (and possibly the feldspathic pyroxenites) between the UG1 and UG2 reef horizons. Depending on the exact location, the radar could be illuminating the UG2 reef directly from the norites immediately below the UG2, or through the Bleskop marker sequence (see Figure 6-2). In the latter case, the Bleskop marker will reflect a portion of the incident power, i.e. decrease the amount of power illuminating the UG2. Furthermore, the sequence will absorb a different amount of power in relation to a homogeneous host medium. The velocity of EM waves in the Bleskop marker is also different from the norites and the possibility exists that the pulse shape might be distorted and retarded. The UG1 chromitite layers, on the other hand, might also be illuminated from the homogeneous feldspathic pyroxenites above, from the norite through the single chromitite stringer discussed in Section 6.2.3 or even through the Bleskop marker from the norites above it.

The abovementioned cases have to be investigated, since it is extremely important to know beforehand if the UG1 and UG2 reef horizons could be seen through the Bleskop marker and the single chromitite stringer. The pulse shape and retardation characteristics are also of critical importance. These characteristics are discussed in the subsequent sections.

### **8.5.1 *Illuminating the UG2 Reef From Below***

Consider the theoretical experiment where the UG2 is illuminated from below through the Bleskop Marker with the transmitter and receiver collocated in the norites, 10 m below the anorthosite-norite interface. The sequence of rock layers to be used in the numeric simulation, is listed in Table 8-1 and based on the simplified planar model approximation as discussed in Section 6.3. The stratigraphic layers have been flipped upside down in Table 8-1 to conform to the model for reflections and transmission in

CHAPTER 8: Propagation and Detection in the Stratified UG1 – UG2 System

a multilayered system as depicted in Figure 7-13, i.e. layers 1 and 12 are the bottom and top layers respectively.

Table 8-1: Stratigraphy for numeric simulation of TM pulse incident on UG2 reef from below.

Layer	Horizon	Rock Type	Dielectric Properties	Thickness
1 (bottom)	Norite	Norite	Approx. as Norite	$\infty$
2	Bleskop Marker	Anorthosite	Approx. as Norite	0.6 m
3		Pegm. Feldsp. Pyroxenite	Approx. as PX 1	0.5 m
4		Chromitite	Approx. as UG2 Top	0.01 m
5		Melanorite	Approx. as PX 1	0.15 m
6		Mesonorite	Approx. as Norite	0.15 m
7		Leuconorite	Approx. as Norite	0.15 m
8	Norite	Norite	Measured as Norite	5.3 m
9	UG2 Reef	Pegm. Feldsp. Pyroxenite	Approx. as PX 1	0.2 m
10		Chromitite	Measured as UG2 Bottom	0.4 m
11		Chromitite	Measured as UG2 Top	0.4 m
12 (top)	Feldspathic Pyroxenite	Feldspathic Pyroxenite	Measured as PX 1	$\infty$

In the theoretic simulation, it was assumed that the transmitter and receiver were collocated at a height of 10 m below the norite-anorthosite (layers 1 and 2) interface. Furthermore, both were assumed to be parallel to the planar interfaces, i.e. their polarization vectors were in the  $x$ - $y$  plane. With this assumption, the entire coordinate system can be rotated about the  $z$ -axis so that the incident and reflected pulses are TM polarized. The total field (infinite series of reflections) at the receiver for a given plane wave excitation  $F(\omega)$  can be calculated as

$$H_{1y}^r = F(\omega) \tilde{R}_{12}^{TM} e^{2ik_{1z}d_1}. \quad (8.13)$$

Equation (8.13) was derived from (7.89) by taking only the upgoing wave and modifying it for TM polarization.  $H_{1y}^r$  is plotted in the time domain for a Ricker

wavelet excitation in Figure 8-23. In addition to the total field solution in (8.13), three other time domain responses were plotted. The second field is the reflection from the UG2 reef horizon (comprising of the pegmatoidal feldspathic pyroxenite and two chromitite layers) in the absence of the Bleskop Marker Sequence

$$H_{1y}^r = F(\omega) \tilde{R}_{89}^{TM} e^{2ik_1 d_8}. \quad (8.14)$$

Thirdly, the reflected field was calculated, in the absence of the Bleskop Marker, with the simplification of a single reflecting interface, being that between the norites and the top section of the UG2 chromitite reef at  $d_9$ , i.e. where the interface between the pegmatoidal feldspathic pyroxenites and the bottom layer of the UG2 chromitite. This was calculated using the following equation:

$$H_{1y}^r = F(\omega) R_{8,11}^{TM} e^{2ik_1 d_9}. \quad (8.15)$$

Finally, the reflected field was calculated, in the absence of the Bleskop Marker, with the entire UG2 reef horizon substituted with a single reflecting interface whose reflection coefficient has a constant amplitude and  $0^\circ$  phase response, i.e.

$$H_{1y}^r = F(\omega) R_{const}^{TM} e^{2ik_1 d_9}. \quad (8.16)$$

$R_{const}^{TM}$  is chosen so that the maximum amplitude of the (8.16) equals that of (8.13).

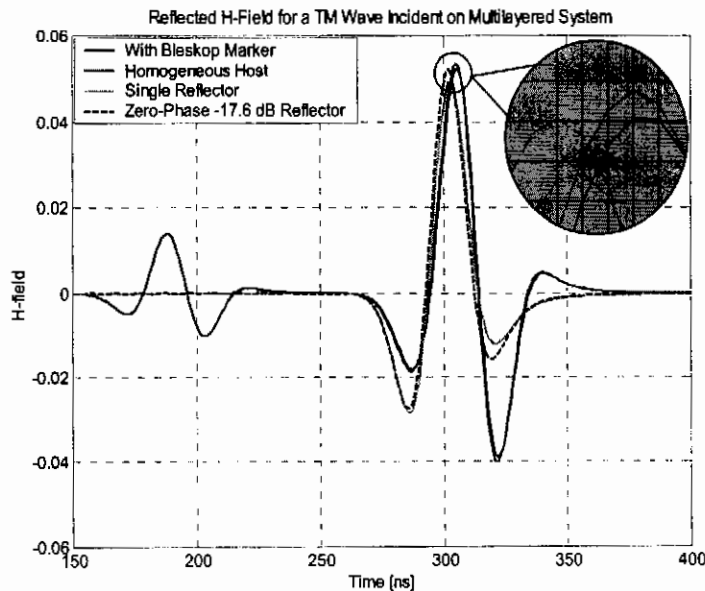


Figure 8-23: Time domain reflections for a TM polarized pulse incident on the UG2 from below. The total time domain field, in the presence of the Bleskop Marker reveals the transmissivity and reflectivity of the Bleskop marker sequence, as well as the reflectivity of the UG2 reef horizon sequence. The peak reflection of the Bleskop

## CHAPTER 8: Propagation and Detection in the Stratified UG1 – UG2 System

Marker is approximately  $-11$  dB lower than the UG2 reef peak reflection. It has been established in the practical experiments discussed in Appendices D – F that the UG2 reflections are dominant in the captured data and it can therefore be assumed that the Bleskop Marker should be visible if the transmitter and receiver are in relatively close proximity to the sequence. The theoretic detection range can be calculated as in Section 8.6 for the UG2 reef. The Bleskop Marker peak in Figure 8-23 is associated with the anorthosite-pegmatoidal feldspathic pyroxenite interface (between regions 2 and 3) at the bottom of the Marker. Even though the dielectric contrast of the chromitite layer is the highest with respect to the host medium, the small thickness results in a very small effective reflection coefficient as discussed in Section 8.4. It is important however, to repeat this simulation when the dielectric properties of all the different layers in the Bleskop Marker sequence have been characterized accurately to determine the effect of the other interfaces implicitly ignored in this simulation.

The pulse shape of the UG2 reef horizon reflection has been altered from the Ricker wavelet due to the different interfaces found in the reef. The total field has been plotted in Figure 8-24 together with the four major superimposing reflections from the four interfaces. All four contribute to the positive peak while mainly the fourth reflection with reversed polarity contributes to the negative peak. The pulse shape deviates from the original Ricker wavelet in the sense that the positive and negative peaks are almost equal in amplitude. If the reef (including the underlying pegmatoidal feldspathic pyroxenites) is replaced with a chromitite (UG2 Top) half-space at the bottom of the original chromitites, it can be seen that this reflection's amplitude is comparable to that of the total field and the time separation between the peaks is in the order of  $0.5$  ns. When this single reflecting surface is replaced with a constant amplitude,  $0^\circ$  phase response reflector, the magnitude of the effective reflection coefficient of the reef can be approximated as  $-17.6$  dB with a time delay of  $3.5$  ns. In a monostatic radar with an average velocity of  $110 \text{ m} \cdot \mu\text{s}^{-1}$ , this implies an increase  $\Delta h$  in the observed depth of the reef as marked by the bottom of the chromitites of

$$\Delta h = 192.5 \text{ mm}. \quad (8.17)$$

For the stratigraphy in Table 8-1 the radar would therefore observe the reef at a depth of  $192.5$  mm deeper than its actual depth.

In Figure 8-23 it is clear from the simulation in the absence of the Bleskop Marker that the amplitude changes to a minimum extent. It appears as though the Marker is almost completely transparent. Chew *et al.* [48] derives an equation for the generalized transmission coefficient relating the downgoing wave amplitude in the  $n$ -th layer to that in the first layer. In some time domain applications this definition (especially where the layers have moderate thickness and the reflection coefficient magnitudes are relatively small) is not a very useful parameter mainly due to the infinite series present in the transmission through a sequence of layers. A new parameter, the effective one-way transmission coefficient is defined as

$$\tilde{T}'_{1N} = \frac{\prod_{j=1}^{N-1} T_{j,j+1} e^{ik_{jz}(d_j - d_{j-1})}}{e^{ik_{1z}d_{N-1}}} \quad (8.18)$$

where  $d_0 = 0$ . It relates the magnitude of the ‘first’ downgoing wave in the  $n^{\text{th}}$  region to the amplitude at the same point if the medium is homogeneous. The effective one-way transmission coefficient’s magnitude in decibels is plotted for the Bleskop Marker in Figure 8-25.

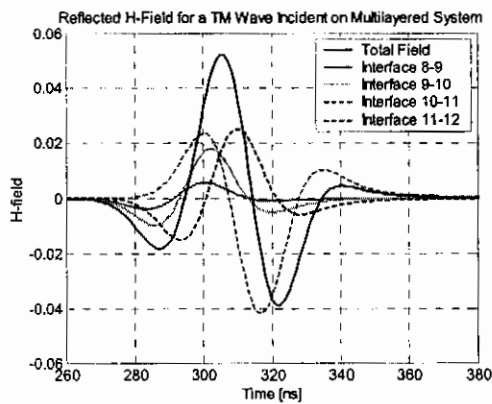


Figure 8-24: Individual contributions to the total reflection of the UG2 reef horizon.

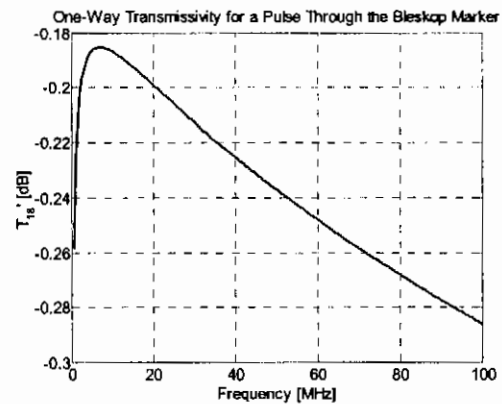


Figure 8-25: One-way transmissivity of the Bleskop Marker sequence.

The transmission loss is less than 0.3 dB across the 100 MHz bandwidth. The Bleskop Marker therefore reflects and absorbs a minuscule amount of the power incident on it. The power reflected is large enough however, to yield a detectable signal at medium ranges.

### 8.5.2 Illuminating the UG1 Layers From Above

Consider the theoretical case where the UG1 chromitite layers are illuminated through the single chromitite stringer above. The transmitter and receiver pair is collocated 10

CHAPTER 8: Propagation and Detection in the Stratified UG1 – UG2 System

m above the single chromitite stringer. The stratigraphy used for this simulation is given in Table 8-2 and is taken from Section 6.3.

Table 8-2: Stratigraphy for numeric simulation of TM pulse incident on UG1 layers from above.

Layer	Horizon	Rock Type	Dielectric Properties	Thickness
1	Norite	Norite	Approx. as Norite	$\infty$
2	Chrome Stringer	Chromitite	Approx. as UG2 Top	0.008 m
3	Feldspathic Pyroxenite	Feldspathic Pyroxenite	Approx. as PX 1	10 m
4	UG1 Layers	Chromitite	Approx. as UG2 Top	0.75 m
5-12		4 X Anorthosite	Approx. as Norite	30 cm
		Chromitite	Approx. as UG2 Top	10 cm
13	Anorthosite	Anorthosite	Approx. as Norite	$\infty$

Once again the transmitter and receiver pair are orientated in the  $x$ - $y$  plane and rotated about the  $z$ -axis for TM polarization. The total reflected field  $H'_{1y}$  is calculated using (8.13). This is plotted in Figure 8-26 for a Ricker wavelet excitation. As in Section 8.5.1, three other reflections are also plotted. The reflection of the UG1 layers in the absence of the chromitite stringer calculated as

$$H'_{1y} = F(\omega) \tilde{R}_{34}^{TM} e^{2ik_{1z}d_1} e^{2ik_{3z}(d_3-d_1)}. \quad (8.19)$$

The reflection of a single feldspathic pyroxenite-chromitite interface calculated as

$$H'_{1y} = F(\omega) R_{34}^{TM} e^{2ik_{1z}d_1} e^{2ik_{3z}(d_3-d_1)} \quad (8.20)$$

and the reflection of a constant amplitude,  $0^\circ$  phase response interface as

$$H'_{1y} = F(\omega) R_{const}^{TM} e^{2ik_{1z}d_1} e^{2ik_{3z}(d_3-d_1)}. \quad (8.21)$$

Eqs. (8.19) - (8.21) have different exponents to that of eqs. (8.14) - (8.16) due to the fact that the host medium is now a combination of norites above and feldspathic pyroxenites below the stringer.

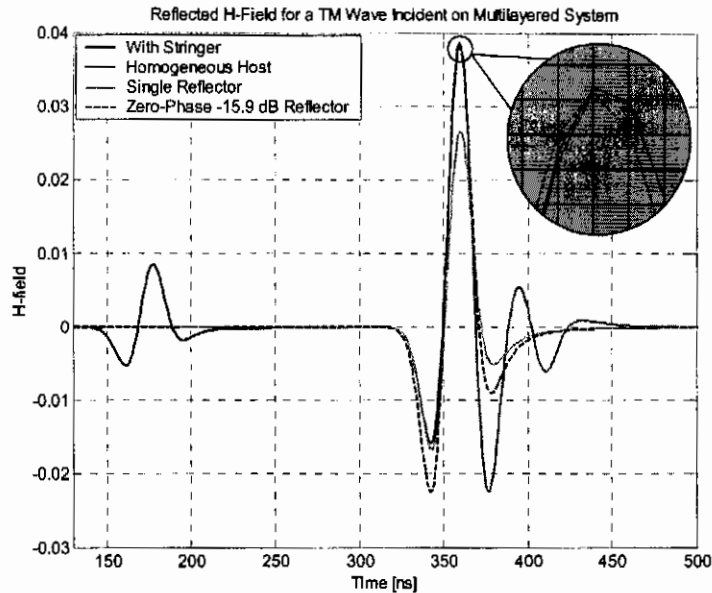


Figure 8-26: Time domain reflections for a TM polarized pulse incident on the UG1 from above.

The reflection of the chromitite stringer is clearly visible and resolved from the UG1 reflection, but 20.8 dB lower than the reflection of the UG1 layers. The observed difference in Figure 8-26 is only 13.2 dB, but due to the increased travelling distance to the UG2 the actual reflection magnitude difference is 7.6 dB higher than the observed value. The chromitite stringer might therefore only be visible when within close range to the transmitter and receiver pair. The minute thickness of this layer makes it virtually invisible at moderate ranges and beyond. The shape of the reflection from the UG1 layers is greatly affected by the sequence of layers in the UG1 reef. The main part of the pulse correlates with that of a Ricker wavelet, but there is an additional oscillating tail. It is clear that the chromitite stringer is virtually 100% transparent when the reflection in the absence of the stringer is compared to when it is present. The total reflection is about 2 dB stronger than that of a single interface between the feldspathic pyroxenites and the chromitite. Furthermore, when the total reflection is compared to the reflection of a constant magnitude, 0° phase response reflector, it can be seen that there is virtually no time delay between the peaks of the reflected fields and the observed depth of the UG1 will be in close correlation with the exact depth of the first chromitite interface. This is strictly true only for the given configuration in Table 8-2.

The effective one-way transmission coefficient as defined in (8.18) cannot be calculated for this case, since the medium below the stringer is not the same as above.

As discussed above however, the one-way transmission loss is extremely low (quantitatively).

This section indicated that the UG1 layers yield a detectable reflection with a slightly modified pulse shape. It is also visible through the chromitite stringer – a virtually transparent layer. The chromitite stringer should only be visible when in close proximity to the radar.

## 8.6 UG2 Detection Range Prediction

This section, together with Section 8.7, sees the culmination of the entire dissertation. The distance up to which the UG2 reef horizon might be detected with borehole radar is calculated here.

It has been proved experimentally that the GeoMole BHR system can image the UG2 and UG1 reef interfaces at distances beyond 30 – 40 m (see Appendices D – F and [8], [94], [97], [98]). At Brakspruit a tunnel was visible up to 60 m from the borehole [8], [97]. The analysis in this section is independent from these experimental observations with the main purpose to confirm them theoretically. It is based on numerous simulations, measurements, assumptions and theoretic calculations. The major assumption and approximations are summarised in Table 8-3.

*Table 8-3: Assumptions and approximation used in the UG2 detection range prediction.*

#	Actual Measurable / Process	Assumption / Approximation
1	Complex stratified geometry.	Perfectly planar, horizontal, limited sequence of rock layers (Section 6.3).
2	Nearly homogeneous layers with unique dielectric and magnetic properties.	Homogeneous, non-magnetic, linear and isotropic layers with dielectric properties approximated by experimental measurements [39].
3	Electromagnetic illumination by a distributed current source (the actual antenna).	Electromagnetic illumination by a point source at the feedpoint of the antenna.
4	Electromagnetic scattering from rough interfaces.	Electromagnetic scattering from a specular, planar interface.

The following key steps summarize the basic procedure for the calculation of the detection range of a planar interface:

## CHAPTER 8: Propagation and Detection in the Stratified UG1 – UG2 System

- Determine the maximum available power to the RX electronics,  $P_{av}$ .
- Determine the noise floor of the RX electronics over the frequency band of interest.
- Calculate the maximum attenuation before the SNR falls below a given threshold.
- Assume an appropriate reflection coefficient magnitude.
- Calculate the signal attenuation as a function of range and determine the maximum range for a given SNR.

The maximum available power  $P_{av}$  for a borehole radar system depends on the exact radar configuration, the nature of the boreholes and the host medium. For a typical configuration and a 500 kHz PRF,  $P_{av}$  is plotted in Figure 8-27.  $P_{av}$  ranges between –37 dBm/Hz at approximately 10 MHz to a maximum of –13 dBm/Hz at 65 MHz after which it tapers off again. The noise floor at the front-end of the receiver is measured and calculated as described in Chapter 4 and plotted in Figure 8-28. For a single trace captured, the noise power spectral density varies between –105 dBm/Hz and –98 dBm/Hz over the majority of the frequency band. The noise level drops by 30 dB when the average of 1024 traces is taken, since the noise in this system is uncorrelated.

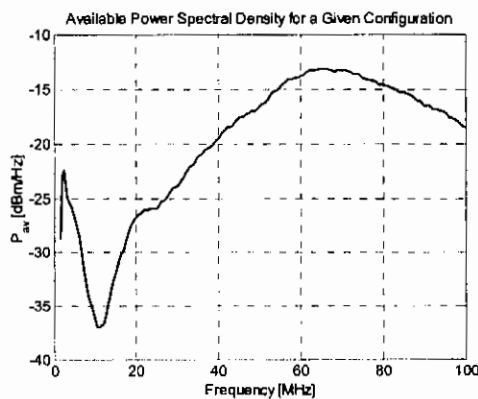


Figure 8-27: Maximum available power spectral density for a typical configuration.

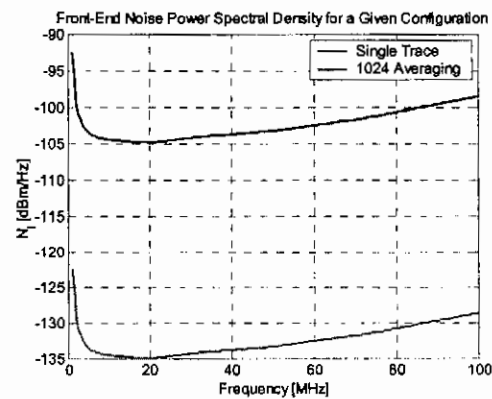


Figure 8-28: Front-end noise power spectral density for a typical configuration.

Using this, the maximum permissible signal attenuation for a given SNR level can be calculated

$$A_{\max} = \frac{N_f \cdot SNR}{P_{av}} \quad (8.22)$$

The signal processing for borehole radars consists mainly of post-processing at the end of a survey, with only the data capturing occurring instantaneously. This enables signal processing techniques that operate on signal with very low SNR, even below 0 dB. The added benefit of user intervention and intelligence also increases the fidelity of low SNR signal processing. In this section the assumption is made that the minimum SNR for detection is 0 dB. The maximum permissible attenuation for this SNR is plotted in Figure 8-29.

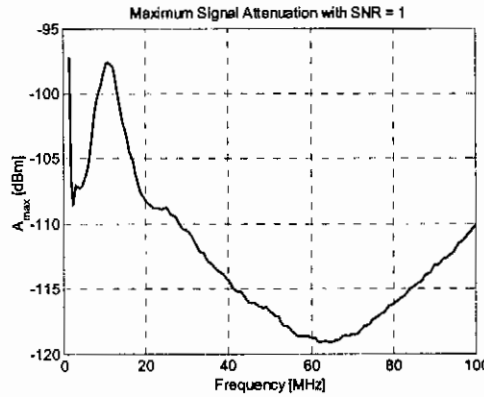


Figure 8-29: Maximum signal attenuation with SNR = 0 dB for the GeoMole borehole radar.

The maximum signal attenuation increases from -97.5 dB at 11 MHz to a maximum of -119 dB at 62 MHz after which it tapers off to -110 dB at 100 MHz. The total theoretical signal attenuation for a monostatic radar illuminating a planar interface is

$$A = p \frac{D_{tx} D_{rx} e^{-2\alpha R_{tot}}}{D_{tx(max)} D_{rx(max)} 4\pi R_{tot}^2} R^2(0^\circ) \quad (8.23)$$

where  $R_{tot}$  is the total path length from the transmitter to the interface and back to the receiver. The most basic configuration is that of a radar where the transmitter and receiver are collocated and collinear polarized in the  $x$ - $y$  plane. The coordinate system can be rotated so that the polarization is entirely TM or TE. With the abovementioned assumptions, (8.23) can be simplified as

$$A = \frac{e^{-2\alpha R_{tot}}}{4\pi R_{tot}^2} R^2(0^\circ). \quad (8.24)$$

In (8.24),  $\alpha$  is calculated from the empirically calculated average propagation velocity of  $110 \text{ m}\cdot\mu\text{s}^{-1}$  and the  $Q$  values empirically calculated in Section 6.8. Signal attenuation as a function of frequency is plotted for a range of vertical heights  $h_1$  ( $R_{tot} = 2h_1$ ) in Figure 8-30, together with the maximum permissible signal attenuation with SNR = 0 dB. The reflection coefficient magnitude was estimated as being -17 dB

across the frequency band – the nominal reflection coefficient of the UG2 reef as illuminated from below taken from Section 8.5.1.

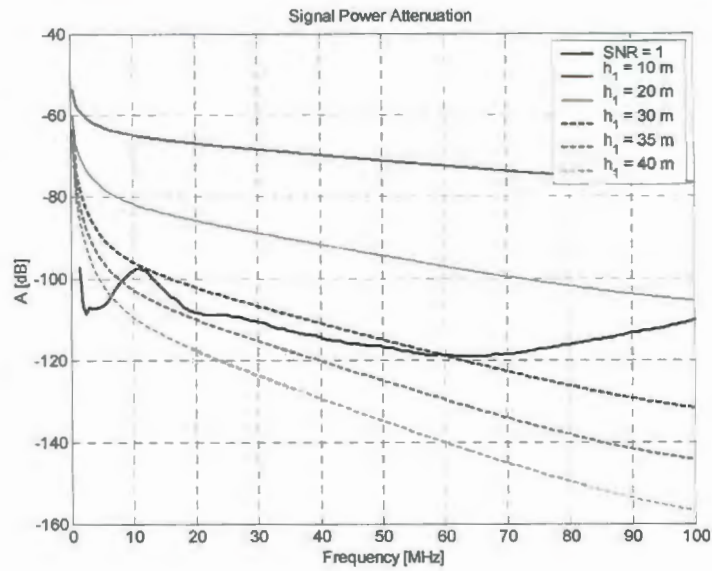


Figure 8-30: Signal power attenuation as a function of frequency for discrete ranges.

At ranges of up to 20 m the UG2’s reflection will have a SNR > 20 dB. At 30 m the SNR of the reflections rapidly decrease to only 3.5 dB at 30 MHz. Beyond 30 m the SNR decreases below 0 dB for the entire frequency band above 10 MHz. The power attenuation surface plot as a function of frequency and range in Figure 8-31 illustrates this rapid falloff of SNR as the range increases above 30 m across the frequency band.

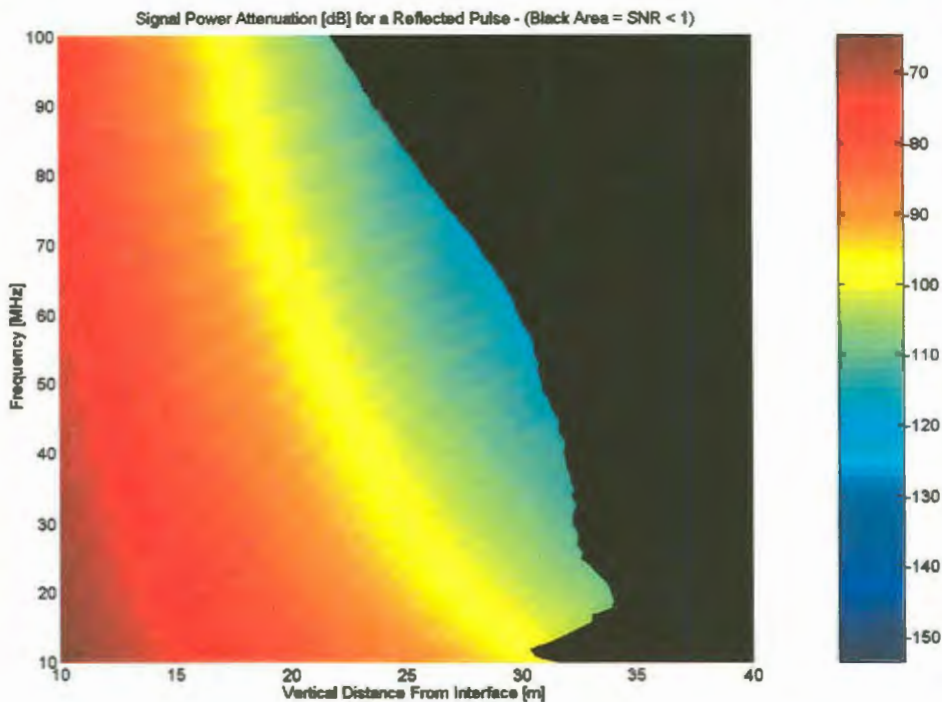


Figure 8-31: Signal power attenuation as a function of frequency and range.

The black area indicates the frequency and range combinations where the SNR is less than unity. The clear cut-off just beyond 30 m is visible. If the reflection coefficient magnitude is increased to -10 dB, the detection range increases to about 35 m. When the measured Q values [39] for norite are used, this range increases to about 70 m, i.e. more than double the distance with the Q values as empirically calculated. As discussed in Section 6.8, the measured values of Q are based on the measurements of small disc samples of the rock and thus subject to uncertainty due to possible rock inhomogeneity. The empirically calculated values of Q were obtained from bulk volume measurements and should therefore yield more accurate estimates for the work in this section.

Practical experiments confirm detection ranges of the UG2 reef horizon in the range of 30 m to 40 m. In some cases, detection ranges of up to 50 m (even 60 m for the tunnels) have been achieved. For detection ranges of 30 m – 40 m, the empirical values of Q and R used in (8.24) are quite accurate. If detection ranges in excess of 40 m are observed, the values of Q and/or R have to be higher than the empirical values. It should be noted however, that interfaces other than dielectric, specularly reflecting planar interfaces might yield significantly greater reflection coefficients and increased detection ranges. A rock-air interface can be detected up to and beyond 40 m because of the increased reflection coefficient magnitude, which is approximately -7 dB. A focussing structure such as a rolling UG1 or a curved tunnel can also significantly increase backscatter and its detection range. If an isotropic radiator is situated at the focal point of a spherical reflector, with an azimuth extent  $l_{az}$  and elevation extent  $l_{el}$ , the optical backscatter power loss due to geometric spreading equals

$$L_{geometric}(r, l_{az}, l_{el}) = \frac{l_{az} l_{el}}{4\pi r^2}. \quad (8.25)$$

The geometric spreading power loss for when an isotropic radiator illuminates a planar interface equals

$$L_{geometric}(r) = \frac{1}{16\pi r^2}. \quad (8.26)$$

The increased power return for a spherical reflector can be seen as the gain of the reflector  $G_{sr}$  and is the ratio of (8.25) and (8.26):

$$G_{sr} = 4l_{az} l_{el}. \quad (8.27)$$

A 1 m high and 10 m wide spherical reflector has an optical gain of 16 dB and a detection range exceeding the predicted 30 to 40 m.

## 8.7 UG2 Reflectivity Estimation

In the final section of this chapter on the application of plane wave propagation, the UG2 reflection coefficient magnitude (reflectivity) is calculated empirically. This calculation is based on the successful and accurate calculation, estimation or approximation of:

- the borehole and UG2 reef horizon geometries,
- the transfer function of the entire radar system, and the
- complex wave number of the host medium.

It is also dependent on the purity of the polarization, whether TM or TE, since it is impossible to determine the relative contributions of the two polarizations. The first step in the reflectivity estimation is to find a suitable experiment, satisfying all the criteria as given in Section 6.8. Secondly, the geometries involved have to be delineated to a predetermined standard configuration. The third step involves the characterization of the radar system. The final step is to use power relationships to estimate the reflectivity. These four steps are discussed in the following subsections.

### 8.7.1 *Experimental Subset that Satisfies Criteria Set*

The accuracy of the reflectivity estimation is dependent on the fidelity of the experimental survey used. The basic criteria for the estimation of the reflectivity of a given horizon include the following:

- an accurately calibrated radar,
- boreholes with a known diameter and filling substance (air or water),
- relatively homogeneous host medium,
- a signal event with a high SNR
- a high fidelity signal event (minimum pulse shape distortion), and
- spatially resolved reflection from the interface under consideration.

The profile scans of the UG1 – UG2 stratigraphy at Bleskop section 162, 13 level west haulage, as discussed in Appendix F, proved to be the experimental results with the highest fidelity. The first profile scan of hole 48 specifically satisfied all the abovementioned criteria and was chosen for the reflectivity estimation of the UG2

reef horizon. The exact radar configuration was accurately logged, enabling its accurate characterization. The boreholes were also surveyed with an orientation sensor and the borehole trajectories were delineated [96]. The borehole collars were matched with the mine map and coordinate system. The local height of the UG2 reef was established from the five radar profiles using a natural neighbour interpolation. It was also tied with the mine plans [95]. The hole 48 borehole was inclined upwards and therefore essentially dry and air-filled. The vertical section (Appendix F) indicates that the borehole was primarily located in the norites for the duration of the survey, with a minor portion in the feldspathic pyroxenites. If the section of the experimental data is chosen to lie in the norites, the host will essentially be homogeneous. Consider the 32 traces recorded with the fibre optic cable 40 m to 45 m into the borehole with the raw data plotted in Figure 8-32.

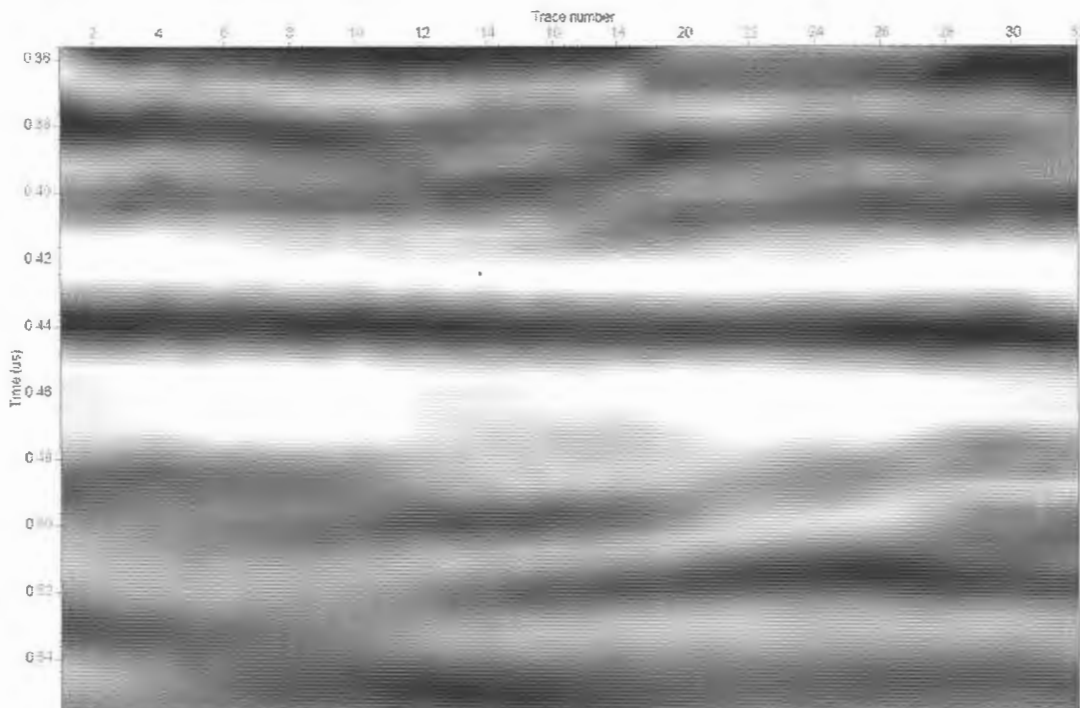


*Figure 8-32: Section of raw data used to estimate UG2 reflectivity.*

The SNR of the reflection (centred at 0.44  $\mu\text{s}$ ) is high enough and the pulse shape is only slightly modified at some of the traces, while it is as resolved from any other reflections as practically possible. It is possible however, to resolve the reflections further by using the pulse recompression algorithm discussed in Chapter 5.

### 8.7.2 Borehole and UG2 Reef Horizon Delineation

In a profile scan, the distance between the transmitter and receiver feed points and the end of the optic fibre cable are 0.8 m and 2.6 m plus the length of the optical spacer (3.15 for this specific survey) respectively. The exact location of the transmitter and receiver can be deduced for each trace with respect to the collar of the borehole and also the UG2 reef horizon, Figure 8-33. For both the transmitter and receiver, their respective polarization vectors have to be found.

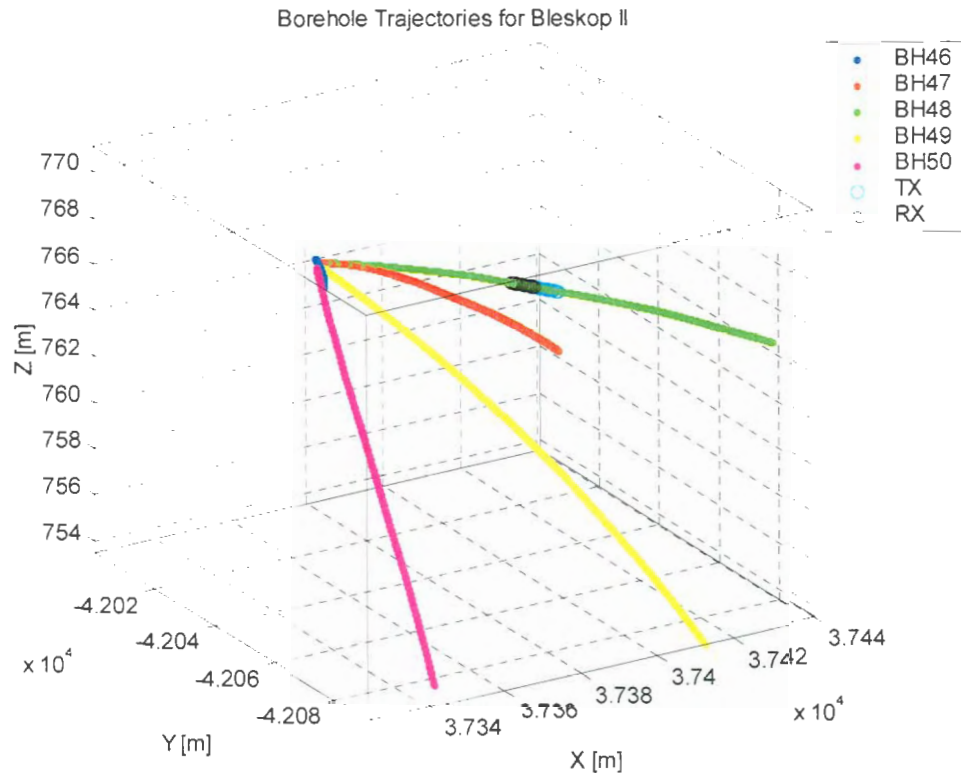


Figure 8-33: Transmitter and receiver locations for reflectivity estimation.

Furthermore, the nadir points of the transmitter and the receiver on the UG2 reef interface have to be found. The characteristic equation of a plane in the Cartesian coordinate system [13] is

$$ax + by + cz = d \tag{8.28}$$

where  $\hat{n} = a\hat{x} + b\hat{y} + c\hat{z}$  is the unity normal vector and  $d$  is the shortest distance between the origin and the plane. It is possible to find (8.28) from 3 points on the plane. Discrete points on the digital elevation surface map of the UG2 reef horizon [95] and in the centre of hole 46 yielded

$$1.096 \times 10^{-2} x - 9.416 \times 10^{-2} y - 0.995 z = 3.593 \times 10^3 \tag{8.29}$$

This is associated with a local dip and strike of  $5.4^\circ$  and  $6.6^\circ$  respectively. The nadir point  $\bar{r}_n$  associated with a given point  $\bar{r}$  can be found using the 3 equations embedded in

$$\bar{r} - \bar{r}_n = c\hat{n} \quad (8.30)$$

and (8.28). The transmitter and receiver feedpoints and nadir points on the UG2 reef interface are plotted in Figure 8-34.

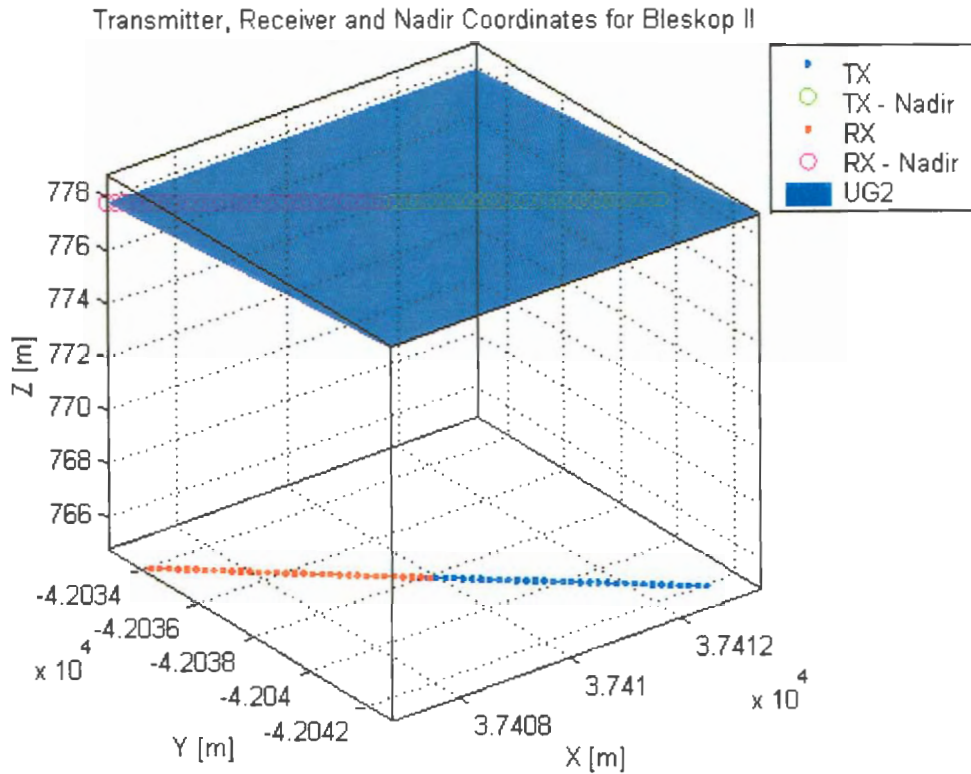


Figure 8-34: Transmitter and receiver feedpoints and nadir points for reflectivity estimation.

The shortest distance between the transmitter and receiver feed points (Fermat's principle [51]) for every trace can be found using Snell's law of refraction and reflection in the plane defined by the transmitter and receiver feed and nadir points. It is therefore necessary to rotate the geometry for each trace so that the aforementioned plane lies entirely in the  $x$ - $z$  plane. This can be done using the following seven steps:

1. Translate the coordinate system so that the transmit nadir point lies at the origin. This yields the coordinates  $\bar{r}_{t1}$ ,  $\bar{r}_{t2}$ ,  $\bar{r}_m = \bar{0}$ ,  $\bar{r}_{r1}$ ,  $\bar{r}_{r2}$  and  $\bar{r}_m$  - the transmitter feed, polarization and nadir and the receiver feed, polarization and nadir coordinates respectively.

2. Find the polar coordinates,  $\phi$  and  $\rho$ , about the  $z$ -axis for all the points.
3. Subtract  $\phi_m$  from  $\phi$  for every coordinate and ensure that  $-180^\circ < \phi \leq 180^\circ$ . Calculate the new Cartesian coordinates  $\bar{r}'_{i1}$ ,  $\bar{r}'_{i2}$ ,  $\bar{r}'_{r1}$ ,  $\bar{r}'_{r2}$  and  $\bar{r}'_m$ .
4. Find the polar coordinates,  $\phi$  and  $\rho$ , about the  $y$ -axis with  $\phi$  measured from the positive  $z$ -axis.
5. Add  $(\pi/2 - \phi_m)$  to  $\phi$  for every coordinate and ensure once again that  $-180^\circ < \phi \leq 180^\circ$ . Calculate the new Cartesian coordinates  $\bar{r}''_{i1}$ ,  $\bar{r}''_{i2}$ ,  $\bar{r}''_{r1}$ ,  $\bar{r}''_{r2}$  and  $\bar{r}''_m$ . The transformed receiver nadir coordinate should now lie on the positive  $x$ -axis.
6. Find the polar coordinates,  $\phi$  and  $\rho$ , about the  $x$ -axis with  $\phi$  measured from the positive  $z$ -axis.
7. Subtract  $\phi_{r1}$  from  $\phi$  for every coordinate and ensure that  $-180^\circ < \phi \leq 180^\circ$ . Calculate the new Cartesian coordinates  $\bar{r}'''_{i1}$ ,  $\bar{r}'''_{i2}$ ,  $\bar{r}'''_{r1}$ ,  $\bar{r}'''_{r2}$  and  $\bar{r}'''_m$ . Both the transmitter and receiver feed and nadir points should now lie in the  $x$ - $z$  plane.

The rotated transmitter and receiver coordinates for reflectivity estimation are plotted in Figure 8-35 and Figure 8-36.

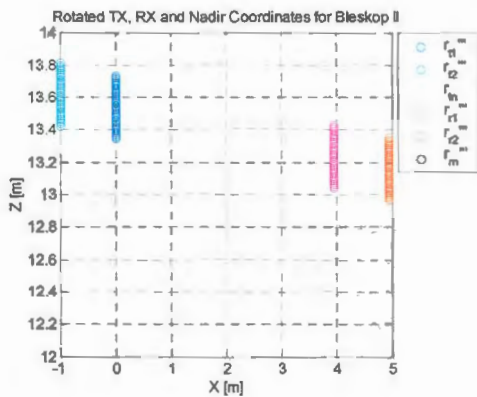


Figure 8-35: Rotated TX and RX coordinates for reflectivity estimation – side view.

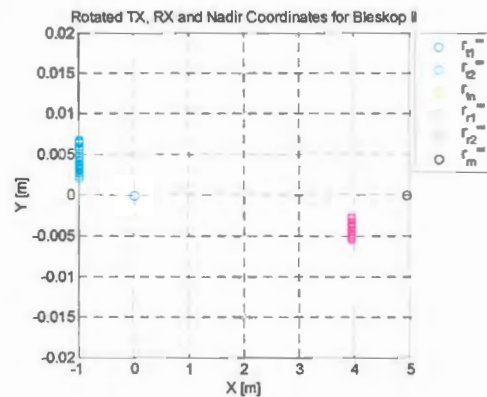


Figure 8-36: Rotated TX and RX coordinates for reflectivity estimation – top view.

Please note that the  $z$ -axis and  $y$ -axis are not on scale with the  $x$ -axis. The nadir coordinates are located exactly below the feed points at  $z = 0$  and not visible on the axes.

The polarization vectors can be found by subtracting the feed point coordinates from the polarization coordinates of the transmitter and receiver,

$$\begin{aligned}\bar{r}_{tx} &= \bar{r}_{t2}^m - \bar{r}_{t1}^m, \text{ and} \\ \bar{r}_{rx} &= \bar{r}_{r2}^m - \bar{r}_{r1}^m.\end{aligned}\tag{8.31}$$

The E-field radiated by the transmitter is a linear superposition of two components, one polarized in the plane of incidence (TM polarization), the other with a polarization perpendicular to the plane (TE polarization). In exactly the same way, the received field has TM and TE polarization components. In order to calculate these components, we have to find the spherical coordinates of the two vectors, with the coordinate system and angles as defined in Figure 8-37 for the transmitter.

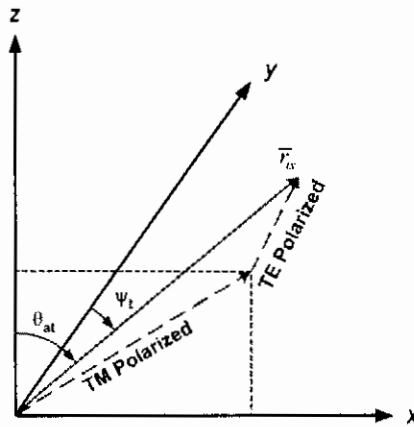


Figure 8-37: TM and TE polarization components defined.

From this the components of the power transmitted in the two polarizations can be found:

$$\begin{aligned}\Omega_t^{TE} &= \cos^2 \psi_t \\ \Omega_t^{TM} &= \sin^2 \psi_t.\end{aligned}\tag{8.32}$$

Eq. (8.32) can be rewritten for the receiver, yielding the components of the power received from the two polarizations. As stated in the introduction of Section 8.7 a dominating transmitter and receiver polarization is required. The components of the power radiated and received in the TM polarization are plotted in Figure 8-38.

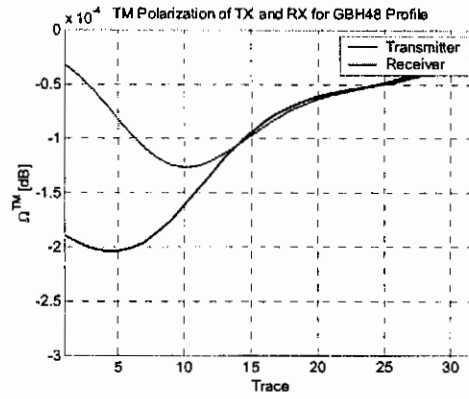


Figure 8-38: TM polarization components for transmitter and receiver.

After it has been established (for this specific section of the experimental survey) that both the transmitter and receiver polarizations are almost purely TM, the geometry can be delineated completely, yielding the geometry as depicted in Figure 8-39.

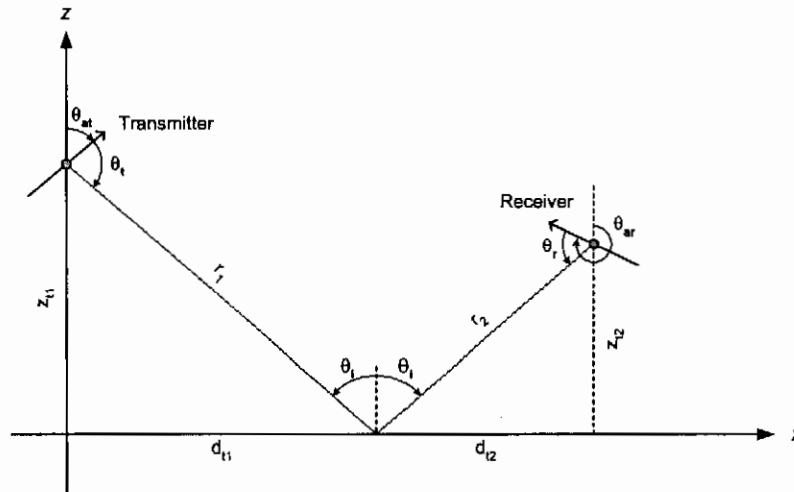


Figure 8-39: Delineated geometry for reflectivity estimation.

When  $\theta_t$  is calculated, ensure that  $\theta_{at} \geq 0$ , i.e. whenever  $\theta_{at} < 0$  add  $2\pi$ .  $\theta_t$  can then be calculated as

$$\theta_t = \begin{cases} \pi - (\theta_i + \theta_{at}) & , \quad \theta_{at} \leq \pi - \theta_i \\ (\theta_i + \theta_{at}) - \pi & , \quad \theta_{at} > \pi - \theta_i \end{cases} \quad (8.33)$$

Ensure that  $-180^\circ < \theta_t \leq 180^\circ$  and then take its absolute value, since the antenna is omnidirectional. When  $\theta_r$  is calculated, also ensure that  $\theta_{ar} \geq 0$ .  $\theta_r$  can then be calculated as

$$\theta_r = \begin{cases} (\pi + \theta_i) - \theta_{ar} & , \quad \theta_{ar} \leq \pi + \theta_i \\ \theta_{ar} - (\pi + \theta_i) & , \quad \theta_{ar} > \pi + \theta_i \end{cases} \quad (8.34)$$

Also ensure that  $-180^\circ < \theta_r \leq 180^\circ$  and take its absolute value. The incidence angle is approximately  $10.5^\circ$  for all the traces, while the transmitter and receiver directivity angles are respectively in the region of  $105^\circ$  and  $84^\circ$ . This concludes the geometric delineation for reflectivity estimation.

### 8.7.3 Radar Configuration and Calibration

For the specific survey under consideration, the USTX 01 transmitter was deployed in hole 48 – a dry, 48 mm borehole. The USRX 01 receiver was also deployed in the dry 48 mm hole 48. The host medium surrounding the borehole for the experimental section was norite. The short fibre optic cable #3 (194 m) was used in conjunction with the 3.15 m optical spacer with the optic cable directly fixed unto the rotating drum. The PH001 SCU was used for this specific experiment, with the attenuation before the ADC set at  $-3$  dB. An averaging factor of 256 samples was used. The aforementioned radar configuration was used in the pulse recompression algorithm to calculate the estimated E-field at the receiver feed point. The bandpass notch filter parameters was set to

$$\begin{aligned} f_1 = 5 \text{ MHz} , f_2 = 60 \text{ MHz} , f_3 = 65 \text{ MHz} , f_4 = 90 \text{ MHz} \\ \Delta f_1 = 5 \text{ MHz} , \Delta f_2 = 5 \text{ MHz} . \end{aligned} \quad (8.35)$$

The E-fields were time-gated using a time domain bandpass filter from 410 ns to 470 ns with Hanning window rising and falling edges of 20 ns lengths. The time-gated E-fields for the 32 traces are plotted in Figure 8-40.

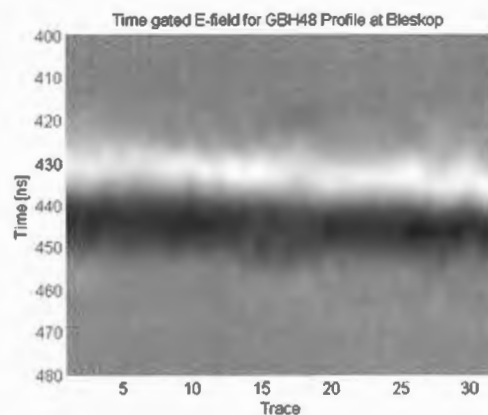


Figure 8-40: Time-gated E-field for reflectivity estimation.

The UG2 reflection is clearly resolved in Figure 8-40. This time-gated E-field data is now used to calculate the power delivered to the receiver electronics,  $P_d$ .

### 8.7.4 Calculating $R^{TM}$ Using Power Relations

The magnitude of the TM polarized reflection coefficient can be calculated theoretically from the power available and the power delivered to the receiver electronics as

$$|R^{TM}| = \sqrt{\frac{P_d}{P_{av} \frac{D_{tx} D_{rx}}{D_{tx(max)} D_{rx(max)}} \cdot \frac{e^{-2\alpha(r_1+r_2)}}{4\pi(r_1+r_2)^2}}} \quad (8.36)$$

given that the transmitter and receiver are both purely TM polarized. The aforementioned condition is satisfied for this experiment as proven in Figure 8-38. The reflectivity estimations for the UG2 reef interface are plotted in Figure 8-41 for the 32 traces as a function of frequency together with the average of these traces.

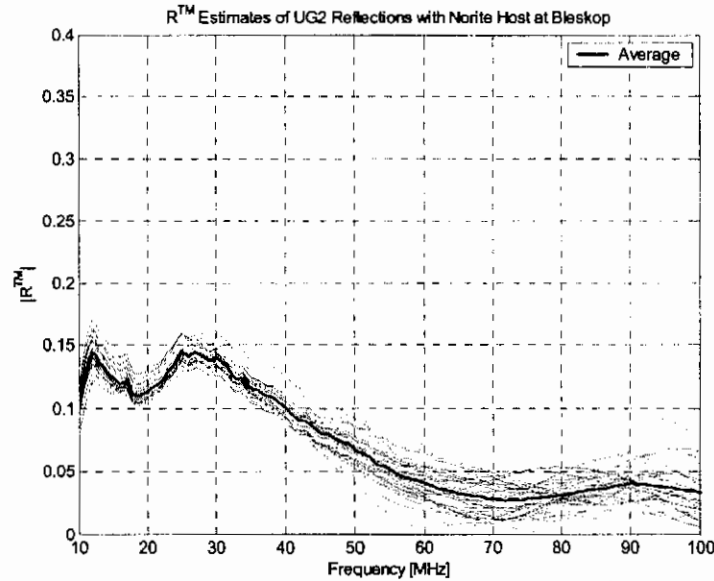


Figure 8-41: Reflectivity estimate of the UG2 reef interface.

The estimated average reflectivity of the UG2 reef interface is between  $-20$  dB and  $-16$  dB in the frequency range of  $10 - 40$  MHz, after which it decreases to  $-28$  dB at  $90$  MHz. In the  $10 - 40$  MHz frequency range the magnitude of the estimated reflection coefficient and the theoretical reflection coefficient calculated in Section 8.3.2 correlates to a very high degree of accuracy. The estimated reflection coefficient at the higher frequencies is lower than the theoretical values and this might be due to a number of reasons, e.g. a pessimistic system transfer function or an underestimated value of  $Q$  at the higher frequencies. It is close enough, however, to confirm the order of magnitude of the UG2 reef interface reflections based on the simplified planar

model, the measured dielectric properties of the rocks and the empirically calculated Q values of norite. This result confirms the accuracy of the characterization and calibration in the first part of the dissertation as well as the propagation study in the latter part. Therefore, this result can be viewed as the culmination of this dissertation.

## **8.8 Concluding Remarks**

In this chapter the theory of plane wave propagation in stratified lossy media was applied to real-life problems.

The Ricker wavelet was used throughout this chapter as the source excitation. Time domain pulse reflections from a single dielectric interface were considered for both polarizations. Of critical importance is the fact that there is an increase in the observed depth of the interface when either or both the half-spaces are lossy. The study of pulse reflections was extended to a sandwiched layer between two half-spaces. The effects of the incidence angle and thickness of the sandwiched layer were investigated. Both of these have a definite effect on the pulse shape and magnitude of the reflections. The first section of this chapter is concluded with the simulation of the reflections of a transmitter-receiver pair deployed in a multi-layered system. Attention was given to the reflections of the UG1 and UG2 horizons as well as the reflectivity and transmissivity of the Bleskop Marker and the single chromitite layer.

In the second part of this chapter, the plane wave propagation theory was used in conjunction with the empirical measurements of the rock properties in Chapter 6, the measured dielectric properties also in Chapter 6 and the pulse recompression and system characterization studies from Chapters 2 to 5. The purpose of this was to estimate the maximum detection range of the UG2 interface as well as its reflectivity. Very good results were obtained that confirmed the accuracy of the measurements, simulations, approximations, theory and models in Chapters 2 to 7. These results are indeed the culmination of this dissertation.

# CHAPTER 9

## CONCLUSIONS & RECOMMENDATIONS

The conclusions made during the progress of this dissertation are presented in this chapter. Recommendations are made for possible future work that may build on the foundation laid by the work presented in this dissertation.

### 9.1 Conclusions

The importance (economical and sociological) of the delineation (imaging) of the geological geometry in the BIC was established in Chapter 1. One of the biggest concerns is the location of potholes in the UG2 reef. The UG2 is one of two economically important horizons in the BIC and is frequently disturbed by the occurrence of potholes as defined in Chapter 6.

All the obvious mapping methods have been tried, but with only limited success in the location and dimension estimation of UG2 potholes [8]. The GeoMole BHR system has been successful in the delineation of various geological structures in different settings over a period of almost 10 years. The application of BHR technology in the delineation of UG2 potholes is a very important possibility.

In this dissertation, five major contributions have been made to the field of imaging platiniferous reefs in the BIC using borehole radar technology:

#### **9.1.1 *Characterization of System Transfer Function***

The system transfer function of a borehole radar was characterized where the transmit and receive antennas were deployed in air- or water-filled boreholes drilled into an absorbing, geologically stratified rock mass. A combination of experimental, numerical and theoretical techniques was used.

The transmitter and receiver probes were characterized in Chapter 3. The power delivered to the TX antenna was estimated for the different transmitter probes, while the relative performance of the different receiver probes was measured. The characteristics and transfer functions of the TX and RX antennas were numerically

simulated with FEKO, a MoM EM simulation software package. A procedure was derived by which the performance of the TX and RX probes could be inferred when deployed in boreholes in the mining environment.

The receiver RF and digital chain was characterized in Chapter 4. The GeoMole receiver chain incorporates a highly configurable optic link - a total of 5184 different configurations are possible. A method was developed by which the gain of any configuration can be determined by means of reference and relative gains. The ADC unit was characterized in the second part of Chapter 4. Three practical measurement configurations were used to measure the time and frequency domain responses, which correlated well with the theoretically predicted transfer function.

The basic system performance parameters were determined in the last part of Chapter 4. The maximum available power was estimated to be higher than  $-25 \text{ dBm.Hz}^{-1}$  for a 0.5 MHz PRF over most of the frequency band, for a number of different deployment configurations. The noise floor was calculated to be less than  $-100 \text{ dBm.Hz}^{-1}$  for a 0.5 MHz bandwidth over the frequency band of interest. The maximum permissible signal attenuation due to spatial dependence (geometric spreading, geometric losses and antenna directivity) was found to be an average of  $-110 \text{ dB}$  for an averaging factor of 512. This parameter is a well-defined figure of merit that can be used to compare different GPR systems.

### **9.1.2 Novel Pulse Recompression Algorithm**

With the current system and processing techniques a resolution of 1 m is possible. This enables the mapping of potholes with a throw of 1 to 2 m. An algorithm was developed in Chapter 5 by which the deteriorated range resolution of the current system can be restored almost to its theoretic maximum. It exploits the characterized system transfer function. The algorithm was tested on laboratory measurements and field experiment data. It effectively reconstructed the E-field and increased the resolution of the system. The algorithm was incorporated in a GUI-based batch-processing pulse recompression program for the processing of field experiment data. Results with the data obtained at Brakspruit I, Bleskop II and Mponeng (gold mine) were presented. The resolution was indeed increased and a number of unresolved targets were resolved. The recompressed E-field data, used in conjunction with the original data, can enhance the accuracy of geometry delineation significantly.

### **9.1.3 Plane Wave EM Propagation in Stratified Absorbing Layers**

The propagation of radiowaves in the rock strata of the UG1 – UG2 system in the Bushveld Igneous Complex was considered in Chapter 6. The geology of the BIC was introduced, the UG1 – UG2 stratigraphy was generalized and a simplified model of a vertical sequence of planar layers was derived. The bulk volume average pulse peak velocity and quality factor of the host rock (norite) were estimated from field experiment data and found to be  $110 \text{ m} \cdot \mu\text{s}^{-1}$  and about 15 at 50 MHz respectively.

Chapter 7 presented the theoretic evaluation of plane wave propagation in stratified lossy matter. It was shown that the basic building block in the understanding of plane wave propagation is the reflection and transmission from an interface between two half-spaces. The choice of the correct Riemann surface in the lower half-space is complicated if both half-spaces are lossy. A paradox was identified where, for a given region in the  $k_{2z}^2$ -complex plane, the causal solution yielded a proper inhomogeneous leaky plane wave with a reflection coefficient larger than unity. It was found however, that this region is associated with pseudo total internal reflection. Realising that a lateral shift occurs at the boundary in this region and using the energy conservation theorem, it was proven that the magnitude of the reflection coefficient as it is defined might be larger than unity.

Criteria were developed to choose the correct branch for TE and TM waves. The final section of Chapter 7 was concerned with reflection and transmission in a multilayered planar system and the criteria for branch choices were defined.

### **9.1.4 Estimation of the Reflected Waveforms**

The theory developed in Chapter 7 was used to estimate the reflected waveforms from the different reef horizons in the UG1 – UG2 system in the BIC. From this it was concluded that the UG1 and UG2 reef horizons yield strong reflections, the Bleskop Marker is virtually transparent (but still yields a relatively strong reflection) and that the single chromitite layer is transparent with a very weak reflection.

These results can be used in signal processing techniques to extract information from the actual captured data.

### **9.1.5 Limitations Imposed on Geometry Delineation Using BHR Technology**

Chapter 8 concluded with the estimation of the detection range and reflectivity of the UG2 reef from field experimental data captured with the GeoMole BHR system. These two studies can be viewed as the zenith of this dissertation, since it incorporated all the work presented. It was found that the minimum detectable distance of a perfectly planar and smooth UG2 interface is at least 30 m. Field experimental data confirmed detection range in the region of 30 – 40 m, while extreme ranges of up to 60 m have been achieved. Possible reasons for this increased detection range have been discussed. The reflectivity of the UG2 interface was estimated to be in the region of –16 to –20 dB - very close to the predicted values.

The key contributions mentioned in Sections 9.1.1 to 9.1.5 added to the maturation of borehole radar technology as a mapping tool used in the imaging of the platiniferous reefs in the BIC.

## **9.2 Recommendations for Future Work**

Due to the broad spectrum of study fields covered in this dissertation and the fact that BHR is a relatively young technology, it was inevitable that some identified problems and study areas could not be covered. The technology is maturing and the techniques and algorithms presented in this dissertation have to be adapted to stay current.

### **9.2.1 System Characterization and Pulse Recompression**

A list of recommendations for future work on system characterization and pulse recompression follows:

- Modelling of the *in situ* antennas can be extended to include a larger variety of configurations, i.e. different borehole diameters and host rocks.
- Verification of the antenna performance when deployed in a borehole.
- Modifying the pulse recompression algorithm for application to new radar topologies as the technology matures [71], [72].
- Improving the algorithm to synthesize the ‘ideal’ pulse for image processing and to remove the artefacts currently introduced by the algorithm.

### **9.2.2 Radiowave Propagation in Stratified Lossy Media**

There are also various fields to be studied in the propagation of radiowaves in stratified lossy media:

- Evaluate the lateral shift at the interface between lossy half-spaces.
- Evaluate the radiation of a vertical electric dipole in stratified lossy media.
- Evaluate the existence and exploitation of natural waveguides and ducts.
- Study the effect of geological defects on radiowave propagation.

### **9.2.3 Software Implementation of Pulse Recompression Algorithm**

Inspired by the results obtained with the pulse recompression algorithm on experimental data, interest has been shown in the implementation of the algorithm in radar data analysis software packages, e.g. SeisWin [99], [100]. The optimal implementation is a replica of the steps outlined in Sections 5.2 and 5.3. If processing power is limited and only qualitative pulse recompression is required, a possible algorithm might incorporate the following steps:

1. Store the receiver chain transfer function (analogue and digital) for a typical configuration in a lookup table.
2. Filter a resampled (1 ns time increment) data trace with a Wiener or zero-phased bandpass and notch filter.
3. Deconvolve the resulting trace with the receiver chain transfer function to find the voltage at the receiver front-end.
4. Integrate the estimated time-domain voltage at the receiver front-end to approximate the plane wave electric field incident upon the receiver antenna.

The final step is only valid for an electrically short dipole and does not compensate for the frequency-dependant magnitude response of the antenna. When the antenna is deployed in a water-filled borehole it might be necessary to use the actual phase response of the antenna.

# APPENDIX A

## KLEINZEE FIELD EXPERIMENT

### A.1 Introduction

The main purpose of the experiment was to undertake a viability study of a borehole radar system in the specific geological setting encountered in the Kleinzee area. The primary goals were to carry out propagation studies in the different stratified layers and to find out whether it is possible to delineate the interfaces between them by means of radar. It was anticipated, or at least hoped, that the interfaces might be apparent either by reflection of propagated waves, or through surface wave phenomena.

### A.2 Geological setting

The Kleinzee alluvial diamond mine is located on the west coast of South Africa, approximately 140 km south of the Orange River mouth. An intensive exploration programme is currently being conducted to delineate and evaluate the potential of a broad ( $\pm 3$  km wide) palaeochannel, which trends roughly parallel to the coast. It was on the edge of this channel that a line of boreholes was sited for the research team to conduct an assessment of the applicability of BHR to this environment. The channel fill sequence, from surface down is, with local variability, as follows:

- 1 - 2m Reddish-brown, fine to medium grained aeolian sand
- ~10m partly calcretised red aeolian sand
- Terrigenous sands with significant clay content, and discontinuous lenses of fluvial silt
- Basal quartz pebble/cobble gravels
- (Weathered, fractured gneissic bedrock)

### A.3 BHR site characteristics

The site that was selected for our BHR tests was not entirely representative of the exploration target area. It was located on the edge of the major palaeochannel, and as

## APPENDIX A: Kleinzee Field Experiment

such, lacked the fluvial sediments, and more particularly, the diamond bearing gravel layers. The geological sequence is as follows:

- 0-1m Red aeolian sand
- 2-10m Calcrete and sand
- 11-18m Aeolian sand with significant clay content
- 19-... Weathered gneiss (clay)

The contact between the overburden and the weathered bedrock is evident mainly through the slight change in colour from the reddish/yellow sand/clay to the paler coloured clay. The sandy texture is also completely absent in the weathered bedrock.

### A.4 Survey geometry and radar downhole configuration

Ten holes were drilled and lined with a PVC pipe with approximately 10 m spacing between the holes as shown in Figure A-1.

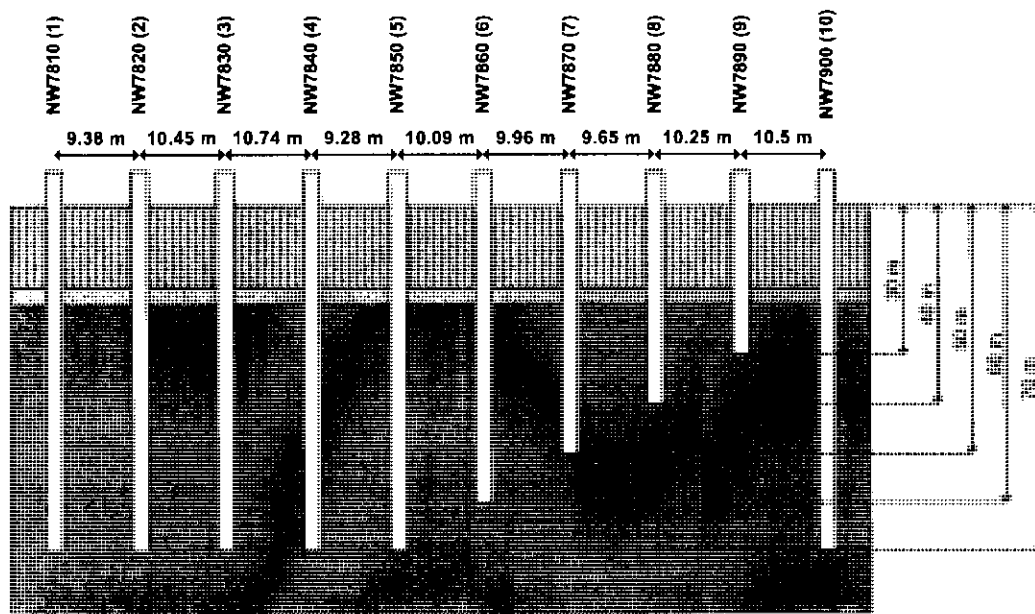


Figure A-1: Geometry of the lined holes indicating depth and spacing.

The diameter of the drill is around 200 mm, while the outside and inside diameter of the blue PVC pipe are 60 and 54 mm respectively. It is filled with loose ground. A wet, mud-drilling process was used to drill the holes. The surveys were conducted about 2 weeks after the holes were drilled and it was assumed that the ground would have dried sufficiently by that time. It was observed however, that the surrounding ground was still wet.

## APPENDIX A: Kleinsee Field Experiment

The geometry of a cross-hole survey between two boreholes is shown in Figure A-2.

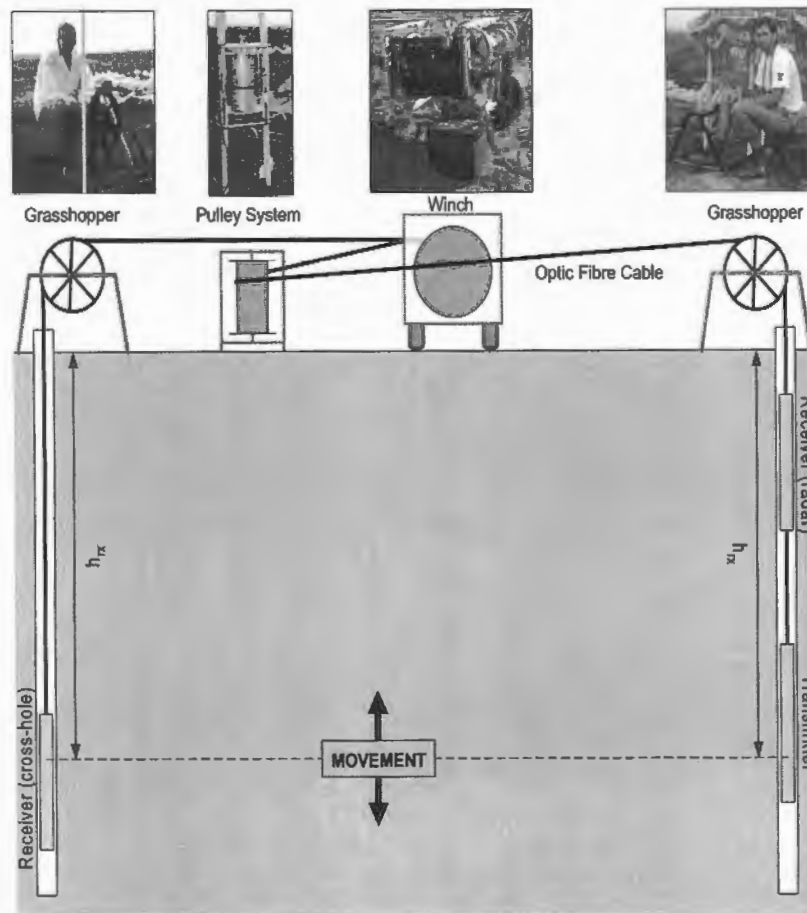


Figure A-2: Geometry and photos of the cross-hole survey.

### A.5 Electrical properties of layered media.

As preparatory work, the electrical properties of samples from some of the layers were measured. A brief summary on the measurement of these properties is presented in this section.

Two layers, representative of the bedrock and the layer just above the bedrock, were measured at a number of discrete frequencies in the band from 10 MHz up to 50 MHz [101]. The first layer, L17m, was taken to be representative of the layer just above the bedrock, while the second layer, L20m, was taken to be representative of the bedrock. The electric properties of both layers are summarized in the following tables:

Table A-1: Dielectric properties of L17m layer sample.

**Measurement of Dielectric Properties of new samples (17m depth)**

Frequency (MHz)	Properties:		
	$\epsilon_r'$	$\epsilon_r''$	$\tan(\delta)$
10	6.07	0.83	0.14
20	5.20	0.65	0.13
30	4.81	0.74	0.15
40	4.56	0.56	0.12
50	4.41	0.45	0.10

Table A-2: Dielectric properties of L20m layer sample.

**Measurement of Dielectric Properties of new samples (20m depth)**

Frequency (MHz)	Properties:		
	$\epsilon_r'$	$\epsilon_r''$	$\tan(\delta)$
10	6.22	1.00	0.16
20	5.61	0.91	0.16
30	4.83	0.82	0.17
40	4.34	0.67	0.16
50	4.30	0.51	0.12

From Table A-1 and Table A-2, it is clear that the electric contrast between these two layers is very subtle. It is clear that the bedrock layer is more lossy than the layer just above the bedrock. Since the material had to be ground up and compacted though, these measurements may not be accurately representative of the rock as found in the field.

## A.6 Theoretical predictions

Based on the geological setting described in Section A.2 and the properties of the different layers as summarized in Section A.5, a number of theoretical predictions were made on the electromagnetic wave propagation through the ground. This was done to give an idea of what the team might be able to measure with the radar, and what maximum distance of propagation might be expected. The reflection coefficient as a function of incident angle,  $\theta_1$ , is plotted in Figure A-3.

## APPENDIX A: Kleinsee Field Experiment

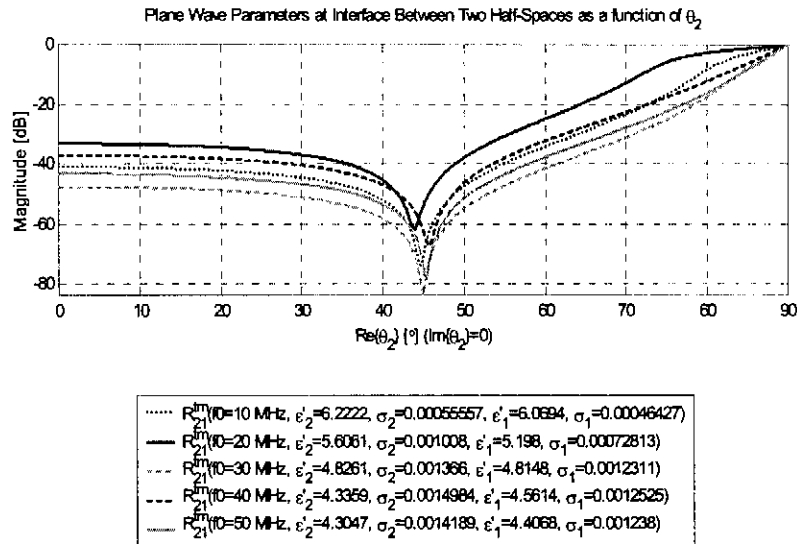


Figure A-3: Reflection coefficient at interface between layers L17m and L20m.

From Figure A-3 it is clear that only a small fraction of the power of the incident wave gets reflected back, with the strongest reflection at 20 MHz. The attenuation due to geometric spreading and dielectric losses are plotted in Figure A-4 to Figure A-5 for the two layers at 50 MHz.

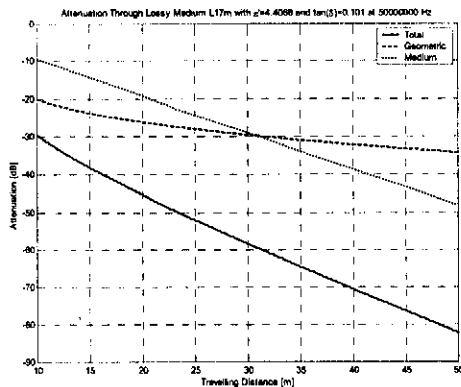


Figure A-4: Attenuation in L17m at 50 MHz.

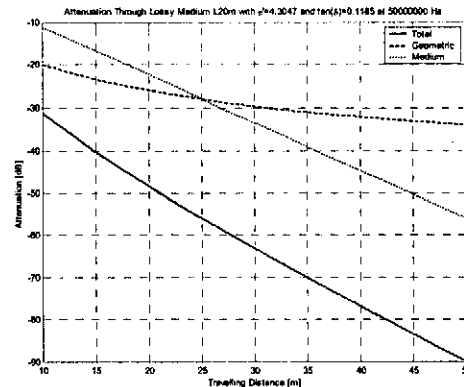


Figure A-5: Attenuation in L20m at 50 MHz.

The signal attenuation experienced from the transmitter to the receiver can next be predicted. For the direct wave, only the travel distance loss and coupling losses are incorporated, while for the reflected wave the reflection coefficient has to be incorporated as well.

From the different simulations and predictions the following can be concluded: The reflections from the interface are very weak, i.e. less than -25 dB except for oblique incidence. It will therefore be difficult to see the interface unless the transmitter and/or receiver is close to the interface. Furthermore, assuming a receiver with a

## APPENDIX A: Kleinzee Field Experiment

sensitivity of  $-90$  dB with respect to transmitted power was available, a direct transmission range of up to 50m would be possible if the coupling to the ground is good and the medium is quite homogeneous.

### A.7 Borehole survey results

A full survey between holes NW7820 and NW7840 was carried out. The radar and cross-hole B-scans of the Up 2 shoot with 512 stacking are shown in Figure A-6 and Figure A-7. The data has been filtered using a 10/20-50/60 bandpass Hanning filter.

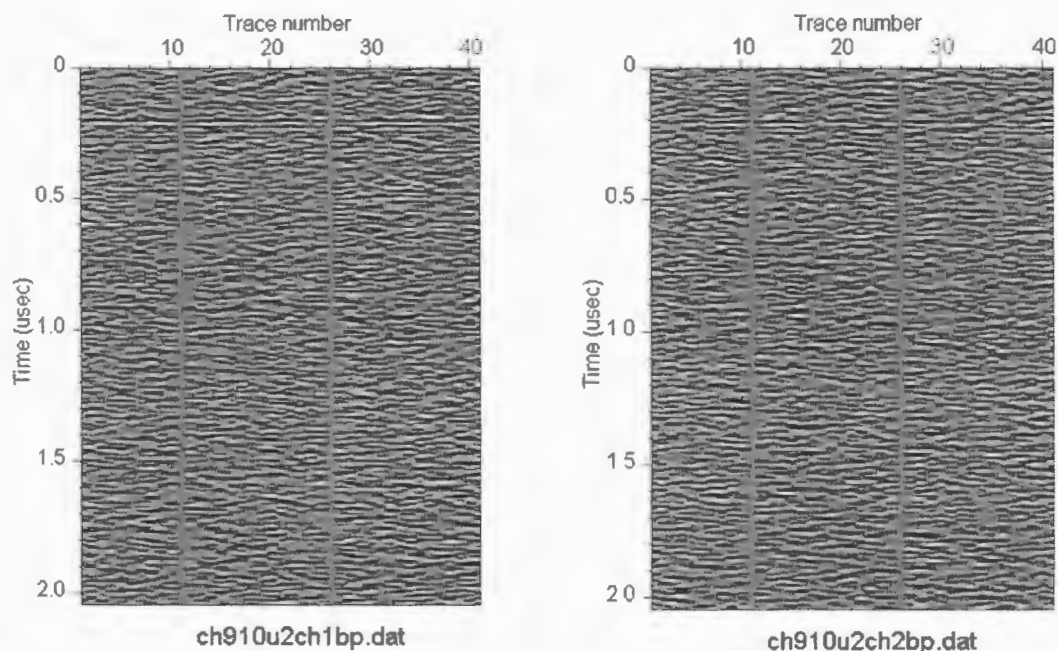


*Figure A-6: Radar B-scan of Up 2 shoot with 512 stacking.*      *Figure A-7: Cross-hole B-scan of Up 2 shoot with 512 stacking.*

In both scans the SNR is so low that virtually no structured receive echoes are visible.

### A.8 Concluding Remarks

Even though magnitude of the direct wave was expected to be relatively low and that of the reflected wave even lower, it was never anticipated that no signal whatsoever would be measured above the noise floor of the system. The results of this trial survey prove that a quantitative analysis of BHR performance is necessary.

# APPENDIX B

## FEKO SIMULATIONS

In this dissertation the numerical simulations of the electromagnetic radiation and response of antennas were done with the FEKO<sup>®</sup> Suite 3.2.1 [78] developed by EMSS. FEKO can be used for EM field analysis with objects of arbitrary shape. The solution is based on the MOM where the EM fields are found by first calculating the electric surface currents on conducting surfaces. The equivalent electric and magnetic surface currents on the surfaces of dielectric solids are also calculated. The radiated EM fields are then calculated from these current distributions. In the FEKO environment, a basic radiating structure is built up of finite-length conducting wires or finite-size conducting triangular surfaces. It is also possible to load these elements with resistive and/or reactive impedances.

### B.1 Limitations of FEKO

One of the first major limitations on the performance and application of FEKO is the meshing of the physical structure simulated. The maximum length of a wire segment or the edge length of a triangular patch has to be less than a tenth of a wavelength (minimum) for numerical convergence. It is good practice to ensure that, if possible, this constraint is satisfied by at least a factor of two. This necessitates the meshing of the physical structure finely enough to ensure that the maximum lengths are within the limits. Since the GeoMole antennas are electrically short and small, this first constraint is easily met. A finer meshing is also necessary whenever a wire runs parallel to a conducting surface to ensure an accurate representation of the surface charge distribution. If a wire has to be segmented, it is necessary that the radius of the shortest segment is less than 3/10 times the length of that segment. When a structure is built up of triangles, it is important to ensure that the ratio of the longest edge to the shortest edge is less than 2 for accurate simulation results. This is of crucial importance when a cylindrical structure has to be meshed, especially if the diameter

---

<sup>®</sup> Copyright by EM Software and Systems, 1998 – 2002.

thereof is very small compared to a wavelength. Typically, the ideal is to mesh a cylinder with at least 8 main rectangles. This implicates that the edge length of the triangles is in the order of a 8<sup>th</sup> of the cylinder diameter and the maximum edge length has to be less than a 4<sup>th</sup> of the cylinder diameter. These additional constraints should be kept in mind when the GeoMole antennas are meshed, since they are more likely to influence simulation accuracy. The total number of elements used to represent the physical model determines the execution time as well as the amount of RAM (random access memory) necessary to solve the matrices. The memory size has a quadratic relationship on the number of elements. For moderate execution times (typically less than 24 hours) the RAM necessary for execution should reside totally on the physical memory, which limits the amount of elements used to mesh the structure. The effective use of symmetry (geometric, electric or magnetic) can ease the RAM requirements significantly.

## **B.2 Verification of Simulated Parameters**

Two very important antenna parameters in Chapter 3 are input impedance and directivity. It is possible to measure the input impedance for the asymmetric resistively loaded antenna in free space using existing techniques. This is virtually impossible when the antenna is deployed in a borehole. However, FEKO can be used to simulate the input impedance of the antenna deployed in a borehole. It is necessary to verify the results obtained with the numeric technique with actual measurements. This verification was done for two different antennas in free space – both were asymmetric resistively loaded antennas, but the one had a thin wire while the other had a conducting half cylinder.

### ***B.2.1 Practical Verification Measurements***

The practical measurements were done by using the HP8753 network analyser and the test jig developed by M. van Rooyen [102]. This test jig allows the measurement of the input impedance of a balanced antenna using the network analyser.

### ***B.2.2 Numerical Verification Simulations***

The two antennas were modelled as close to reality as possible. The feed point of the antenna with the conducting half cylinder is shown in Figure B-1 below:



Figure B-1: Feed point of antenna with conducting half cylinder.

The green cylindrical segments are the conducting wire, while the coloured segments are the discrete resistors. The resistors, conducting wire and feed segments have a length of 6.25 mm and a radius of 1.5 mm. The arrow indicates the feed segment. The conducting half cylinder is meshed into 1044 metallic triangles with a maximum edge length of 7.5 mm.

### B.2.3 Verification Results

The real and imaginary parts of the input impedances obtained with practical measurements and numeric simulations are plotted in Figure B-2 and Figure B-3 for both antennas.

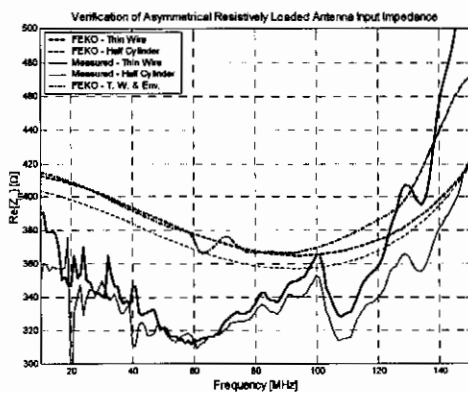


Figure B-2: Real part of antenna input impedance.

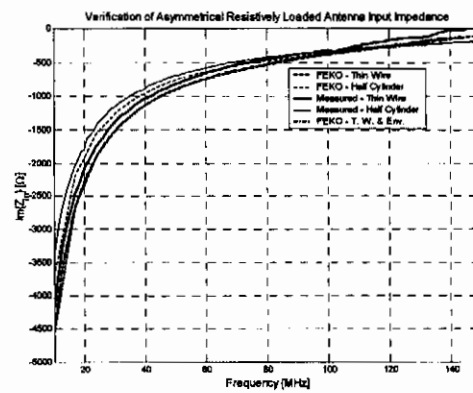
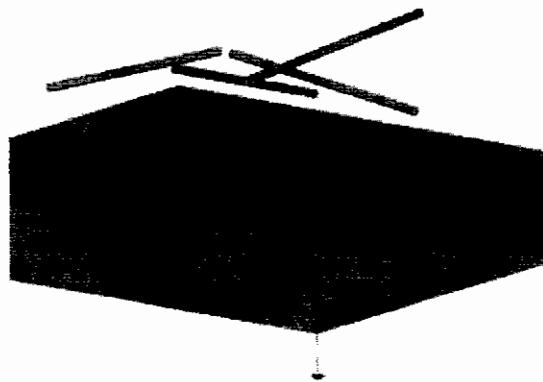


Figure B-3: Imaginary part of antenna input impedance.

The real part of the input impedance for both antennas is slightly lower than simulated with a maximum deviation of 33.6% at 150 MHz for the thin wire antenna and 16.9% at 24 MHz for the conducting half cylinder antenna. The simulated real input

## APPENDIX B: FEKO Simulations

impedance is bigger than measured at the lower frequencies and smaller at the high frequencies. The antenna was placed 80 cm above a reinforced concrete floor and in close proximity to the metallic workbenches on which the network analyzer is situated. The floor might act as a reflecting ground plane that forms an image of the actual antenna and accordingly drops the real part of the input impedance. The metallic pipes of the workbenches might also affect the antenna input impedance. Finally, the test jig used actually influences the antenna if the antenna is not physically symmetric around the feed point. Without the test jig, the field lines would not cross the plane, in which the test jig would be deployed, perpendicular. If the test jig is connected, the field lines are forced to terminate perpendicular to this plane and this certainly influences the antenna input impedance. A third simulation was done where the concrete floor, workbenches' metallic edges and the ground wire of the test jig were modelled (Figure B-4). The real part of the input impedance changes slightly at the lower frequencies and drastically at the higher frequencies, following the measured results more accurately. The maximum deviation is reduced to less than 19% at 150 MHz. The absolute value of the imaginary part of the input impedance is slightly lower than simulated with a deviation of less than 17.3% for the thin wire antenna below 100 MHz and less than 13% for the conducting half cylinder antenna. The deviation for the antenna simulated with the ground wire and the environment is less than 16% below 100 MHz, but in close correlation with the simulation for the antenna alone.



*Figure B-4: Geometry of third simulation, including the test environment.*

The measured and simulated reflection coefficients, matched to 50  $\Omega$ , of both antennas are plotted in Figure B-5 and Figure B-6.

## APPENDIX B: FEKO Simulations

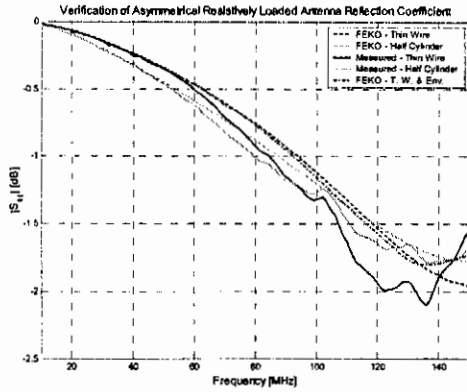


Figure B-5: Magnitude of reflection coefficient.

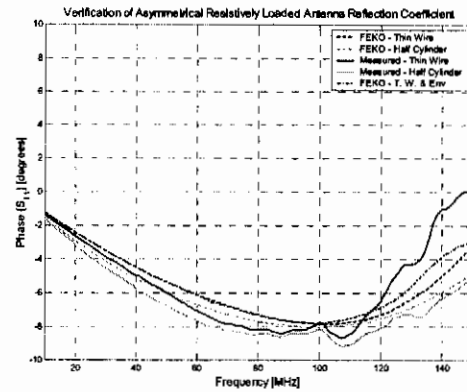


Figure B-6: Phase of reflection coefficient.

At the lower frequencies the magnitude difference is very small – less than 0.23 dB below 100 MHz for the thin wire and less than 0.13 dB for the conducting half cylinder. The maximum magnitude difference for the thin wire is 0.42 dB and 0.15 dB for the conducting half cylinder. The maximum phase deviation for the thin wire is  $3.8^\circ$  at the high frequencies and  $1.2^\circ$  for the conducting half cylinder.

Considering that the measuring accuracy of the network analyser, with the standard calibration kit, is  $\pm 0.3$  dB, the practical measurements correlate very well with the numeric simulation results. If the antenna is modelled realistic, FEKO can simulate the input impedance of the asymmetric resistively loaded antenna with a good degree of accuracy.

### B.3 Meshing of Various Antenna Topologies

As stated in Section B.1, the meshing of the physical radiating structure is of utmost importance in the numeric simulation of EM radiation. The meshing of the different antenna topologies encountered in the dissertation is discussed in the following section.

#### B.3.1 General Considerations

The simulations were carried out at 101 equally spaced frequency points between 1 MHz and 401 MHz for the free space antennas and at 125 equally spaced points between 1 MHz and 125 MHz for the deployed antennas. The frequency range was decreased to half the Nyquist frequency for a 250 Msps sampled signal. Any information above 125 MHz has to be disregarded as a result of aliasing.

## APPENDIX B: FEKO Simulations

The resistively loaded arm was simulated as discrete wire segments with finite thickness. The resistors were realized by the loading of the appropriate segment with a series impedance with only a real component. The unloaded arm was simulated as 9 flat surfaces built up with a number of triangular conducting segments. The first surface simulates the cap of the cylinder, while the 8 other surfaces make up the cylinder walls. Care is taken to ensure electrical contact between the two arms.

A voltage feed is realized by the impartation of a given voltage over the feed segment, the segment connected to the cap of the cylinder. This segment is not loaded.

Due to the physical configuration, magnetic symmetry in two axes can be used to significantly reduce computation time and the resource requirements. With the antenna axis collocated with the  $z$ -axis, magnetic symmetry in both  $x$  and  $y$ -axis can be used.

### **B.3.2 Calibration Antennas**

The calibration antennas are quite easy to simulate in FEKO since they are not potted in a dielectric and only consist of metallic segments of which some are resistively loaded.

The segmented structure realized in FEKO for both the TX and RX antennas is plotted in Figure B-7.



*Figure B-7: Segmented structure for TX and RX calibration antennas.*

The resistively loaded arm consisted of 163 discrete wire segments, of which 9 were loaded resistively. The resistively loaded segments' length was fixed at 6.25 mm and the radii of all the segments were fixed at 1.5 mm. The unloaded arm of the TX antenna (431 mm long) consisted of 1060 conducting triangular patches. The maximum edge length was fixed at 10 mm with the maximum edge length on the circumference of the cylinder fixed at 7.5 mm – yielding a total of 13 rectangular patches. In the case of the RX antenna (526 mm) a total number of 1300 triangular

patches were used to construct the unloaded arm. A close-up of the feed segment of the TX/RX antenna is plotted in Figure B-8.

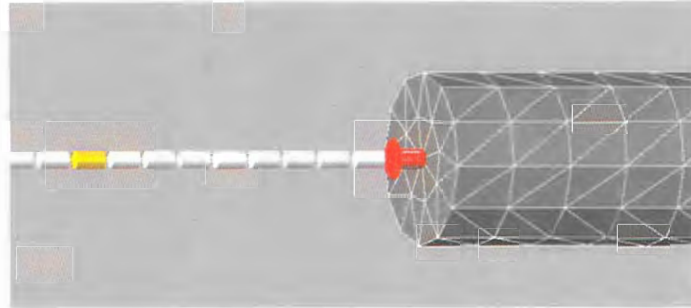


*Figure B-8: Feed segment of the calibration antennas.*

In Figure B-8 the realization of the feed segment, metallic wires, resistors and metallic cylinder are clearly visible.

### **B.3.3 Free-space GeoMole Antennas**

The construction of the GeoMole antennas, even in free space, was more difficult than that of the calibration antennas. The potting material used in these antennas influences antenna performance and has to be simulated accurately.

The TX antenna consists of a 610 mm resistively loaded arm with 48 discrete resistors and a 1 m conducting copper pipe of 27.5 mm diameter. The RX antenna has the same configuration only with a 650 mm copper pipe. The antenna structure is contained in a tight fitting PVC pipe with 32 mm outer diameter and is potted with a dielectric potting material.

In FEKO it is possible to create two regions with different dielectric properties. A closed surface has to be built with triangular patches. These patches are then defined as the boundary between two dielectric regions and the dielectric properties of these regions have to be specified. In order to construct the GeoMole antennas a cylindrical closed surface is therefore constructed with the geometries of the PVC pipe. The radius of the pipe is 2 mm more than the copper pipe and the incremental length is 10 mm on both ends. The inside of the closed surface is defined at the potting material dielectric, while the outside is defined as free space. The antenna structure (metallic and resistive segments) is then built in the closed region defined as the potting material dielectric. The structure built in FEKO is depicted in Figure B-9. This picture was realized by the insertion of a cutplane at  $y = 5$  mm.

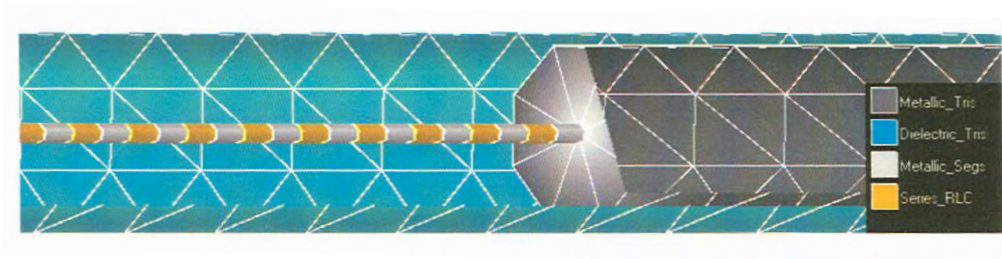


Figure B-9: Free space GeoMole antenna constructed in FEKO.

The length and radius of the wire segments were fixed at 6.25 mm and 1.5 mm respectively. The meshing for the conducting cylinder restricted the maximum triangle edge length to 20 mm and the maximum edge length about the circumference to 15 mm. The constraints of the meshing of the potting material and conducting pipe were the same. Both antennas were constructed with 98 wire segments. The TX antenna had 808 metallic and 1328 dielectric triangles, and the RX antenna had 536 metallic and 1040 dielectric triangles.

### **B.3.4 Deployed GeoMole Antennas**

The deployed GeoMole antennas were the most complicated to construct in a numerical simulation environment such as FEKO. This was mainly due to the increased complexity of the structure, as well as to the limitations placed on the number of segments by the available computer resources.

The general case with a probe deployed in the centre of a 48 mm diameter borehole in a particular host medium was considered. The same approach taken in Section B.3.3 was adopted to construct this antenna structure. The definition of  $N$  dielectric regions with different dielectric properties are facilitated in FEKO by the creation of  $N-1$  closed surfaces with dielectric patches. Three different regions were defined by the creation of two closed surfaces. The first region represented the probe containing the antenna structure, the second region the matter filling the space between the probe and the borehole surface and the third region the host medium (rock). Inherent to this realization of the physical problem is the termination of the boreholes at a finite length on the top and the bottom. The minimum distance with minimum effect on radiation had to be found. This was done with an iterative process, with the resulting cut-off length of 0.5 m at the top and the bottom.

The close-up view of the TX antenna, as described above, is plotted in Figure B-10.

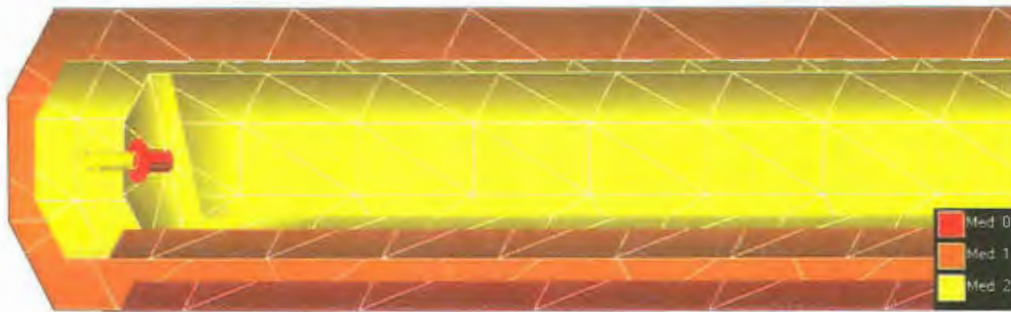


Figure B-10: Section of borehole deployed GM antenna as constructed in FEKO.

The picture was realized by means of two cutplanes at  $z = 0.01$  m and  $y = 0.005$  m. The three dielectric mediums (0, 1 and 2) are indicated. The outside of the borehole (medium 0) is taken as the host medium – simulated with the measured dielectric properties of the rock under investigation. The gap (closed region) between the borehole and the PVC housing (medium 1) is taken as the medium in which the probe is deployed, either air or water with a given salt contents. The closed region within the PVC housing (region 2) is taken as the potting material in which the antenna metallic and resistive structures are contained. The metallic and resistive structures were meshed in the exact way as was done with the free space antennas discussed in the previous section. The meshing for the borehole restricted the maximum triangle edge length to 30 mm and the maximum edge length about the circumference to 30 mm as well. Finer meshing of the borehole resulted in a depletion of the physical RAM resources. This resulted in a total of 2738 dielectric triangles (potting material and borehole) for the TX antenna and 2272 for the RX antenna.

Considering the results obtained with these meshing constraints, as discussed in Chapter 3 and Section B.5, it was decided that the constraints yielded acceptable error margins. The models as discussed in this section were used for all numeric simulations.

## B.4 Calculating Directivity and Efficiency

The fact that FEKO may encounter difficulty to predict the gain (or directivity) of the GeoMole antennas in a lossy dielectric host medium was briefly introduced in Section 3.4.3.3 . In this section, the problem area is identified, discussed and a solution is postulated and tested.

## APPENDIX B: FEKO Simulations

Consider the specific case of a GeoMole RX antenna deployed in a 48 mm air-filled borehole in a norite host medium. The directivity of the antenna as calculated with FEKO, with the meshing as defined in Section B.3.4, is plotted for different frequencies as a function of the angle  $\theta$  in Figure B-11.

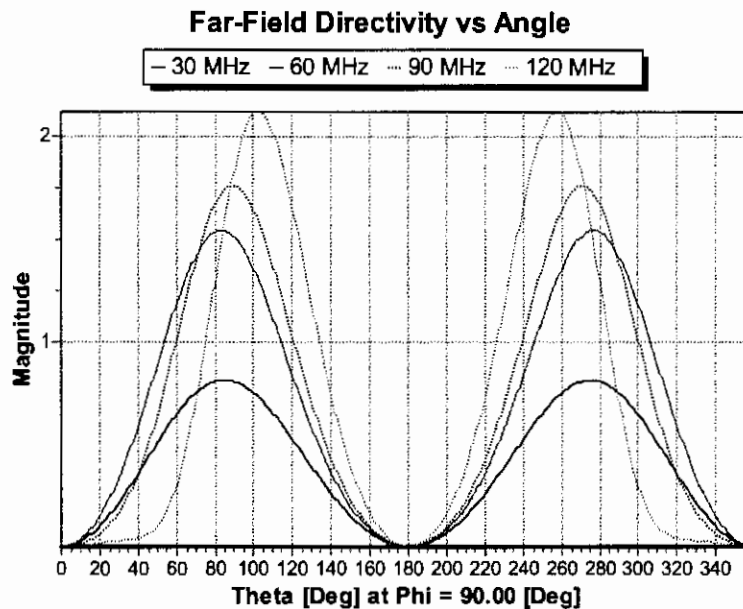


Figure B-11: Deployed GeoMole RX antenna directivity as calculated by FEKO.

Above 60 MHz the numerically calculated directivity 'seems' to be correct with the maximum at more or less  $90^\circ$ . At 30 MHz the failure to calculate the directivity correctly is clearly visible. With the definition of directivity given as ... *the ratio of the radiation intensity in a certain direction to the average radiation intensity* [11], it is eminent that the directivity is larger than unity at least at one spherical direction. Over  $4\pi$  steradians, the directivity at 30 MHz never rises to, or above, unity. No obvious reason for this anomaly was identified. When the FEKO calculated directivity was compared to the normalised, time-averaged radial power flux density at a sufficiently large radial distance, it was observed that the shape of the directivity was indeed correct, but the scaling thereof was wrong for some or other reason. One possible explanation for this is that FEKO does not calculate the far field intensity correctly when the host medium has dielectric losses. An algorithm was developed to calculate the directivity off-line from FEKO near field calculations. The main steps of the algorithm are listed below:

## APPENDIX B: FEKO Simulations

1. Use FEKO to numerically simulate the radiation of the EM structure. Export the electric and magnetic near field values calculated at 5, 15, 25, and 35 m radial distances. Also export the currents on the wire segments.
2. The antenna structure has magnetic symmetry about the  $z$ -axis and therefore only the field values at a fixed value of  $\phi$  have to be calculated. The field values are calculated for the  $2\pi$  radians real space of  $\theta$  with a  $1^\circ$  resolution.
3. Calculate the average real power delivered to the antenna using (3.18), where  $I_{ant}$  is the feed segment current and  $V_{ant}$  is the impressed voltage over it.
4. Calculate the total power loss in the discrete resistors and the associated efficiency using (3.7).
5. Calculate the input impedance defined as

$$Z_{in} = \frac{V_{ant}}{I_{ant}}. \quad (B.1)$$

6. Calculate the radial component of the time-averaged power flux density from the electric and magnetic near field values at each defined point in space, defined as

$$S_{r(avg)} = \text{Re} \left[ 0.5 \left( E_\theta H_\phi^* - E_\phi H_\theta^* \right) \right]. \quad (B.2)$$

7. Calculate the denominator of (3.8),  $D_{den}$ , which reduces to a one-dimensional integral for magnetic symmetry about the  $z$ -axis:

$$D_{den}(r) = 0.5 \int_0^{2\pi} S_{r(avg)}(r, \theta') \sin \theta' d\theta'. \quad (B.3)$$

8. Integration is done using the recursive adaptive Simpson quadrature evaluation of the function to a specified error. The MATLAB implementation 'quad' was used for this evaluation. It was necessary to take the discrete values of  $S_{r(avg)}$  and transform them into a continuous periodic function. Due to the low values of integrand, the integrand was normalized before integration and denormalized at the end.
9. Calculate the directivity as the quotient of (B.2) and (B.3).
10. Calculate the far-field radiated power

$$P_{rad} = 4\pi r^2 e^{2ar} D_{den}(r). \quad (B.4)$$

## APPENDIX B: FEKO Simulations

11. Calculate the real antenna efficiency as the quotient of (B.4) and the average real power delivered to the antenna as calculated in step 3.

The antenna efficiency is a by-product of the directivity calculations. The directivity and antenna efficiency, as calculated with the abovementioned algorithm, are plotted in Figure B-12.

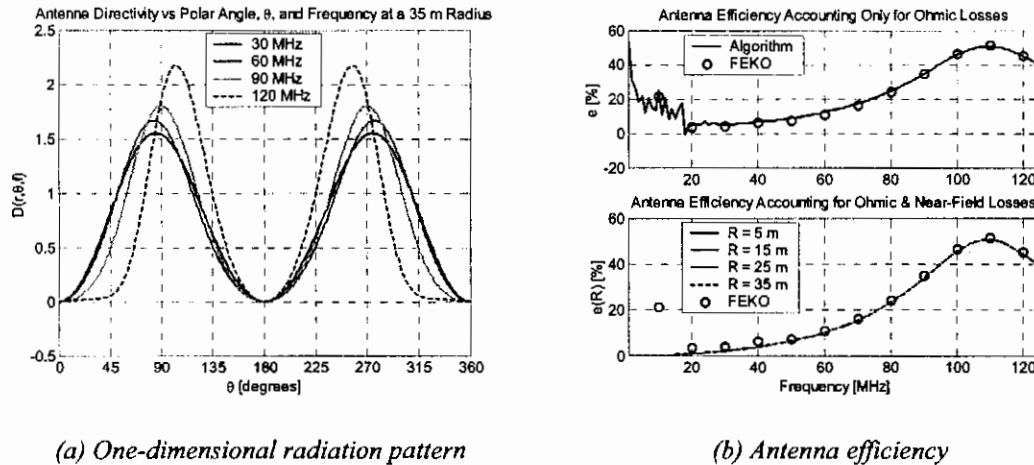


Figure B-12: Antenna directivity and efficiency as calculated with algorithm.

The directivity has the same shape as when calculated with FEKO, but the scaling is correct so that the integral of the directivity over the  $4\pi$  steradians yields 1. The algorithm also yields an improved estimation of the antenna efficiency.

## B.5 Antenna Simulations in Various Host Media

In Chapter 3, Section 3.7, the antenna transfer function and characteristics when deployed in a borehole was given only for a norite host medium. It is however highly likely that the antenna will be deployed in a variety of different host mediums due to the heterogeneity of the BIC. The dielectric properties of 7 different layers in the BIC have been measured [39], i.e. the chromitite leader, norite, pyroxenite (PX1 and PX2), olivine and UG2 reef (UG2 top and UG2 bottom) layers. Since only the results for norite were given in Section 3.7, the results for the other layers will be presented in this section. In addition to the BIC layers, the results for the VCR hanging wall [38] will also be given. Even though it is a layer of a totally different geological setting, the applicability of the theory and principles in this dissertation applies directly to this setting. Excellent results have been obtained with the proposed algorithms. For this reason these results were included.

## APPENDIX B: FEKO Simulations

The layers of practical importance are the pyroxenites and the UG2 reef. The characteristics and transfer functions of the GeoMole TX antenna deployed in these host media are plotted in Figure B-13 to Figure B-16.

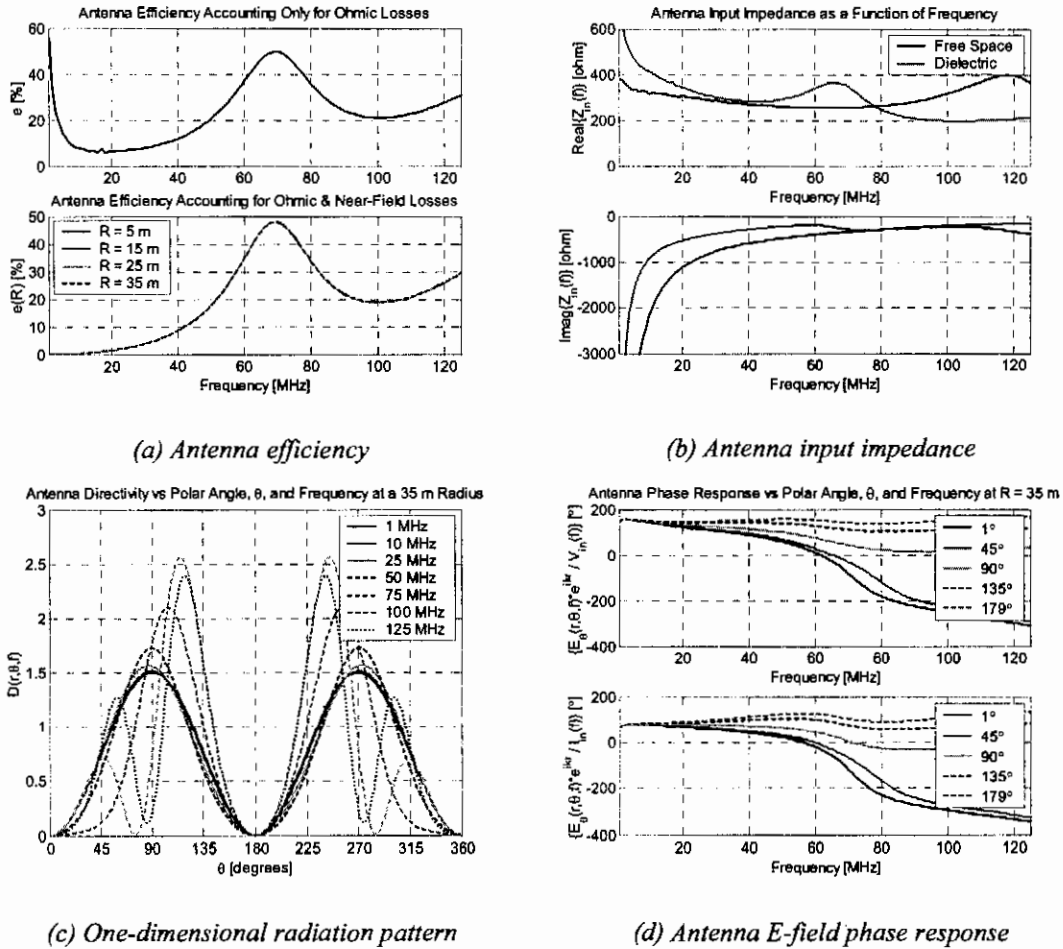
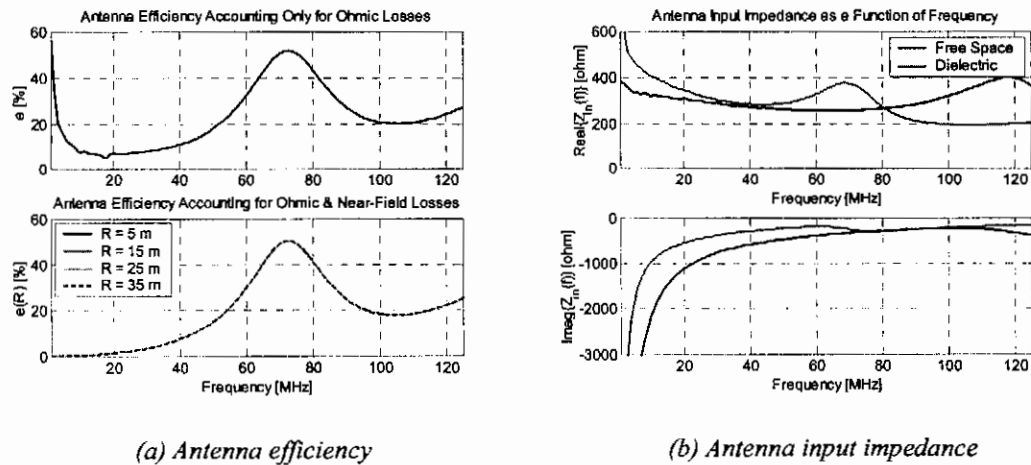
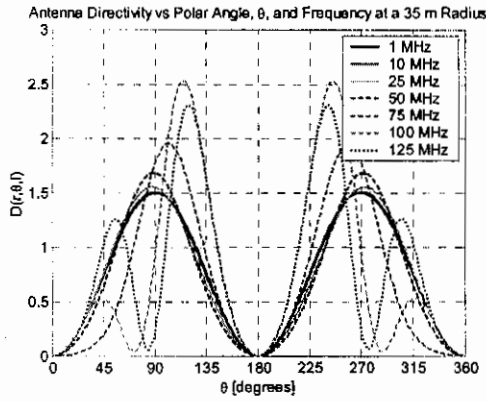


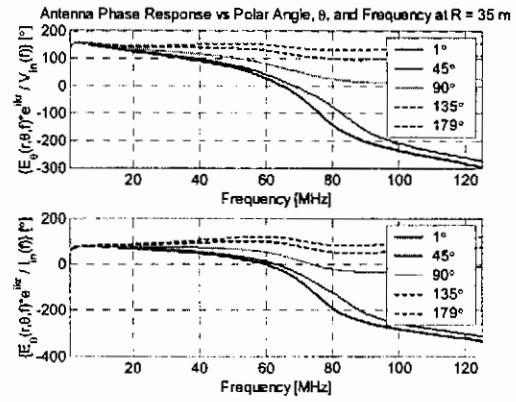
Figure B-13: GeoMole TX antenna deployed in a borehole in pyroxenite (PX1) host medium.



## APPENDIX B: FEKO Simulations

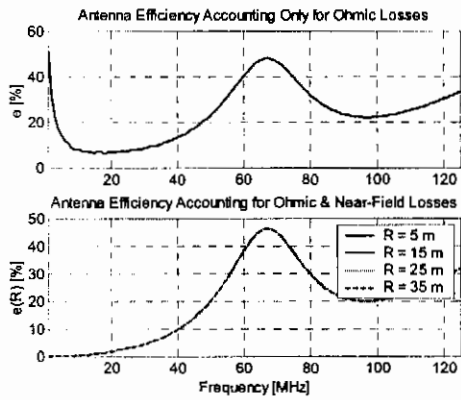


(c) One-dimensional radiation pattern

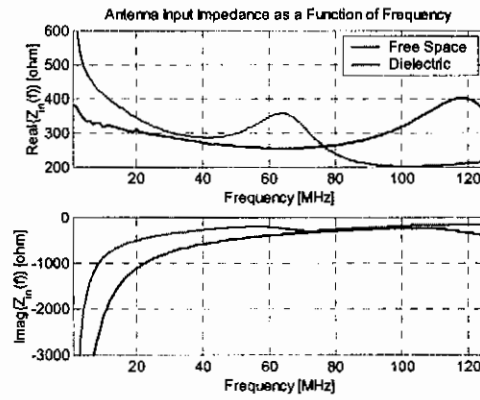


(d) Antenna E-field phase response

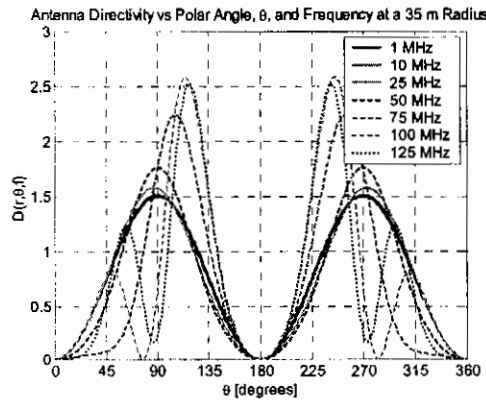
Figure B-14: GeoMole TX antenna deployed in a borehole in pyroxenite (PX2) host medium.



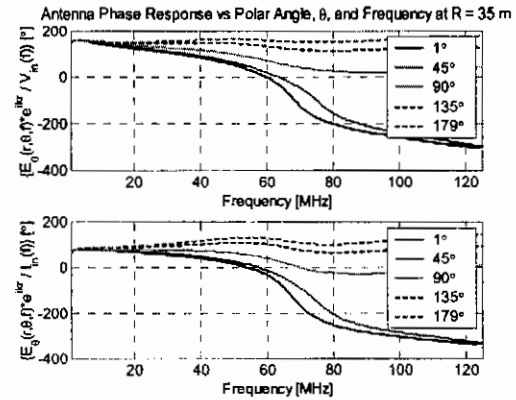
(a) Antenna efficiency



(b) Antenna input impedance



(c) One-dimensional radiation pattern



(d) Antenna E-field phase response

Figure B-15: GeoMole TX antenna deployed in a borehole in UG2 bottom host medium.

## APPENDIX B: FEKO Simulations

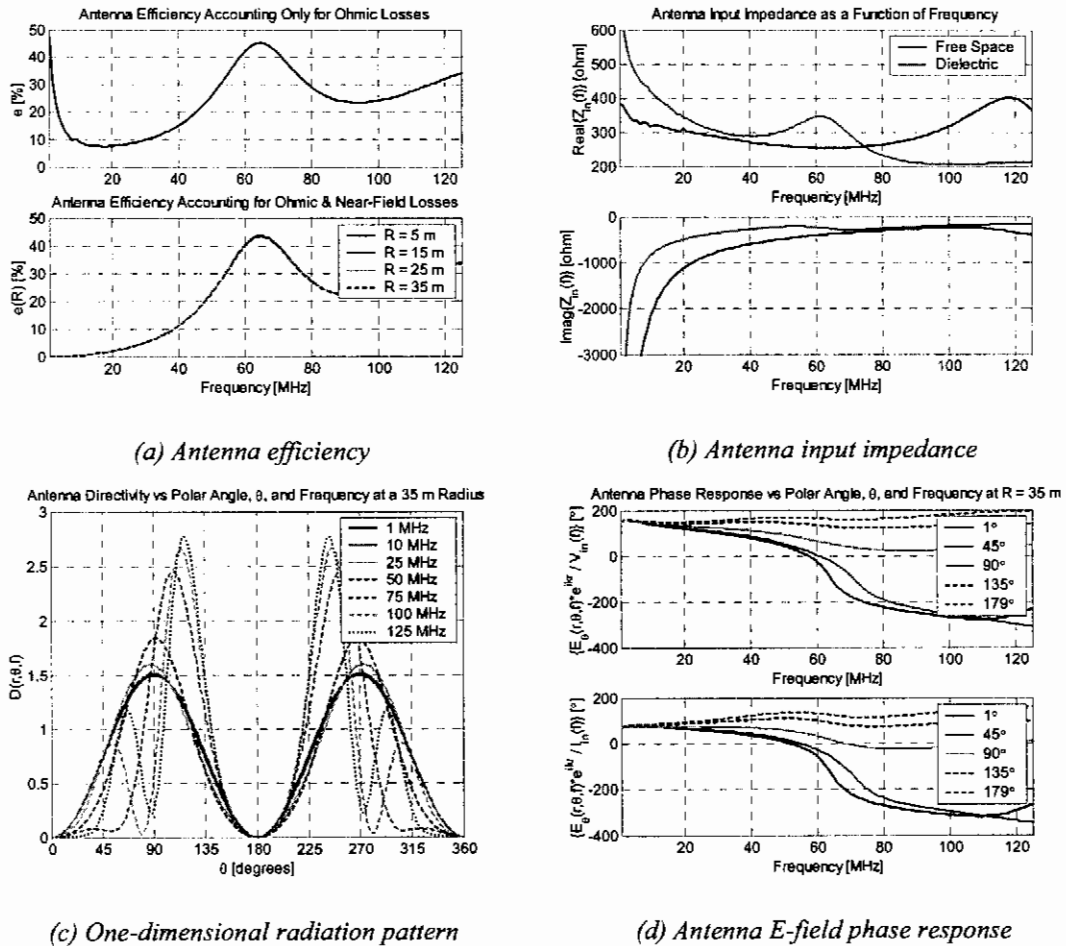


Figure B-16: GeoMole TX antenna deployed in a borehole in UG2 top host medium.

The basic performance of the antenna in the different host media is basically the same, but subtle differences are observed upon closer examination. The first resonances occur at different frequencies for the different host media. The mean values of the resistive input impedance also vary slightly. Furthermore, the host media affects the radiation pattern (especially the sidelobes) and phase responses. The responses for the RX antennas were not discussed, since the effect of the different host media are more or less the same.

The characteristics and transfer function of the GeoMole RX antenna deployed in a 48 mm air-filled borehole in the VCR hanging wall are plotted in Figure B-17.

## APPENDIX B: FEKO Simulations

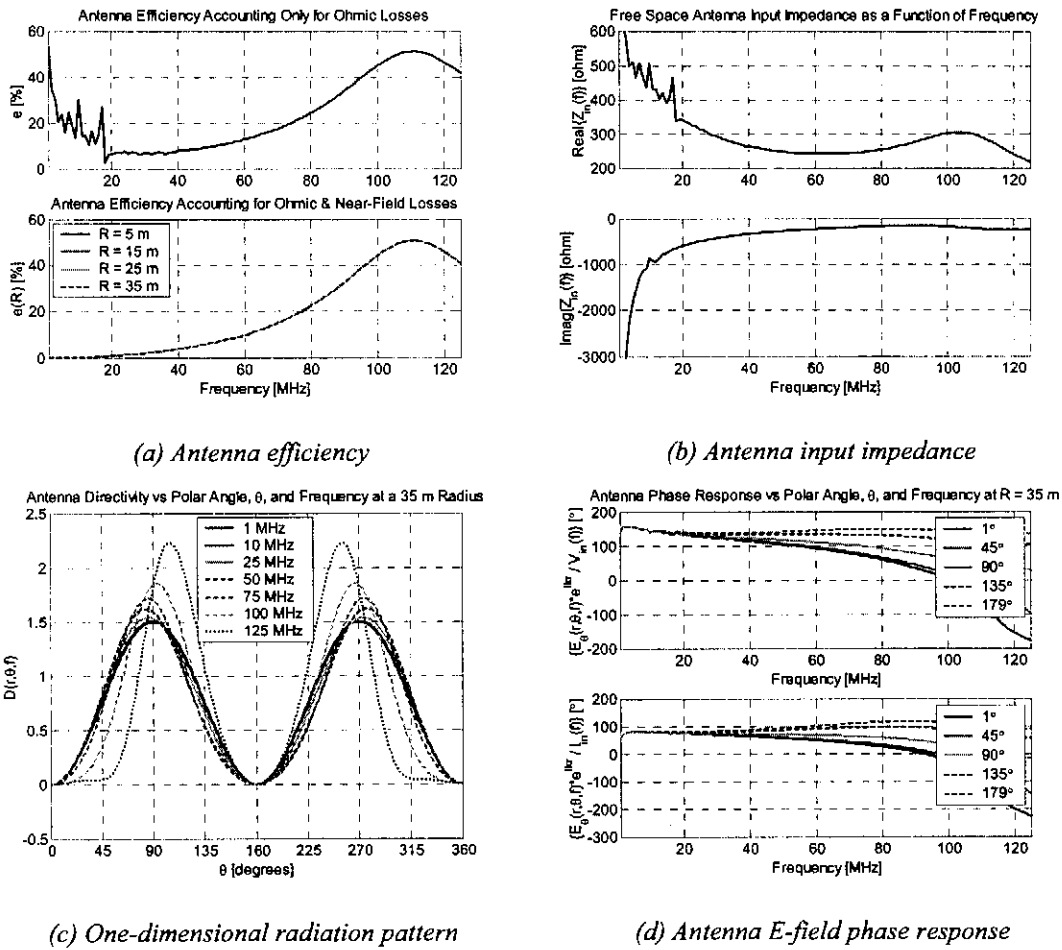


Figure B-17: GeoMole RX antenna deployed in a borehole in VCR hanging wall host medium.

When compared to Figure 3-40, it is evident that the 1<sup>st</sup> resonance only shifts from 109 MHz to 110.5 MHz. The other characteristics are virtually identical, except for the incremental frequency offset.

# APPENDIX C

## ADDITIONAL DAQ MEASUREMENT RESULTS

The DAQ measurement results, additional to that already presented in Chapter 4 are presented in this appendix. The GeoMole inventory consisted of 3 DAQ units and all of these have been characterized. To prevent the annoying repetition of similar results, the results of only one of the DAQ units were presented in Chapter 6. The results for the other units are presented here.

### C.1 Long-Pulse Response Results for the Different ADC's

The responses for the two channels of the three ADC units currently used are plotted in Figure C-1 to Figure C-3 for different range and stacking settings.

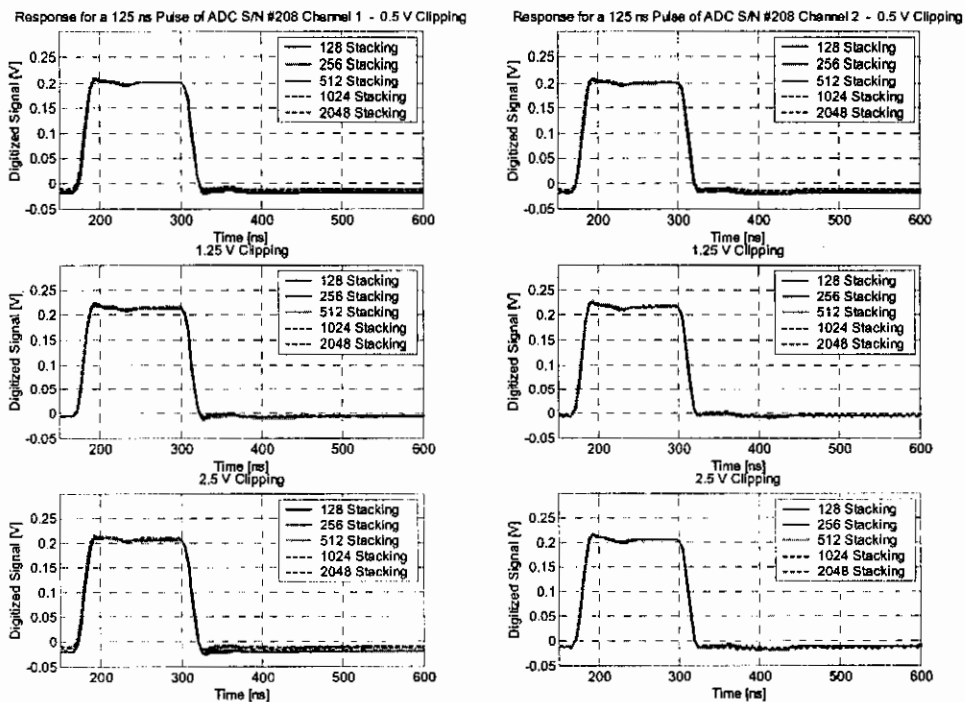


Figure C-1: 125 ns pulse response of ADC serial number #208.

## APPENDIX C: Additional DAQ Measurement Results

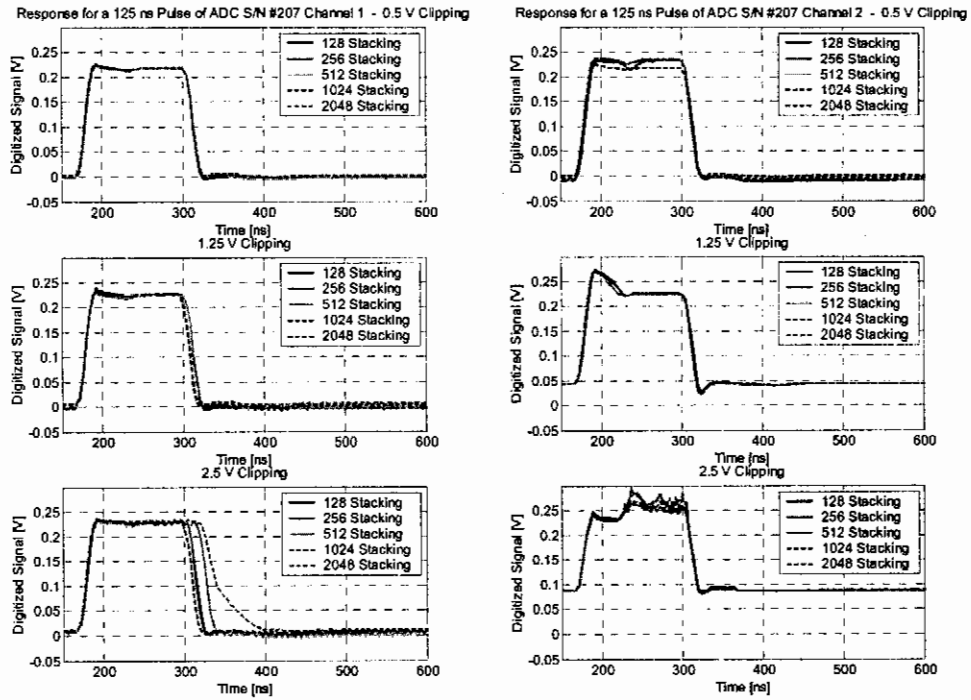


Figure C-2: 125 ns pulse response of ADC serial number #207.

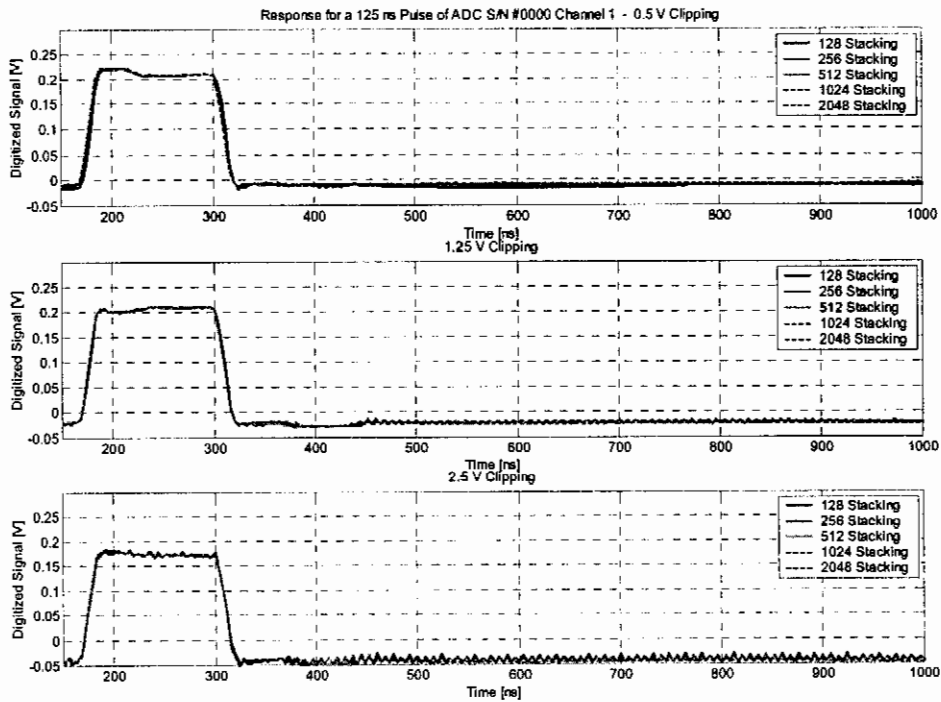


Figure C-3: 125 ns pulse response of ADC serial number #0000.

ADC serial number #208 has a very consistent response to a 125 ns pulse for the various settings. The two channels are also closely matched. In processing experimental data obtained at Brakspruit, it became evident that there might be a bit

## APPENDIX C: Additional DAQ Measurement Results

error of some kind within the ADC units. A zoomed plot of the response for the ADC serial number #208 is shown in Figure C-4.

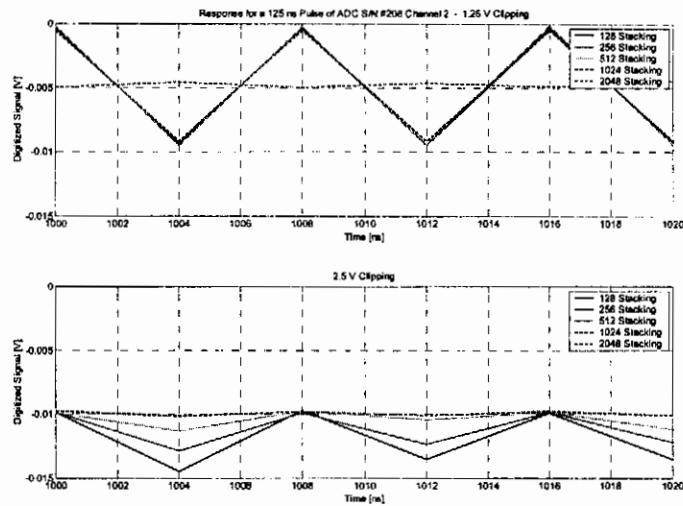


Figure C-4: Zoomed response of ADC serial number #208 indicating repetitive bit error.

For the 1.25 V clipping, the error seems to be present in all of the samples averaged, since it stays constant irrespective of the stacking used. The error for the 2.5 V clipping however seems to be of a more random process since the error decreases as the stacking is increased. The details of this apparent error are however beyond the scope of this dissertation.

ADC serial number #207 has an unreliable response to a 125 ns pulse for the various settings and the two channels are not matched at all. The 2.5 V clipping on the first channel yields inconsistent responses for the different stacking values. Furthermore a strong overshoot is present with the 1.25 V clipping on the second channel, while the 2.5 V clipping on the second channel produces very peculiar responses. Channel 1 also shows signs of repetitive bit errors.

ADC serial number #0000 is an experimental unit used for development purposes. The unit has a consistent response to a 125 ns pulse for the various settings, but channel 2 is not functional. It also shows signs of repetitive bit errors.

# APPENDIX D

## BLESKOP I FIELD EXPERIMENT

### D.1 Introduction

An extensive series of experiments with the GeoMole borehole radar was conducted at Anglo Platinum's Bleskop mine near Rustenburg, between 24 and 29 September. Its purpose was to establish radar propagation conditions in the layers that host the UG2. Attention was given to pulse speed and absorption; reflection by chromitite layers; and the possible existence of natural waveguides for long-range wave propagation.

### D.2 Borehole Geometry

Three borehole fans were drilled into the hard rock above and below the UG2 in winze BL1W descending from 12 crosscut north. Each fan consisted of three 10 m long boreholes drilled at angles of  $+45^\circ$ ,  $0^\circ$  and  $-45^\circ$  with respect to the plane of the UG2. The spacing between fans was about 20 meters.

Two 40 m long horizontal boreholes (GBH6 and GBH7), which had previously been drilled close to these fans for normal geological exploration purposes, were also exploited for the borehole radar experiments. Figure D-1 shows the configuration.

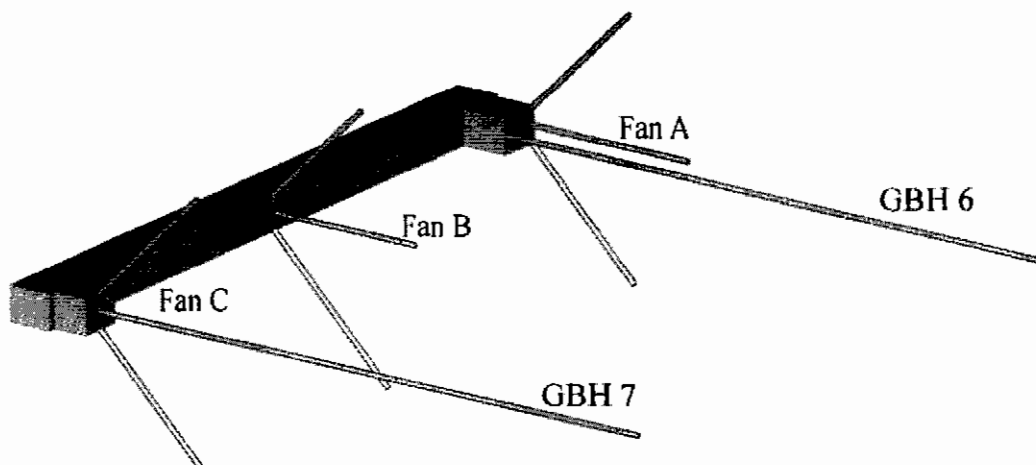


Figure D-1: Part of BL1W\_12 winze and the radar boreholes.

## APPENDIX D: Bleskop I Field Experiment

The collars of three of the boreholes, and their location in the geological system, are shown in Figure D-2 and Figure D-3.

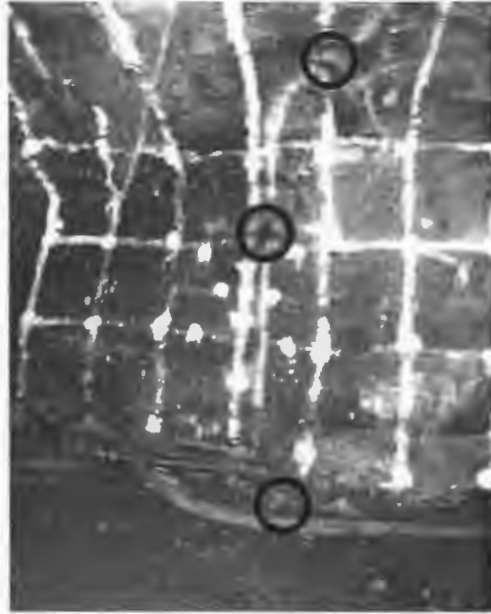


Figure D-2: Three boreholes (collars circled) at one of the stations.

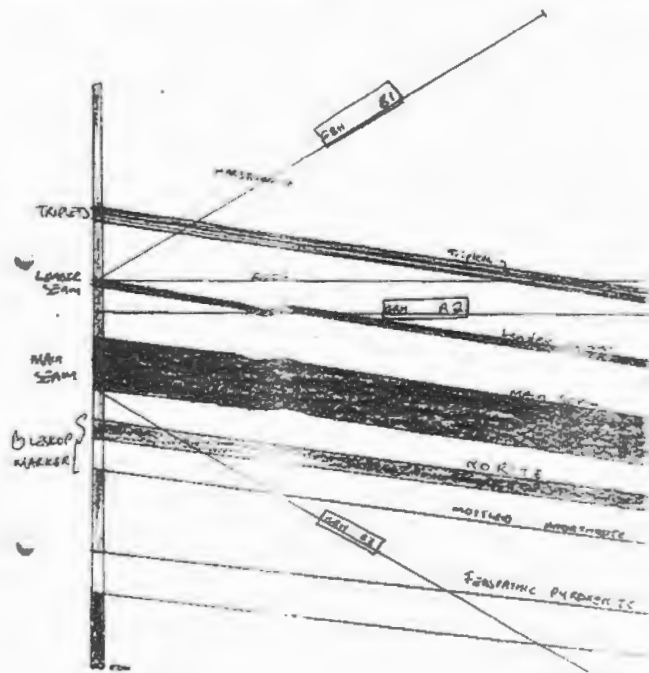


Figure D-3: Cross-section of station B showing intersections with different strata. (Courtesy of Mr Kabelo Tlhapi, Senior Geologist, Bleskop ARD)

### D.3 Summary of the Experiments

A total of 13 experiments were conducted from 25 to 29 September 2001. These comprised eleven cross-hole surveys between 10 holes, and two profile surveys of boreholes GBH6 and GBH7. (In a profile survey the transmitter and receiver are collocated, as they move down the borehole. In a cross-hole survey the transmitter and receiver are placed in different boreholes and either or both are displaced.)

### D.4 Experimental Results

The average velocity at which the radar pulse propagates through the different media and its absorption versus distance are important parameters. They govern the calibration, observation distance and resolution of the radar.

#### D.4.1 Propagation Speed in the UG2 Footwall

The three surveys between the  $-45^\circ$  holes (A3, B3 and C3) allows for an estimation of the propagation speed in the UG2 footwall. The radar scan with the transmitter in borehole A3 and the receiver in B3 is shown in Figure D-4.

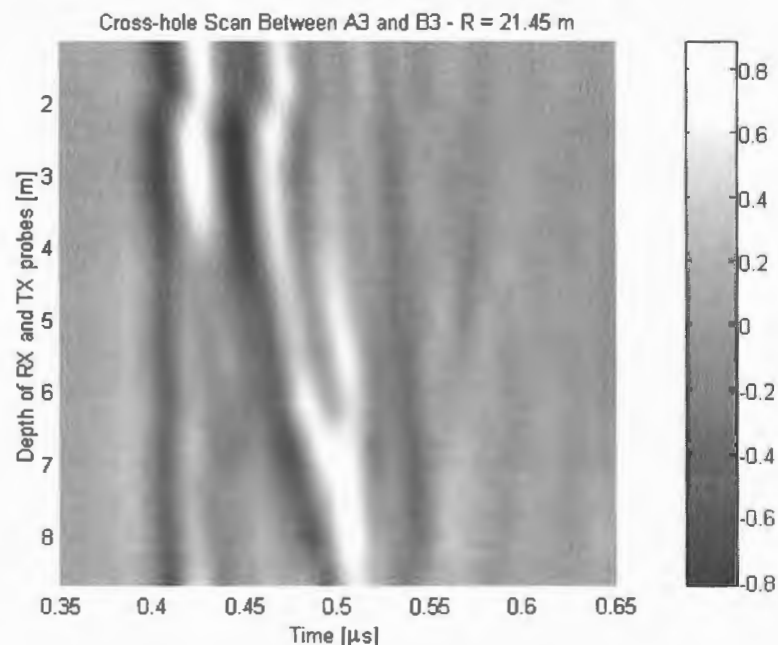


Figure D-4: Cross-hole survey between holes A3 and B3.

The radar scan in Figure D-4 was built up from thirteen individual scans where the transmitter was stationary at a given height in hole A3 and the receiver was moving up/down in hole B3. For each individual scan, the trace was selected where the

## APPENDIX D: Bleskop I Field Experiment

transmitter and receiver feedpoints were at approximately the same height. These steps have been repeated for a radar scan between holes B3 and C3 and also between holes A3 and C3. The radar scan with the transmitter in hole C3 and the receiver in hole B3 is shown in Figure D-5, while the radar scan with the transmitter in hole C3 and the receiver in hole A3 is shown in Figure D-6.

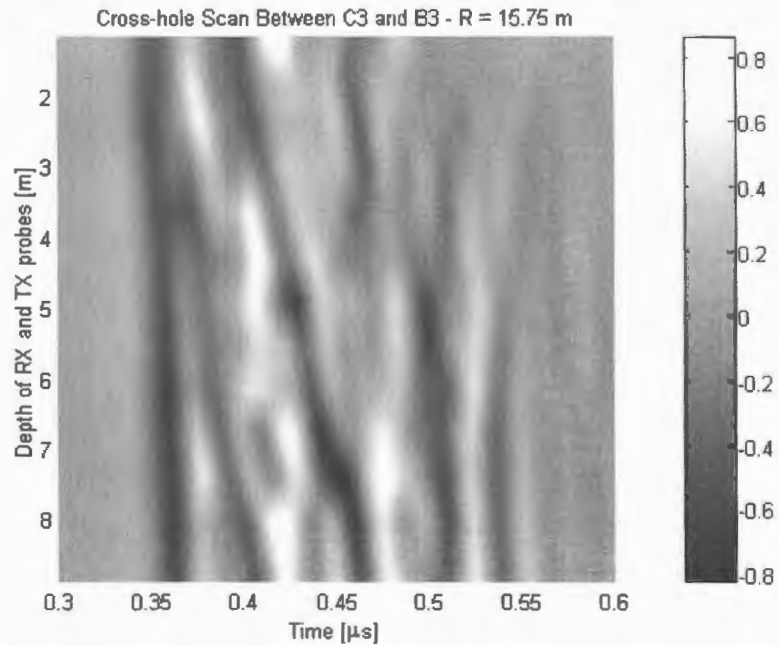


Figure D-5: Cross-hole survey between holes B3 and C3.

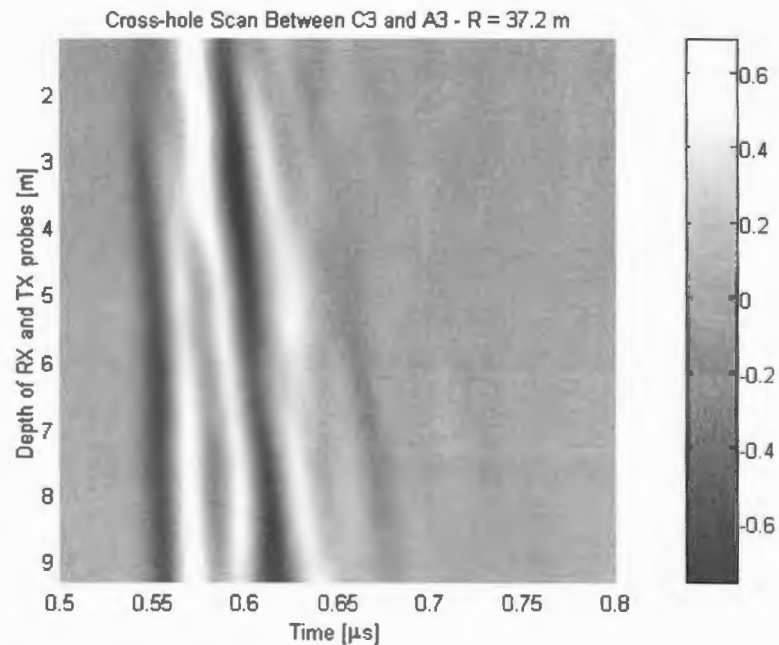


Figure D-6: Cross-hole survey between holes A3 and C3.

## APPENDIX D: Bleskop I Field Experiment

Consider the results of the first radar scan between holes A3 and B3. The zero time offset,  $t_0$ , for this specific shoot has been established as

$$t_0 = 0.188 \mu s. \quad (D.1)$$

Irrespective of the depth of the transmitter and receiver pair, the time at which the first signal is received,  $t_{fb}$ , is

$$t_{fb} = 0.395 \mu s. \quad (D.2)$$

From this and the distance between the boreholes,  $R = 21.45$  m, the average propagation speed through the footwall can be calculated as about three times slower than the speed of light in vacuum

$$\begin{aligned} v_{norite} &= \frac{21.45 \text{ m}}{0.395 \times 10^{-6} \text{ s} - 0.188 \times 10^{-6} \text{ s}} \\ &= 103.6 \text{ m} \cdot \mu s^{-1}. \end{aligned} \quad (D.3)$$

This corresponds closely (within 10%) to the predictions from our laboratory measurements of the dielectric properties of core samples of the rocks that host the UG2. The predicted velocity of EM waves in norite, based on the measured dielectric properties of norite, is  $\pm 113 \text{ m} \cdot \mu s^{-1}$ .

### **D.4.2 UG2 Detection Range**

We are especially interested in the range at which the UG2 can be detected with the radar operating in its footwall. A conservative estimate can be drawn from the Bleskop data as follows.

Consider the crosshole radar scan between boreholes GBH6 and GBH7, Figure D-7. After about 0.9 ms, a very strong reflection is detected. With the borehole spacing of 40 meters, this corresponds to a reflector about 20 m below the UG2. This is approximately the vertical separation between the UG2 and the UG1 at Bleskop. It can therefore be assumed that the reflection is from the UG1. It can further be assumed that the UG2 will be at least as good a reflector. Therefore, since the holes are about 40 meters apart, UG2 detection ranges of about 60 meters seem possible in cross-hole mode with the radar deployed between the UG2 and the UG1. This is equivalent to a maximum detection range of 30 m when the transmitter and receiver are collocated, as in the case of profile scans.

## APPENDIX D: Bleskop I Field Experiment

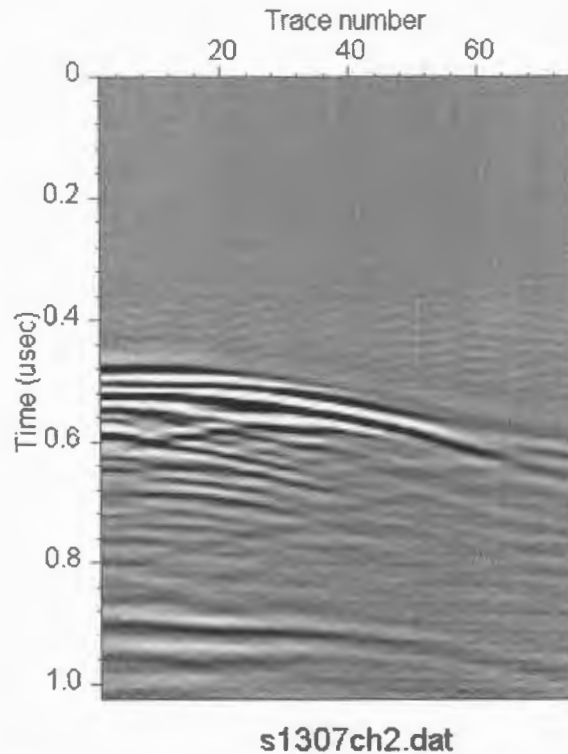


*Figure D-7: Cross-hole survey between holes GBH6 and GBH7.*

### D.5 Concluding Remarks

The UG2 footwall provides promising propagation conditions for the mapping of economically important geological features, such as potholes, by an appropriately designed borehole radar technique. Furthermore, the UG1 and UG2 reefs seem to have a large enough reflectivity to be detectable radar targets up to about 30 m in profile scan mode.

# APPENDIX E

## BRAKSPRUIT I FIELD EXPERIMENT

### E.1 Introduction

A borehole radar trial was conducted in the UG2 stratigraphy of the BIC at Anglo Platinum's Bleskop mine to investigate the transparency of the host rocks and whether there is adequate dielectric contrast between the UG2 and its foot or hanging walls (Appendix D). It was established that the footwall (norite) indeed supports the propagation of measurable radiowaves over more than 50 m and that the chromitites associated with the UG2 and UG2 reef horizons do provide ample contrast for mapping by the GeoMole BHR system with a resolution of 1 – 2 m [94].

The feasibility of pothole location by the GeoMole BHR system had to be confirmed with a follow up experiment in the BIC stratigraphy. The approach of this experiment should be the estimation of pothole dimensions with the BHR technique where the dimensions are already known from conventional techniques. The Brakspuit I field experiment were designed and conducted with this goal in mind and will be discussed in this appendix.

### E.2 Location, Geological Setting and Borehole Geometry

The exact location of the Brakspuit and Bleskop mine in the larger Anglo Platinum Rustenburg Section is shown in Figure E-1. The proposal was to drill a fan of three 120 m long boreholes with the holes traversing in the host rock between the UG2 and UG1 reef horizons [94]. The ideal was for the holes to be as close to the UG1 as possible and about 20 m from the UG2. Furthermore, the holes had to be dry and clean. In order to fulfil the goal of the experiment the boreholes had to pass near a number of known potholes, tunnels and stopes. The exact site for this experiment, together with the proposed boreholes, is depicted in Figure E-2 [97]. The tunnels are below the UG2 on Brakspuit Level 11 and the dashed ellipses indicate potholes of known location and dimensions.

APPENDIX E: Brakspruit I Field Experiment

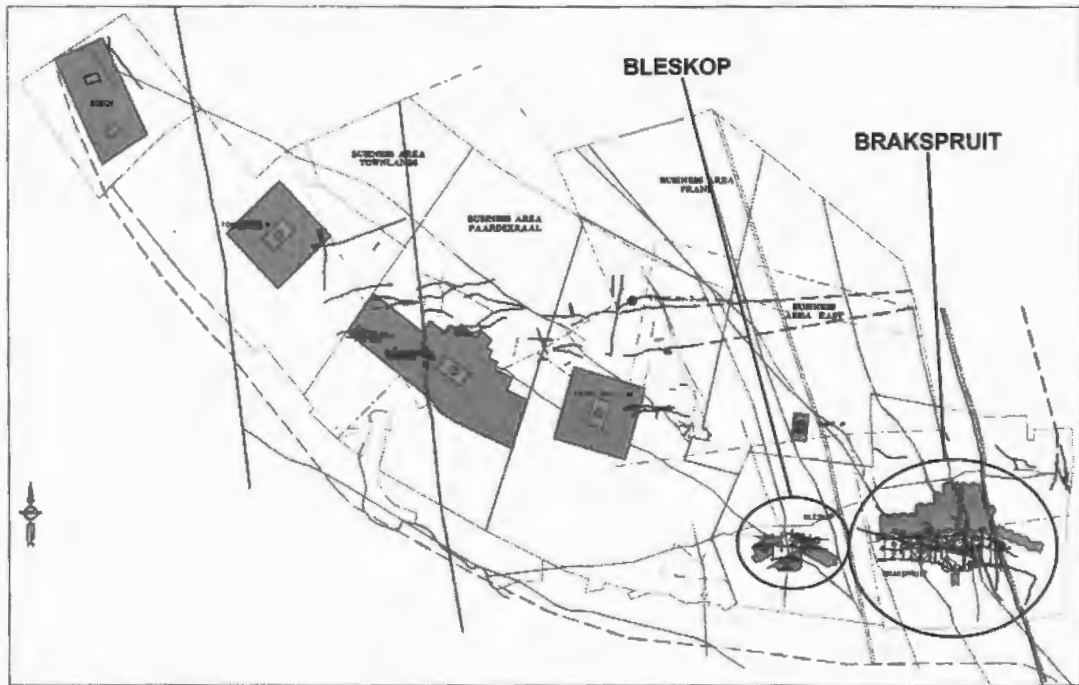


Figure E-1: Location of Brakspruit and Bleskop mines.

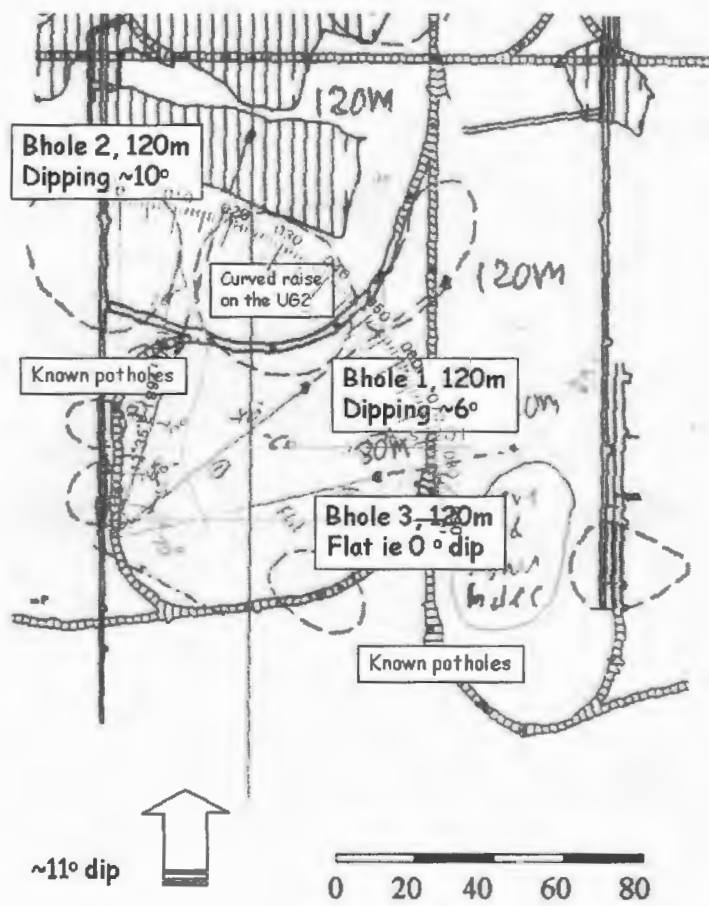


Figure E-2: Proposed location of boreholes in experimental site at Brakspruit Level 11.

(Courtesy of I. M. Mason, Professor, University of Sydney)

APPENDIX E: Brakspruit I Field Experiment

If the holes were indeed drilled as intended, they would lie in the norite host rock below the UG2. Upon inspection it was revealed that the holes deviated quite significantly from the intended plan due to the compromises made during the drilling process. The survey parameters of the three boreholes are given in Table E-1, showing the differences between the intended and actual boreholes.

Table E-1: Comparison between actual and intended borehole collar coordinates and directions.

Borehole	Length True / Design [m]	Coordinate 1 [m] (East to West)	Coordinate 2 [m] (North to South)	Elevation [m]	Dip True / Design [°]	Azimuth True / Design [°]
1	120 / 120	-41 451,461	+2 842 731,404	842,259	+1°09'33'' -6°	64°51'15'' 53°
2	70 / 120	-41 451,459	+2 842 730,428	841,854	-10°34'25'' -10°	37°57'31'' 18°
3	30 / 120	-41 451,340	+2 842 731,405	841,772	-9°49'42'' +0°	87°03'21'' 80°

The collars of the actual boreholes are depicted in Figure E-3.

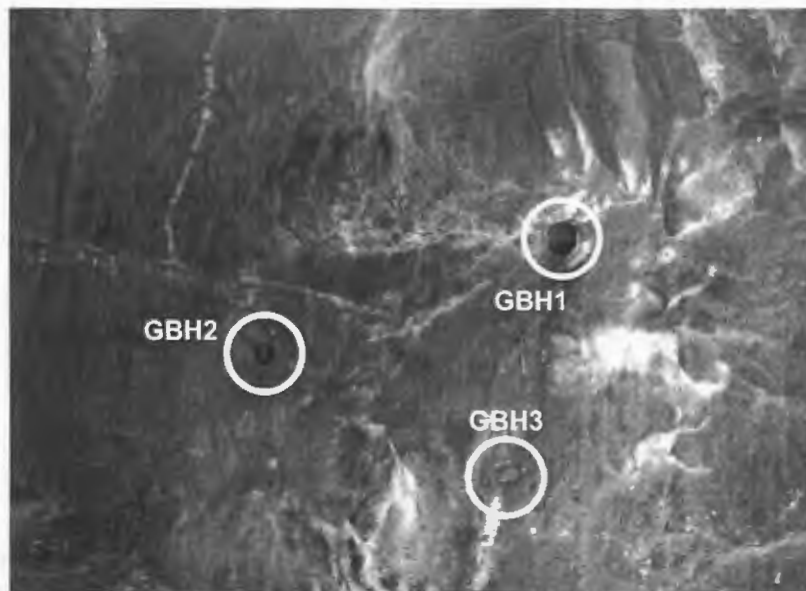
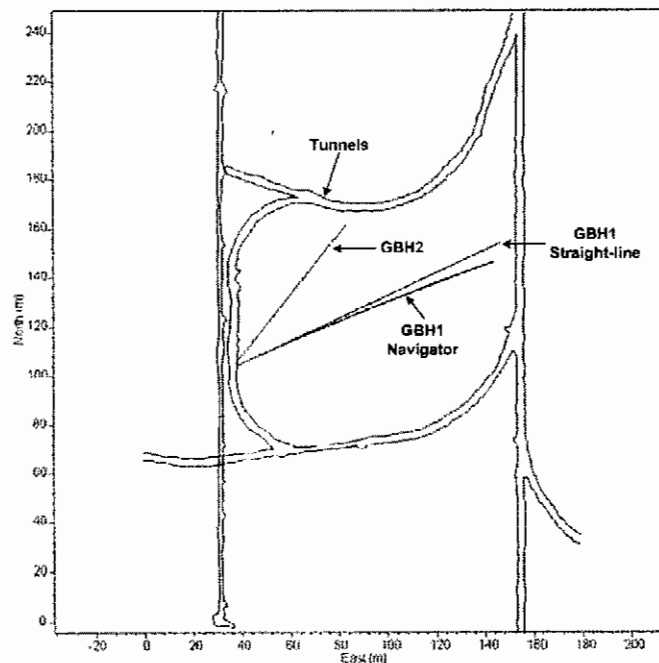


Figure E-3: GBH1 - GBH3 boreholes at Brakspruit Level 11.

## APPENDIX E: Brakspruit I Field Experiment

Borehole GBH3 was found to be short and partly blocked at the collar and was subsequently not used in the survey due to the risk involved in losing a radar probe. The length of the GBH1 borehole was surveyed with a CMTE Navigator orientation sensor with a triaxial magnetometer and a triaxial accelerometer [103]. The trajectory of the borehole was inferred from these measurements based on a path integration algorithm. The starting point was tied to the collar coordinate and the resulting trajectory is plotted in Figure E-4 together with the straight-line borehole from the surveyor's data.



*Figure E-4: Comparison of navigator inferred trajectory vs. the straight-line trajectory.*

It is clear that the actual borehole deviates from the straight-line borehole inferred from the surveyor's data. This is of crucial importance if geometry delineation has to be done accurately. The data can be corrected to remove the deviations from a straight line if the borehole trajectories are known.

### E.3 Experiment Configuration

The experimental configuration for the Brakspruit experiment was relatively simple. In essence it consisted of two profile scans of the GBH1 and GBH2 boreholes and a set of cross-hole surveys between these two boreholes. In the profile scan of the two boreholes, transmitter and receiver probes separated by an optical spacer were traversed along the distance of the borehole using the non-retractable Crouklamp

pulley mechanism. The received waveforms were captured as the probes were moving in and out of the holes. In the cross-hole survey of the two boreholes a receiver was positioned at a discrete number of locations along the length of the GBH1 borehole as a transmitter was traversing in and out of the GBH2 borehole. The results of these experiments are presented in Sections E.4 and E.5.

## E.4 Profile Scan Results

The profile (ingoing) scan of the GBH1 borehole is plotted in Figure E-5. The USTX 01 and USRX 01 probes were used together with the 3.1 m optical spacer. A bandpass filter (5 – 80 MHz with 10 MHz Hanning window edges) and an automatic gain control filter were used to process the data in the frequency and time domain.

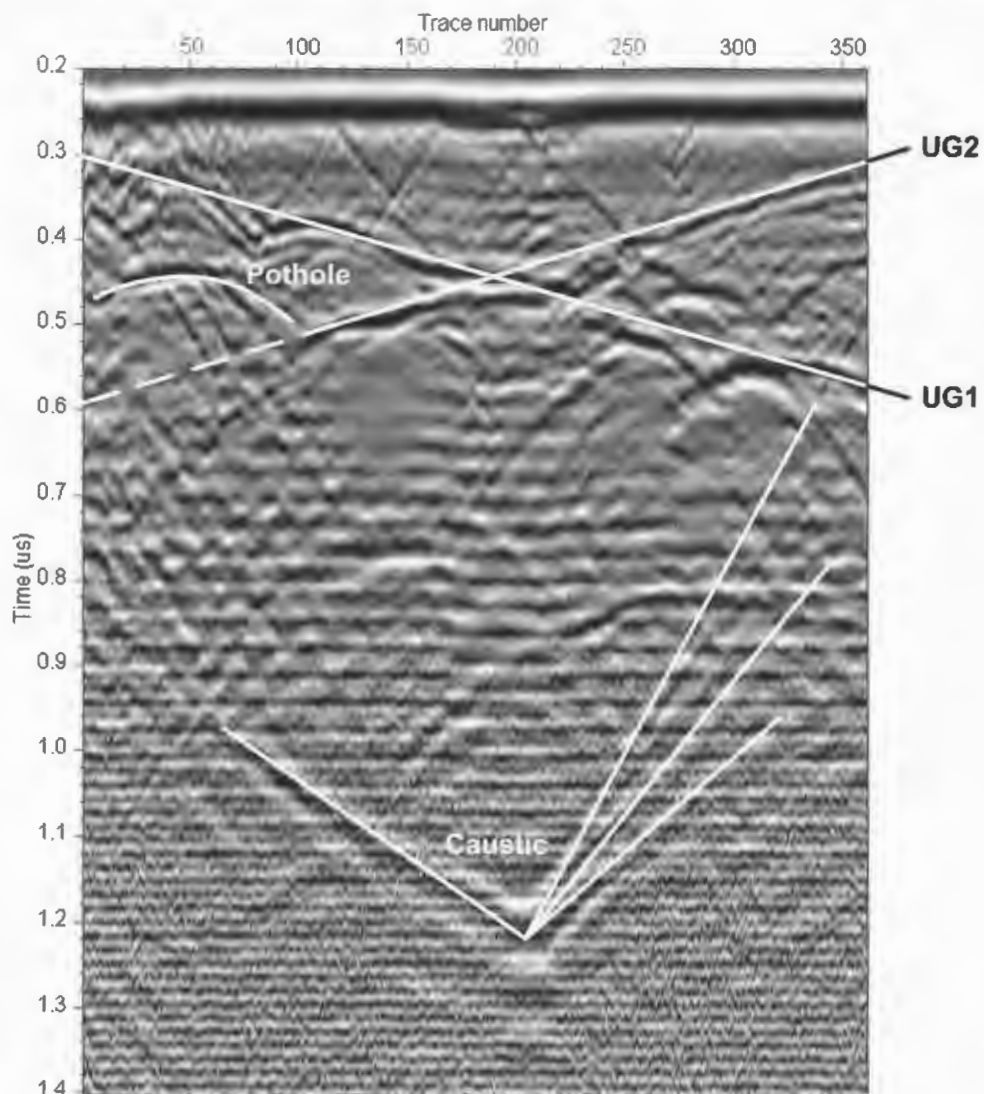


Figure E-5: Profile (ingoing) of GBH1 with basic interpretations.

## APPENDIX E: Brakspruit I Field Experiment

A number of basic interpretations are superimposed on the two-dimensional (time (radial range) vs. traversed distance) data field. The radar is located between the UG1 and UG2. It has an omnidirectional radiation pattern and therefore receives echoes from an omnidirectional region with the axis along the borehole axis. The echoes from the UG1 and UG2 would therefore superimpose onto the same image plane. The reflections from the UG1 interface starts at the upper left corner (close to the radar) and move downwards (further away) as the radar is pulled into the borehole. The signature of the reflections follows a diagonal line as would be expected for a planar interface. The basic trend has been superimposed on the data field. There are clear deviations from the ideal straight line indicating that the reef was not uniformly planar. The specific pattern has been associated with pillowing in the UG1 [97]. The reflections from the UG2 interface are best understood when followed from the end of the hole. Along the length of the borehole it moved closer to the UG2 reef and further away from the UG1. At the end of the hole the reflection is therefore closest and moves further away towards the collar of the hole. The signature of the UG2 reflections is much closer to that of a uniformly planar interface, especially when the echoes from trace 110 to the end is viewed. There is a disturbance in the range (height) of the UG2 in a range of 75 traces centred on trace 215. That region of the borehole has also been associated with a shear plane. In the unfiltered data quite severe saturation of the receiver was observed in this region. This is indicative of a local disturbance of some kind. In the definition and design of the experiment it was stated that one of the goals has to be the estimation of the signature of an existing pothole of known dimensions. The GBH1 and GBH2 boreholes were therefore intentionally drilled from below a known pothole, Figure E-2. In the data field the linear signature of the UG2 abruptly disappears between the collar and trace 110 and a maximum throw of ~7 m is clearly visible as marked on the data field.

The profile (ingoing) scan of the GBH2 borehole is plotted in Figure E-6. The exact configuration of the GBH1 profile was used. A bandpass filter (5 – 80 MHz with 10 MHz Hanning window edges) and an automatic gain control filter were used to process the data in the frequency and time domain.

## APPENDIX E: Brakspruit I Field Experiment

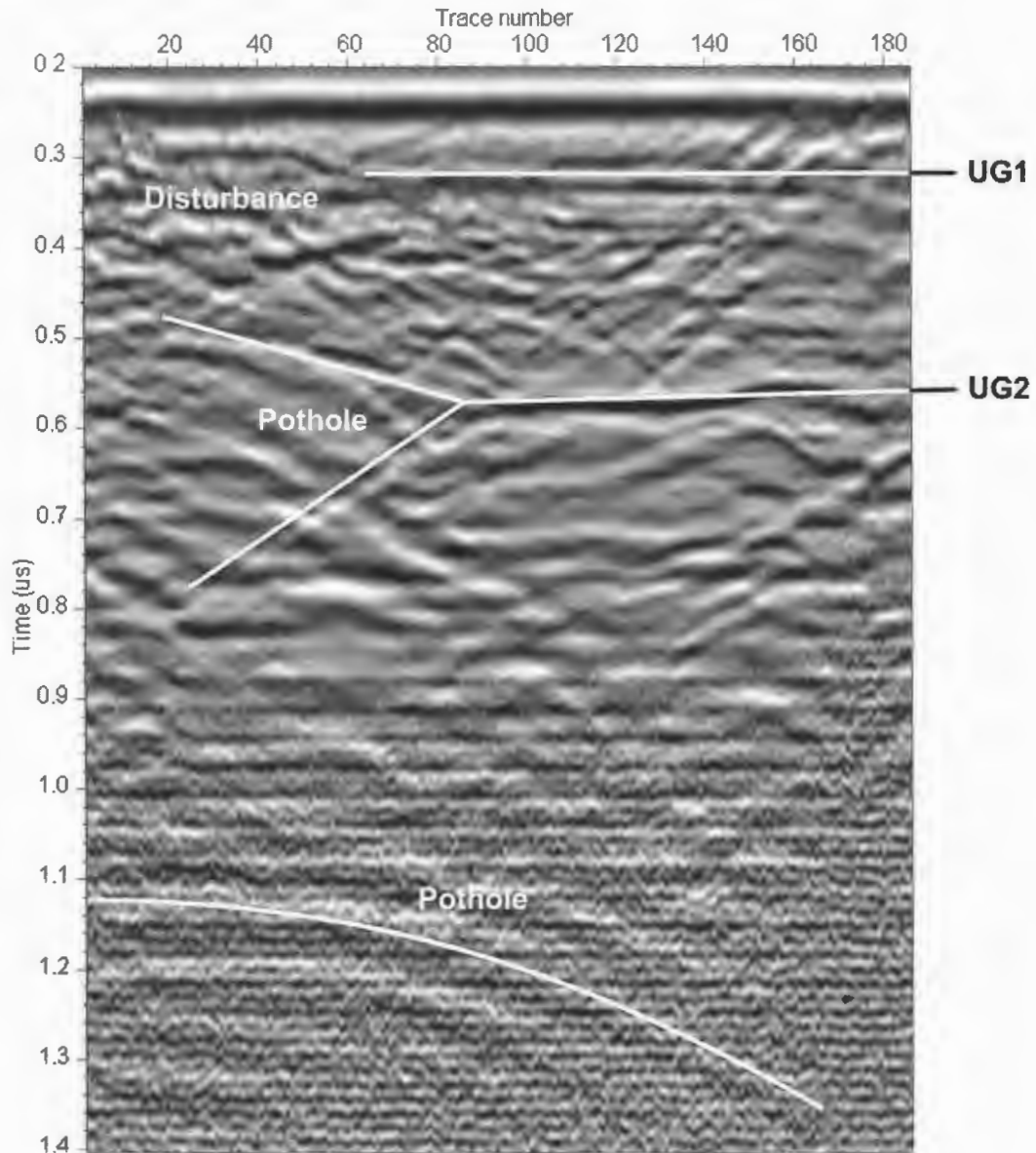


*Figure E-6: Profile (ingoing) of GBH2 with basic interpretations.*

This borehole was drilled with a dipping angle so that it paralleled the UG1 and UG2 reef horizons. The collar was once again just below a pothole in the UG2. The signatures of the UG1 and UG2 reflections are almost parallel straight lines as would be expected for the given geometrical configuration. An interesting 90° rotated V-shaped signature is visible from the collar to trace 90 with the corner of the V connected to the straight-line signature of the UG2. It has been associated with the pothole in the UG2 [97]. There are quite severe disturbances in the area of the UG1 reflections up to trace 65. A signature of a sideswipe pothole is also visible beyond 1.1  $\mu\text{s}$  [97].

## E.5 Cross-hole Survey Results

One of the cross-hole surveys between GBH2 and GBH1 is plotted in Figure E-7. The USTX 01 transmitter was pulled into GBH2 from the collar to the end of the borehole while the USRX 02 receiver was stationary in GBH1 at a distance of 40 m from the collar. A bandpass filter (5 – 80 MHz with 10 MHz Hanning window edges) and an automatic gain control filter were used to process the data in the frequency and time domain.

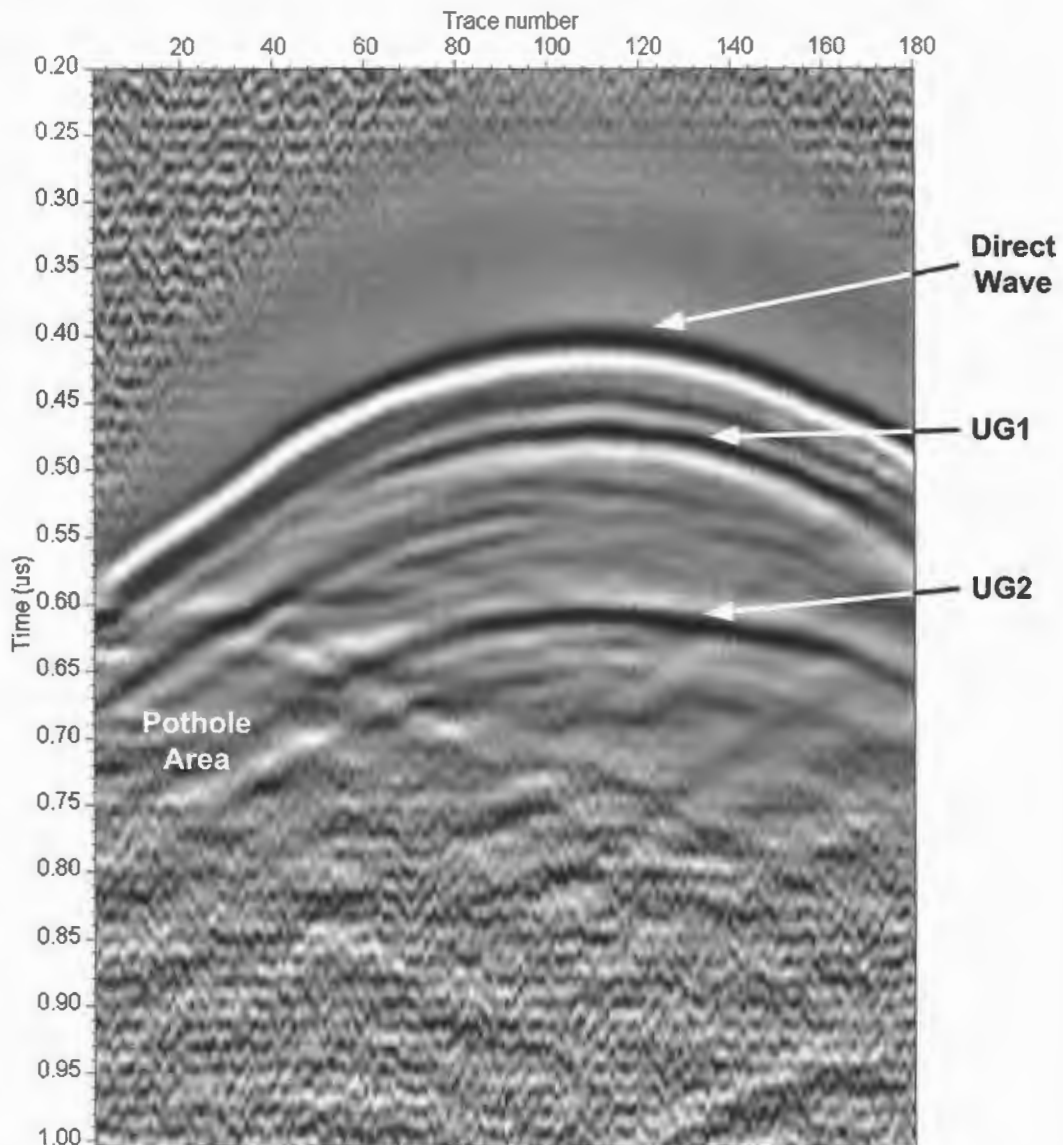


Figure E-7: Cross-hole survey between GBH2 (TX ingoing) and GBH1 (RX stationary @ 40 m).

In this survey both the TX and RX probes are situated in the norite host rock between the UG1 (bottom) and the UG2 (top). The first arrival is that of the direct wave that propagates relatively undisturbed to the receiver. The forward scattering reflections

from the UG2 and UG1 interfaces arrive some time later with ample time domain resolution. Since the boreholes (for the section of interest) are closer to the UG1, the reflections from the UG1 arrive first and are followed by the UG2 reflections. The area close to the collar is contaminated by the existing pothole and therefore influences the reflections in that area as can be seen in the data field.

## **E.6 Concluding Remarks**

The main purpose of the Brakspruit I experiment was to confirm the feasibility to map the dimensions of geological structures (potholes, rolls, dykes, etc.) in the BIC, with specific interest in the layers between the UG1 and UG2 reef horizons. Even though the experiment was designed as a fan of three boreholes and only two boreholes (one of only 70 m) were eventually drilled, the results obtained from the profile scans and cross-hole surveys indeed confirmed the abovementioned capability of the GeoMole BHR system.

In the delineation of the geometry, not only the BHR system is of critical importance, but also the software package used for data processing and the physical understanding of EM wave propagation in the stratified medium.

Since the focus of this dissertation is not on the actual delineation of the geometry, only basic interpretations of the data field were made in this appendix. An extensive effort has been put forward in the delineation of the geometry of the specific site and the reader is referred to the appropriate documents for further information on the results obtained by this effort [8], [97], [103].

# APPENDIX F

## BLESKOP II FIELD EXPERIMENT

### F.1 Introduction

During the Bleskop I trial borehole experiment (Appendix D) it was established that the norite host rock between the UG1 and UG2 reef horizons in the BIC is translucent to the HF and VHF frequencies of the GeoMole BHR system. It was furthermore established that the UG1 and UG2 chromitite layers provide ample dielectric contrast for reflections with good SNR. The Brakspruit I experiment (Appendix E) was conducted to confirm the results of the Bleskop I experiment and to determine the feasibility of mapping geological defects (potholes, dykes, rolls, etc.) in the BIC with BHR technology.

The Bleskop II experiment was initiated after the significant results obtained during the previous experiments were accepted as a proof of concept. The purpose of this experiment was to assess the base of the UG2 reef at a given site at the Bleskop mine in the Anglo Platinum Rustenburg Section. Where the geometry at Brakspruit was known apriori, the behaviour of the UG2 and UG1 reefs at this site was not exactly known beforehand. The capabilities of the GeoMole BHR system, associated processing and interpretation to delineate 'relatively' unknown geometry were therefore put to the test.

The successful prediction of potholes, rolls, etc. will testify that the GeoMole BHR system can be used effectively to give the mining engineers apriori knowledge about the area they are planning to mine and might even convince them not to mine that area.

### F.2 Location, Geological Setting and Borehole Geometry

The location of the Brakspruit mine in the larger Anglo Platinum Rustenburg Section is shown in Figure E-1, Appendix E. The proposal was to drill a fan of three 100 m boreholes from the face of 13 Level West Haulage, Section 162, Bleskop (BL294). The boreholes were to be drilled in the norite host rock between the UG1 and the UG2

## APPENDIX F: Bleskop II Field Experiment

with the distance from the UG2 a minimum of 10 m. Their collars had to be close together with  $30^\circ$  azimuth spacing between them, as depicted in Figure F-1. The dashed ellipse indicates the estimated geometry of a known pothole.

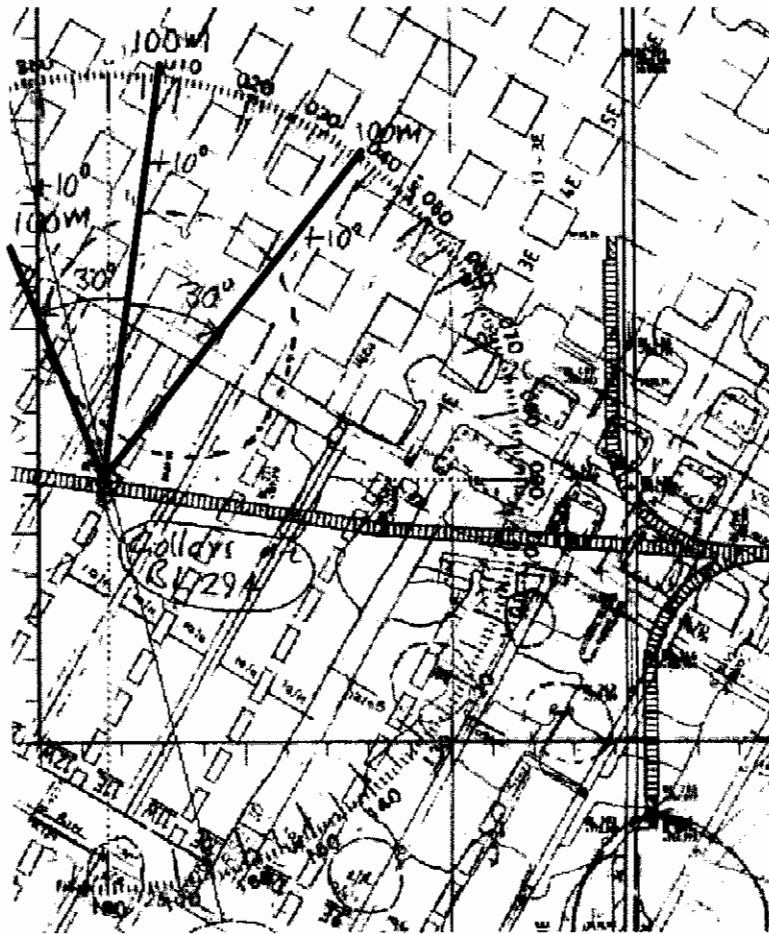


*Figure F-1: Proposed location of boreholes at 13 Level West Haulage, Bleskop.*

The three proposed boreholes were drilled as specified and an additional two boreholes were also drilled. The azimuth direction of these boreholes bisected the angles between the proposed boreholes and they were drilled with a negative elevation angle, where the original boreholes were drilled with a positive elevation angle. The collars of the five holes are depicted in Figure F-2. These boreholes were all surveyed with the CMTE Navigator orientation sensor and their trajectories were inferred from the obtained data based on a path integration algorithm. The starting points were tied with the exact collar locations according to the surveyor's data. The plan view of the site and the five boreholes are given in Figure F-3, together with the estimated contour lines of the UG2 reef horizon (discussed in Section F.6).

APPENDIX F: Bleskop II Field Experiment



Figure F-2: GBH46 - GBH50 borehole collars at 13 Level West Haulage, Bleskop.

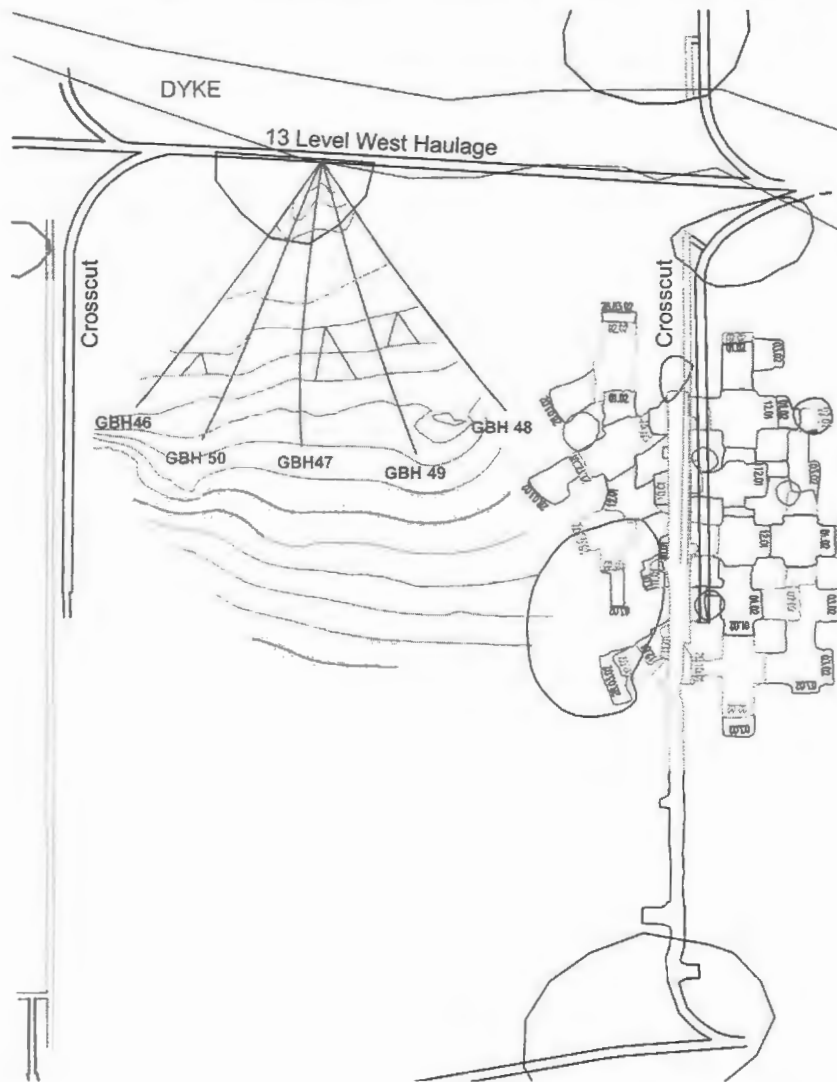


Figure F-3: Plan view of boreholes in relation to site geometry at 13 Level West Haulage, Bleskop.

## APPENDIX F: Bleskop II Field Experiment

The trajectories as viewed from the south at 0° elevation angle are depicted in Figure F-4.

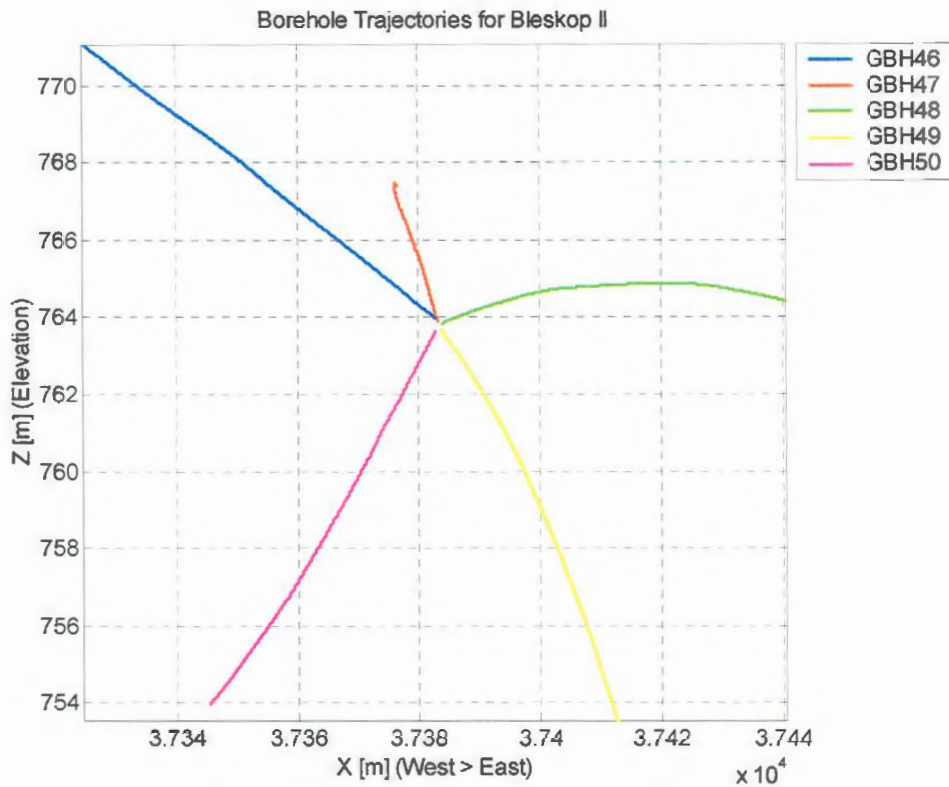


Figure F-4: Projection of boreholes on the west-to-east – elevation plane.

The actual boreholes clearly deviate from a straight line. The GBH48 borehole starts with a positive inclination angle that slowly decreases to a horizontal borehole and eventually starts to bend down at the end of the borehole. The designed and true directions of the boreholes (at the collar) are given in Table F-1.

Table F-1: Designed vs. true borehole lengths and directions.

Borehole	Length		Dip		Azimuth	
	True / Design [m]		True / Design [°]		True / Design [°]	
GBH46	100 / 97.7		7°9'50'' / 10°		213°35'24'' / 210°	
GBH47	100 / 90.63		5°58'48'' / 10°		187°55'12'' / 180°	
GBH48	100 / 97.7		3°48'00'' / 7 °		147°33'00'' / 150°	
GBH49	100 / 97.7		-1°27'36'' / -5°		165°23'24'' / 165°	
GBH50	100 / 96.4		-6°44'24'' / -10°		201°39'00'' / 195°	

## APPENDIX F: Bleskop II Field Experiment

Even though the true directions are a couple of degrees from the designed values, the deviations are small enough to yield a good platform for radar measurements. One of the boreholes is 10 m shorter than proposed, while the other boreholes are all within 4 m of the proposed lengths. The GBH49 and GBH50 boreholes are declined and water-filled. These boreholes were flushed with 'clean' water to minimise the salt contents of the water in the boreholes. The other boreholes were essentially dry, even though traces of water were observed at the collars of these holes.

The stratigraphic sections of the boreholes, as determined from the drill cores, are depicted in Figure F-5 and Figure F-6.

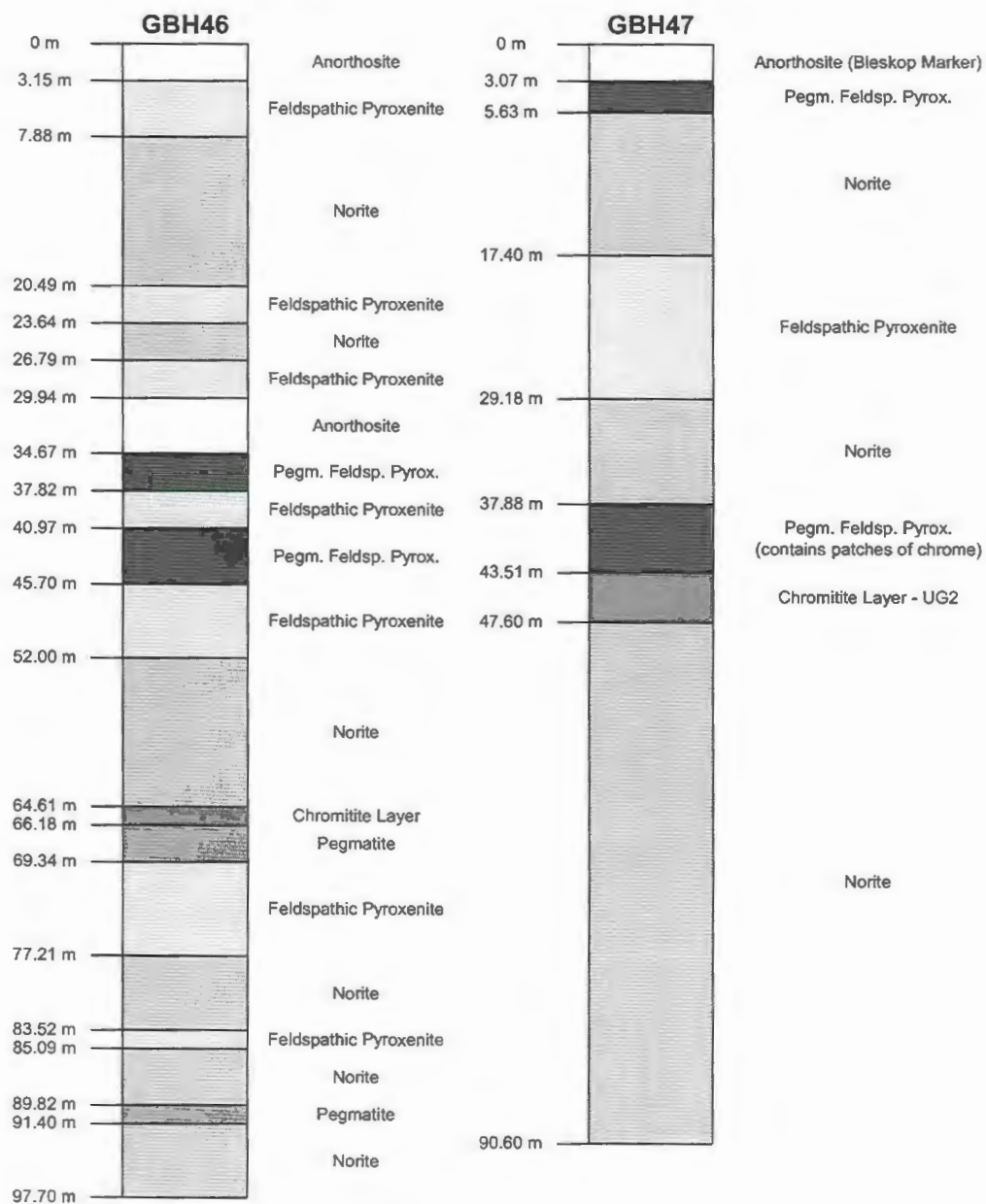


Figure F-5: Stratigraphic sections of the GBH46 and GBH47 boreholes.

## APPENDIX F: Bleskop II Field Experiment

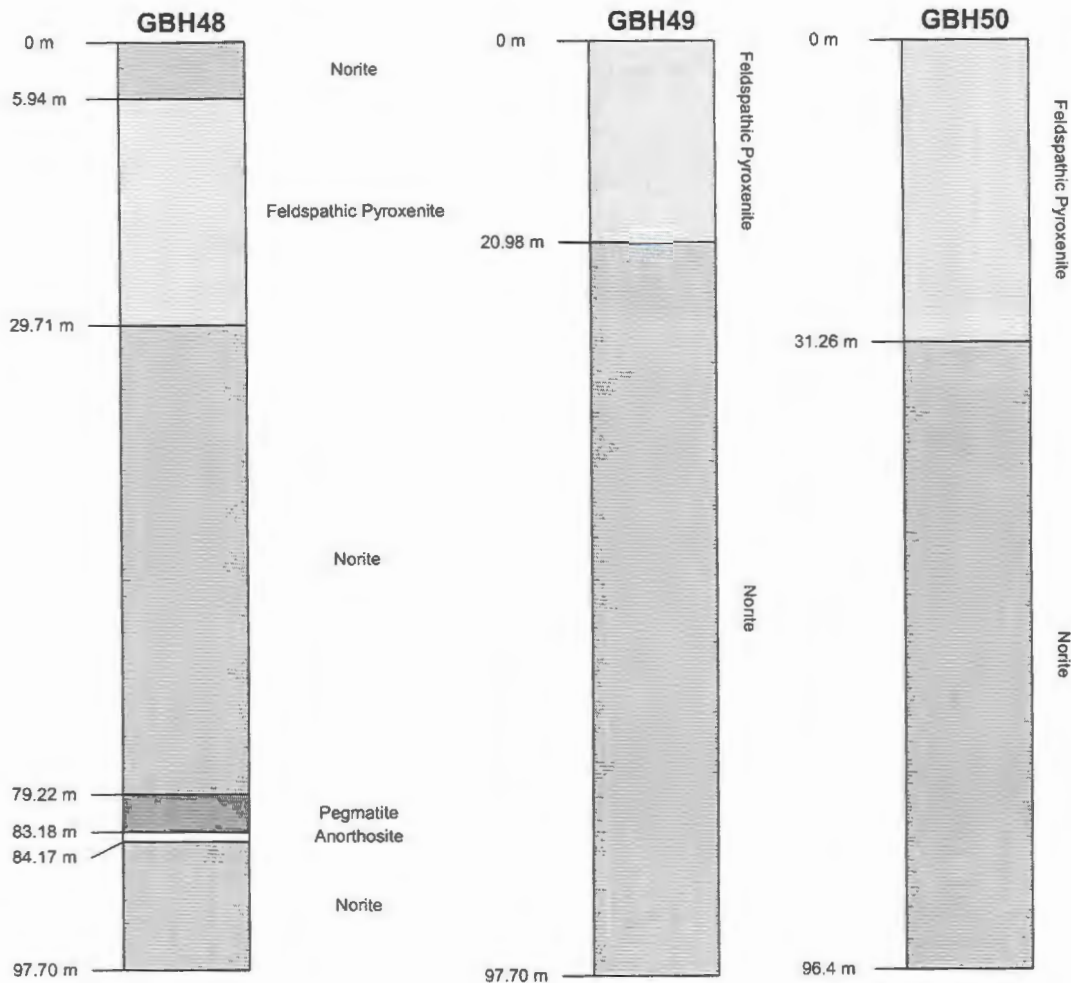
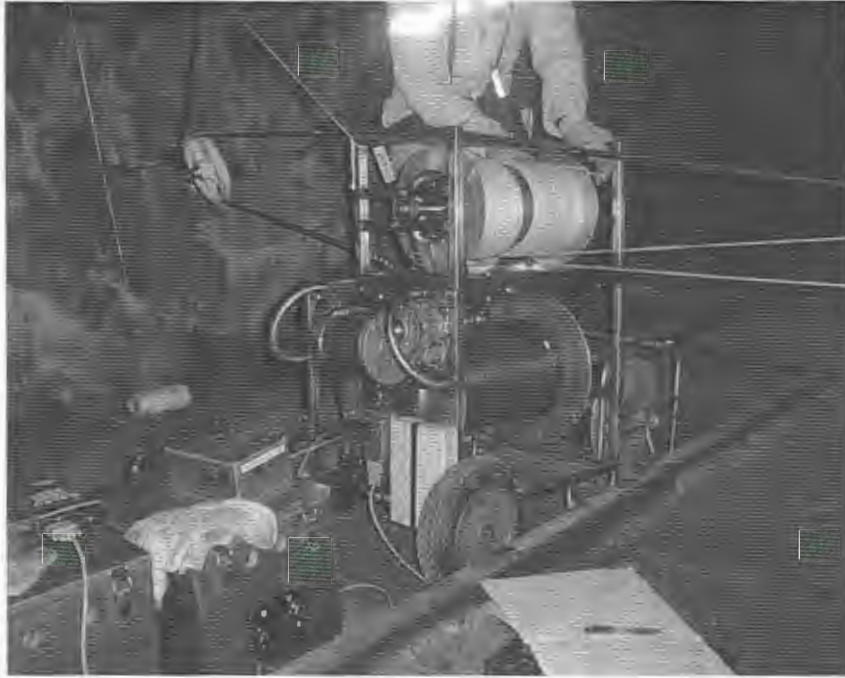


Figure F-6: Stratigraphic sections of the GBH48, GBH49 and GBH50 boreholes.

From these sections it is clear that the down holes are in mostly homogeneous host rock with the understanding that both the pyroxenites and norites are viewed as host rock. The GBH46 borehole traverses through different layers for its entire length. The GBH47 borehole traverses through a couple of layers, while the GBH48 borehole traverses through host rock for almost the entire length.

### F.3 Experimental Configuration

The same basic configuration was used at Bleskop II as was used for the Brakspruit I experiment. Profile scans were done of the five boreholes with a transmitter and receiver interconnected with an optical spacer. The probes traversed the lengths of the boreholes. Thy physical configuration for these profiles scans is depicted in Figure F-7.



*Figure F-7: Physical configuration of profile scans at Bleskop, 13 Level West Haulage.*

A number of cross-hole surveys were carried out between the five boreholes. In any cross-hole survey a transmitter was located in the one borehole with a receiver located in a different borehole. The transmitter and receiver probes were pulled (at the same speed) in and out of the boreholes. The results of these experiments are presented in Sections F.4 and F.5.

## **F.4 Profile Scan Results**

The profile (ingoing) scans of the GBH46 – GBH50 boreholes are plotted in Figure F-8 and Figure F-9. The USTX 03 and USTRX 03 probes (interconnected with the 4.6 m optic spacer) were used in all but one of the presented results. The results of the profile scan of GBH48 with a USTX 01, USRX 01 and 3.1 m optical spacer are plotted in Figure F-8 (d) to examine the relative performance of the different probes. In Chapter 3 it was suggested that the USTX 03 is a more powerful transmitter and this claim had to be investigated on the basis of field experimental data. A bandpass filter (5 – 80 MHz with 10 MHz Hanning window edges) and an automatic gain control filter were used to process the data in the frequency and time domain.

## APPENDIX F: Bleskop II Field Experiment

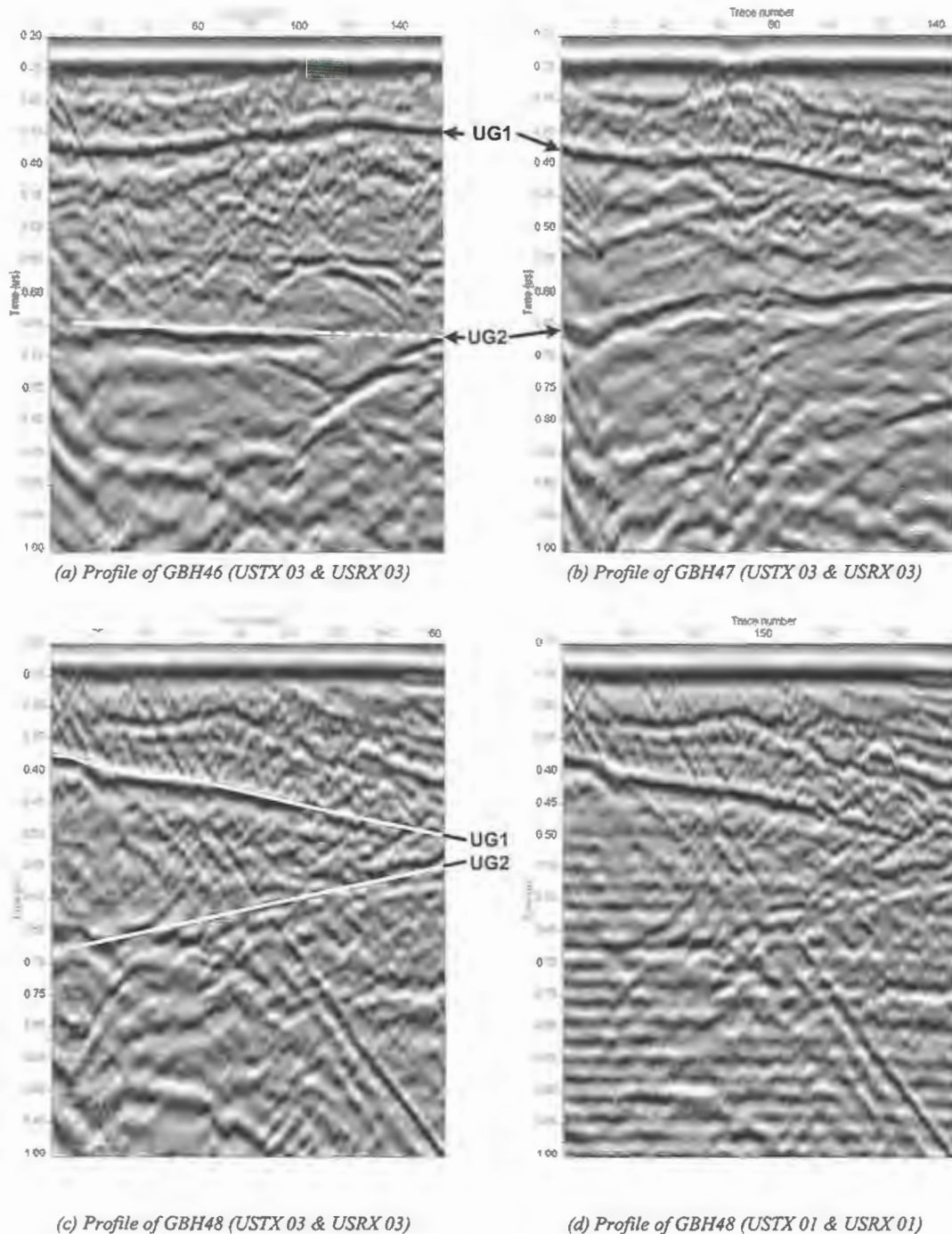


Figure F-8: Profile scans of GBH46 - GBH48 with elementary interpretations.

The signatures of the UG1 and UG2 reef interfaces are prominent in the profiles of the GBH46 – 48 boreholes, as well as a huge amount of secondary reflections. These reflections might be from potholes, dykes, fractures, man-made structures, etc. and will not be investigated further in this appendix. When the two profiles of the GBH48 borehole are compared, it is clearly visible that the received signal with the USTX 03 transmitter has a better SNR and the reflections are more vivid – indicative of a

## APPENDIX F: Bleskop II Field Experiment

stronger and broader frequency response. It confirms the results obtained with the rooftop calibration measurements in Chapter 3.

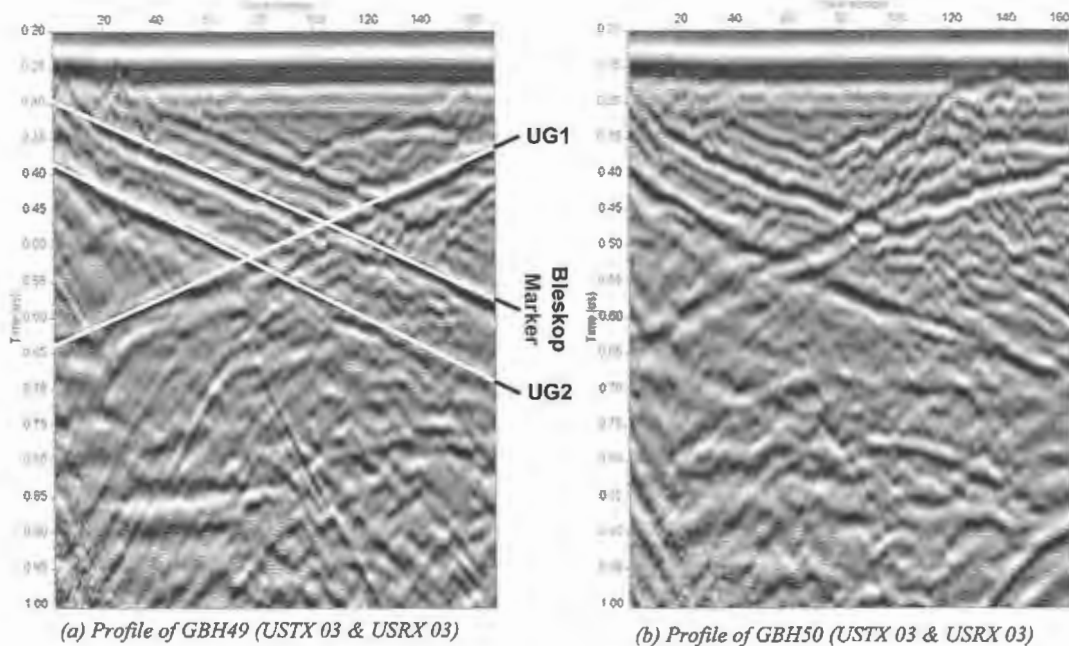


Figure F-9: Profile scans of GBH49 – GBH50 with elementary interpretations.

The echoes from the UG1 and UG2 reef horizons have relatively linear signatures in the profiles of the GBH49 and GBH50 boreholes. In addition to the reflections from the UG2, two other straight-line signatures are visible with the same slope as the UG2 signature. One of these has been associated with the Bleskop Marker sequence, while the other might be associated with another interface in the BIC stratigraphy (above the boreholes).

### F.5 Cross-hole Survey Results

The cross-hole survey between GBH46 and GBH48, as well as the survey between GBH49 and GBH50, are of critical importance in this dissertation. They are used for the estimation of the average pulse peak velocity and quality factor of the host rock (Chapter 6). The results for these two cross-hole surveys are plotted in Figure F-10. In both surveys the USTX 03 (most powerful) transmitter was deployed in one borehole, while the USRX 02 (most sensitive) receiver was deployed in the other. Both probes were pulled out (in) of the boreholes at the same instance and the same speed. A bandpass filter (5 – 80 MHz with 10 MHz Hanning window edges) and an

## APPENDIX F: Bleskop II Field Experiment

automatic gain control filter were used to process the data in the frequency and time domain.

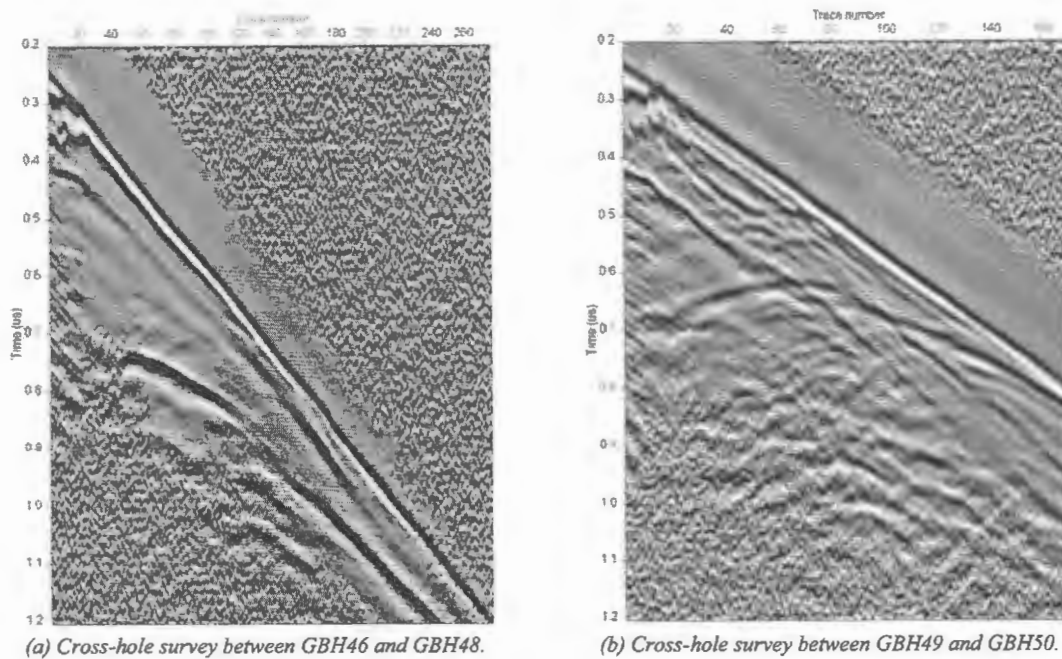


Figure F-10: Cross-hole surveys between GBH46 and GBH48, and GBH49 and GBH50.

In these two experiments, the direct wave is the primary return of interest. It is resolved from any of the secondary reflections in both experiments and therefore suitable for the estimation of the average pulse peak velocity and quality factor of the host rock. In both experiments the reflections from the UG1 and UG2 reef horizons are visible, but of no significant interest in this dissertation and will not be considered.

### F.6 Concluding Remarks

The Bleskop II experiment was the first experiment in which the design and execution was placed under strict control. The drilled boreholes conformed to the proposed design for the first time. An accurate logbook was kept of the exact configuration of each profile scan or cross-hole survey. Painstaking care was also taken to ensure good optical connections at the various optical interfaces. This experiment was also the first experiment conducted after the calibration of the GeoMole BHR system. This provided the operator for the given experiment with additional a priori knowledge with regard to the performance of the given configuration. Finally, all the boreholes were surveyed by the mine surveyors and with the CMTE Navigator orientation sensor – allowing the delineation of the borehole trajectories. All of the

## APPENDIX F: Bleskop II Field Experiment

abovementioned attributes of the Bleskop II experiment contributed to fidelity and firm ground of this experiment for data interpretation, signal analysis and geometry delineation. The design of the experiment and the configuration of the system yielded the first experimental data that conformed to the requirements for the signal analysis set out in Chapters 6 and 8.

In addition to the academic interest, very valuable operation information was gained from this experiment. Due to the high fidelity of this experiment, the delineation of the geometry was carried out using numerous imaging techniques [98]. Digital elevation maps of both the UG1 and UG2 reefs have been formed; known objects to the sides of the boreholes were mapped; unknown objects (a dyke and two potholes) were found and a number of anomalies, that might be potholes, were also found. A contour map of the UG2 reef interface is imposed of the mining map in Figure F-3.

The results obtained with the Bleskop II experiment [95],[98] confirm that the GeoMole BHR system, together with the appropriate techniques and knowledge, can be used to delineate known and unknown geological structures in the BIC.

# APPENDIX G

## PULSE RECOMPRESSION PROGRAM

The basic interface and working of the GUI-based batch-processing pulse recompression algorithm will be presented in this appendix. The main GUI console is depicted in Figure G-1.

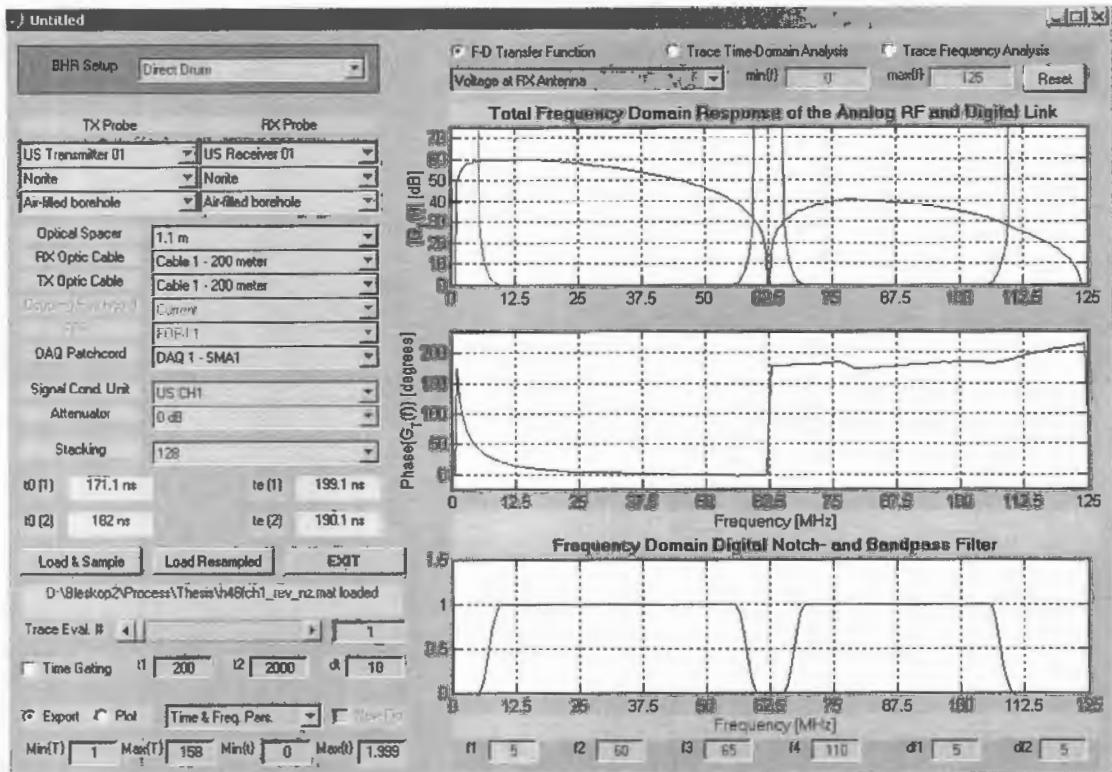


Figure G-1: Main GUI console of batch-processing pulse recompression algorithm.

The top left section of the console is used to select the radar configuration. The specific component is selected from the drop-down boxes as depicted in Figure G-2. The underlying signal processor calculates the necessary transfer functions. If data has been loaded, the transfer functions are applied to it. The time-offsets for the first break and main event are also calculated and displayed. The user can select the data to be plotted in two of the axes in the main console. The first set of data that can be plotted is the magnitude and phase response of the different frequency domain transfer functions. Secondly, the time domain response (front-end voltage or feedpoint E-field) can be displayed if a data set is loaded in the console. The final set of data that can be plotted is the frequency domain analysis of the loaded data. The

## APPENDIX G: Pulse Recompression Program

third axes displays the selected bandpass and notch filter. The parameters of this filter can be set interactively at the bottom right interface.

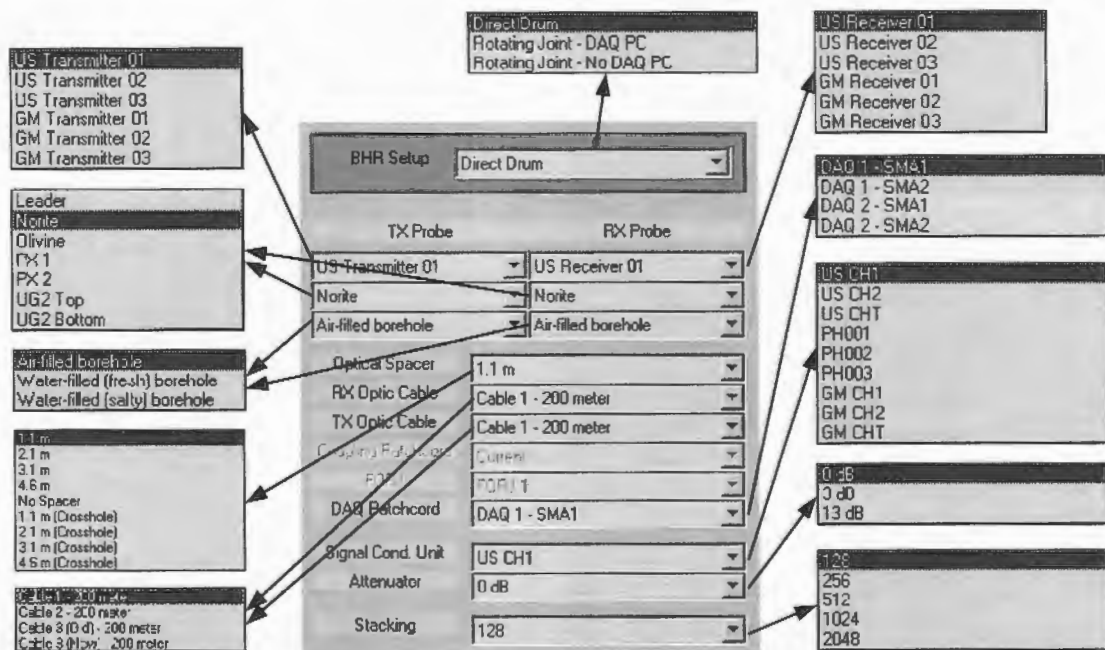


Figure G-2: GeoMole BHR system configuration console.

The field experiment data control interface is depicted in Figure G-3. The raw data captured with the radar (in \*.dat format) can be loaded into the workspace of the console with the 'Load & Sample' button. The data is interpolated (1 ns time intervals) and can be stored for future use. Data that has already been resampled can be loaded with the 'Load Resampled' button. The data is loaded into the workspace and the specific trace to be analysed can be selected by the sliding bar or with a text entry.

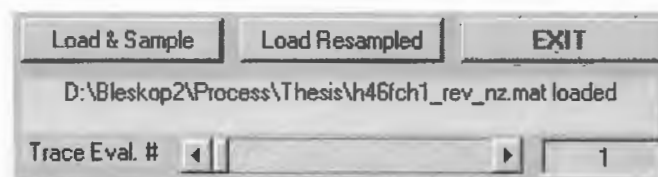


Figure G-3: Field experiment data control interface.

The data can also be time-gated by means of the time-gating interface, Figure G-4. The user specifies the start and stop time of the gate, as well as the length of the Hanning window rising and falling edges.



Figure G-4: Time-gating interface.

## APPENDIX G: Pulse Recompression Program

The real-time data analysis capability of the console is quite useful, but in some cases the user might want to process the data off-line. A data plot and export interface has been provided (Figure G-5). The different parameters that can be exported are listed, as well as the parameters that can be plotted onto separate figures and axes. When the ASCII export options are chosen, the relevant data is exported in the ASCII file format that can be used in other software packages, i.e. SeisWin. When data is plotted, the user has control over the ranges (trace and time) to be plotted. Data can also be plotted on the same axis for comparative evaluations.

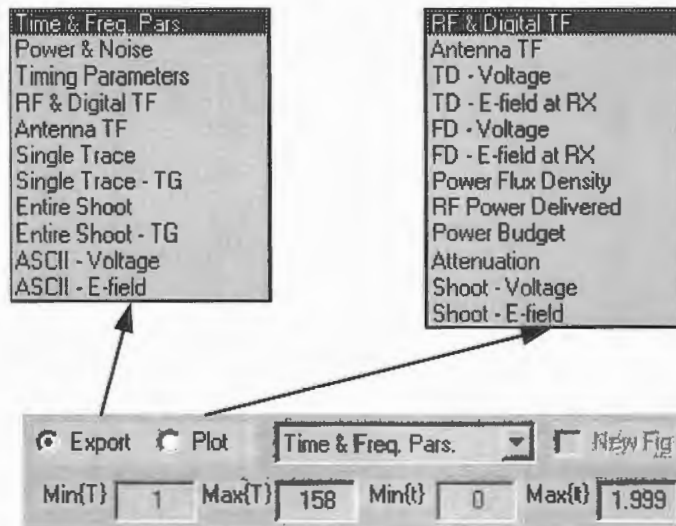


Figure G-5: Plot and export control interface.

Only the basic functionality of the GUI-based algorithm was presented in this appendix. It demonstrates the capability of the algorithm to do batch-processing and allow highly configurable system configurations.

# APPENDIX H

## CALIBRATION FACILITY CIRCUIT DIAGRAMS

The circuit diagrams of the electronic devices designed and built for the rooftop calibration facility are presented in this appendix.

### H.1 Calibration Receiver Electronics

The circuit diagram for the calibration receiver, as discussed in Section 3.4.5, is plotted in Figure H-1.

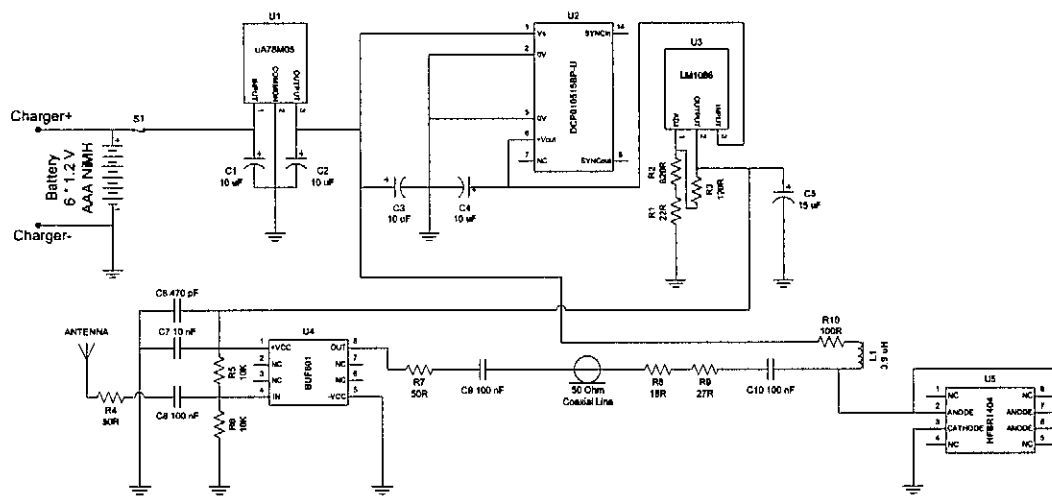


*Figure H-1: Calibration receiver circuit diagram.*

### H.2 Calibration Transmitter Electronics

The circuit diagram for the calibration transmitter, discussed in Section 3.4.3, is plotted in Figure H-2. The four different subsystems in the transmitter (voltage regulation, pulse generation, trigger generation and build-in test equipment) are shaded for easy interpretation.

APPENDIX H: Calibration Facility Circuit Diagrams

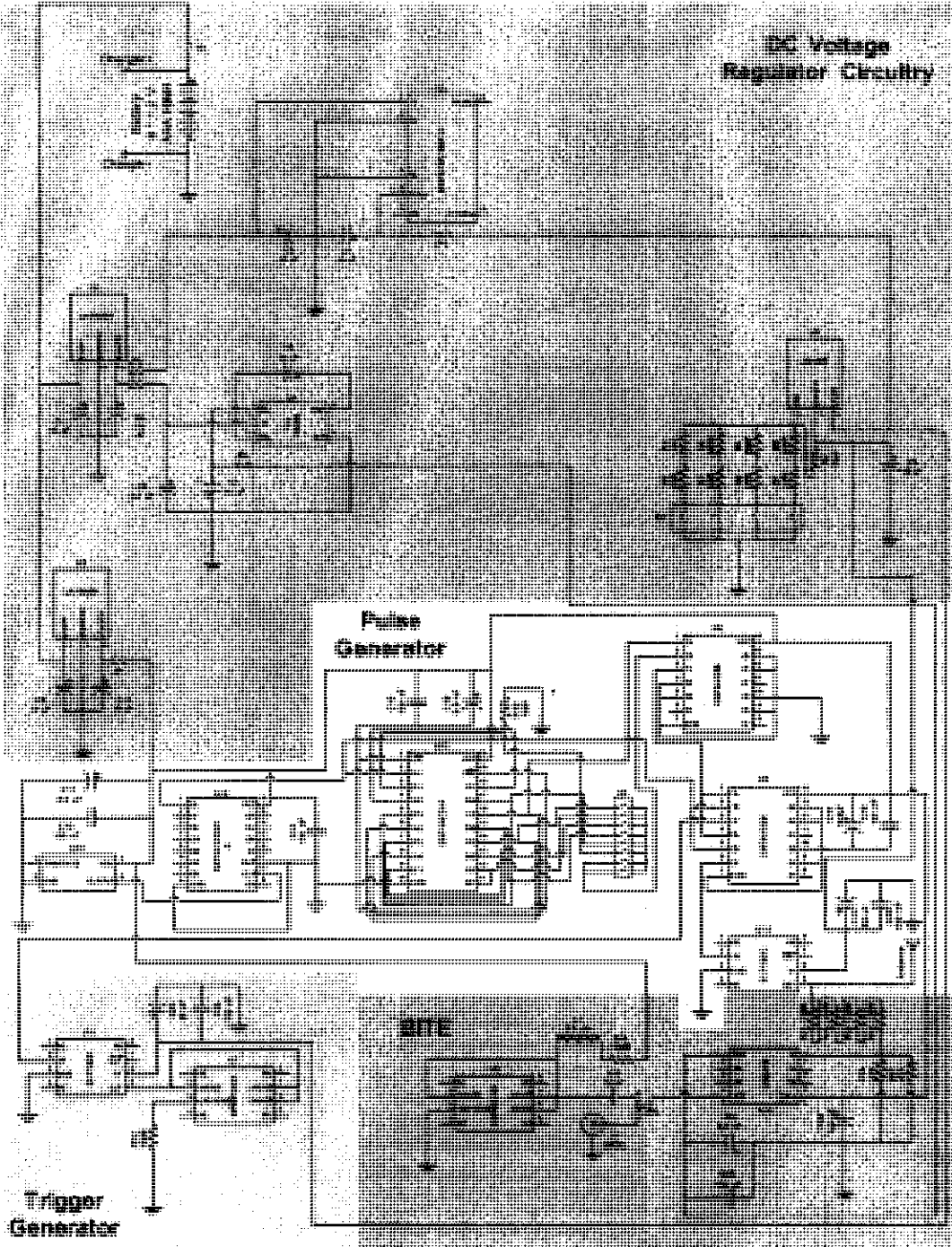


Figure H-2: Calibration transmitter circuit diagram.

# BIBLIOGRAPHY

- [1] P. Annan, *Introduction to GPR: Tutorial*, 8<sup>th</sup> Int'l. Conf. on GPR, Gold Coast, Australia, 23 - 26 May 2000.
- [2] D. J. Daniels, D. J. Gunton and H. F. Scott, "Introduction to Subsurface Radar", *IEE Proceedings F 135(4)*, 1988, pp. 278-320.
- [3] D. M. Claassen, *Electromagnetic Characterization of Wideband Borehole Radar Imaging System*, PhD thesis, University of Oxford, Trinity term 1995.
- [4] J. Hargreaves, *A Multichannel Borehole Radar for Three Dimensional Imaging*, PhD thesis, University of Oxford, Trinity term 1995.
- [5] C. M. Simmat, N. Osman, M. R. Levinson, J. E. Hargreaves & I. M. Mason, "Application of Borehole Radar to VCR Gold Mines in the Witwatersrand Basin, South Africa", *Proc. of the Workshop on Remote Sensing by Low-Frequency Radars*, Naples, Italy, September 20-21, 2001.
- [6] C. M. Simmat, N. Osman, J. E. Hargreaves & I. M. Mason, "Borehole Radar Imaging from Deviating Boreholes", *Proc. SPIE*, Vol. 4758, pp. 404 - 409, 9<sup>th</sup> Int'l. Conf. on GPR, Santa Barbara, USA, 29 April – 2 May 2002.
- [7] *Geology of Southern Africa*, [Online], Impala Platinum Holdings, Available at: <<http://www.implats.co.za/operations/geology.asp>>, Accessed: 12 February 2003.
- [8] I. M. Mason, *Bleskop Draft Final Report 2002-1*, Internal report, GeoMole SA, Sydney, 19 June 2002.
- [9] J. G. Proakis & D. G. Manolakis, *Digital Signal Processing: Principles, Algorithms, and Applications*, Third Edition, Prentice-Hall, New Jersey, 1996.
- [10] A. Papoulis, *The Fourier Integral and its Applications*, McGraw-Hill Book Company, New York, 1962.
- [11] W. L. Stutzman, G. A. Thiele, *Antenna Theory and Design*, Second Edition, John Wiley & Sons, New York, 1998.
- [12] R. E. Ziemer & W. H. Tranter, *Principles of Communications: Systems, Modulation, and Noise*, Fourth Edition, John Wiley & Sons, New York, 1995.

- [13] G. Strang, *Introduction to Linear Algebra*, Wellesley-Cambridge Press, Wellesley, 1993.
- [14] D. M. Pozar, *Microwave Engineering*, Second Edition, John Wiley & Sons, New York, 1998.
- [15] P. Le R. Herselman, *A 500 – 4000 MHz Stepped-Frequency Technique to Measure the Range and Height of a Simple Target Using Vertically Scanning and Dispersive Transmit and Receive Antennas*, Project report, Dept. of E&E Eng., University of Stellenbosch, November 2001.
- [16] M. D. van Wyk, *An Active Antenna for Borehole Pulsed Radar Applications*, MScEng thesis, Dept. of E&E Eng., University of Stellenbosch, December 2001.
- [17] A. A. Lestari, A. G. Yarovoy & L. P. Ligthart, “Characterization Of Transient Bow-Tie Antennas For Ground Penetrating Radar”, *Proc. SPIE*, Vol. 4758, pp. 80 - 85, 9<sup>th</sup> Int’l. Conf. on GPR, Santa Barbara, USA, 29 April – 2 May 2002.
- [18] A. G. Yarovoy, G. Mur & L. P. Ligthart, “GPR Antenna Simulation in Time Domain”, *ibid.*, pp. 74 – 79.
- [19] K. J. Ellefsen & D. L. Wright, “Radiation Pattern Of A Borehole Radar Antenna”, *ibid.*, pp. 68 – 73.
- [20] V. Mikhnev, Y. Maksimovitch & P. Vainikainen, “Analysis of Antennas for Step-Frequency Ground Penetrating Radar”, *ibid.*, pp. 86 – 90.
- [21] C. C. Bantin, “Pulsed Communications Link Between Two Dipoles”, *IEEE AP Magazine*, Vol. 44, No. 5, pp. 75 – 82, 5 October 2002.
- [22] G. S. Smith, “Teaching Antenna Radiation From a Time-Domain Perspective”, *American Journal of Physics*, Vol. 69, No. 3, pp. 288 – 300, March 2001.
- [23] G. S. Smith, “Teaching Antenna Reception and Scattering From a Time-Domain Perspective”, *American Journal of Physics*, Vol. 70, No. 8, pp. 829 – 844, August 2002.
- [24] G. S. Smith, “Erratum: ‘Teaching Antenna Reception and Scattering From a Time-Domain Perspective’ [Am. J. Phys. 70 (8), 829 – 844 (2002)]”, *American Journal of Physics*, Vol. 70, No. 10, p. 1056, October 2002.

- [25] B. Scheers, Y. Plasman, M. Piette, M. Acheroy & A. Vander Vorst, "Laboratory UWB GPR System For Landmine Detection", *Proc. SPIE*, Vol. 4084, pp. 747 – 752, 8<sup>th</sup> Int'l. Conf. on GPR, Gold Coast, Australia, 23 - 26 May 2000.
- [26] B. Woods & P. van der Merwe, *The GEOMOLE Borehole Radar System Incorporating ST-type Optics and the Optics-free Transmitter*, Internal report, GeoMole SA, Stellenbosch, September 2001.
- [27] E. du Sautoy, *An Experimental Study on a 10-100MHz Borehole Radar System*, Project report, Dept. of E&E Eng., University of Stellenbosch, November 2001.
- [28] R. G. Cawthorn, "The Discovery of the Platiniferous Merensky Reef in 1924", *Trans. of the Geol. Soc. of South Africa*, Vol. 102, No. 3, pp. 178 – 183, September 1999.
- [29] R. G. Viring & M. W. Cowell, "The Merensky Reef on Northam Platinum Limited", *ibid.*, pp. 192 – 208.
- [30] K. G. Lomborg, E. S. Martin, M. A. Patterson & J. E. Venter, "The Morphology of Potholes in the UG2 Chromitite Layer and Merensky Reef (Pothole Reef Facies) at Union Section, Rustenburg Platinum Mines", *ibid.*, pp. 209 – 220.
- [31] J. K. Schweitzer, C. J. Hatton & S. A. de Waal, "Economic Potential of the Rooiberg Group: Volcanic Rocks in the Floor and Roof of the Bushveld Complex", *Mineral Deposita*, Vol. 30, pp. 168 – 177, 1995.
- [32] D. R. Jessey, *Layered Cr-Pt Mafic-Ultramafic Complexes*, [Online], Available at: <<http://geology.csupomona.edu/drjessey/class/GSC433/Layered.htm>>, Accessed: 12 February 2003.
- [33] *Platinum Today: Production: South Africa*, [Online], Johnson Matthey, Available at: <<http://www.platinum.matthey.com/production/africa.php>>, Accessed: 12 February 2003.
- [34] *Virtual Travelogue of the Eastern Bushveld Complex*, [Online], University of Witwatersrand, Available at: <[http://www.wits.ac.za/geosciences/bushveld/bush\\_vft1.htm](http://www.wits.ac.za/geosciences/bushveld/bush_vft1.htm)>, Accessed: 11 August 2003.
- [35] F. Hollender & S. Tillard, "Modelling Ground-penetrating Radar Wave Propagation and Reflection with the Jonscher Parameterization", *Geophysics*, Vol. 63, No. 6, pp. 1933-1942, November 1998.

- [36] A. K. Jonscher, "The Universal Dielectric Response", *Nature*, No. 267, pp. 673 – 679, 1977.
- [37] G. R. Olhoeft, "Electrical, Magnetic, and Geometric Properties that Determine Ground Penetrating Radar Performance", *Proc. of GPR'98*, 7<sup>th</sup> Int'l. Conf. on GPR, University of Kansas, pp. 177-182, May 1998.
- [38] M. Rütshlin, *Measurement of Vaal Reef and VCR Foot- and Hanging Wall Dielectric Properties*, Internal report, GeoMole SA, Stellenbosch, July 2001.
- [39] M. Rütshlin, Personal communication from Mr. M. Rütshlin, PhD student, University of Stellenbosch,, January 2003.
- [40] H. A. Haus & J. R. Melcher, *Electromagnetic Fields and Energy Volume 1*, Prentice-Hall, New Jersey, 1989.
- [41] H. A. Haus & J. R. Melcher, *Electromagnetic Fields and Energy Volume 2*, Prentice-Hall, New Jersey, 1989.
- [42] S. Ramo, J. R. Whinnery & T. van Duzer, *Fields and Waves in Communication Electronics*, Third Edition, John Wiley & Sons, New York, 1994.
- [43] A. Ishimaru, *Electromagnetic Wave Propagation, Radiation and Scattering*, Prentice-Hall, New Jersey, 1991.
- [44] I. V. Lindell, *Methods for Electromagnetic Field Analysis*, Clarendon Press, Oxford, 1992.
- [45] L. B. Felsen & N. Marcuvitz, *Radiation and Scattering of Electromagnetic Waves*, Prentice-Hall, New Jersey, 1973.
- [46] J. R. Wait, *Electromagnetic Waves in Stratified Media*, 2<sup>nd</sup> Edition, Pergamon Press, New York, 1970.
- [47] L. M. Brekhovskikh, *Waves in Layered Media*, Academic Press, New York, 1960.
- [48] W. C. Chew, *Waves and Fields in Inhomogeneous Media*, Van Nostrand Reinhold, New York, 1990.
- [49] R. W. P. King, M. Owens & T. T. Wu, *Lateral Electromagnetic Waves*, Springer-Verlag, New York, 1992.

- [50] L. J. du Toit & J. H. Cloete, "Specular Reflection of Plane Waves by a Planar Conductor Coated with Lossy Layers", *Trans. of the SAIEE*, pp. 9 – 13, March 1991.
- [51] M. Born & E. Wolf, *Principles of Optics: Electromagnetic Theory of Propagation, Interference and Diffraction of Light*, Pergamon Press, New York, 1970.
- [52] A. A. Oliner, "Historical Perspectives on Microwave Field Theory", *IEEE Trans. on MTT*, Vol. MTT-32, No. 9, pp. 1022 – 1045, September 1984.
- [53] H. A. Haus, *Waves and Fields in Optoelectronics*, Prentice-Hall, New Jersey, 1984.
- [54] T. Xu & G. A. McMechan, "GPR Attenuation and its Numerical Simulation in 2.5 Dimensions", *Geophysics*, Vol. 62, No. 4, pp. 403 – 414, March - April 1997.
- [55] K. J. Ellefsen, "Effects of Layered Sediments on the Guided Wave in Crosswell Radar Data", *Geophysics*, Vo. 64, No. 6, pp. 1698 – 1707, November – December 1999.
- [56] I. M. Mason & C. M. Simmat, *Dispersion and Attenuation*, Internal report, GeoMole, Sydney, 7 February 2003.
- [57] I. M. Mason, *Modelling Propagation Through a Lossy Medium*, Internal report, GeoMole, Sydney, 9 May 2002.
- [58] G. Turner & A. F. Siggins, "Constant Q Attenuation of Subsurface Radar Pulses", *Geophysics*, Vol. 59 No. 8, pp. 1192 – 1200, August 1994.
- [59] J. D. Irving & R. J. Knight, "Estimation an Correction of Wavelet Dispersion in GPR Data", *Proc. Of the 8<sup>th</sup> Int'l. Conf. on GPR*, Gold Coast, Australia, pp. 561 – 566, 2000.
- [60] N. Ricker, "The Form and Nature of Seismic Waves and the Structure of Seismograms", *Geophysics*, Vol. 5, No. 4, pp. 348 – 366, October 1940.
- [61] N. Ricker, "A Note on the Determination of the Viscosity of Shale from the Measurement of Wavelet Breadth", *Geophysics*, Vol. 6, No. 3, pp. 254 - 258, July 1941.

- [62] N. Ricker, "Wavelet Functions and their Polynomials", *Geophysics*, Vol. 9, pp. 314 – 323, 1944.
- [63] N. Ricker, "The Computation of Output Disturbances from Amplifiers for True Wavelet Inputs", *Geophysics*, Vol. 10, pp. 207 – 220, 1945.
- [64] N. Ricker, "The Form and Laws of Propagation of Seismic Wavelets", *Geophysics*, Vol. 18, pp. 10 – 36, 1953.
- [65] IEEE Std. 211-1997, *IEEE Standard Definitions of Terms for Radio Wave Propagation*, Revision of IEEE Std. 211-1990, IEEE, New York, December 1997.
- [66] A. G. Chernokalov, N. Chubinsky & A. Krampuls, "A Method Of Amplitude And Phase Correction Of GPR System Transient Response", *Proc. SPIE*, Vol. 4084, pp. 324 – 328, 8<sup>th</sup> Int'l. Conf. on GPR, Gold Coast, Australia, 23 - 26 May 2000.
- [67] R. T. Hill, *Surface & Airborne Radar Fundamentals and Systems Acquisition Considerations: Short Course*, 6 – 9 May 2003, CSIR, Pretoria.
- [68] M. I. Skolnik, *Introduction to Radar Systems*, McGraw-Hill, New York, 1962.
- [69] D. K. Barton, *Modern Radar System Analysis*, Artech House, Norwood, 1988.
- [70] F. E. Nathanson, *Radar Design Principles: Signal Processing and the Environment*, Second Edition, Scitech Publishing, New Jersey, 1999.
- [71] P. J. van der Merwe, *The Design of a Monostatic, Ultra Wide Band, VHF, Pulse Radar for Detection of Close-in Targets*, MScEng thesis, Dept. of E&E Eng, University of Stellenbosch, March 2003.
- [72] B. K. Woods, *Development of an Active Pulsed Radar Receiver for a Monostatic Borehole Radar Tool*, MScEng thesis, Dept. of E&E Eng, University of Stellenbosch, March 2003.
- [73] P. L. Herselman *et al.*, *Kleinzee Trial Borehole Radar Survey on 22–27 March 2001*, Internal report, GeoMole SA, Stellenbosch, March 2001.

- [74] W. J. A. van Brakel, M. D. van Wyk, M. Rütshlin & J. H. Cloete, "The Effect Of Wet Drilling In Kaolinitic Strata On Borehole Radar Performance", *Proc. SPIE*, Vol. 4758, pp. 392 - 397, 9<sup>th</sup> Int'l. Conf. on GPR, Santa Barbara, USA, 29 April – 2 May 2002.
- [75] B. Edde, *Radar: Principles, Technology and Applications*, Prentice Hall, 1992.
- [76] T. T. Wu & R. W. P. King, "The Cylindrical Antenna with Non-reflecting Resistive Loading", *IEEE Trans. on AP*, Vol. AP-13, pp. 369-373, May 1965.
- [77] R. H. Clarke & J. Brown, *Diffraction Theory and Antennas*, Ellis Horwood, England, 1980.
- [78] *FEKO User's Manual*, EM Software & Systems, Stellenbosch, South Africa, 28 March 2002.
- [79] *Low Cost, Miniature Fiber Optic Components with ST, SMA, SC and FC Ports*, Technical Data Sheet, Agilent Technologies, S.I., 2000.
- [80] LEMO Technical Data Sheet, S.I., S.a.
- [81] J. Hargreaves, Personal communication from Dr. J. Hargreaves, Electronic engineer, GeoMole , Sydney, 18 March 2002.
- [82] *HP 8970B Noise Figure Meter Operating Manual*, Operating Manual No. 08970-90031, Hewlett Packard, California, September 1987.
- [83] R. E. Collin, *Antennas and Radiowave Propagation*, McGraw-Hill, 1985.
- [84] W. H. Press, B. P. Flannery, S. A. Teukolsky & W. T. Vetterling, "Optimal (Wiener) Filtering with the FFT", §13.3 in *Numerical Recipes in FORTRAN: The Art of Scientific Computing*, Second Edition, Cambridge University Press, Cambridge, 1992.
- [85] P. Z. Peebles, Jr., *Probability, Random Variables, and Random Signal Principles*, Third Edition, McGraw-Hill, 1993.
- [86] M. S. Smiley, *The Wiener Filter*, [Online], Available at: <<http://www.owl.net.rice.edu/~msmiley/elec431/wiener.htm>>, Accessed: 6 August 2003.
- [87] S. Haykin, *Adaptive Filter Theory*, Third Edition, Prentice-Hall, New Jersey, 1996.

- [88] F. Vos, Personal communication with Mr. F. Vos, Managing geologist, Anglo Platinum Rustenburg Section, Rustenburg, 9 September 2002.
- [89] M. Rütshlin, *The Dielectric Properties of the Bleskop Marker*, Internal report, GeoMole SA, Stellenbosch, 12 March 2003.
- [90] F. Vos, *UG2 – UG1 Stratigraphy: Bleskop Shaft*, Internal report, Amplats, Rustenburg Platinum Mines Ltd., Rustenburg Section, Rustenburg, 26 February 2003.
- [91] F. Vos, *Merensky Reef Technical Report and UG2 Reef Technical Report*, Internal report, Amplats, Rustenburg Platinum Mines Ltd., Rustenburg Section, Rustenburg, 23 March 2000.
- [92] *Directory of Mining, Mineral and Related Terms*, [Online], InfoMine Inc., Vancouver BC, Available at: <<http://www.infomine.com/dictionary/>>, Accessed: 24 June 2003.
- [93] *Dictionary*, [Online], CompuCated Technologies, Available at: <<http://dictionary.ansme.com>>, Accessed: 24 June 2003.
- [94] J. H. Cloete & I. M. Mason, *Evaluation of the GeoMole Borehole Radar for the Detection of UG2 Potholes*, Internal report, GeoMole SA, Stellenbosch, 23 November 2001.
- [95] I. M. Mason & J. H. Cloete, *Borehole Radar Project at RPM Bleskop: Preliminary Report 2002 – 1*, Internal report, GeoMole SA, Stellenbosch, 17 June 2002.
- [96] W. J. A. van Brakel & C. M. Simmat, *Comparison between Wessel and Carina's RAT File Interpretations*, Internal report, GeoMole SA, Stellenbosch, 27 June 2002.
- [97] I. M. Mason, J. H. Cloete & P. Le R. Herselman, *GeoMole Borehole Radar Trials Brakspruit, Rustenburg Platinum Mines*, Internal report, GeoMole SA, Stellenbosch, 28 February 2002.
- [98] I. M. Mason & J. H. Cloete, *UG2 Borehole Radar Project at RPM Bleskop Mine, Report 2002 – 1*, Internal report, GeoMole SA, Stellenbosch, 15 July 2002.

- [99] C. Simmat, *Wiener Filters in SeisWin*, [Online], Personal Email from C. Simmat, PhD student, University of Sydney, <carina@es.usyd.edu.au>, 27 March 2003.
- [100] M. Li, *Seismic Applications of Interactive Computational Methods*, MSc thesis, University of Sydney, July 2000.
- [101] M. Rütshlin & J. H. Cloete, *Measurement of Dry Borehole Samples for Kleinzee, March 2001*, Internal report, GeoMole SA, Stellenbosch, 14 June 2001.
- [102] M. W. van Rooyen, *Simple Broadband Measurements of Balanced Loads Using a Network Analyser*, MSc thesis, University of Stellenbosch, 2000.
- [103] I. M. Mason, *Testing the CMTE Navigator at Level 11 of R.P.M., Brakspruit*, Internal report, GeoMole SA, Sydney, December 2001.